
BACKGROUND PROCESSES AFFECTING THE MACHINE-DETECTOR INTERFACE AT FCC-EE

WITH FOCUS ON SYNCHROTRON RADIATION AT 182.5 GeV BEAM ENERGY

DISSERTATION

ZUR ERLANGUNG DES DOKTORGRADES
AN DER FAKULTÄT FÜR MATHEMATIK, INFORMATIK UND NATURWISSENSCHAFTEN
FACHBEREICH PHYSIK

DER UNIVERSITÄT HAMBURG



VORGELEGT VON
MARIAN LÜCKHOF

HAMBURG

2020

Gutachter/innen der Dissertation:	Prof. Dr. Wolfgang Hillert Prof. Dr. Rüdiger Schmidt
Zusammensetzung der Prüfungskommission:	Prof. Dr. Wolfgang Hillert Prof. Dr. Rüdiger Schmidt Prof. Dr. Daniela Pfannkuche Prof. Dr. Eckhard Elsen Dr. Bernhard Holzer
Vorsitzende/r der Prüfungskommission:	Prof. Dr. Daniela Pfannkuche
Datum der Disputation:	12.03.2021
Vorsitzender Fach-Promotionsausschuss PHYSIK: Leiter des Fachbereichs PHYSIK: Dekan der Fakultät MIN:	Prof. Dr. Günter Hans Walter Sigl Prof. Dr. Wolfgang Hansen Prof. Dr. Heinrich Graener

Eidesstattliche Versicherung

Hiermit versichere ich an Eides statt, die vorliegende Dissertationsschrift selbst verfasst und keine anderen als die angegebenen Hilfsmittel und Quellen benutzt zu haben.

Die eingereichte schriftliche Fassung entspricht der auf dem elektronischen Speichermedium.

Die Dissertation wurde in der vorgelegten oder einer ähnlichen Form nicht schon einmal in einem früheren Promotionsverfahren angenommen oder als ungenügend beurteilt.

Hamburg, den 18. Dezember 2020

Unterschrift des Doktoranden

Abstract

Synchrotron radiation is a significant background source at circular lepton colliders. The current interaction region (also referred to as Machine-Detector Interface) design concept at FCC-ee includes only a very basic estimate of this background source. Collimators – as flexible mitigation method of the photon background – are not part of the design yet.

This thesis provides a detailed overview on expectable synchrotron radiation backgrounds, also looking into the impact of different machine conditions. Current design concepts for mitigation are tested, at the same time giving an initial collimation proposal to improve machine and detector protection.

By employing extensive Monte-Carlo simulations, it is possible to characterize the current status and to show which circumstances allow additional upstream collimators to significantly enhance the shielding of the interaction region.

The findings of this thesis can be used to improve the machine-detector interface layout and help as a starting step towards a possible FCC-ee technical design.

Zusammenfassung

Synchrotronstrahlung ist ein wichtiger Untergrundeﬀekt in Ringbeschleunigern, in denen beispielsweise Leptonen zur Kollision gebracht werden. Das aktuelle Konzept der FCC-ee Wechselwirkungszone (auch genannt Machine-Detector Interface) beinhaltet nur eine grundlegende Abschätzung der Synchrotronstrahlung. Kollimatoren – als zusätzliche, flexible Methode zur Verringerung des Photon-Untergrunds – sind nicht Teil des Entwurfs.

Diese Arbeit zielt darauf ab, einen detaillierten Überblick des erwartbaren Synchrotronstrahlungs-Untergrunds bereit zu stellen und bezieht dabei auch Einflüsse durch Änderungen der Strahl-Charakteristik ein. Das aktuelle Konzept der Wechselwirkungszone wird dabei getestet, während gleichzeitig ein erster Vorschlag für den Einsatz von Kollimatoren gemacht wird, um den Schutz von Maschine und Detektor zu verbessern.

Durch ausgedehnte Monte-Carlo Simulationen ist es möglich, den aktuellen Stand zu charakterisieren und zu zeigen, unter welchen Umständen Kollimatoren in der Lage sind, Synchrotronstrahlung noch wirkungsvoller zu reduzieren.

Die Resultate der vorliegenden Arbeit können weiterführend genutzt werden, um erste Schritte in ein technisches Design-Konzept des FCC-ee zu vereinfachen.

Contents

1	Introduction	1
2	Basic Storage Ring Physics	7
2.1	Coordinate System and Design Orbit	8
2.2	Transverse Beam Dynamics	9
2.3	Circular Colliders – Other Relevant Parameters	15
3	The FCC-ee Design	18
3.1	Design Layout of the Collider	18
3.2	The Interaction Region	21
4	Particle Beams and Interactions with Surroundings	31
4.1	Synchrotron Radiation	31
4.2	Thermal Photons	43
4.3	Beam - Gas	47
4.4	Touschek	54
4.5	Beamstrahlung	56
5	The Simulation Tools	58
5.1	Basic Idea	58
5.2	The Tools	59
6	SuperKEKB	61
6.1	Beam Parameters and General Layout	61
6.2	The Interaction Region - Main Challenges	63
7	Simulation Results	74
7.1	The Geometry in MDISim	74
7.2	Beam Generator in MDISim	79
7.3	Upstream Magnets	83
7.4	Statistics/Uncertainties	87
7.5	Default Conditions	87
7.6	Interaction with the Beam-pipe Material	99
7.7	Radiation from Special Magnets	104
7.8	Fixed Mitigation Measures for Synchrotron Radiation	113
7.9	Mitigation Through Collimators	124
8	Conclusion	144
A	Geometry Transformations within MDISim	146

CONTENTS

A.1 General Considerations	146
A.2 SingleBend – An Example	147
Bibliography	151

Acronyms

GDML Geometry Description Markup Language.

BS beamstrahlung.

CDR Conceptual Design Report.

CEPC Circular Electron Positron Collider.

CERN Conseil Européen pour la Recherche Nucléaire.

CLIC Compact Linear Collider.

DESY Deutsches Elektronen Synchrotron.

FCC Future Circular Collider.

FFQ Final Focus Quadrupoles.

HER High Energy Ring.

HERA Hadron Elektron Ring Anlage.

HOM Higher-Order Modes.

ILC International Linear Collider.

IP Interaction Point.

IR Interaction Region.

KEK High Energy Research Facility.

LEP Large Electron Positron Collider.

LER Low Energy Ring.

LHC Large Hadron Collider.

MC Monte-Carlo.

MDI Machine-Detector-Interface.

RF Radio Frequency.

Acronyms

SR Synchrotron Radiation.

Glossary

$B\rho$ Magnetic rigidity.

C Orbit length.

$$C_\gamma = \frac{4\pi}{3} \frac{r_e}{E_0^3}, \text{ constant.}$$

C_0 Design orbit (length) of a machine.

$$C_q = \frac{55}{32\sqrt{3}} \frac{\hbar}{mc}, \text{ constant.}$$

$D(s)$ Dispersion function.

E_b Beam energy.

F_{loss} Individual machine acceptance (loss factor).

$I_{1,2,3,4,5}$ Synchrotron radiation integrals.

$$I_b = N e f n_b, \text{ beam current.}$$

N_{MC} Total number of particles in a beam used in a Monte-Carlo simulation.

N_b Number of bunches/beam.

$N_{\text{loss, MC}}$ Particles lost in Monte-Carlo simulation.

N_p Number of particles/bunches.

N_γ Total number of radiated photons.

P_{SR} Synchrotron radiation power.

P_{tot} Total radiated power.

Q Working point.

R_{loss} Loss rate.

T Temperature.

T_0 Revolution time.

U_0 Energy loss/turn.

$\Psi(s)$ Phase function.

Υ Beamstrahlung parameter.

$$\alpha(s) = -\frac{\beta'(s)}{2}, \text{ derivative of the oscillation amplitude, Twiss parameter.}$$

- α_p Momentum compaction factor.
- $\beta(s)$ Betatron oscillation amplitude.
- $\beta_{x,y}^*$ Beta function at the interaction point.
- p Particle momentum.
- δ $\Delta p/p_0$, energy deviation from design particle.
- $\dot{n}_p = \mathcal{L}\sigma_p$, event rate in a collision.
- ℓ^* Distance between interaction point and first final-focus quadrupole.
- ϵ Courant-Snyder invariant.
- ϵ_c Critical photon energy.
- ϵ_x Horizontal emittance.
- $\eta = \alpha_p - \frac{1}{\gamma^2}$, the phase slip factor.
- γ Lorentz gamma = $\frac{E_b}{m_0c^2}$.
- $\gamma(s) = \frac{1+\alpha^2(s)}{\beta(s)}$, Twiss parameter (not to be confused with the Lorentz gamma factor γ).
- \hbar Reduced Planck constant.
- κ Emittance ratio = $\frac{\epsilon_y}{\epsilon_x}$.
- $\langle\epsilon\rangle$ Average photon energy.
- \mathcal{H} Dispersion \mathcal{H} -function.
- \mathcal{L} Luminosity.
- ρ Bending radius.
- ρ_γ Photon density.
- σ' Beam divergence.
- σ_δ Equilibrium energy spread.
- σ_{loss} Cross section considering machine acceptance.
- σ_p Cross section of a process.
- σ_{scatter} Cross section for certain scattering process.
- $\sigma_{x,y}$ Transverse beam size.
- σ_z Bunch length.
- σ^* Beam size at the interaction point.
- $\sigma_{x,y}^*$ Horizontal and vertical beam size at the interaction point.
- \sqrt{s} Collision energy.
- τ Beam life time.
- τ_x Horizontal damping time.

τ_y Vertical damping time.

τ_z Longitudinal damping time.

θ Bending angle.

θ_x Half crossing angle.

\vec{B} Magnetic induction.

\vec{E} Electric field strength.

\vec{F}_L Lorentz force.

\vec{v} Particle speed.

ξ Beam-beam parameter.

c Speed of light, in vacuum.

f Collision frequency.

$j_{x,y,z}$ Damping partition numbers.

k Normalised quadrupole strength.

k_0 Dipole strength.

k_B Boltzmann constant.

m_0 Particle rest mass.

n_p Particle density.

n_γ Number of photons radiated/particle.

q Particle charge.

r_e Classical electron radius.

$t\bar{t}$ Highest beam energy at FCC-ee with 182.5 GeV, also known as top.

1 | Introduction

This thesis summarizes backgrounds which affect the **Machine-Detector-Interface (MDI)** at **FCC-ee**, focusing on the **Synchrotron Radiation (SR)** background, before suggesting a possible additional mitigation scheme.

After the 2013 Update of the European Strategy for Particle Physics, the **Future Circular Collider (FCC)** Study was launched in 2014. It states that, in order to maintain Europe's leading role in particle physics, an *ambitious post-LHC accelerator project at CERN* shall be proposed. Design studies for accelerator projects in global context shall be launched, focusing on proton-proton and electron-positron colliders which access novel energy regimes.

Especially after the discovery of the Higgs boson in 2012, the emphasis is now on an electron-positron collider which allows to study the Higgs boson *with unprecedented precision* [1]. Intensive R&D programmes have been launched in order to deliver a **Conceptual Design Report (CDR)** as input for the following strategy update starting in 2018. The **FCC** programme consists of three different projects, working towards the final goal of a hadron collider with 100 TeV centre-of-mass energy.

FCC-ee. Considered to be the first stage of the integrated programme, **FCC-ee** describes the concept of a circular lepton collider, used as precision machine to investigate the heaviest particles known in the standard model of particle physics. The **Large Electron Positron Collider (LEP)** at **CERN**, in operation from 1989 to 2000, enhanced the experimental basis of the standard model with precise measurements of the Z and W bosons. Limited in energy, however, it could not reach the Higgs threshold, reaching a final (maximum) center-of-mass energy of 209 GeV.

The implementation of **FCC-ee** is foreseen in stages, starting at 45.6 GeV beam energy to study the Z and continuing at 80 GeV with the W boson.

A third stage at 120 GeV allows to do detailed measurements of the Higgs boson, before moving on to the highest foreseen beam energy of 182.5 GeV for investigations of the top quark – the operational model is also shown in Fig. 1.1 [2].

FCC-hh. A hadron collider with centre-of-mass energy as high as 100 TeV. It is supposed to allow particle physics observations at highest energies and address questions of Beyond-Standard-Model physics. Based on challenging high-field dipoles with fields in the 16 T to 20 T range, **FCC-hh** would reach 80 km to 100 km in circumference, which also defines the size of **FCC-ee** as both machines shall be installed in the same tunnel [3].

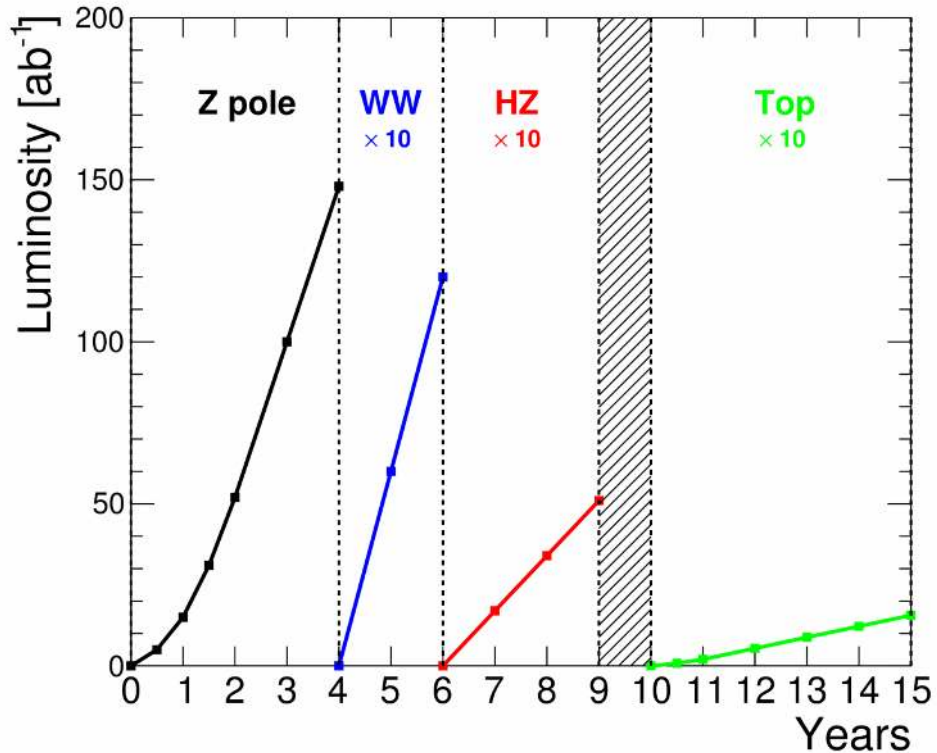


Figure 1.1: The operational model for **FCC-ee**. The plot is directly taken from [2] and shows integrated luminosities for the Z running (black), the WW threshold (blue), Higgs factory (red) and the top pair (green) as a function of time (years of operation). A one-year shutdown to prepare the collider for highest energy is highlighted by the pattern.

FCC-eh. For further explorations of the proton quark structure, the **FCC** study includes an option for electron-proton collisions. For this scenario, one of the interaction points of the hadron machine could be devoted to collisions of 60 GeV electrons with the 50 TeV proton beam [3].

The strategy update from June 2020 considers the Higgs boson to play a key role in the experimental exploration of the fundamental laws of physics. And, although **LHC** with the *High-Luminosity Upgrade* presently remains the leading experimental facility for this purpose, the strategy update expressed strong favour for a new electron-positron collider, also based on input provided by the recently published **FCC CDR** documents [2, 3]. Such a facility, a *Higgs-factory*, is supposed to produce the Higgs boson in a very clean environment to enable precision measurements [4]. The proposed collider could be either linear or circular.

Linear electron-positron colliders benefit from the absence of strong energy losses due to synchrotron radiation and can therefore reach centre-of-mass energies of 200 GeV to 500 GeV (**International Linear Collider (ILC)**, [5]) or even 1.5 TeV to 3 TeV (**Compact Linear Collider (CLIC)** [6]). These projects, proposed at a time when the exact mass of the Higgs was still unknown, pose alternative designs to a circular collider and are still under consideration as possible Higgs-factories.

Also in the discussion is the **Circular Electron Positron Collider (CEPC)** in China. The **CEPC** is of comparable size as **FCC**, but supposed to operate in an regime of 90 GeV to 250 GeV centre-of-mass energy, therefore reaching not as high as **FCC-ee** [7].

Given the size of FCC-hh, the electron-positron collider FCC-ee would be able to reach collision energies (\sqrt{s}) ranging from 90.2 GeV to 365 GeV with – at the same time – acceptable energy loss due to synchrotron radiation.

Despite the energy loss in the arcs, a circular machine can host several instead of only one experiment and produce higher luminosities based on increased repetition rates, as shown in Fig. 1.2 (which considers the FCC-ee with two interaction points (IP)). Still, energy and intensity of the synchrotron radiation can pose serious constraints on machine and experiments. Which is the reason why the machine design needs to be based on careful estimates of the radiation backgrounds.

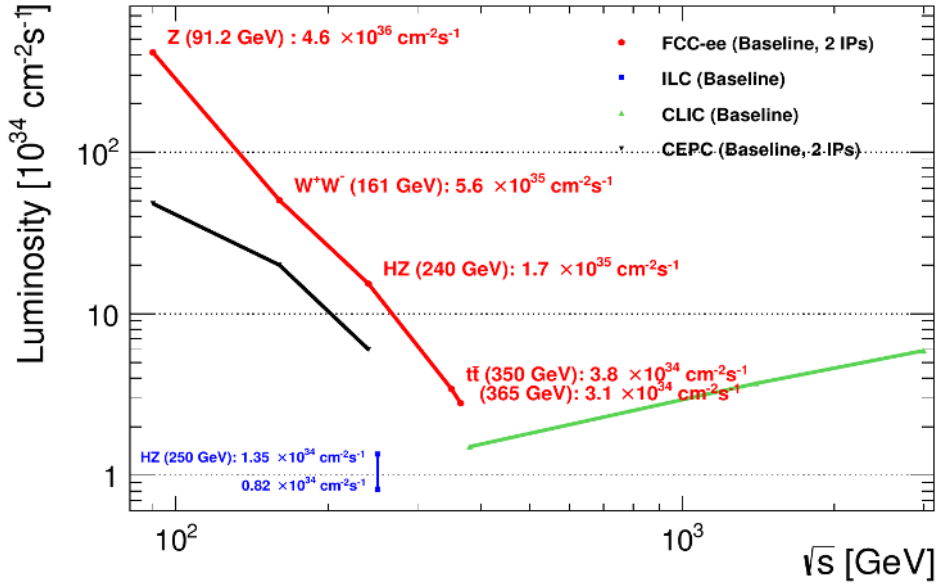


Figure 1.2: Baseline design luminosity for 2 interaction points (IP) as function of the centre-of-mass energy \sqrt{s} . For comparison, the plot also shows luminosity goals for ILC (vertical blue line), CEPC (black) and CLIC (green) [8]. For the energy regime ≤ 1 TeV, FCC-ee provides highest luminosities.

Integrating accelerator and detector, the Interaction Region (IR) is a key issue of the collider design and ensures its success. Designing the interaction region means to find a trade-off between requirements from machine side as well as those from experiment side with the detector specifications. Only then, the accelerator can deliver sufficiently high collision rates with, at the same time, an acceptably low level of backgrounds.

This process needs to take into account all possible background sources and evaluate their relevance with respect to operation conditions and sensitive equipment (such as machine components or the detector).

Main background sources for FCC-ee are synchrotron radiation – photons radiated by beam particles – and off-energy particles due to scattering of the beam with residual gas atoms/molecules in the beam pipe.

While the MDI is an integral part of the initial design phase, it remains important during operation as well. Backgrounds change with running conditions, therefore ensuring smooth and safe machine and detector operation means to constantly account for changing backgrounds in the MDI.

This thesis enhances the current understanding of the synchrotron radiation back-

ground and its impact on the design of the FCC-ee MDI. Experience from past accelerators such as LEP at CERN or HERA at DESY proofed the impact of this background source on machine operation [9, 10, 11]. Not carefully evaluating backgrounds through synchrotron radiation could even render operation of the machine impossible.

Towards the CDR, the MDI design layout has been studied considering several aspects. Not only synchrotron radiation, but also backgrounds due to beam-gas scattering and those driven by luminosity. Also the magnetic layout with solenoid compensation scheme and the heating from Higher-Order Modes (HOM) have been taken into account [12]. These efforts result in a rather advanced layout, which – based on the limits of a conceptual study – is expected to be capable of handling the dominating backgrounds. This design will be used in the framework of the presented study.

The following characteristics are identified to play key roles in the MDI design phase:

- reaching high luminosities
- tolerable levels of background at the detectors, also considering the synchrotron radiation load
- masking scheme with fixed synchrotron-radiation masks and shielding of the beam-pipe
- movable absorbers (collimators) further upstream
- dimensions of the vacuum chamber, based on beam-sizes and available space
- flexibility with respect to future upgrades

The literature (basically summarized in the CDR) discussed these topics, some of which in depth, others need more refined studies in order to arrive at reliable estimates of expectable conditions in the FCC-ee MDI. Synchrotron radiation is certainly one such aspect that needs more detailed, extensive work.

As has been pointed out for instance in [13, 12], a number of steps are missing towards a better understanding of the synchrotron radiation background:

- more realistic optics, including the detector solenoid
- magnet misalignments and changes in closed orbit, eventually a beam passing off center through the final focus magnets
- more realistic beam distributions, including tails
- collimation scheme

In the framework of this thesis, a study is presented which aims to achieve more detailed simulations by addressing these points.

By doing so, the simulation tools have been tested and enhanced in order to arrive at a tool-set which can provide more reliable results. Conditions in the MDI can change at any time during operation – for example a steering error can cause the beam to deviate from the design orbit. As a result, it might pass off-axis through the strong final-focus magnets, which means that synchrotron radiation

of considerable energy is generated very close to the detector.

The **MDI** design phase needs to take such scenarios into account, not only to test the existing mitigation measures but also to develop a dedicated collimation scheme further upstream of the experiments.

The work in the context of this thesis will test the current **MDI** layout and answer, by means of extended Monte-Carlo simulations, how well the detector is protected. Initial assumptions which lead to the current layout are investigated to examine whether or not those have been reasonable or need modifications.

The literature so far does not address a collimation scheme in detail, including systematic studies. However, experience from past machines – such as **LEP** – showed the importance of having a system of movable collimators to mitigate synchrotron radiation at the experiments.

Collimators can be expected to significantly relax the conditions around the detector. They can intercept fractions of the synchrotron radiation at distances of several tens or even hundreds of meters upstream of the experiment and prevent part of the synchrotron radiation from even reaching the detector.

Simulation results presented in this thesis are based on **MDISim**, a tool-kit developed at **CERN** (and still under development) which provides an interface to **Mad-X**, **Root** and **Geant4** [14]. It is used to set up the accelerator geometry and, considering the optics functions, generate a realistic beam distribution at some point upstream of the detector. The beam is subsequently tracked downstream towards the experiment, taking into account interactions with magnetic fields and the material of the beam-pipe.

Each beam particle will generate synchrotron radiation photons, which in turn can be tracked – also considering the interaction with matter. Thus, it is possible to construct a detailed picture of conditions in the central interaction region with respect to synchrotron radiation.

By having access to the geometry of accelerator and detector elements, collimators can be inserted upstream of the interaction point, which allows to study the impact of these elements on the photon background. At the same time, the initial distribution of particles in the beam can be changed, allowing to examine the influence of these conditions on the photon background.

The results show that the assumptions which have shaped the initial design phase of the **FCC-ee MDI** hold, at least assuming rather ideal conditions in the machine. However, strong evidence can be found for the dependence of these conditions on the initial distribution of particles in the beam. For example, considering significant tails lead to completely different scenarios.

The introduction of collimators upstream certainly helps to mitigate the synchrotron radiation background and relax conditions at the detector. At the same time, initial conditions noticeably influence the effect of upstream collimators.

Hence, simulation results and therefore the estimate of synchrotron radiation backgrounds depends strongly on initial conditions of the beam. This is one manifestation of the fact that background conditions in the **MDI** cannot be finally answered. It is an effort which needs constant adjustments and careful evaluation of constantly changing background conditions during machine operation.

This thesis focuses on the synchrotron radiation background for **FCC-ee** at maximum beam energy of 182.5 GeV.

After giving a short introduction to fundamental accelerator physics in Chapter 2, a detailed description of FCC-ee and the interaction region with presentation of the current MDI design based on the CDR follows in Chapter 3.

Interactions of the beam with its' surroundings are described in Chapter 4, summarizing background processes which are important for FCC-ee.

Chapter 5 gives an overview on MDISim, explaining the simulation tools used to study synchrotron radiation backgrounds in the FCC-ee MDI.

Chapter 6 contains a summary of the MDI design at SuperKEKB, highlighting why it is interesting for the FCC-ee design study and therefore modeled with MDISim to benchmark the simulation tools.

An extensive description of the simulation results is done in Chapter 7. The accelerator geometry used in Monte-Carlo (MC) simulations is introduced first. Default synchrotron radiation backgrounds are estimated and current mitigation measures foreseen in the CDR design are tested.

The layout for a possible collimation scheme is proposed in the last part of this chapter. This collimation scheme is a first step towards an overall sufficient protection scheme for the FCC-ee MDI which can adapt to changing background conditions.

The conclusion in Chapter 8 summarizes the outcome of the simulations and highlights the most important points.

2 | Basic Storage Ring Physics

Accelerators are designed to accelerate particle beams along a certain defined trajectory, the *design orbit*. Electromagnetic fields are used to steer charged particles, using the Lorentz force \vec{F}_L .

$$\vec{F}_L = q(\vec{E} + \vec{v} \times \vec{B}) \quad (2.1)$$

Where q is the charge of the particle species, \vec{E} the electric and \vec{B} magnetic field, respectively. \vec{v} denotes the particle speed.

Particles in modern accelerators often travel close to speed of light c , such that magnetic fields become more relevant: an electric field of 3×10^8 V/m would be required to achieve the same effect as a magnetic field of 1 T ($\vec{E} = c\vec{B}$), which is far out of reach for technical applications [15].

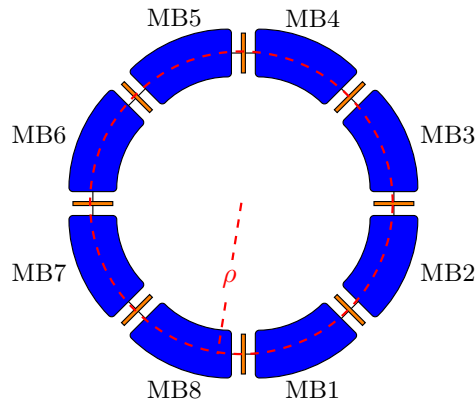


Figure 2.1: Example sketch for an accelerator, considering elements of linear optics: *bending magnets* which basically define the design orbit (with the radius ρ) and *quadrupoles* to provide transverse focusing all along the ring. Field free sections between the magnets are referred to as *drift spaces*.

Hence, in all modern particle accelerators, magnets are used to guide the particle beams. These machines can either be linear (linear accelerator, linac) or circular, as is the case for storage rings such as FCC-ee. In a storage ring, the beam can circulate many times around the design orbit, defined by bending magnets, as depicted in Fig. 2.1.

Since the particles all have a non-zero and differing angular divergence, the beam would soon dissipate and particles would be lost in collisions with the beam-pipe wall (vacuum chamber). Thus, focusing magnets (quadrupoles) are used to steer the particles back towards the ideal orbit, thereby focusing the beam repeatedly around the orbit. The oscillations caused by this repeated focusing are called *betatron oscillations*.

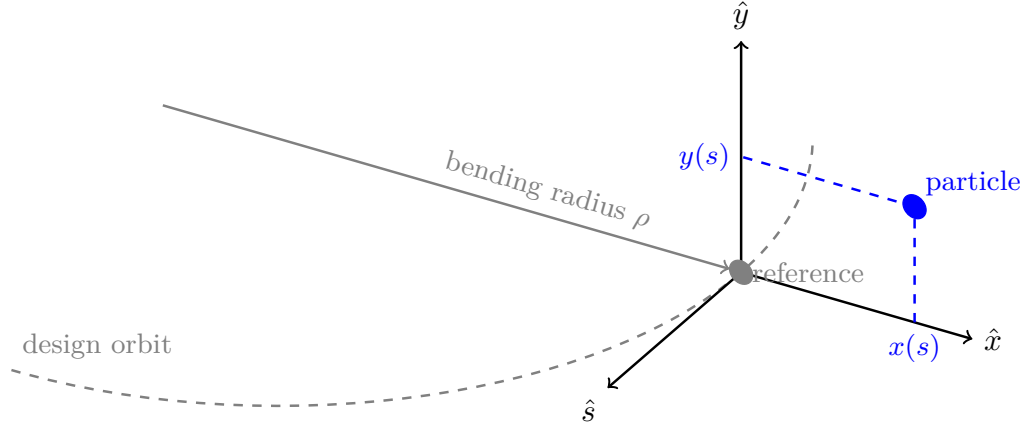


Figure 2.2: Frenet-Serret or Courant Snyder coordinate system used to describe particle motion in an accelerator. The rectangular system is based on the ideal orbit and moves with the reference particle (having exactly design energy) around the orbit, with the longitudinal axis always pointing in direction of motion. \hat{x} and \hat{y} are referred to as transverse dimensions and define together with \hat{s} the three axes of the coordinate system.

In the following, basic beam dynamics in such an accelerator will be discussed, with focus on *linear beam dynamics*, considering dipole and quadrupole magnets as the main components. This allows to introduce key concepts and quantities required to better understand the following chapters.

2.1 Coordinate System and Design Orbit

As introduced above, dipole magnets define the design (or ideal) orbit of a circular accelerator. In order to describe the particle motion, a rectangular coordinate system is used, which is centered on the design orbit. The longitudinal axis \hat{s} is directed tangentially along the particle motion, as shown in Fig. 2.2. \hat{x} and \hat{y} are referred to as *transverse coordinates*, where \hat{x} is directed radially outwards.

Charged particles in magnetic dipole fields will travel on a circular path with constant radius, given that Lorentz and centrifugal forces cancel each other. The radius ρ of such a circle would then depend on the particle energy, or momentum p – a particle with design energy would have the *design momentum* p_0 . From this condition, it is possible to derive a quantity known as *magnetic rigidity* $B\rho$.

$$B\rho = \frac{p_0}{|q|} \quad (2.2)$$

Equation (2.2) shows how the particle momentum influences the bending radius: higher energy particles with $p > p_0$ are less efficiently bent in a given magnetic field of strength \vec{B} , leading to higher bending radius, an effect called *dispersion*. The magnetic rigidity further allows to estimate the general size of a storage ring, once the particle species and design energy are known.

Following a more general approach by taking higher order fields into account, magnetic fields can be described by a *multipole expansion*. Since transverse beam dimensions (x, y) can safely be assumed as much smaller than the radius ρ of a

circular accelerator, it is possible to expand the magnetic field as given in Eq. (2.3) [15].

$$B_y = B_{y0} + \frac{dB_y}{dx}x + \frac{1}{2!} \frac{d^2B_y}{dx^2}x^2 + \frac{1}{3!} \frac{d^3B_y}{dx^3}x^3 + \dots \quad (2.3)$$

Which can also be written in an energy independent form.

$$\frac{q}{p}B_y(x) = \frac{q}{p}B_{y0} + \frac{q}{p} \frac{dB_y}{dx}x + \frac{q}{p} \frac{1}{2!} \frac{d^2B_y}{dx^2}x^2 + \frac{q}{p} \frac{1}{3!} \frac{d^3B_y}{dx^3}x^3 + \dots \quad (2.4)$$

$$\frac{q}{p}B_y(x) = \frac{1}{\rho} + kx + \frac{1}{2!}mx^2 + \frac{1}{3!}ox^3 \quad (2.5)$$

The resulting terms in Eq. (2.5) can be associated with certain magnet types as demonstrated in Table 2.1. The lowest two terms in red are dipole and quadrupole contribution. Since these are either constant or depend linear on the transverse particle position, they are referred to as *linear optics*.

Table 2.1: Most important multipoles and corresponding magnets with their effects on the beam.

Multipole	Magnet	Effect
Dipole	$\frac{1}{\rho} = \frac{q}{p}B_{y0}$	Bending
Quadrupole	$k = \frac{q}{p} \frac{dB_y}{dx}$	Focusing
Sextupole	$m = \frac{q}{p} \frac{d^2B_y}{dx^2}$	Chromaticity compensation
Octupole	$o = \frac{q}{p} \frac{d^3B_y}{dx^3}$	field error/ compensation

All higher order multipoles are either used for specific compensation schemes (for example chromaticity or field error compensation/cancellation) or describe field errors due to imperfections in the fabrication process.

The presented study is mainly concerned with linear optics, where dipoles and quadrupoles are the essential elements to guide the beam along the design path.

2.2 Transverse Beam Dynamics

One of the first steps in designing a storage ring is to specify the design orbit by dipole magnets, as those bend a beam of charged particles (illustrated in Fig. 2.1). The coordinate system which moves around the design orbit but also specifies transverse dimensions has been introduced earlier: the *Frenet-Serret* or *Courant-Snyder* system.

While the beam circulates around the machine, the particles of the beam will also move in the transverse plane.

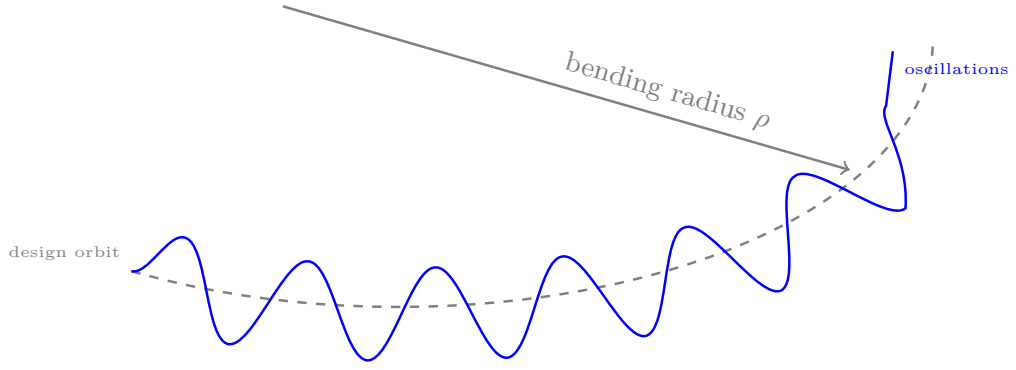


Figure 2.3: Transverse betatron oscillations. Focusing quadrupole forces repeatedly kick the particle back towards the design orbit, thereby introducing oscillations, as indicated by the blue curve.

Equation of Motion – Betatron Oscillation, Emittance and Tune

Equations (2.6) and (2.7) describe the general equations of motion for a particle in the transverse planes [15].

$$x(s)'' + \left(\frac{1}{\rho(s)^2} - k(s) \right) x(s) = \frac{1}{\rho(s)} \frac{\Delta p}{p_0} \quad (2.6)$$

$$y''(s) + k(s)y(s) = 0 \quad (2.7)$$

As mentioned earlier, this introduction will assume only linear magnetic fields acting on the beam, which considers dipole and quadrupole magnets. Coupling between both transverse planes (x and y) can thus be assumed as sufficiently weak such that in the following both planes are considered to be *decoupled*.

For simplicity, this discussion only refers to particle motion in the horizontal plane, looking at an ideal particle with 0 dispersion $D(s)$. This approach leads to the *homogeneous Hill's equation*.

$$x''(s) + k(s)x(s) = 0 \quad (2.8)$$

With the *normalised quadrupole strength* $k(s)$. Following the general convention, negative $k(s)$ means a horizontally focusing quadrupole, while it defocuses vertically. Vice versa for positive $k(s)$ [16].

The Hill's equation describes transverse oscillations around the particle orbit, as depicted in Fig. 2.3. General solutions are found to be of the form

$$x(s) = \sqrt{\epsilon \beta(s)} \cos(\Psi(s) + \phi) \quad (2.9)$$

$$x'(s) = -\sqrt{\frac{\epsilon}{\beta(s)}} (\alpha(s) \cos(\Psi(s) + \phi) + \sin(\Psi(s) + \phi)) \quad (2.10)$$

These oscillations are called betatron oscillations, which requires to introduce new quantities: the *amplitude function* $\beta(s)$, $\alpha(s)$ (basically the derivative of $\beta(s)$) and a constant of particle motion, ϵ (see next paragraph for details). Note, that amplitude $\beta(s)$ as well as the phase $\Psi(s)$ both depend on the actual location around the ring.

According to Liouville's theorem, the phase space volume is constant over time, given that the equations of motion are canonical. In an accelerator, this condition

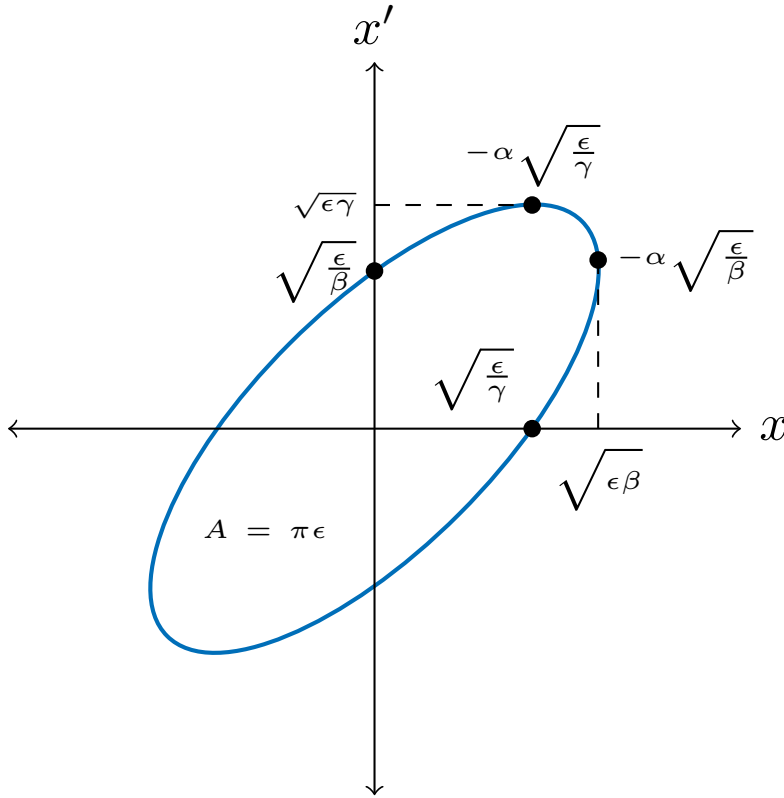


Figure 2.4: Illustration for the phase space ellipse in the horizontal plane (x, x') . As indicated, the Twiss parameters $\alpha(s)$, $\beta(s)$ and $\gamma(s)$ specify orientation and shape of the ellipse, while the area stays constant with an emittance ϵ .

is in general valid which allows to consider the area of the *phase space ellipse* $A = \pi\epsilon$ as Courant-Snyder invariant [15]. This invariant is also called the *geometric emittance* and characterized by ϵ , as in Eq. (2.11).

Note, that synchrotron radiation leads to energy loss and introduces damping of the oscillation (as laid out in more detail below), such that Liouville's theorem does not apply anymore.

If the transverse particle position is observed at the same location after each turn, the points would successively map out an ellipse in phase space, as depicted in Fig. 2.4 and 2.5. As the area of the phase space ellipse is constant over time, only shape and orientation of that ellipse change, described with the Twiss parameters $\beta(s)$, $\alpha(s)$ and $\gamma(s) \equiv \frac{1+\alpha^2(s)}{\beta(s)}$.

$$\gamma(s)x^2(s) + 2\alpha(s)x(s)x'(s) + \beta(s)x'^2(s) = \epsilon \quad (2.11)$$

Figure 2.4 additionally visualizes the concept. Emittance and amplitude function further allow to derive the beam size as in Eq. (2.12), assuming a Gaussian shaped distribution and corresponding to one standard deviation.

$$\sigma = \sqrt{\epsilon\beta(s)} \quad (2.12)$$

The description of transverse motion can be simplified by introducing *normalised coordinates*, which are related to the physical transverse coordinates through a

Floquet transformation [17] according to

$$\vec{x}_N = T \vec{x} \quad (2.13)$$

with the transformation matrix T (2.14).

$$T = \begin{pmatrix} \frac{1}{\sqrt{\beta}} & 0 \\ \frac{\alpha}{\sqrt{\beta}} & \frac{1}{\sqrt{\beta}} \end{pmatrix} \quad (2.14)$$

Solutions in normalised coordinates are of the following form

$$x_N = A \sin(2\pi Q_x n + \phi_0) \quad (2.15)$$

$$x'_N = A \cos(2\pi Q_x n + \phi_0) \quad (2.16)$$

Where n denotes the number of turns for turn-by-turn motion, with A and ϕ_0 being amplitude and initial phase. Q_x is the horizontal betatron tune (introduced in the next paragraph). These coordinates transform the phase space ellipse to a simple circle, as depicted in Fig. 2.5.

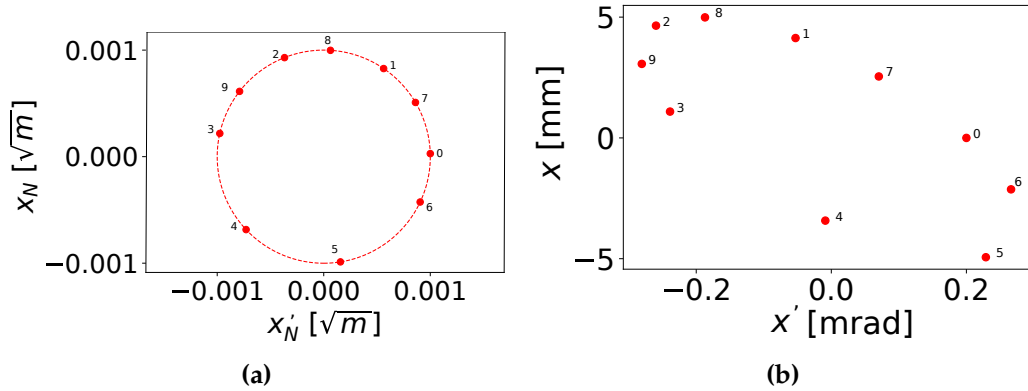


Figure 2.5: Example points for the evolution of particle motion in phase space. (a) horizontal particle positions observed at the same reference point for ten subsequent turns in normalised coordinates. (b) the same points transferred back to physical transverse coordinates, resulting in an ellipse in phase space.

$\Psi(s) = \int_0^s \frac{ds}{\beta(s)}$ allows to define a *phase advance* between two points in the accelerator, s_1 and s_2 .

$$\Delta\Psi = \Psi(s_1) - \Psi(s_2) = \int_{s_1}^{s_2} ds \frac{1}{\beta(s)} \quad (2.17)$$

Such that it is possible to calculate the total number of betatron oscillations over one turn around the machine, called the *betatron tune*, Eq. (2.18). This quantity is also referred to as the *working point* Q .

$$Q \equiv \frac{1}{2\pi} \oint ds \frac{1}{\beta(s)} \quad (2.18)$$

Magnet fabrication is inevitably subject to imperfections, causing the final magnet to have field errors. Field errors lead to additional deviations from the design orbit as the particle experiences unwanted deflections.

As in a storage ring the magnetic lattice periodically repeats itself every new turn,

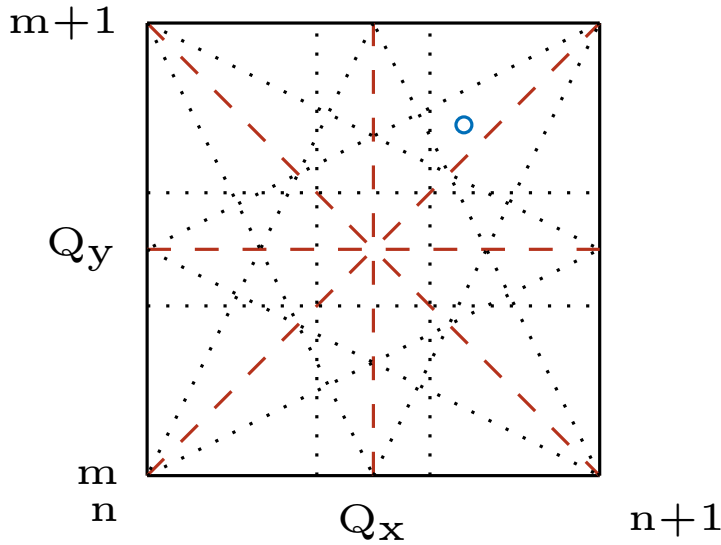


Figure 2.6: Example sketch of a Q_x - Q_y diagram. It shows the resonance lines for first (solid line), second (dashed line) and third (dotted line) order. One possible working point is shown in blue.

the particle eventually gets deflected at the same location over and over again. Such a resonance causes the oscillation amplitude (and thereby the beam size) to grow and can possibly lead to particle loss.

Due to this effect, safe operation of an accelerator means to choose a working point Q sufficiently far away from resonances. Certain resonances are caused by each magnet family individually – the most dominant one by dipole magnets according to:

$$Q = p \quad (2.19)$$

with $p \in \mathbb{Z}$. Quadrupoles, sextupoles and all higher order multipoles can drive additional resonances, such that general optical resonances of order m occur in both planes for

$$mQ = p, \quad (2.20)$$

where $m, p \in \mathbb{Z}$. If the lattice introduces coupling between horizontal and vertical plane, for example through detector solenoids or skew quadrupoles, coupling resonances may occur if the condition

$$mQ_x + nQ_y = p \quad (2.21)$$

is fulfilled, again with $m, n, p \in \mathbb{Z}$. In a Q_x - Q_y diagram, resonance regions can be visualized with lines, as schematically shown in Fig. 2.6. The working point of an accelerator must be chosen carefully, to avoid those resonance lines. Especially for a storage ring, where the beam is supposed to circulate for up to several hours, even weak resonances can cause considerable beam blow up.

Dispersion and Momentum Compaction

The discussion so far assumed that the momentum deviation δ ,

$$\delta \equiv \Delta p / p_0 \quad (2.22)$$

is 0. However, particles will lose energy while travelling around the machine – for example by emitting synchrotron radiation. Energy loss means that the particle momentum p will deviate from the design, with the direct consequence of orbit changes in the dipoles, as illustrated in Fig. 2.7.

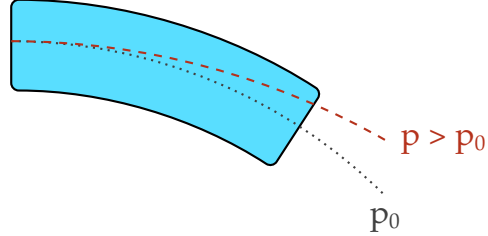


Figure 2.7: Trajectory through a dipole magnet for two particles. The reference particle (p_0) would follow the design orbit, while a particle with positive momentum offset ($p > p_0$) is less deflected in the bend, following a longer orbit.

The *inhomogeneous Hill's equation*, Eq. (2.6) shows that a momentum offset only contributes for $1/\rho(s) \neq 0$ which is the case in dipole magnets. The following assumes a homogeneous field without gradient and therefore $k(s) = 0$, such that Eq. (2.6) simplifies [15].

$$x''(s) + \frac{1}{\rho^2(s)}x(s) = \frac{1}{\rho(s)}\delta \quad (2.23)$$

The solution – called *dispersion function* $D(s)$ – defines the closed orbit for a momentum offset $\delta = 1$. According to Eq. (2.23), with the resulting dispersion function, a particle has an offset x_{tot} , that is comprised of the actual horizontal amplitude $x(s)$ with the additional offset caused by an arbitrary momentum deviation $\delta \neq 0$.

$$x_{\text{tot}}(s) = x(s) + D(s)\delta \quad (2.24)$$

The particle would then oscillate not around the design orbit but a new *dispersion orbit*.

The practical consequence of dispersion is a change in orbit length. It is either longer or shorter than the design orbit C_0 , for particles having higher or less than design energy (Fig. 2.7 visualizes the effect).

The time for a particle to fulfill one turn around the machine and the arrival time at the RF will therefore also change. Differences in orbit length C can be described using the *momentum compaction* α_p .

$$\Delta C = \delta \oint ds \frac{D_x(s)}{\rho(s)} = \alpha_p \delta \quad (2.25)$$

The time required for one full turn around the ring of length C now depends on the particle energy, where the new orbit length is proportional to the energy deviation δ .

An alternative definition of the momentum compaction factor is based on the *synchrotron radiation integrals*, see Section 4.1. It then directly expresses a relation between the change of beam parameters and the emission of synchrotron radiation.

The phase slip factor η can be introduced

$$\eta = \alpha_p - \frac{1}{\gamma^2}. \quad (2.26)$$

Which accounts for a change in arrival time of particles at the RF cavities and becomes zero at transition energy, where all particles would arrive at the same time (independent of their energy). The phase slip factor η allows to express the change in arrival time proportional to the energy deviation δ .

$$\frac{\Delta T}{T} = \left(\alpha_p - \frac{1}{\gamma^2} \right) \delta = \eta \delta \quad (2.27)$$

Since particles with different momentum offset travel either longer ($\delta > 0$) or shorter ($\delta < 0$) orbit lengths than the synchronous particle ($\delta = 0$), they arrive either later or earlier at the RF cavity, which leads to *synchrotron oscillations*.

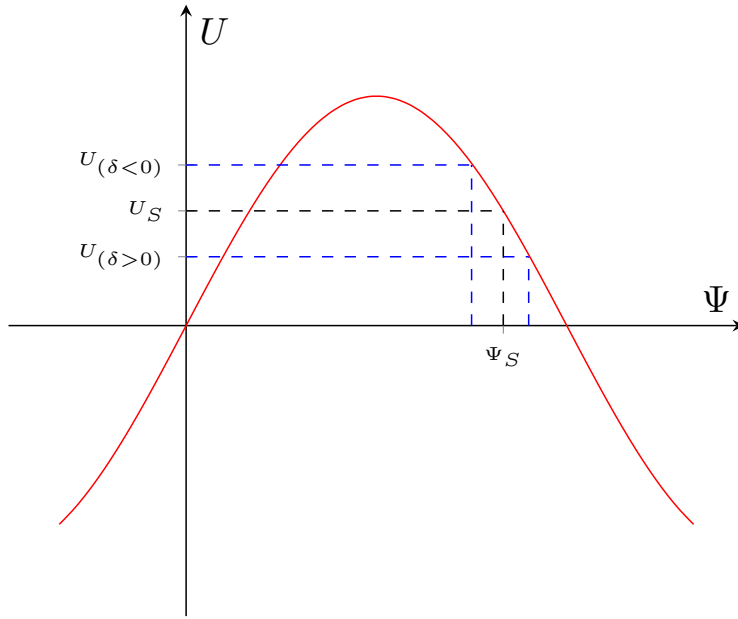


Figure 2.8: The accelerating RF voltage U as function of the phase Ψ . A synchronous particle would arrive with the synchronous phase Ψ_S and receive just the right amount of voltage U_Ψ . Particles with more ($\delta > 0$) or less ($\delta < 0$) than design momentum receive either less or more accelerating voltage. This effect reduces the momentum offset and leads to phase focussing.

According to Fig. 2.8 the particles thus receive a different portion of the accelerating voltage (either less or more than the synchronous particle) and therefore will move towards the synchronous phase due to this *phase focussing* effect of the RF.

2.3 Circular Colliders – Other Relevant Parameters

Luminosity

Colliders are used to produce physics events by bringing particles into collision, such that they interact according to certain physical laws. The event rate \dot{n}_p should therefore be as high as possible and is an important quantity used to define a *luminosity* \mathcal{L} .

$$\dot{n}_p = \mathcal{L} \sigma_p \quad (2.28)$$

The cross section σ_p is a natural constant describing the probability for a certain physics process to occur. Since it is constant, the only way to increase an event rate is to provide more luminosity \mathcal{L} .

The luminosity can be increased either by having more particles in a bunch of a given beam or by decreasing the beam size at the interaction point, σ^* – this becomes immediately clear by looking at Eq. (2.29).

$$\mathcal{L} = \frac{f N_b N_1 N_2}{4\pi \sigma_x^* \sigma_y^*} \quad (2.29)$$

N_p are the numbers of particles in a bunch of beam 1 and 2, respectively. f describes the collision frequency and N_b the number of bunches in a beam. $\sigma_{x,y}^*$ describe horizontal and vertical beam sizes at the interaction point.

However, there are limits as to how much one can increase the luminosity. For once, from a certain particle population N_p in a bunch, collective effects will occur. On the other hand, increasing the bunch population and with it the beam current I_b means that more RF power is required to restore the energy loss due to synchrotron radiation. But the available RF power is of course not unlimited (operational costs need to be kept on a manageable level).

Another reason is a limited reduction of the beam size at the interaction point due to the finite focussing forces in the final focus quadrupoles (small beta insertion) [15].

Beam-Beam Tune Shift

While the beams are brought into collision, particles of one bunch will be subject to the Lorentz force, generated by electromagnetic fields of the opposing beam. These fields (either attractive or repulsive, depending on the particle charge) are highly non-linear and will deflect particles, depending on the particle amplitude [18].

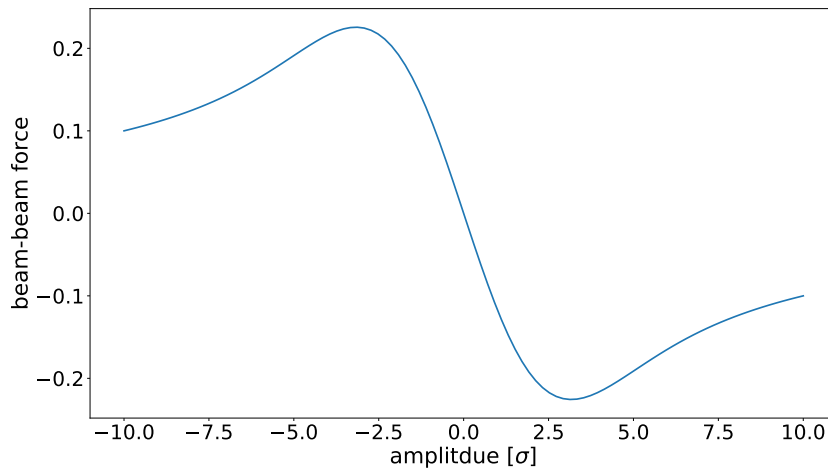


Figure 2.9: Visualization of the beam-beam force for a round beam. The force is almost linear in the amplitude range of $\pm 1 \sigma$. Outside of that region, the force is highly non-linear.

Figure 2.9 shows the beam-beam force in the case of round beams, as a function of the particle amplitude, given in σ . For small amplitudes (less or close to 1σ), the force is linear and can be considered to act as an additional quadrupole, introducing a tune shift ΔQ .

This tune shift depends on the phase advance between interaction points and can be described with the so called *beam-beam parameter* ξ , which is defined for both planes individually [18].

$$\xi_{x,y} = \frac{Nr_e\beta_{x,y}^*}{2\pi\gamma\sigma_{x,y}(\sigma_x^* + \sigma_y^*)} \quad (2.30)$$

Note, that the beam-beam parameter in Eq. (2.30) is given for the assumption of non-round beams with $\sigma_x \neq \sigma_y$ – as is the case for lepton machines such as FCC-ee. r_e denotes the classical electron radius, while $\beta_{x,y}^*$ is the amplitude function at the interaction point.

For small ξ and a tune far away from linear resonance lines, $\xi \approx \Delta Q$ can be assumed [18].

Very dense beams with small beam sizes $\sigma_{x,y}$ and high bunch populations N_p are used in modern colliders to increase luminosity, as can be seen from Eq. (2.29). At the same time, these factors enhance the beam-beam parameter, according to Eq. (2.30), while at the same time high energies with large Lorentz factors γ reduce it.

Particles at large amplitudes are subject to increasingly non-linear forces, the tune shift is dependent on the amplitude and can not be considered linear any longer. In general, effects arising from this beam-beam deflection can have several consequences – such as unstable beams, beam blow up or a reduction of the lifetime τ .

3 | The FCC-ee Design

The following chapter briefly summarizes the design of the FCC-ee, before detailing the interaction region in particular. A short description of the underlying design principles is provided, which helps to understand how FCC-ee is supposed to reach into unprecedented energy and luminosity regimes.

The introduction then highlights how synchrotron radiation drives the interaction region design. It describes an asymmetric optics layout which is required to reduce the critical energy of photons (ϵ_c) generated upstream.

The magnet layout around the interaction point and the current design of the central detector chamber complete this summary. The chapter therefore provides the baseline understanding of the interaction region and limitations by synchrotron radiation before moving on to the simulations and analysis of the photon background.

3.1 Design Layout of the Collider

FCC-ee shall provide a flexible research infrastructure for particle physics. The machine, following the FCC-hh footprint, would reach a circumference of about 100 km (see also Fig. 3.1 (b)). Such a scale allows beam energies as high as 182.5 GeV with a tolerable synchrotron radiation loss of 50 MW per beam – a global constraint for the entire design [2].

The machine is supposed to run at different energy levels, starting with 45.6 GeV and 80 GeV to study the Z and W bosons. Operation at 120 GeV would allow detailed examinations of the Higgs boson and ZH couplings, while the highest beam energy of 182.5 GeV (the $t\bar{t}$ threshold) would be used to study the top quark – the heaviest particle known in the standard model. These energy levels are unprecedented and therefore pose new limitations with respect to synchrotron radiation.

Unprecedented luminosities are supposed to be delivered at two experiments, which are located in the straight sections, indicated as PA and PG in Fig. 3.1 (a). This layout assumes a two-fold symmetry to match the footprint of the hadron machine FCC-hh. Except for the interaction regions, where the lepton machine would deviate by around 12 m to 15 m – necessary to allow an asymmetric interaction region layout which reduces the energy of synchrotron radiation photons generated upstream of the interaction point.

By focusing the beams to small sizes of μm in the horizontal and nm in the vertical plane, the particle density and therefore the luminosity is increased [21].

Using this technique, FCC-ee is supposed to reach luminosities as high as

3.1. DESIGN LAYOUT OF THE COLLIDER

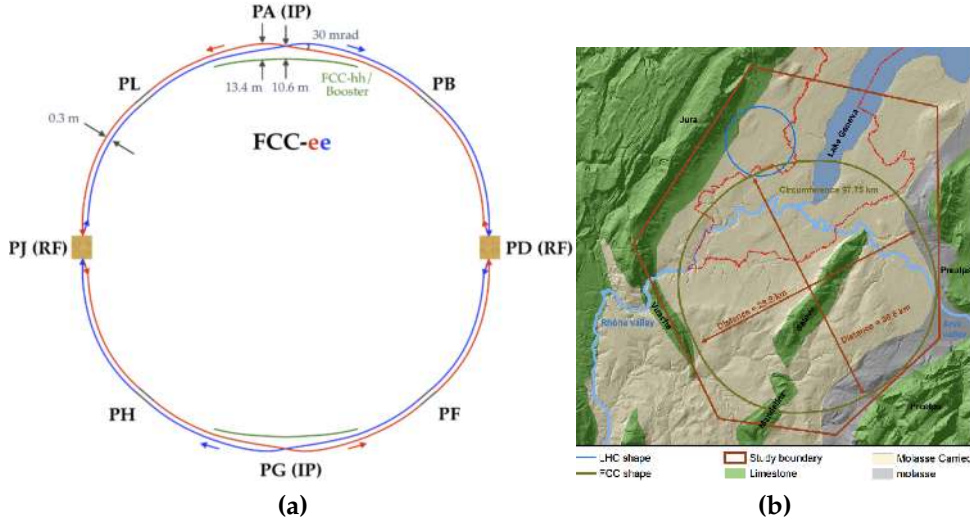


Figure 3.1: (a) double ring design for *FCC-ee* [19]. The plot shows the current layout according to the CDR [2]. Two straight sections, *PJ* and *PD* host the RF, while interaction points are located in the straight sections *PA* and *PG* (labelled with *IP* in the plot). (b) possible location of the machine in the Geneva area close to *CERN* [20]. The blue circle depicts the location of the current LHC.

$2.3 \times 10^{36} \text{ cm}^{-2} \text{ s}^{-1}$, which is foreseen at the Z pole. This is only possible with such small beam sizes and a high beam current I_b of almost 1.4 A, using more than 16000 bunches per beam in a double ring layout.

For the higher energies, beam currents are reduced by subsequently lowering the number of bunches N_b . Smaller beam currents are required to match the global constraint of 50 MW energy loss per beam due to synchrotron radiation. Table 3.1 summarizes important parameters for all beam energies E_b .

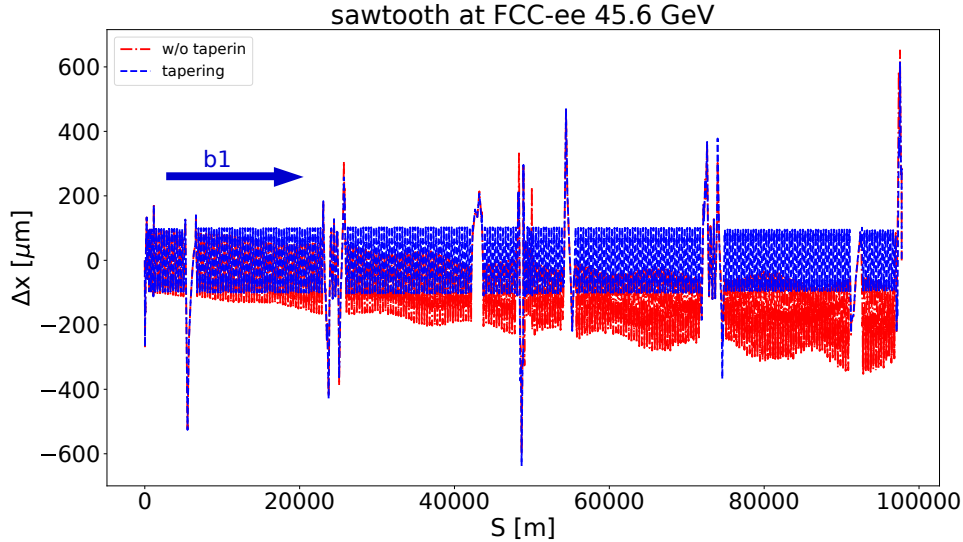


Figure 3.2: The effect of tapering at lowest beam energy in *FCC-ee*, 45.6 GeV. While the red curve presents the uncorrected horizontal closed orbit with radiation, the blue curve shows the closed orbit with radiation and tapering. Tapering prevents the orbit deviations from growing continuously worse and keeps them on a rather constant level. A Δx of 0 μm would mean to be on the reference orbit.

The double ring design of *FCC-ee* allows to simultaneously adjust the field of all magnets to the local beam energy, a method called *tapering*. The only exception

are detector solenoids, which are kept constant at 2 T.

Tapering is required to account for energy losses from synchrotron radiation and to reduce the so called *sawtooth effect*. This effect describes the motion of the beam, which drifts towards the centre of the ring due to the energy loss, before being pushed outside again after the energy is restored in the **RF** cavities.

An energy deviation of $\pm 1.2\%$ between entry and exit at the **RF** would create intolerable optics distortion due to the horizontal dispersion in the arcs (optics deviation). Tapering allows to keep these deviations from the ideal orbit C_0 at a tolerable level – an example of the effect at 45.6 GeV is shown in Fig. 3.2. While deviations from the closed orbit grow continuously for a case with synchrotron radiation without tapering (shown in **red**), these deviations are kept on a constant level with tapering (shown in **blue**).

Machine Parameters

Table 3.1: Selection of machine parameters for FCC-ee. The beam current is denoted as I_b and the bunch population as N_p , while N_b refers to the number of bunches. $\sigma_{x,y}^*$ and $\beta_{x,y}^*$ denote the horizontal and vertical beam size and betatron amplitude at the interaction point, respectively. The bunch length σ_z is shown considering either synchrotron radiation (SR) or collisions (beamstrahlung, BS). The lifetime τ closes this exempt of design parameters – a full list can be consulted in the **CDR** [2].

	Z	W	H (ZH)	$t\bar{t}$
E_b [Gev]	45.6	80	120	182.5
\mathcal{L} [$10^{34} \text{ cm}^{-2}\text{s}^{-1}$]	230	28	8.5	1.55
N_b	16640	2000	328	48
N_p [10^{11}]	1.7	1.5	1.8	2.3
I_b [mA]	1390	147	29	5.4
ϵ_x [nm]	0.27	0.83	0.63	1.46
ϵ_y [pm]	1.0	1.7	1.3	2.9
β_x^* [m]	0.15	0.2	0.3	1.0
β_y^* [mm]	0.8	1.0	1.0	1.6
σ_x^* [μm]	6.4	13	13.7	38.2
σ_y^* [nm]	28	41	36	68
σ_z (SR) [mm]	3.5	3	3.15	1.97
σ_z (BS) [mm]	12.1	6	5.3	2.54
RF Acceptance [%]	1.9	2.3	2.3	3.36
DA Acceptance [%]	1.3	1.3	1.7	-2.8/+2.4
U_0 [GeV]	0.036	0.34	1.72	9.21
P_{SR} [MW]	50	50	50	50
τ (Rad. Bhabha) [min]	68	59	38	40
τ (beamstrahlung) [min]	>200	>200	18	18

3.2 The Interaction Region

Beams with high intensities, that are supposed to reach novel energy regimes for circular e^+e^- machines, require a careful design of the interaction region. A balance between luminosity goals and synchrotron radiation puts strict constraints on the design. These limitations affect engineering design (magnets, vacuum system, etc) as well as machine optics and are based on prior experience, for example from B-factories or LEP [9].

The interaction region – as a special part of the collider – needs to meet several requirements:

- Large drift spaces are needed to host high-energy particle physics experiments.
- High luminosities require strong focusing very close to the interaction point, leading to an increase of the betatron amplitudes.
- Critical energies of incoming synchrotron radiation from upstream dipoles need to be reduced as much as possible.
- The dispersion needs to be reduced when entering the straight section and shall vanish at the experiment (interaction point) in order to not dilute the luminosity.

The corresponding lattice structure is also called *mini-beta insertion* [22].

Photon Energies – Considerations for the IR

Experience from LEP showed the importance of the synchrotron radiation background. It affected machine operation as well as the environment of experiments [9].

In particular, the critical energy ϵ_c of photons coming from the last upstream dipole magnets shall be kept as low as possible. At LEP2, the average critical energy from the last upstream dipoles was around 72 keV (over a distance of 260 m from the interaction point); critical energies in the arc dipoles were about a factor 10 higher. Further details are presented in Section 7.9.

For the FCC-ee design it was chosen to accordingly limit the critical energy to ≤ 100 keV over the last 500 m upstream of the interaction point, while it shall be kept below 1 MeV over the length of the entire machine. This limit of 1 MeV ensures to avoid neutron production. Furthermore, the last upstream dipole magnet should be located at least 100 m away from the interaction point.

These energy limits have been set based on the rapidly changing interaction of photons with matter in energy regions between 10 keV to 100 keV – as demonstrated in Fig. 3.3 for lead. Photon energies up to 10 keV are dominated by the Photoelectric effect and therefore subject mostly to absorption in the material. Even though the cross section for Rayleigh scattering reaches a maximum within the same energy range, the probability for Rayleigh scattering is not as high as for the Photoelectric effect.

At higher energies though, scattering becomes more and more relevant, as the cross section for the Compton-Effect increases between 10 keV to 100 keV, before

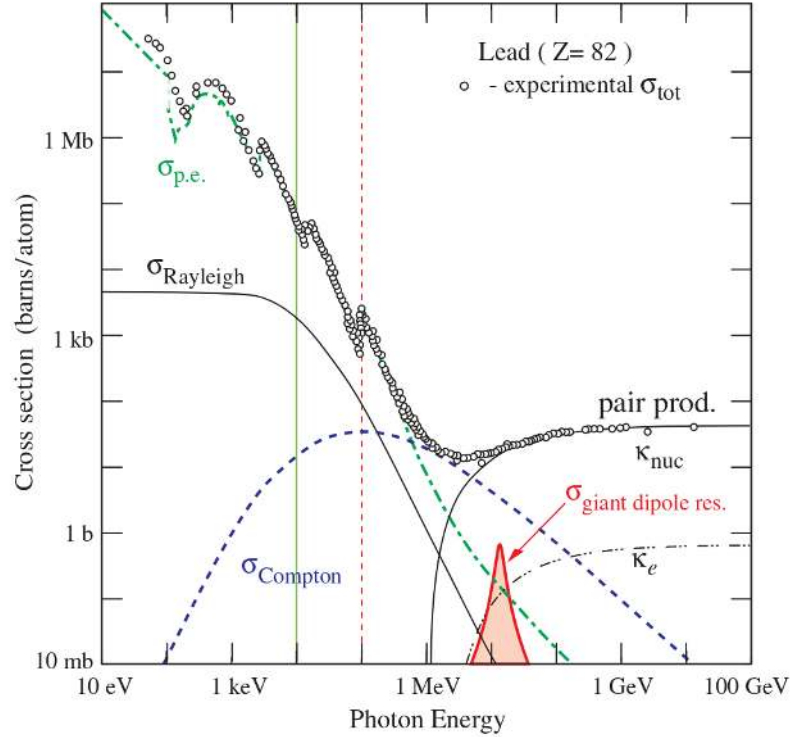


Figure 3.3: Cross section of different photon interactions with lead as function of the photon energy. The Photoelectric effect dominates the entire regime of low energies from 0.1 keV to 10 keV – in this range, photons are mostly absorbed by the material. The cross section drops further between 1 keV to 100 keV. At the same time, Compton-scattering becomes more and more likely before dominating around 1 MeV. Scattering processes do not directly absorb photons, therefore photon energies between 10 keV to 100 keV or higher are difficult to handle. Vertical lines highlight 10 keV (green) and 100 keV (red). Courtesy Helmut Burkhardt, CERN.

dominating around 1 MeV photon energy (according to the blue dashed line in Fig. 3.3). Compton scattered photons will be much more difficult to stop even in heavy material (high atomic number Z), as they are less likely to be just absorbed but rather scatter around several times.

Entering the MeV regime, the cross section for pair production increases fast, which is even more disadvantageous in terms of background mitigation, as it leads to additional e^+e^- pairs. Around 10 MeV, Giant dipole resonance generates neutron flux, a process that should be avoided as well (radioactive activation of components).

Geometry Layout and Asymmetric IR Optics

The interaction region layout is based on an asymmetric optics concept for incoming and outgoing beams with a horizontal crossing angle of $2\theta_x = 30$ mrad at the interaction points. Figure 3.4 presents the interaction region within ± 1.5 km around the interaction point and displays the asymmetric layout: incoming beams are bent only gently on the last 500 m upstream but strongly downstream of the interaction point.

Figure 3.5 shows the betatron oscillation amplitude and dispersion as examples of the optics around ± 1 km of the interaction point (at FCC-ee $t\bar{t}$). A rather regular

3.2. THE INTERACTION REGION

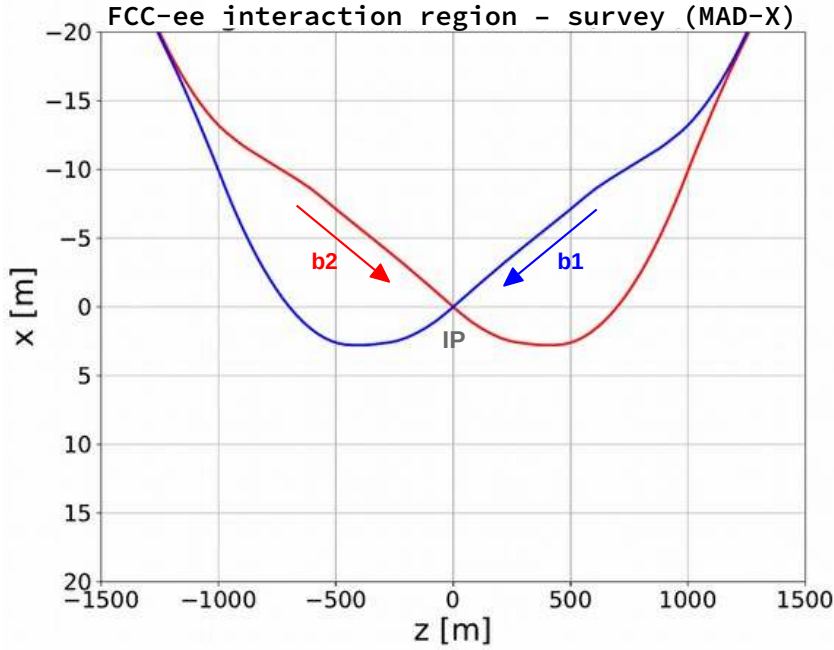


Figure 3.4: The interaction region in more detail showing how the incoming beam follows an almost straight trajectory. Outgoing beams are bent more strongly in order to return to the FCC-hh footprint. Maximum distance between the FCC-hh footprint and the FCC-ee ring in this area amounts to 12 m to 15 m – entirely resulting from the asymmetric interaction region and horizontal crossing angle.

oscillation pattern in the arc (between -1000 m to -800 m upstream and 350 m to 1000 m downstream) is changing into an asymmetric pattern within the interaction region. This asymmetry is a direct result from reducing the critical energy of the last upstream dipole magnets by increasing the bending radius to meet the constraint of ≤ 100 keV. As mentioned above, these magnets appear almost straight in Fig. 3.4.

Very close around the interaction point, the highest peaks for the betatron oscillation can be identified. Those are caused by the strong focusing in the final focus magnets.

Figure 3.5 (b) shows how the horizontal dispersion is reduced to zero at the experiment. In general, the dispersion reflects the asymmetry of the interaction region layout.

A selection of dipole magnets upstream and downstream of the interaction point is characterized in Table 3.2. The table compares analytic estimates (as defined in Section 4.1) for critical energy ϵ_c , synchrotron radiation power P_{SR} and mean photon energy $\langle e \rangle$, based on the bending radius ρ and the magnetic field B . Note the differences between upstream and downstream magnets. More details will be discussed during the analysis in Chapter 7, where also a sketch of the arrangement of the upstream dipoles is provided with Fig. 7.15.

3.2. THE INTERACTION REGION

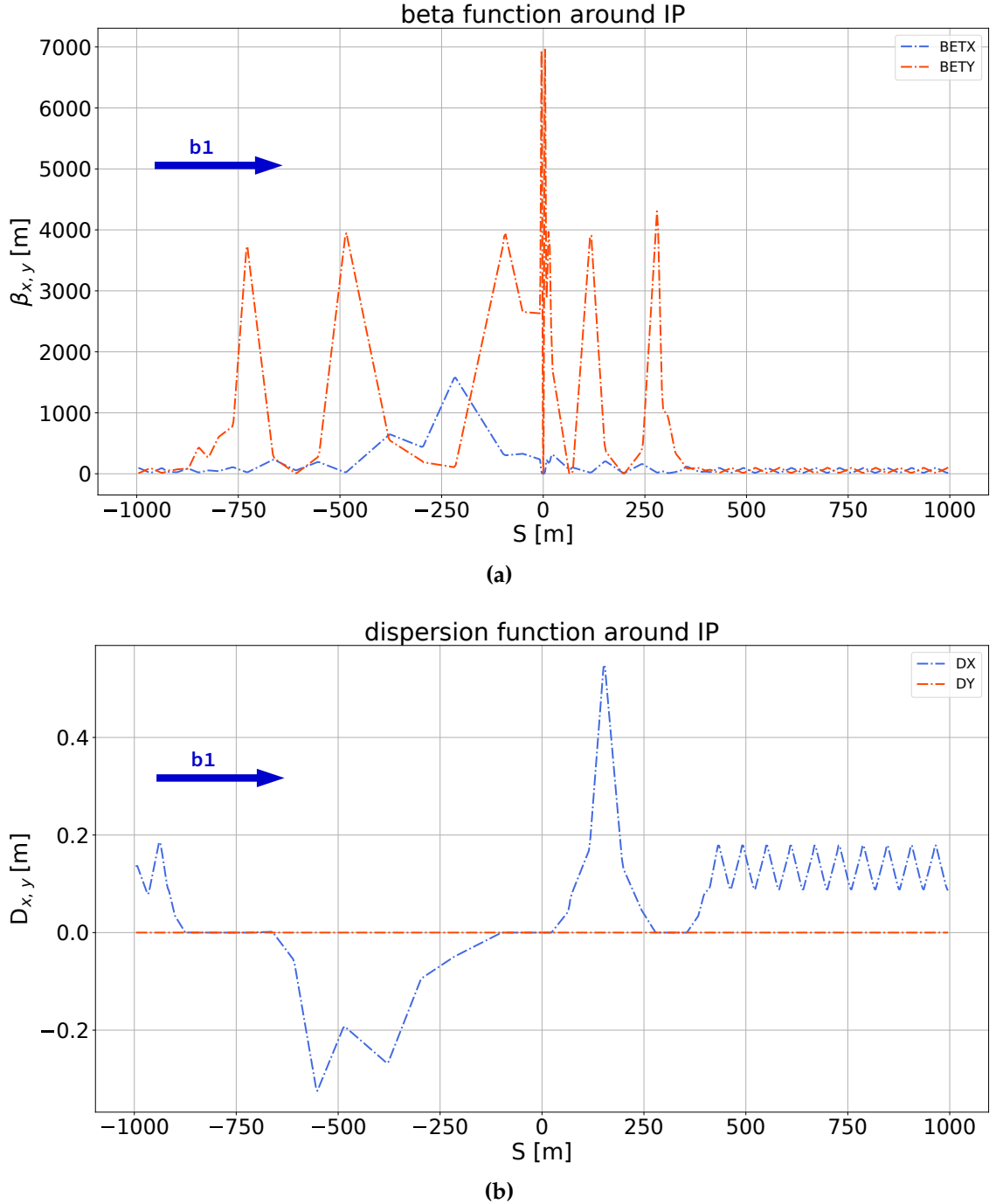


Figure 3.5: FCC-ee interaction region optics at $t\bar{t}$, within ± 1 km around the interaction point ($S = 0$ m). The beam direction is indicated by a blue arrow. This example demonstrates the asymmetry in the optics upstream and downstream of the interaction point. (a) horizontal and vertical beta function. The change of rather regular oscillations into an irregular pattern is a result of the asymmetry, required to reduce the critical energies of upstream dipole magnets. (b) dispersion function, showing how the horizontal dispersion is reduced to 0 at the experiment ($S = 0$ m).

Final Focus Magnets & Detector Solenoid

Strong focusing magnets close to the interaction point are supposed to provide small beam sizes required to reach high luminosities. The typical small-beta-insertion includes a quadrupole doublet on either side, having a total of four **Final Focus Quadrupoles (FFQ)**. In general, these quadrupoles should be located

3.2. THE INTERACTION REGION

Table 3.2: Selection of parameters characterizing upstream (upper half) and downstream (lower half) dipole magnets closest to the interaction point. These analytic estimates are given for the top energy, 182.5 GeV. The two last upstream dipole magnets, BC1L.2 and BWL.2 are highlighted in blue. Note that L describes an integral length. The smaller the magnet location S, the closer this magnet is located to the interaction point.

NAME	S [m]	L [m]	ϵ_c [keV]	ρ [km]	B [T]	P_{SR} [kW]	$\langle\epsilon\rangle$ [keV]
BWL.2	215.4	116.2	98.9	136.4	0.00446	0.506	30.4
BC1L.2	294.8	75.29	89.2	151.16	0.00403	0.267	27.5
BC2L.2	550.8	62.23	224	60.12	-0.0101	1.4	69.1
BC3L.2	606.3	51.36	578	23.34	0.0261	7.64	178
BC4L.2	661.2	50.8	596	22.61	0.0269	8.05	184
BC1.1	63.68	40.61	691	19.52	0.0312	8.64	213
BC2.1	68.55	0.7729	1430	9.41	-0.0647	0.708	441
BC3.1	114.6	41.93	742	18.16	0.0335	10.3	229
BC4.1	150.5	31.18	336	40.10	0.0152	1.57	104
BC5.1	195.6	41.08	972	13.88	0.0439	17.3	299

close to the interaction point – the distance between front face of the innermost quadrupole and the interaction point is denoted as ℓ^* .

Since FCC-ee is designed with a horizontal crossing angle and supposed to have separate quadrupoles for both beams, ℓ^* was chosen to be 2.2 m [19]. The doublet consists of the two magnets QC1L/R and QC2L/R (where L stands for left, representing upstream quadrupoles for beam 1. Downstream quadrupoles for beam 1 are on the right, therefore labelled with R).

As the parameters in Tab. 3.3 show, the doublets are located symmetrically around the interaction point and reach high gradients with about 79 T/m to 100 T/m between lowest and highest beam-energy. The first quadrupole QC1 is vertically focusing, therefore the gradient is negative, while the second quadrupole focuses horizontally.

This region is also covered by the detector solenoid. It has a cylindrical shape, stretching over 4 m on either side of the interaction point and measures 3.8 m in diameter.

The operating field was chosen to be a constant 2 T – independent of the machine operating conditions. The field strength was chosen as a compromise between requirements for the experiment and minimization of vertical emittance blow-up. An ℓ^* of only 2.2 m thus means that the final focus elements will be partly covered by the detector solenoid, which requires the installation of shielding and a compensating solenoid – further details can be found in the CDR and references therein [2].

Requirements for Experiments

Synchrotron radiation drives the MDI design as this type of background needs to be reduced as much as possible at the location of the experiments, especially with high beam energies such as 182.5 GeV. However, despite considerations due to background, the design must ensure enough space for the detectors as well. Two different types of backgrounds are considered in background studies for the

3.2. THE INTERACTION REGION

Table 3.3: Location, length and gradient of the final focus magnets in the FCC-ee interaction region at lowest and highest beam energy. Note that the magnets are sliced in three (QC1) and two (QC2) slices to move the centre of focusing closer to the interaction point. The slices can have different polarity, for example at the Z only one slice is vertically focusing while all three slices are at $t\bar{t}$ [2].

NAME	S [m]	L [m]	B'(Z) [T/m]	B'(t \bar{t}) [T/m]
QC1L1	2.2	1.2	-78.6	-100
QC1L2	3.48	1	7.01	-100
QC1L3	4.56	1	28.4	-100
QC2L1	5.86	1.25	2.29	58.81
QC2L2	7.19	1.25	9.05	68.18
QC1R1	-2.2	1.2	-79.66	-99.60
QC1R2	-3.48	1	5.16	-99.85
QC1R3	-4.56	1	36.55	-99.73
QC2R1	-5.86	1.25	7.61	63.03
QC2R2	-7.19	1.25	4.09	77.91

detector, machine induced and luminosity driven.

All these backgrounds potentially lead to additional occupancy in the detectors and need to be carefully estimated. While high intensities need consideration at the Z running with luminosities in the order $10^{36} \text{ cm}^{-2}\text{s}^{-1}$, while the energy of synchrotron radiation is more challenging at the highest beam energy of 182.5 GeV [2].

This section only briefly summarizes the impact of these background types – on the detector in particular – by reporting which additional studies have been performed outside of the analysis within this thesis to arrive at a more complete picture of the background situation in the FCC-ee interaction region. These studies influence the design of the central detector chamber model shown below and used in the context of this study.

Luminosity dependent. Once the beams are brought into collision, additional backgrounds are generated during interactions of the beams with each other. High energy photons can be radiated from *beamstrahlung* (the mechanism is explained in Section 4.5). These photons either scatter with each other, generate additional e^+e^- pairs or interact with the electromagnetic field of the opposing bunch and produce hadrons.

Detailed simulations (invoking the entire detector geometry) have estimated the effects of pair production and $\gamma\gamma \rightarrow \text{hadron}$ processes at lowest and maximum beam energy. Both effects, pair creation and the hadron production, appear to cause only moderate rates in the detector and are therefore not considered as serious limitation in terms of occupancies or energy – the results are described in [2, 23].

Machine-Induced. More important in the context of this thesis are the machine induced backgrounds such as synchrotron radiation or beam-gas scattering. Those are always present, even if only one beam circulates in the machine. Synchrotron radiation has been identified as the most important background

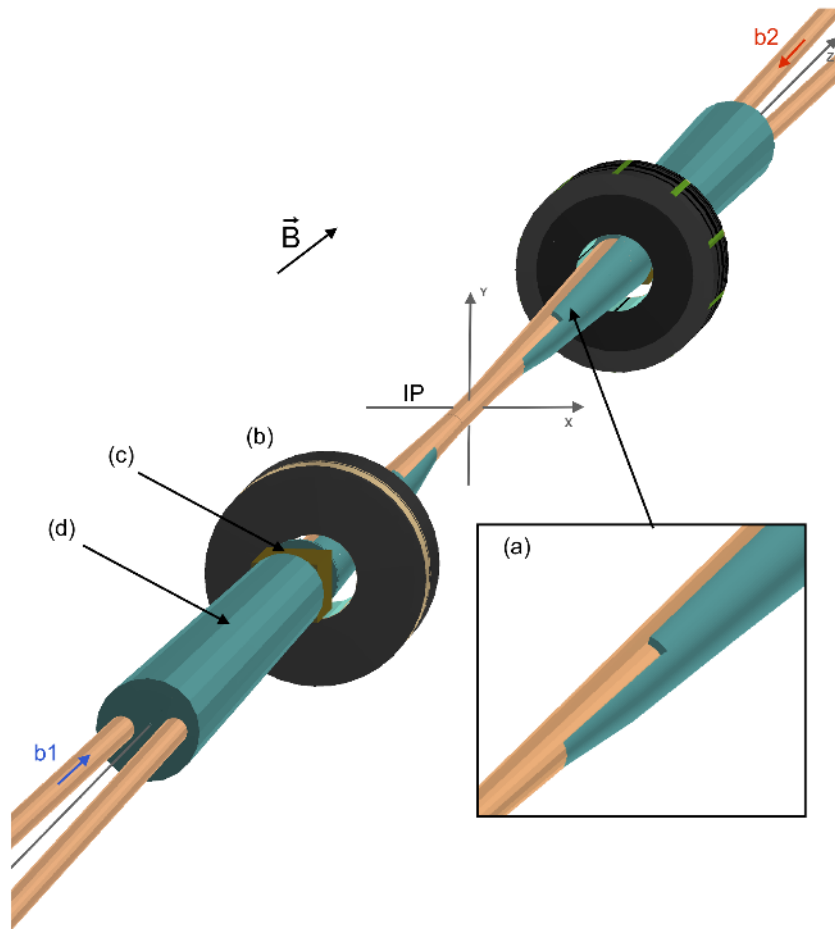


Figure 3.6: A 3D model of the central interaction region in *Geant4*. Black disks represent the luminosity counter (*LumiCal*), elements in turquoise blue display the tungsten shielding. While the shielding is only 0.1 mm thick from point (a) to (b) and not covering the entire azimuth, a full 15 mm cone (d) covers the part after the *LumiCal*.

source. Photons coming from the upstream dipole magnets and final focus quadrupoles could scatter towards the detector, penetrate the beam-pipe and cause hits. Two measures have therefore been implemented in the actual design:

1. Fixed absorbers – synchrotron radiation masks made from tantalum – are supposed to be installed 2.1 m from the interaction point, right at the front face of QC1L/R. These shall minimize the amount of photons coming from the last upstream bending magnets to reach the central chamber.
2. Since a certain fraction can be expected to forward scatter off the masks, additional shielding around the beam-pipe provides protection of the sensitive detector elements.

This shielding is realised by a 5 μm gold coating inside the central chamber (which is made from Beryllium) and another tungsten shielding around the outer beam-pipe (represented as turquoise blue elements in Fig. 3.6). The concept is also shown in Fig. 3.9 in a 2D sketch.

An early study analysed the effect of the tungsten shielding on the occupancy caused by synchrotron radiation photons [23]. While the rate can be neglected at Z running (45.6 GeV beam energy), synchrotron radiation was identified as

dominating background source at $t\bar{t}$. The shielding was found to significantly reduce the number of photons causing hits in the detector. Figure 3.7 shows the hits per sub-detector per bunch crossing with and without shielding. It compares hits caused by pair production and synchrotron radiation.

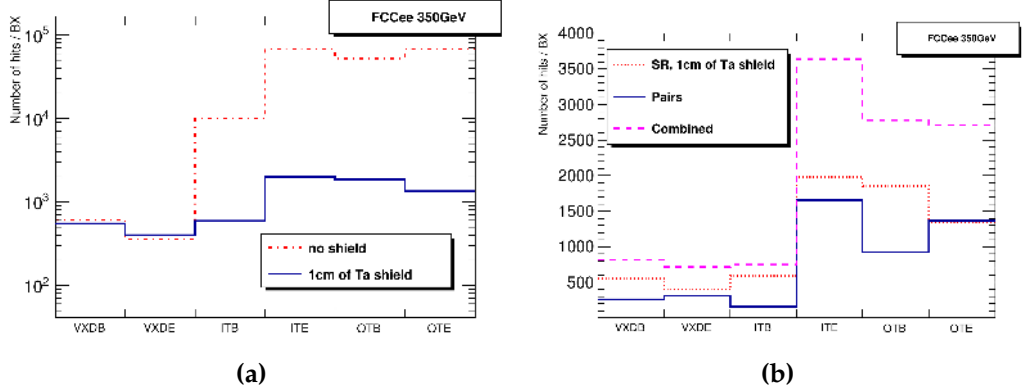


Figure 3.7: Hits per sub-detector per bunch crossing. (a) a heavy material covering the beam-pipe substantially reduces the number of hits. (b) the effect of the shielding for two different background sources, synchrotron radiation and pair creation. Note that the data has been analysed for an early design with slightly less beam energy of 175 GeV [23].

As far as the interaction region is concerned, the design needs to accomplish a trade-off between detector requirements on one side and the measures needed for background protection and beam instrumentation on the other side. A successful MDI design provides experimental conditions as clean as possible.

Current Design Concept – Central IR

Additional complications for the MDI design are caused by the flexibility required for FCC-ee, since the machine is supposed to run at different beam energies. A possible layout for FCC-ee is shown in Fig. 3.8 and 3.9 (± 10 m and ± 3 m around the interaction point, respectively).

A description of the inner layout of the central interaction region (± 10 m around the interaction point) shall be given in this paragraph. It will be the baseline for a geometry used in simulations of the synchrotron radiation background with MDISim.

Figure 3.9 presents an enhanced top view on the current design, with beam pipe dimensions, location of synchrotron radiation masks and tungsten shielding on the outer beam-pipe wall [2]. The cross section of the beam pipe is assumed to be circular, having a default radius of 30 mm. The radius decreases to 20 mm inside QC2.

From the first synchrotron radiation mask at 5.44 m, the beam-pipe diameter decreases to a radius of 15 mm, which is also the radius of the central chamber. A second mask is foreseen at 2.1 m, right downstream of QC1. The innermost masks are shown as small wedges in Fig. 3.9. Supposed to be made from tantalum, the masks shield the central chamber from radiation mainly produced in the last upstream bending magnets.

Another part of the protection scheme can be provided by subsequently reducing the radius of the upstream beam-pipe, as partly depicted in Fig. 3.8 and discussed

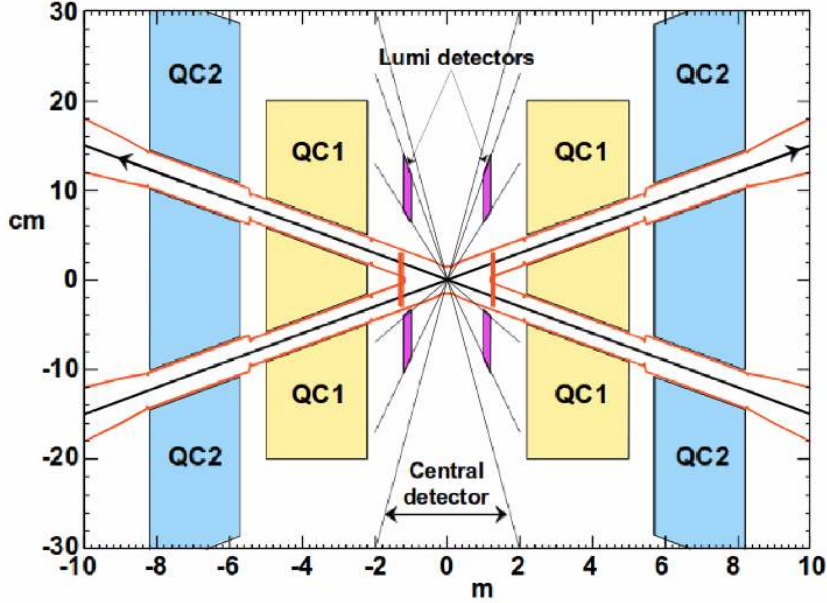


Figure 3.8: Top view on the central interaction region with the interaction point at the center (0), note differing scales on x and y axis. Magnets of the final focus doublet are shown in blue and yellow [24].

later. Such a geometry can help to naturally collimate a certain fraction of photons upstream of the central interaction region.

Figure 3.9 displays the location of the luminosity counter which is situated very close to the beam pipe and requires careful protection. At the same time it puts space constraints for the shielding, and is the reason why shielding in this part does not cover the full azimuth – also shown in Fig. 3.6.

A layer of heavy material (likely tungsten or lead), is supposed to cover the outer beam pipe, as shown in cyan in Fig. 3.9. This layer ranges from 0.1 mm to 15 mm thickness and acts as an absorber. It would stop synchrotron radiation that penetrates the beam-pipe wall from entering the inner detector regions – especially forward scattered photons from the mask tips. First simulations, propagating the arriving photons (partly generated with MDISim) into inner detector regions, showed that this shielding seems sufficient [25].

Figure 3.9 also features the compensating solenoid in light green, covering the space between luminosity counter and the front face of QC1.

While this layout is based on fixed shielding inside and outside of the beam-pipe, synchrotron radiation collimators have not been considered yet. At LEP, movable collimators have proven to be an indispensable part of the background protection system and therefore should not be neglected in the design of the FCC-ee either. Possible locations of collimators and their effect, mainly on the synchrotron radiation background, are subject of this thesis.

3.2. THE INTERACTION REGION

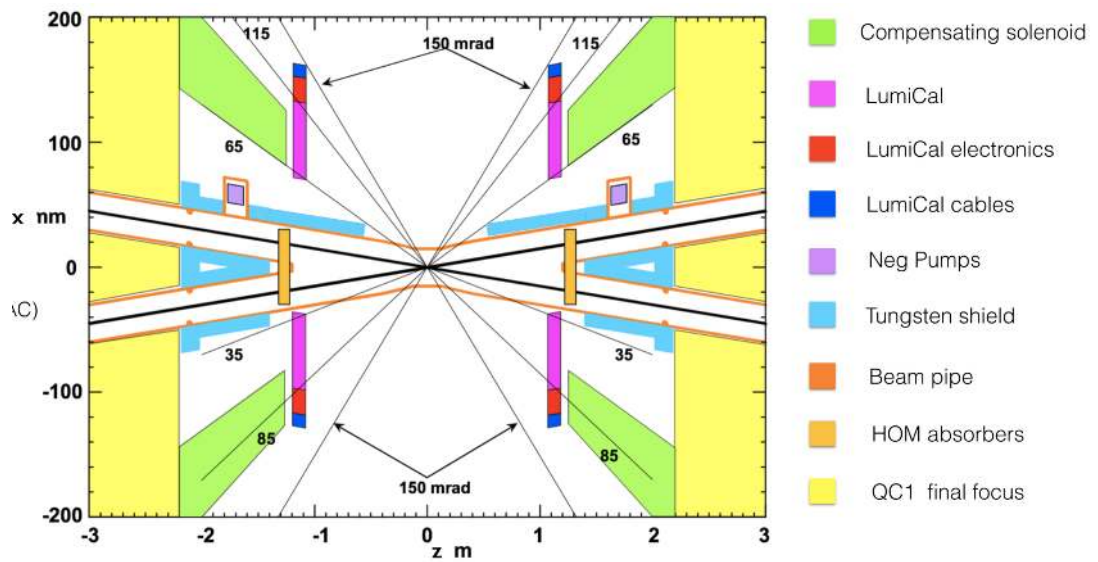


Figure 3.9: Enhanced view on the central chamber (± 3 m) in x , showing the physical aperture as orange line. Additional elements are indicated according to the legend on the right [2]. Note differing scales on the axis, z (longitudinal) in m, while x (transverse) in mm.

4 | Particle Beams and Interactions with Surroundings

A particle beam travelling in perfect vacuum, at the absolute temperature minimum ($T = 0$ K) and in absence of electromagnetic fields, would follow a straight trajectory without losing its energy or changing direction. Only the divergence – always present in a bunch of particles – leads to a widening of the bunch, such that eventually the beam would dissolve.

In an accelerator, however, one would aim for the beam to follow a defined trajectory – the design orbit. For this, the beam must be steered and repeatedly focused by magnetic fields.

In order to reduce disturbances from surroundings, the beam travels in a *beam-pipe* or *vacuum chamber*, which should provide state-of-the-art vacuum. Even though modern pumps reach pressures in the 10^{-9} mbar range, there are inevitably other particles present.

The beam-pipe is never at absolute zero. Hence, it will emit *Thermal Photons* due to black-body radiation at a temperature $T > 0$ K. On the other hand, residual gas atoms are always present since the vacuum is not perfect. Both effects lead to scattering of beam particles.

And finally, the bunch is focused, thereby decreasing the distance between particles, leading to yet another source of scattering of particles within the bunch itself.

All of these effects will influence the beam, lead to interactions and possibly *particle backgrounds*. Those effects need to be considered in order to design an accelerator, especially backgrounds in the interaction region of a collider, where detectors observe particle collisions at the interaction point.

The first thing that needs to be done in order to let a beam circulate in a storage ring is to steer and focus it – even in perfect vacuum and at absolute zero ($T = 0$ K). Electromagnetic fields act on the beam and allow to steer it along the design orbit. Effects of those fields on the beam lead to *synchrotron radiation* backgrounds – the first topic of this chapter.

4.1 Synchrotron Radiation

Accelerated charged particles radiate photons when forced on a circular path [26]. First observed in a synchrotron, this effect was called synchrotron radiation and is a significant beam induced background process in circular lepton machines.

It influences the accelerator design as it determines the overall size of the machine by the maximum practical beam energy. An important figure for that is the *energy loss per turn*.

This energy has to be replaced by the **Radio Frequency (RF)** system and needs to be on a level which allows to operate the machine at reasonable cost.

Besides this (possibly significant) energy loss, synchrotron radiation impacts the lattice design as well. Competing processes of *radiation damping* and *quantum excitation* will eventually establish an *equilibrium emittance*. This equilibrium determines the final beam size which in turn defines the beam-pipe dimensions (physical aperture). Adjustments on the beam size are accomplished via the lattice (the arrangement of magnetic elements) of the accelerator.

Another example for the influence on accelerator optics design is the *saw-tooth orbit* (as introduced in the previous section) which is why magnet strengths are adjusted locally to keep those orbit deviations on a tolerable level [19]. Without such tapering, increased particle loss and subsequently lifetime reduction would be the consequences.

Side effects such as heat deposit and gas desorption influence the vacuum chamber specifications and design. The heat generated by the radiation over the entire length of the machine needs to be manageable. Considering this heat input, it is also important to pay attention to the fact that synchrotron radiation is usually emitted in very narrow cones along the beam.

Experience from past machines such as **LEP** and **HERA** demonstrated possible effects of power deposition on accelerator hardware [10, 11].

Last but not least, detectors at the interaction points are sensitive to radiation and can only tolerate a certain level of photon backgrounds. For this reason, synchrotron radiation has to be estimated carefully in order to find suitable running conditions, paired with a protection scheme for detector and machine components. All of this is considered during the design of the **MDI**.

Basic Properties

Radiation from Accelerated Charged Particles

From electrodynamics, it is known that accelerated charged particles radiate electromagnetic waves. Typical accelerator applications, either in a linear or a circular machine, accelerate particles to high beam energies E_b , such that they can be considered relativistic ($v \approx c$ and $E \approx pc$) with large gamma factors.

$$\gamma = \frac{E_b}{m_0 c^2} \quad (4.1)$$

Where m_0 denotes the electrons' rest mass and c the speed of light.

The power P_{SR} , generated by an accelerated charged particle, can be described using Lamours' formula [15].

$$P_{SR} = \frac{e^2}{6\pi\epsilon_0 m_0^2 c^3} \left(\frac{d\vec{p}}{dt} \right) \quad (4.2)$$

With the vacuum permeability ϵ_0 . For accelerators such as **FCC-ee**, it is safe to assume relativistic particles, such that Eq. (4.2) can be written as Lorentz-invariant

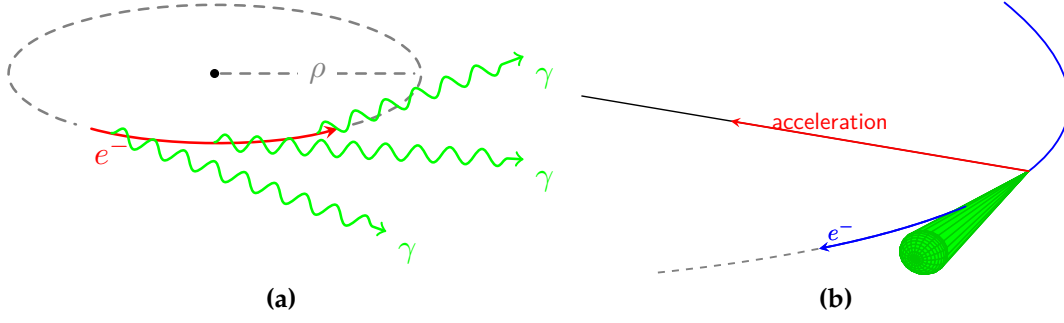


Figure 4.1: (a) example for an electron on a circular path, continuously emitting synchrotron radiation photons along the trajectory. (b) sketch of the spatial radiation distribution in the laboratory frame, showing a narrow cone strongly boosted in forward direction. It also indicates that the accelerating force acts perpendicular to the direction of motion.

form (Eq. (4.3)), using $d\tau = \frac{1}{\gamma} dt$.

$$P_{\text{SR}} = \frac{e^2 c}{6\pi\epsilon_0} \frac{1}{(m_0 c^2)^2} \left[\left(\frac{d\vec{p}}{d\tau} \right)^2 - \frac{1}{c^2} \left(\frac{dE}{d\tau} \right)^2 \right] \quad (4.3)$$

For purely circular motion in vacuum the energy does not change, such that $dE/d\tau \rightarrow 0$ since the accelerating forces act perpendicular to the direction of motion (compare Fig. 4.1 (b)), which simplifies Equation (4.3).

$$P_{\text{SR}} = \frac{e^2 c}{6\pi\epsilon_0} \frac{1}{(m_0 c^2)^2} \gamma^2 \left(\frac{dp}{dt} \right)^2 \quad (4.4)$$

Where $dp/dt = p\omega = p\frac{c}{\rho}$ and ρ is the bending radius. It is possible to recast Eq. (4.4) into Eq. (4.5) [27, 28], using C_γ .

$$P_{\text{SR}} = C_\gamma \frac{c}{2\pi} \frac{E_b^4}{\rho^2} \quad (4.5)$$

Note, that particle energy E_b as well as the bending radius ρ are machine characteristics. C_γ , on the other hand, is a constant defined by particle properties (Eq. (4.6)).

$$C_\gamma = \frac{4\pi}{3} \frac{r_e}{(m_0 c^2)^3} \approx 8.85 \times 10^{-5} \text{m/GeV}^3 \quad (4.6)$$

Where r_e is the classical electron radius – the approximation shown here holds particularly for electrons/positrons.

Expressions (4.4) and (4.5), respectively, show how the radiated power scales with rest mass, beam energy and machine size. Heavy particle species are much less affected than leptons. Limits in reaching high beam energies for electron machines are also imposed, since P_{SR} scales with the fourth power of the beam energy and only the inverse square of the radius.

Hence, circular e^+/e^- machines which aim for energy regimes out to several 100 GeV need to become larger in size.

Synchrotron radiation is usually not an issue in linear accelerators, as the acceleration is parallel to the direction of motion. The radiated power then scales with the energy gain per unit track length, dE/dx and not with γ^2 [15].

The energy loss per turn U_0 , as expressed in Eq. (4.7), determines the required RF voltage to regain the lost energy after each single turn. It is obtained by integrating the radiated power along the ring for a full revolution period.

$$U_0 = \oint dt P_{\text{SR}} = \frac{C_{\gamma} E_b^4}{\rho}. \quad (4.7)$$

Expression (4.7) was simplified by assuming an isomagnetic lattice, where all bending magnets have the same radius $\rho(s) = \rho_0 \equiv \rho$. As a consequence, they all exert the same field on the beam. This is an adequate first order approximation for large machines such as FCC.

The RF voltage has to be chosen such that it compensates the energy loss per turn in order for the particle beam to be stable. For FCC-ee, the beam loses about 36 MeV/turn at lowest beam energy of 45.6 GeV, increasing to about 9 GeV/turn for operation at 182.5 GeV.

It is possible to estimate the total radiated power P_{tot} by considering the energy loss per turn U_0 and beam current I_b , as expressed in Eq. (4.8).

$$P_{\text{tot}} = \frac{U_0 N_e}{T_0} = \frac{U_0 I_b}{e} \quad (4.8)$$

P_{tot} is an important quantity for every accelerator design, as it allows to estimate the total power lost and thereby operational costs caused by synchrotron radiation losses. For FCC-ee, it amounts to roughly 49 MW per beam for all energies, which requires that the beam current is reduced for higher energies.

Distributed over a length of almost 100 km, a power of 1 kW/m can be expected, taking both beams into account. As a comparison, LEP generated on average 0.67 kW/m, about a factor 2 less [29]. The vacuum system needs to be able to handle this constant power input on the material.

Both of these quantities can be expressed in practical units to provide a simple way to estimate the energy loss in a circular accelerator, according to Eq. (4.9) and (4.10) [15].

$$U_0 [keV] = 88.46 \frac{E^4 [GeV]}{\rho [m]} \quad (4.9)$$

$$P_{\text{SR}} [kW] = 88.46 \frac{E^4 [GeV] I [A]}{\rho [m]} \quad (4.10)$$

Table 4.1 presents figures of merit for synchrotron radiation in different machines. Comparing LEP with LHC demonstrates in which way beam energy and particle species influence synchrotron radiation effects. Even FCC-ee, with much larger radius and less momentum generates much higher energy loss per turn than LHC. Hence, energy loss per turn and critical energy are usually less significant for hadron machines, given a mass ratio of

$$m_p / m_e \approx 1836$$

4.1. SYNCHROTRON RADIATION

Table 4.1: Figures of merit, comparing synchrotron radiation at different accelerators. The estimate for SuperKEKB assumes a generic bending radius of $C_0/2\pi$ and might differ to a more precise calculation.

	E_b [GeV]	ρ [m]	U_0 [MeV]	ϵ_c [keV]	P_{SR} [MW]
LEP	45.6	3026	126	70	0.4
	94.5	3026	2300	619	13
LHC	7000	2784	0.0067	0.044	0.0078
SuperKEKB	4	0.480	1.76	0.29	6.33
	7	0.480	2.43	1.58	6.32
FCC-ee	45.6	10190	36	22	50
	182.5	10190	9190	1323	50

The Spectrum of Radiation from a Dipole Magnet

While quantities like radiated power and energy loss per turn have been derived earlier in global terms, the focus is now on energy and emission spectra for a dipole magnet. This allows a characterization of single magnets or magnet types which will be used later on in the analysis of simulation results in the context of this study.

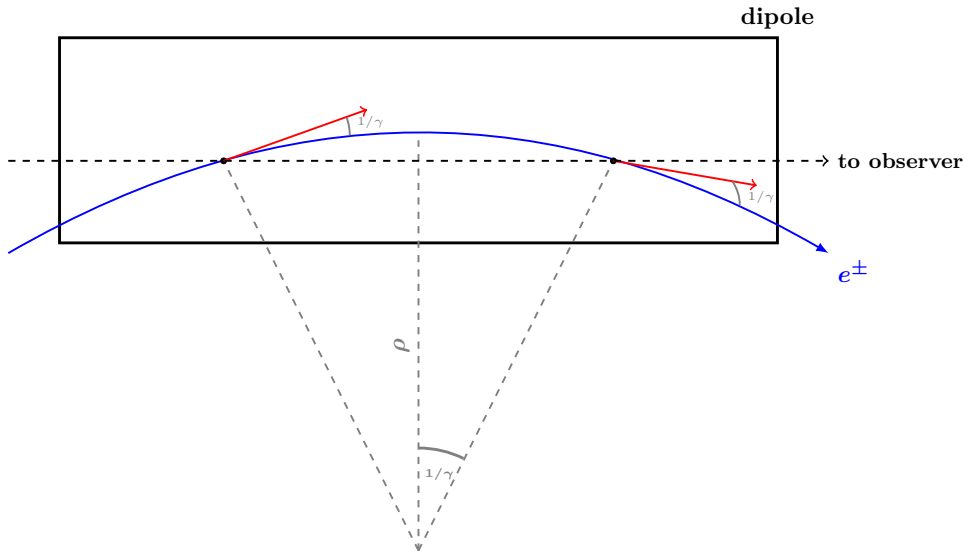


Figure 4.2: Geometric considerations for the traversal of a beam through a rectangular dipole magnet.

The majority of radiation in a circular machine will be generated in the arc dipole magnets. The magnetic rigidity $B\rho$ (Eq. (2.2)) is known to relate field and radius of a dipole magnet, considering the design momentum p_0 . It basically expresses how *stiff* a beam will be in its reaction to a bending field of given strength B (Fig. 4.2 shows geometric considerations).

Photons will be emitted all along the curved path, with an average angle of $1/\gamma$ in the laboratory frame. High energy colliders like LEP or FCC-ee accelerate particles to very high Lorentz factors $\gamma \gg 1$. Synchrotron radiation will be thus emitted in very narrow opening angles on μrad scale or below, as illustrated in

Fig. 4.1 (b). Which is why this radiation potentially deposits up to several ten or even hundred W onto localized spots on the vacuum chamber surface – another challenge for the mechanical design.

Knowing the radiated power P_{SR} in Eq. (4.5), it is possible to express a *spectral angular power distribution*

$$\frac{d^2 P}{d\Omega d\omega}$$

Hence, N electrons will radiate a total power of

$$P_0 = \frac{e^2 c \gamma^4}{6\pi \epsilon_0 \rho^2} N,$$

according to Eqs. (4.4) and (4.5).

It is therefore interesting to derive a *photon spectrum*, based on the *critical energy* ϵ_c .

$$\epsilon_c = \hbar \omega_c \quad (4.11)$$

The critical energy divides the energy spectrum of a magnet in two areas of equal radiation power – a typical spectrum is presented in Fig. 4.3. Equation (4.15) expresses this fact. In practical terms, half of the power is radiated below ϵ_c and the other half above.

Equation (4.11) can be used to relate spectral angular power density and spectral angular photon flux. Integrating the latter over the solid angle $d\Omega$ leads to the photon spectrum [30] (with photon energies $\epsilon = \hbar \omega$).

$$\frac{d\dot{n}}{d\epsilon/\epsilon} = \frac{1}{\hbar} \frac{dP}{d\omega} = \frac{P_0}{\epsilon_c} S(\xi) \quad (4.12)$$

Here, $S(\xi)$ describes the normalized power spectrum (the subscript d refers to dipoles)

$$S_d(\xi) = \frac{9\sqrt{3}}{8\pi} \xi \int_{\xi}^{\infty} dz K_{5/3}(z) \quad (4.13)$$

Using the normalized photon energy $\xi \equiv \epsilon/\epsilon_c$, while $K_{5/3}$ denotes the modified Bessel function of second kind. This spectrum is normalized such that integration over all frequencies results in the total amount of power (Eq. (4.14)).

$$\int_0^{\infty} S(\xi) d\xi = 1 \quad (4.14)$$

$$\int_0^1 S(\xi) d\xi = 0.5 \quad (4.15)$$

Such a power spectrum can also be defined for a quadrupole, assuming the critical energy at 1σ offset from the reference axis (more details in Section 4.1 below and in [31]).

$$S_q(\xi) = \frac{9\sqrt{3}}{8\pi} \xi \int_0^{\infty} dz \left(1 - \operatorname{erf}(\xi/\sqrt{2}z)\right) K_{5/3}(z) \quad (4.16)$$

Here, erf refers to the error function. The spectrum has been plotted in Fig. 4.3 for both types of magnets: a **dipole (blue)** and **quadrupole (red)**. It demonstrates

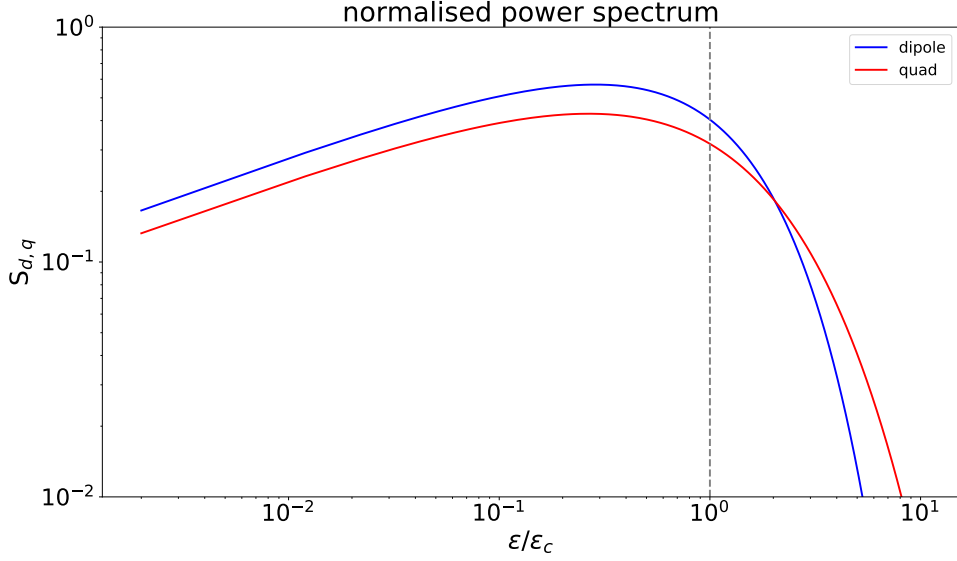


Figure 4.3: Function $S(\xi)$ for *dipole* and *quadrupole* magnet. The spectrum is shown as a function of normalized photon energy ϵ/ϵ_c . A dashed vertical line highlights the critical energy.

how the quadrupole generates less radiation up to the ϵ_c , but tends to develop a longer so called *high energy tail*, producing more photons with energies above ϵ_c .

A few more quantities can be used to characterize the synchrotron radiation. Starting with Eq. (4.12) and then integrating over all energies allows to determine the *photon flux* per single electron.

$$\dot{n} = \frac{P_0}{\epsilon_c} \int_0^\infty d\xi \frac{S(\xi)}{\xi} = \frac{15\sqrt{3}}{8} \frac{P_0}{\epsilon_c} \quad (4.17)$$

The *average photon energy* $\langle \epsilon \rangle$ can be written as in Eq. (4.18), which evaluates to about one third (30.70 %) of the critical energy.

$$\langle \epsilon \rangle = \frac{P_0}{\dot{n}} = \frac{8\sqrt{3}}{45} \epsilon_c \quad (4.18)$$

Practical figures of merit. The spectrum of radiation emitted from a dipole magnet was just described. Some important figures of merit to characterize magnets shall be briefly summarized here.

Each dipole magnet has a certain bending radius ρ . It is therefore possible to define a deflection angle θ , according to Eq. (4.19), and subsequently define the dipole strength k_0 .

$$\rho = \frac{L}{\theta} = \frac{1}{k_0} \quad (4.19)$$

k_0 allows to estimate the critical energy ϵ_c of a bending magnet according to Eq. (4.20).

$$\epsilon_c = \frac{3}{2} \hbar c \frac{\gamma^3}{\rho} \quad (4.20)$$

The number of photons n_γ – radiated by each particle in a bending magnet – can be assessed by taking into account the Lorentz factor γ and bending radius ρ .

$$n_\gamma = \frac{5}{2\sqrt{3}} \frac{e^2 \gamma L}{4\pi \epsilon_0 c \hbar \rho} \quad (4.21)$$

4.1. SYNCHROTRON RADIATION

With Eq. (4.21) and (4.18), the energy loss per turn can be calculated according to

$$U_0 = n_\gamma \langle \epsilon \rangle, \quad (4.22)$$

and thus the power radiated in a dipole magnet, by multiplying U_0 and beam current I_b .

$$P_{\text{SR}} = I_b U_0 \quad (4.23)$$

Given the number of photons radiated per particle in a bunch, the total number of photons, N_γ is estimated by multiplying n_γ with the bunch population N_p .

$$N_\gamma = n_\gamma N_p \quad (4.24)$$

Radiation from Focusing Magnets

The synchrotron radiation spectrum from a dipole magnet and quantities related to it have been just introduced in the previous subsection.

However radiation is also emitted in focusing magnets, like the quadrupoles, if particles do not pass these magnets on reference axis but at a certain distance r .

$$r = \sqrt{x^2 + y^2}$$

In such a case, the field will force particles back towards the reference axis, resulting in a deflection not unlike the principle mechanism in dipole magnets. The consequence is that the particle emits synchrotron radiation – as is illustrated in Fig. 4.4.

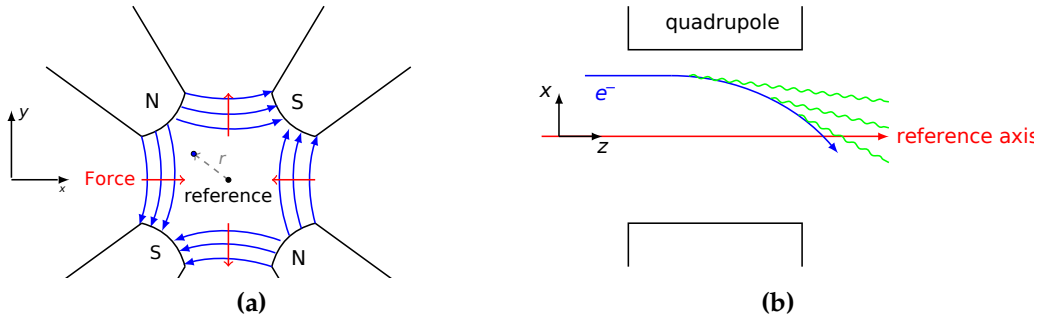


Figure 4.4: Cross-sections through a horizontally focusing quadrupole magnet. (a) transverse view with field lines in blue and the resulting force as red arrows. The reference axis is indicated as black dot, with an offset electron as blue dot. (b) longitudinal view on the same situation. The focusing field would deflect a horizontally offset particle back on axis, which causes synchrotron radiation to be emitted.

This problem is especially relevant in strong final focus magnets, as used for low- β insertions of a collider aiming for high luminosities, such as FCC-ee. The beam tends to have large oscillation amplitudes (β function) in these magnets since they focus it down to the small size needed to produce high luminosities (compare Fig. 3.5 in Section 3.2).

Hence, radiation from these quadrupoles can be severe, especially with beam tails and/or orbit offsets. Particles in the tails tend to be far off the center of a quadrupole and can potentially generate very hard radiation, also observed at

LEP [9]. Though more severe in the final focus elements, the effect is relevant in focusing elements all along the ring.

Based on the quadrupole strength k

$$k = \frac{1}{B\rho} \frac{\partial B_y}{\partial x}, \quad (4.25)$$

the field seen by a particle can be expressed using Eqs. (4.26) and (4.27).

$$B_x = x B\rho k \quad (4.26)$$

$$B_y = y B\rho k \quad (4.27)$$

These expressions embody the fact that the **field strength in a quadrupole depends linearly on the transverse particle position**. The term $B\rho k$ can also be referred to as the *quadrupole gradient* g .

Similar to a bending magnet, it is possible to derive a bending angle θ (which depends on the distance r to the quadrupole centre).

$$\frac{\theta}{L} = r \frac{1}{B\rho} \frac{\partial B_y}{\partial x} = r k \quad (4.28)$$

It is therefore possible to derive figures of merit for a quadrupole – such as ϵ_c , number of photons n_γ and mean energy – only now explicitly dependent on the distance r of a particle from the reference axis.

Beam Dynamics with Synchrotron Radiation

Synchrotron radiation has significant effects on the beams circulating in storage rings. Among a dominating energy loss per turn (U_0), radiating photons also contributes to *emittance damping* in all three planes (horizontal, vertical and longitudinal). With the fact that energy is radiated only in discrete quanta (photons), synchrotron radiation generates noise on the beam – *quantum excitation* – which tends to increase the emittance. Quantum excitation and radiation damping are thus competing mechanisms, such that eventually the beam reaches an equilibrium emittance.

Five synchrotron radiation integrals $I_{1,2,3,4,5}$ are defined to describe these effects on the dynamics of an ultra-relativistic particle in a storage ring [21, 32].

1st Integral, I_1

As discussed earlier, the momentum compaction factor α_p is used to describe changes in the length of the closed orbit, ΔC , caused by changes of the particle energy. This can be expressed according to Eq. (4.30). The first synchrotron radiation integral I_1 is defined using the horizontal dispersion following Eq. (4.29). Note, that it is not directly related to radiation effects but more to longitudinal dynamics.

$$I_1 = \oint ds \frac{D_x}{\rho} \quad (4.29)$$

It allows to write the momentum compaction as in Eq. (4.31).

$$\frac{\Delta C}{C_0} = \alpha_p \delta + O(\delta^2) \quad (4.30)$$

$$\alpha_p = \frac{1}{C_0} \left. \frac{dC}{d\delta} \right|_{\delta=0} = \frac{1}{C_0} \oint ds \frac{1}{\rho} = \frac{I_1}{C_0} \quad (4.31)$$

2nd Integral, I_2

By defining the second synchrotron radiation integral I_2 in Eq. (4.32), the energy loss per turn can be written in the form of Eq. (4.33).

$$I_2 = \oint ds \frac{1}{\rho^2} = 2\pi \frac{cB}{E/q} \quad (4.32)$$

$$U_0 = \frac{C_\gamma}{2\pi} E_b^4 I_2 \quad (4.33)$$

Where I_2 is a lattice property and therefore independent of beam parameters. U_0 is required to describe the *vertical damping time* τ_y .

$$\tau_y = 2 \frac{E_b}{U_0} T_0 \quad (4.34)$$

With the nominal beam energy E_b and revolution time T_0 .

3rd Integral, I_3

The competition of quantum excitation and radiation damping in the longitudinal plane lead to an *equilibrium momentum spread*, σ_δ .

$$\sigma_\delta = C_q \gamma^2 \frac{I_3}{j_z I_2} \quad (4.35)$$

j_z denotes the *longitudinal damping partition number*, and the constant C_q is given by

$$C_q = \frac{55}{32\sqrt{3}} \frac{\hbar}{mc} \approx 3.832 \times 10^{-13} \text{ m}, \quad (4.36)$$

where the numerical approximation in Eq. (4.36) holds for electrons (positrons). \hbar denotes the reduced Planck constant. Equation (4.35) invokes the beam energy as well as the dipole bending radius with I_2 and the newly introduced third synchrotron radiation integral I_3 .

$$I_3 = \oint ds \frac{1}{\rho^3} \quad (4.37)$$

4th Integral, I_4

Describing the horizontal plane is a bit more complicated due to the coupling with the longitudinal plane, introduced by dispersion in the dipole magnets. The emission of photons will result in a decrease of the particle momentum p , thereby introducing damping in the horizontal plane. With changing position x in the

dipoles, the field may vary additionally, presenting also quadrupole components (to first order) k :

$$k = \frac{e}{p} \frac{\partial B}{\partial x}. \quad (4.38)$$

The fourth synchrotron radiation integral is introduced to account for these effects.

$$I_4 = \oint ds \frac{D_x}{\rho} \left(\frac{1}{\rho^2} + 2k \right) \quad (4.39)$$

In all straight sections, this integral would not contribute, as $1/\rho \approx 0$. The horizontal emittance ϵ_x evolves over time as

$$\frac{d\epsilon_x}{dt} = -\frac{1}{T_0} \frac{U_0}{E_b} \left(1 - \frac{I_4}{I_2} \right) \epsilon_x. \quad (4.40)$$

Introducing the horizontal damping partition j_x , allows to express a *horizontal damping time* τ_x .

$$j_x = 1 - I_4/I_2 \quad (4.41)$$

$$\tau_x = \frac{2}{j_x} \frac{E_b}{U_0} T_0 \quad (4.42)$$

Since longitudinal and horizontal planes are coupled by non-zero dispersion, I_4 is also used to describe the longitudinal damping partition j_z with the longitudinal damping time τ_z .

$$j_z = 2 + I_4/I_2 \quad (4.43)$$

$$\tau_z = \frac{2}{j_z} \frac{E_b}{U_0} T_0 \quad (4.44)$$

5th Integral, I_5

Damping of the emittance due to radiation losses do not yet cover all effects of synchrotron radiation on particle dynamics.

Accounting for the quantum physical nature of photon emission in energy quanta $\hbar\omega$ means to consider quantum excitation. This effect adds noise on the particle beam, increasing the emittance and thereby counteracting the effects due to radiation damping.

Both effects will eventually establish an equilibrium momentum spread σ_δ . It can be shown that the horizontal emittance does not only experience damping but also a driving term (second term on the rhs of Eq. (4.45)).

$$\frac{d\epsilon_x}{dt} = -\frac{2}{\tau_x} \epsilon_x + \frac{2}{j_x \tau_x} C_q \gamma^2 \frac{I_5}{I_2} \quad (4.45)$$

The fifth synchrotron radiation integral as derived in Eq. (4.46) is mainly determined by the lattice itself (a fact comprised in the \mathcal{H} function).

$$I_5 = \oint ds \frac{\mathcal{H}}{|\rho^3|} \quad (4.46)$$

$$\mathcal{H} = \gamma_x D_x^2 + 2\alpha_x D_x D_x' + \beta_x D_x'^2 \quad (4.47)$$

Finally, an equilibrium emittance ϵ_0 is defined in Eq. (4.48), again influenced by particle energy (through the Lorentz- γ) and lattice parameters (I_2, I_5).

$$\epsilon_0 = C_q \frac{\gamma^2}{j_x} \frac{I_5}{I_2} \quad (4.48)$$

Robinson Theorem. Horizontal and longitudinal emittance damping both include factors which depend on the lattice. I_2 and I_4 comprise details of the dipoles in a lattice and it is thus possible to define the damping partition numbers j_x and j_z , which can be added.

$$j_x + j_z = 3 \quad (4.49)$$

Considering further that for a vertical damping partition it is possible to assume (at least in a perfectly flat machine) $j_y = 1$, the so called *Robinson theorem* relates all three damping partition numbers $j_{x,y,z}$.

$$j_x + j_y + j_z = 4 \quad (4.50)$$

This important theorem basically states that it is possible to shift damping between single planes (horizontal, vertical or longitudinal), while the overall damping remains constant. As a result of this relation, the damping time in one plane can be reduced but only at the cost of increasing it in another plane.

4.2 Thermal Photons

The discussion in this section assumes the beam to propagate in a vacuum chamber and lift the condition of $T = 0$ K. *Thermal Photons* will be emitted by the beam-pipe due to black-body radiation. Subsequently, beam particles can undergo Compton scattering on these low energy photons, thereby loosing up to several percent of their energy – a schematic visualization is provided in Fig. 4.5.

First considered in astrophysics, it was applied to high-energy accelerators in [33]. Since the effect depends on the electron energy, it becomes increasingly relevant for high-energy accelerators and has been measured at LEP [34].

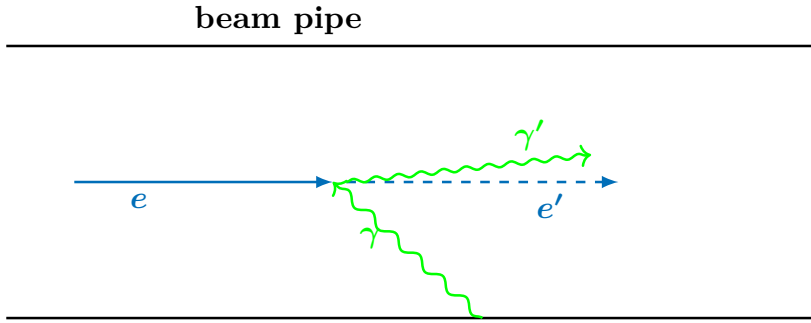


Figure 4.5: Schematic visualization of inverse Compton scattering in the beampipe. A low energy photon (γ) emitted from the beam-pipe scatters with the high energy particle from the beam (denoted as e). The beam particle looses energy while the photon is strongly boosted in energy (γ').

This section presents an estimate of the lifetime due to scattering on Thermal Photons at FCC-ee, which has been performed in the context of this thesis, basically following the approach in [35].

Scattering and the beam lifetime. Particles that undergo scattering do not necessarily stay in the machine. They can be lost from the beam and contribute to the backgrounds at the detector.

By loosing a certain fraction of the particles, the beam will have only a limited lifetime while circulating in the storage ring. As scattering is a statistical process, only a fraction of particles will loose enough energy to fall out of the energy acceptance.

Taking into account that fraction of lost particles allows to estimate the beam lifetime due to a given scattering process. A key parameter is the inverse scattering probability, provided by the cross section σ_{scatter} for a process and the density of particles n_p on which the scattering occurs.

$$P_{\text{scatter}} = \sigma_{\text{scatter}} n_p \quad (4.51)$$

Since $\sigma_{\text{loss}} \leq \sigma_{\text{scatter}}$ (not all scattered particles are actually lost), the lifetime contribution can be written as

$$\tau_{\text{loss}} = \frac{1}{c\sigma_{\text{loss}} n_p} \quad (4.52)$$

With the speed of light c . This lifetime is higher than the one considering only σ_{scatter} .

Equation (4.52) does not take into account the individual energy acceptance of a machine, F_{loss} . This acceptance determines the actual fraction of lost particles. Since it cannot be determined analytically, Monte-Carlo (MC) generators have to be used in order to produce a sufficient amount of events. That allows to estimate the fraction of events with an energy loss higher than the energy acceptance of the machine.

Thermal Photons and Compton Scattering

Black body radiation, according to Planck's law, will result in a photon density following the spectrum of Eq. (4.53) [33].

$$dn_{\text{P}} = \frac{k^2 dk}{\pi^2 (c\hbar)^3 (e^{(k/k_{\text{B}}T)} - 1)} \quad (4.53)$$

With the photon energy $k = \hbar\omega$, the speed of light c and \hbar , the reduced Planck constant ($\hbar/2\pi$). k_{B} denotes the Boltzmann constant and T the temperature of the black body. For the LEP beam pipe an assumption of $T \approx 300$ K was used to estimate a total number of photons per cm^3 [33, 36].

$$n_{\text{P}} = \frac{2.4(k_{\text{B}}T)^3}{\pi^2 (c\hbar)^3} \approx 0.55 \times 10^9 \text{ cm}^{-3} \quad (4.54)$$

At this temperature, an average photon energy of $\langle \epsilon \rangle = 2.7k_{\text{B}}T \approx 0.07$ eV can be estimated. Which is significantly smaller than the beam energy. Figure 4.6 shows a typical spectrum of photon energies, generated for a temperature of 296.15 K. A red dashed line indicates the analytic solution, while the spectrum has been generated with a Monte-Carlo generator.

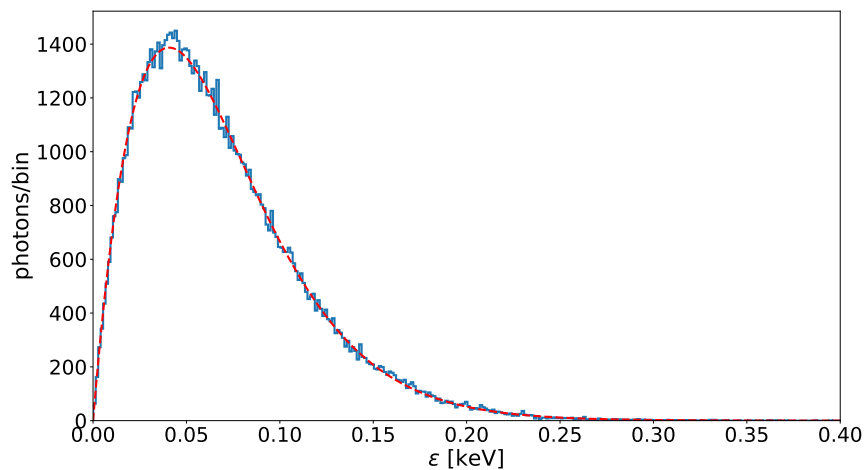


Figure 4.6: Typical energy distribution for Thermal Photons around 300 K, from a Monte-Carlo generator. The red dashed line represents the analytic solution.

Even though these photons have very small energies, the high-energy electron might transfer a considerable amount of its initial energy during the scattering process to the photon.

The process is described for an electron at rest. After a Lorentz boost into the electron rest frame (quantities in that system are denoted by an asterisk *), the energy of the photon can be described with Eq. (4.55), where ψ is the incident angle between electron and photon.

$$k_i^* = \gamma k_i (1 - \beta \cos \psi) \quad (4.55)$$

k_i denotes the fraction of initial photon to beam energy, $\hbar\omega/E_b$. With the Lorentz-boost, the photon energy is enhanced by a factor γ (about 10^5 for a 50 GeV electron)!

With the ratio of photon energies before and after scattering, according to Eq. (4.56) [35]

$$x = \frac{k_f^*}{k_i^*} = \left(1 + \frac{k_i^*}{m_e} (1 - \cos \theta) \right)^{-1}, \quad (4.56)$$

it is possible to estimate the maximum of transferred energy, assuming an angle θ after scattering. The final photon energy reaches a minimum for backscattering ($\psi = 180^\circ$).

$$x_{\min} \approx 1 - \frac{4\gamma k_i^*}{m_e} \quad (4.57)$$

While, if the photon is forward scattered ($\theta = 0^\circ$), x reaches it's maximum and $k_f^* = x k_i^*$. Transferring back from the electron rest frame into the lab frame would then contribute with another factor γ . Hence, the photon would roughly gain an overall energy of

$$k_{\max} \approx \gamma^2 k_i. \quad (4.58)$$

In [33], the maximum photon energy in the lab frame was found to be

$$k_{\max} \approx 4\gamma^2 k_i \quad (4.59)$$

which is comparable, up to the factor 4. Possible maximum photon energies according to Eq. (4.58) are summarized in Tab. 4.2.

Table 4.2: Highest photon energies from inverse Compton scattering in FCC-ee, considering lowest and highest beam energy.

E_b [GeV]	k_{\max}
45.6	557 MeV
182.5	8.9 GeV

Lifetime due to Thermal Photons

An estimate of the lifetime τ due to Thermal-photon scattering at FCC-ee is based on the total cross section σ_C . The inverse lifetime may be expressed in the form of Eq. (4.60), where the ρ_γ replaces the general particle density n_p .

$$\frac{1}{\tau} = \rho_\gamma c F_{\text{loss}} \sigma_C \quad (4.60)$$

Assuming a temperature of 23 °C, the resulting photon density ρ_γ would be around $5.26 \times 10^{14} \text{ m}^{-3}$. A lower lifetime limit results from taking a loss factor of $F_{\text{loss}} = 1$

(worst case assumption) together with the photon density and the Thomson cross section $\sigma_T = \frac{8\pi}{3} r_e^2$ and yields about 26.5 hours.

$$\tau_{\min} = \frac{1}{\rho_\gamma c \sigma_T} \approx 26.48 \text{ h} \quad (4.61)$$

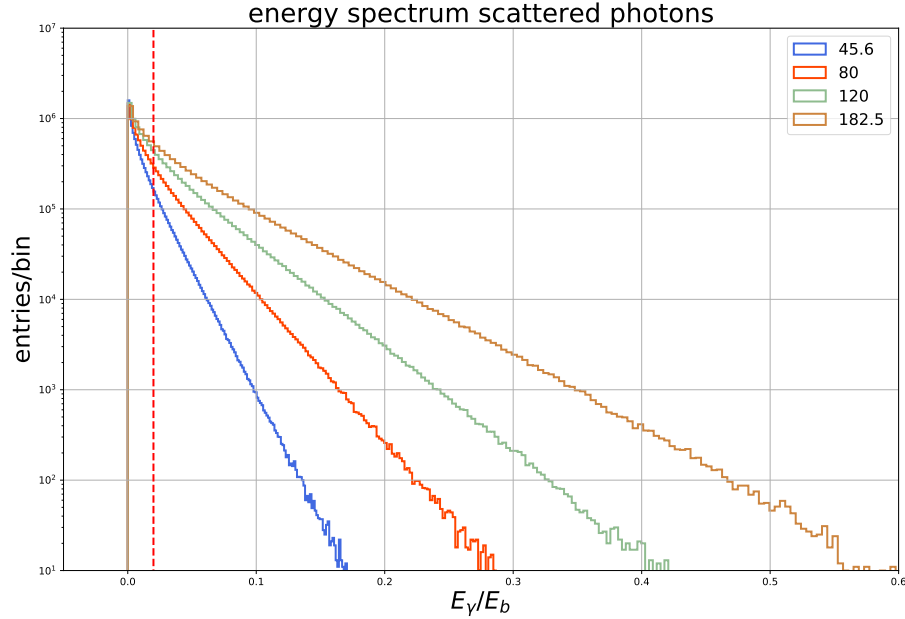


Figure 4.7: Energy spectrum of photons after Compton scattering with beam particles for each design energy. A vertical red dashed line denotes 2% energy transfer. The spectrum is used to find F_{loss} for every beam energy by determining the fraction of particles that loose $\geq 2\%$ of their energy.

With the Monte Carlo approach, it is possible to estimate the loss factor F_{loss} , while the study presented here assumes the cross section to be $\sigma_C \approx 0.665$ barn for high energies [31].

In order to derive F_{loss} for each energy, a Monte Carlo code was written in the framework of this study, to generate the energy spectrum of scattered particles. As noted earlier, this approach follows the method described in [35]. Resulting photon energies are shown in Fig. 4.7, where the 2% energy acceptance at FCC-ee is highlighted with a red dashed line.

From that spectrum, the loss factor (fraction of particles lost from the beam) is found to be about 19% at 45.6 GeV beam energy and 58% at 182.5 GeV. Those are close to similar estimates for 2% energy acceptance in [31]. Lifetimes considering these numbers are summarized in Tab. 4.3.

These lifetimes are fairly high, considering other limiting factors such as radiative Bhabha scattering and beamstrahlung (39 min and 18 min at 182.5 GeV beam energy), as reported in the FCC-ee CDR [2].

Table 4.3: Summary of loss factors and resulting lifetime estimates at different design energies. The lifetime decreases for increasing beam energy, as expected.

Energy [GeV]	F_{loss} [%]	τ [h]
45.6	18.90	140
80	34.77	76
120	46.59	56
182.5	57.93	46

4.3 Beam - Gas

The previous section described a scenario where the beam travels inside a vacuum chamber at certain temperature $T > 0$ K. As a result, the beam-pipe would (due to black body radiation) emit low energy photons and particles of the beam can scatter on these Thermal Photons, which influences the lifetime of the beam. Still, the discussion was yet considering perfect vacuum such that no other scattering source had been present – a condition that is now lifted, which will lead to the effect of *Beam-Gas scattering*.

Beam-Gas (or Coulomb-) scattering of beam particles with residual gas atoms in the vacuum chamber is another type of background which has to be considered, as particles can be lost from the beam after scattering with those residual gas atoms.

Once lost from the beam, these particles might reach the detector and induce backgrounds. Another effect of Beam-Gas scattering is a lifetime reduction.

Two processes will result from Beam-Gas scattering

- *elastic scattering* – meaning deflection of beam particles or
- *bremsstrahlung* – energy loss due to radiation of photons within the field of the nucleus

Both of which will be shortly introduced below.

Elastic Scattering

A description of elastic scattering of electrons with heavy nuclei can be done based on the Rutherford cross section [26].

Two possible extreme cases can be identified with respect to the scattering angle θ , depicted in Fig. 4.8. First, small angles from scattering with a large *impact parameter* b . In such a scenario, the potential of the nucleus decreases more rapidly, with the result that the scattering cross section will flatten off for small angles – this is taken into account by using a cut-off angle θ_{min} .

$$\frac{d\sigma}{d\Omega} \approx \left(\frac{Z\alpha\hbar c}{p v} \right)^2 \frac{1}{(\theta^2 + \theta_{\text{min}}^2)^2} \quad (4.62)$$

Where p is the particle momentum ($\gamma m_0 v$, with $v \approx c$ in the relativistic limit). Z denotes the charge multiplicity of the nucleus and α the fine-structure constant.

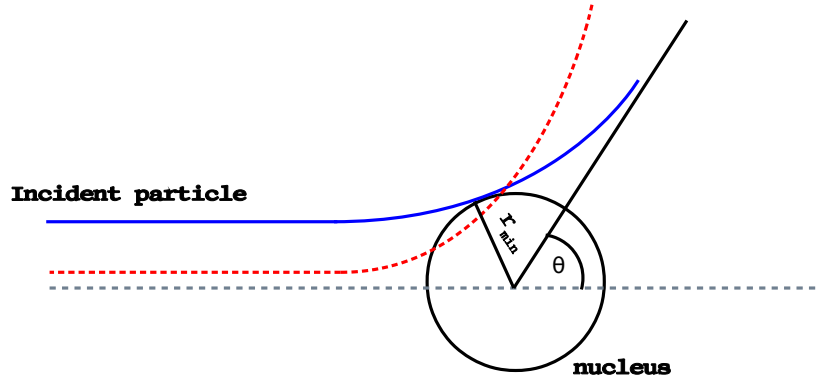


Figure 4.8: Phenomenological sketch of elastic scattering events, depicting two different impact parameters. *blue*: large impact parameter (small scattering angle); *red*: small impact parameter (large scattering angle).

Second, large angles from particles scattering with small impact parameter. The differential cross section in that case is expressed as in Eq. (4.63).

$$\frac{d\sigma}{d\Omega} \approx \left(\frac{Z\alpha\hbar c}{pv} \right)^2 \frac{1}{\theta^4} \quad (4.63)$$

Figure 4.9 compares both cases, showing how the corrected cross section for small angles (Eq. (4.62)) flattens out with $\theta \rightarrow 0$ instead of growing further.

Regarding the lifetime for FCC-ee, this study only considers the unscreened case for the moment and Equation (4.63) is used. The small angle approximation is sufficiently accurate, given average scattering angles not much larger than the angular divergence of the beam, σ' .

$$\sigma' = \sqrt{\gamma(s)\epsilon} \quad (4.64)$$

With the Twiss parameter $\gamma(s)$ as introduced in Chapter 2. According to Eq. (4.64), at locations with a small beta-functions (such as the interaction point), the beam will develop a large divergence. Average values for the beam divergence at FCC-ee (considering lowest and maximum beam energy) are summarized in Tab. 4.4.

Table 4.4: Average divergence of the beam in the arcs and at the interaction point for the lowest and highest beam energies foreseen in FCC-ee.

Energy [GeV]	Location	σ'_x [μrad]	σ'_y [μrad]
45.6	arc	2.12	0.13
	IP	42.43	34.96
182.5	arc	5.80	0.26
	IP	38.21	42.54

In the arc, the divergence is on average about a few μrad in the horizontal and less than $1 \mu\text{rad}$ in the vertical plane. At the interaction point it increases significantly, reaching maximal values between about $35 \mu\text{rad}$ to $42 \mu\text{rad}$.

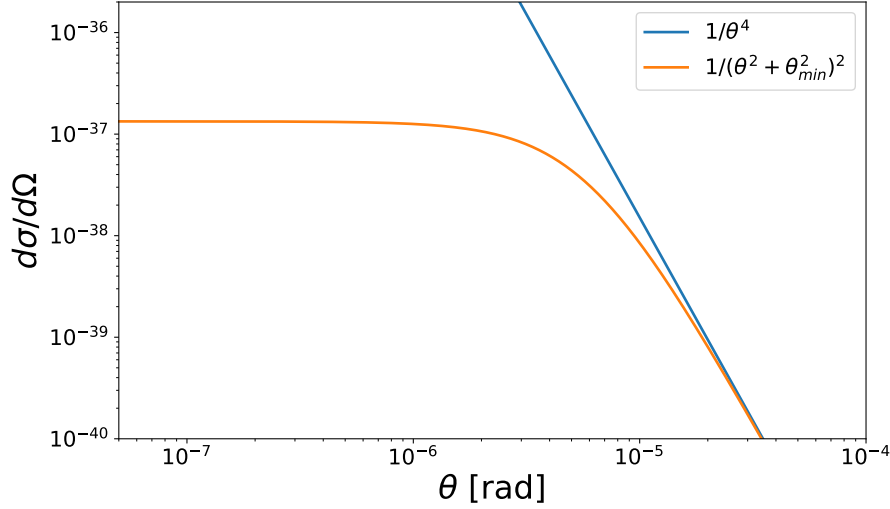


Figure 4.9: Comparison of the small angle approximation and a more general case including the cut-off angle. Note the double logarithmic scale.

The total cross section is obtained by integration over the full solid angle, starting at a certain θ_{\min} which is given by the angular divergence of the beam, since angles below this are not relevant.

$$\sigma = 2\pi\alpha(\hbar c)^2 \left(\frac{Z}{E_b}\right)^2 \frac{1}{\theta_{\min}^2} \quad (4.65)$$

Where $(\hbar c)^2$ can be conveniently written as $3.8927 \times 10^{-4} \text{ barn GeV}^2$. Note that Eq. (4.65) scales with the inverse square of the beam energy.

Assuming a constant pressure of 10^{-9} mbar as in [37], the average density would be around $2.45 \times 10^{11} \text{ molecules/m}^3$. As for the gas composition, this study assumes two different cases, H_2 and N_2 , where the latter has an atomic number Z of 7, comparable to CO . CO and N_2 composed the residual gas at LEP [36] (which had a 'warm' beam-pipe about room temperature of nearly 300 K).

The estimates are summarized in Tab. 4.5 and 4.6 for two different θ_{\min} . Assuming the residual gas to be entirely composed of hydrogen, the lifetimes are no less than 15 h , reaching as high as 10^5 h for large angular divergence and highest beam energy. Considering nitrogen as the gas component, the estimates significantly drop down to 1.25 h at 45.6 GeV with small θ_{\min} , but still reach 10^3 h to 10^4 h for large angular divergence of about $45 \mu\text{rad}$.

These estimates indicate that Beam-Gas elastic scattering can be considered as to not put any severe constraints on the lifetime in FCC-ee.

Beam-Gas Bremsstrahlung

The elastic Beam-Gas scattering can be assumed to have negligible lifetime contribution in high energy accelerators. Inelastic scattering, in which the electron

Table 4.5: Lifetime estimates for lowest and highest energy at FCC-ee for θ_{min} of 1 μ rad. The lifetimes are based on Eq. (4.65).

Gas	Energy [GeV]	σ [barn]	τ_{BG} [h]
H ₂	45.6	251	15
	182.5	15	245
N	45.6	3069	1.25
	182.5	102	20

Table 4.6: Lifetime estimates for lowest and highest energy at FCC-ee for θ_{min} of 45 μ rad. The lifetimes are based on Eq. (4.65).

Gas	Energy [GeV]	σ [barn]	τ_{BG} [h]
H ₂	45.6	0.12	31018
	182.5	0.008	496833
N	45.6	1.52	2532
	182.5	0.09	40557

interacts with the field of the nucleus and radiates a photon, is a more important consideration for these machines. It can contribute to backgrounds in the detector. Beam lifetimes at FCC-ee due to inelastic scattering have been estimated in the context of this study, while the contribution to detector backgrounds is summarized from another publication [37].

Lifetime Estimate

The differential cross section can be written as [38].

$$\frac{d\sigma_{eBrem}}{dk} = 4\alpha r_e^2 \frac{1}{k} \left[\left(\frac{4}{3} - \frac{4}{3}k + k^2 \right) (Z^2(L_{rad} - f) + ZL'_{rad}) + \frac{1}{9}(1 - k^2)Z(Z + 1) \right] \quad (4.66)$$

Where k is the energy loss of the electron. L_{rad} and L'_{rad} are radiation logarithms which can either be found tabulated or approximated for elements $Z \geq 5$.

$$L_{rad} = \ln(184.15Z^{-1/3}) \quad (4.67)$$

$$L'_{rad} = \ln(1194Z^{-2/3}) \quad (4.68)$$

f is the Coulomb correction, α and r_e are fine-structure constant and classical electron radius.

The second term in angular brackets of Eq. (4.66) can be neglected as it is assumed to be very small (in [38], the author states a 2.5 % error on the result if this term is neglected).

Expression (4.66) for the differential cross section can be further simplified using the unit radiation length, defined as

$$\frac{1}{X_0} = 4\alpha r_e^2 \frac{N_A}{A} (Z^2(L_{rad} - f) + ZL'_{rad}), \quad (4.69)$$

which allows to reshape Eq.(4.66) into a rather convenient form.

$$\frac{d\sigma_{\text{eBrem}}}{dk} = \frac{A}{N_A X_0} \frac{1}{k} \left(\frac{4}{3} - \frac{4}{3}k + k^2 \right) \quad (4.70)$$

This result can be integrated to find the total cross section. Note, that the integration is done from k_{min} up to 1 since Eq. (4.70) diverges for $k \rightarrow 0$.

$$\sigma_{\text{eBrem,BG}} = \frac{A}{N_A X_0} \left(-\frac{4}{3} \log k_{\text{min}} - \frac{5}{6} + \frac{4}{3} k_{\text{min}} - \frac{k_{\text{min}}^2}{2} \right) \quad (4.71)$$

Assuming an energy acceptance of 2% as k_{min} and again N_2 as the main scattering component with the same density as in the elastic case, the cross section is $\sigma_{\text{eBrem,BG}} = 5.36 \text{ barn}$. It is independent of the initial electron energy.

The resulting lifetime from Eq. (4.52) with $\sigma_{\text{scatter}} = \sigma_{\text{loss}}$ as a worst case scenario would be around $\tau_{\text{BG}} = 7056 \text{ h}$.

Possible Contribution to Detector Backgrounds

Additionally to the lifetime contribution, scattered particles can induce backgrounds at the experiments. A characterization of these effects was done in [37] and will be shortly reviewed here. The focus has been on high-intensities in FCC-ee, at 45.6 GeV beam energy. This run scenario would be of most concern regarding Beam-Gas backgrounds due to the large beam currents of almost 1.4 A.

The approach is based on a detailed Monte-Carlo simulation, done with MDISim [14]. The machine environment around the interaction point was modeled and a beam tracked in Geant4 for about 1 km, starting 850 m upstream of the interaction point. Figure 4.10 shows the resulting loss rate distribution.

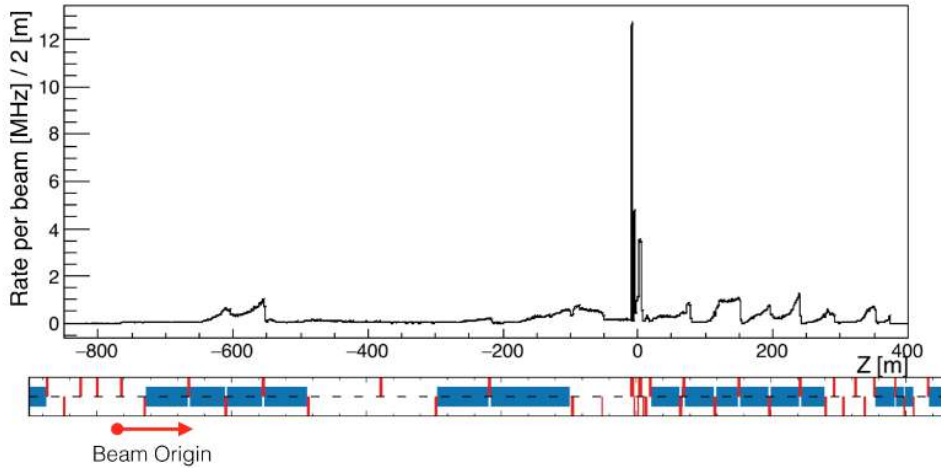


Figure 4.10: Distribution of losses due to Beam-Gas scattering over the tracking length in Geant4 [37]. Below the plot, a schematic visualization of the beam line. Blue rectangles represent dipoles, red lines quadrupoles. The start position is indicated as well. A concentration of losses is observed close to the interaction point at $z = 0 \text{ m}$ and downstream ($z \geq 0 \text{ m}$).

Baseline quantity for the characterization is the scatter rate, given per beam according to

$$N_{\text{loss}} = \frac{N_{\text{loss,MC}}}{N_{\text{MC}}} N_p N_b \frac{10^{-9} \text{ mbar}}{P_{\text{MC}}}. \quad (4.72)$$

$N_{\text{loss, MC}}$ and N_{MC} are the particles lost in the Monte-Carlo (MC) simulation and the total number of particles used, respectively. The number of particles per bunch is specified by N_p and the number of bunches per beam by N_b .

It should be pointed out, that the approach used strong biasing in the pressure by a factor of 10^9 . This way, a sufficient number of results could be processed within a reasonable amount of time. The biasing is taken into account by the factor $10^{-9} \text{ mbar}/P_{\text{MC}}$ (P_{MC} is the gas pressure assumed in the Monte-Carlo simulation).

In order to finally quantify the losses, a loss rate R_{loss} was introduced using the revolution time for FCC, T_0 of 0.33 ms.

$$R_{\text{loss}} = \frac{N_{\text{loss}}/\text{beam}}{\Delta t} \quad (4.73)$$

An analytic formula was used to compare the performance of the MC approach. For an average arc cell, that formula gave 192.3 kHz/m/beam, which was compared with the MC result of 189.1 kHz/m/beam – both results seem to agree well.

Loss peaks in the spectrum are very dominant in the interaction region, close to $z = 0$ m. These peaks can be explained by taking into account the aperture restrictions around the final-focus magnets, QC2L/R and QC1L/R. The beam pipe is reduced from a 70 mm diameter to only 30 mm in the central chamber (see Fig. 4.11 as additional visualization).

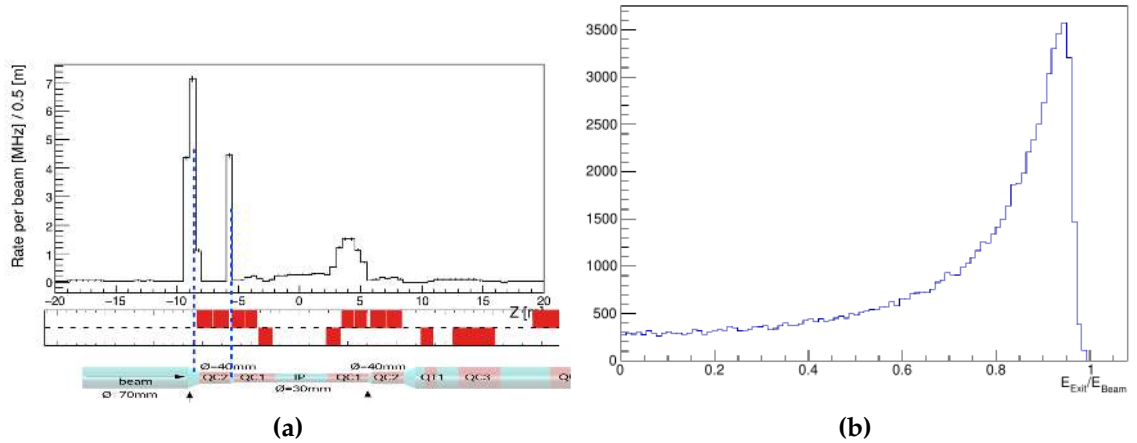


Figure 4.11: (a) closeup of the loss spectrum in figure 4.10 in the interaction region. Below that plot, a picture of the 3D geometry in MDISim displays the aperture limits around the central chamber. (b) depicts the energy distribution of lost particles. Note that the spectrum is normalized to the beam energy [37].

Loss rates to be expected at all machine settings are summarized in Tab. 4.7. Apparently, the loss rates are all around 100 MHz per Ampere and beam. As for the energy, the simulation shows that the majority of lost particles keep 80 % to 100 % of their initial energy, as can be seen from the distribution in Fig. 4.11 (b).

A more realistic pressure profile for the vacuum conditions has been taken into account as well. This profile was obtained from the Vacuum Group at CERN, considering effects of synchrotron radiation and pumping performance with the Molflow program [39].

4.3. BEAM - GAS

Table 4.7: Loss rates to be expected at all four beam energies, according to the MDISim simulation described above. R_{MDI} refers to the whole machine section simulated (1 km), while R_{IR} refers to the interaction region (± 20 m around the IP) [37].

Setup	I [mA]	R_{MDI} [MHz]	R_{IR}	R_{MDI}/I [MHz/A]
Z	1390	147	29.2	105
W	147	15.8	3.43	107
H	29	2.96	0.536	102
T	5.4	0.526	0.0959	97

It was found that with a more realistic pressure profile, the number of abundant losses increases, resulting in additional 40 % losses for the entire machine. Pressure profile and loss distributions with and without that profile are shown in Fig. 4.12.

With roughly 100 MHz loss rate per Ampere of beam current, the losses in the interaction region have been estimated. The results can be used for further studies, for example full detector simulations. Early results are encouraging and show that the contribution to backgrounds is negligible when compared, for instance, with luminosity driven background like radiative Bhabha scattering or $\gamma\gamma \rightarrow \text{hadron}$ [23].

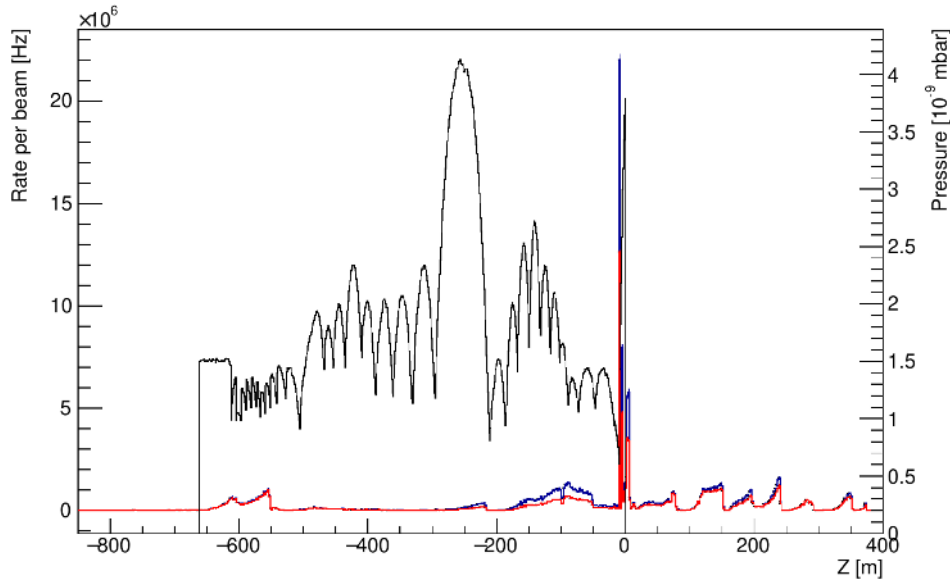


Figure 4.12: Pressure profile for the relevant section of the beam line, together with default (red) and modified (blue) loss distribution after taking into account the pressure profile.

4.4 Touschek

The previous two sections were concerned with scattering process that occur due to external scattering sources outside of the bunch: Thermal Photons emitted from the beam-pipe and Beam-Gas scattering on residual gas atoms.

This section introduces single Coulomb scattering between particles of the same bunch, an effect known as *Touschek Scattering*.

Those scattering processes can lead to an energy exchange, such that transverse momenta are transformed into significant longitudinal momenta. Subsequent energy deviations can easily reach the energy acceptance of the machine and subsequently lead to particle loss [40]. First observed in the ADA storage ring, it is a considerable effect for low-energy machines and can limit the lifetime significantly, for example of synchrotron light sources [41].

Besides the lifetime contribution, Touschek scattering can additionally lead to emittance increase or non-Gaussian tails. Particles might as well hit the beam-pipe wall, due to energy deviation and dispersion in the dipoles. This can contribute to detector backgrounds, given that losses occur close enough to the interaction point. If particles hit the beam pipe wall here, it is likely that the resulting showers can reach the experiment.

The lifetime contribution can be estimated based on Eq. (4.74) [40].

$$\frac{1}{N} \frac{dN}{dt} = \frac{1}{\tau} = \frac{Nr_0^2 c}{8\pi\sigma_x\sigma_y\sigma_s} \frac{\lambda^3}{\gamma^2} D(\xi) \quad (4.74)$$

With transverse and longitudinal beam sizes $\sigma_{x,y}$ and σ_s , respectively. The energy acceptance is denoted by λ and the Lorentz factor by γ . $D(\xi)$ is a universal function, where $\xi = (\epsilon_{RF}/\gamma\sigma_p)$. ϵ_{RF} denotes the energy (RF) acceptance of the machine and σ_p can be considered as the individual RMS transverse momenta of the particles. Equation (4.74) scales with the inverse square of the Lorentz factor. That indicates a negligible contribution for FCC-ee, where γ ranges from 8.9×10^4 to 3.57×10^5 .

Although Touschek scattering is most relevant for low energy machines or machines with very dense beams, it should be considered for FCC-ee as well since the nano beam scheme requires very small and therefore dense bunches in order to reach high luminosities. Again, the low-energy machine (at 45.6 GeV beam energy) is presumably more affected by this process than configurations at higher energies, for example $t\bar{t}$ with 182.5 GeV beam energy.

The following overview presents lifetime estimates resulting from Mad-X [42], where different assumptions with respect to certain parameters have been used. Bunch length σ_s and momentum spread δ_p will have different values for scenarios with and without collision. Table 4.8 presents the Touschek lifetimes based on different input parameters for FCC-ee Z and $t\bar{t}$. The lifetimes are found to be significantly higher with a beam energy of 182.5 GeV than for 45.6 GeV – as could be expected.

These lifetimes are considerably longer than other limiting effects, such as radiative Bhabha scattering or beamstrahlung, as reported in [2]. With those effects considered, the lifetime reduces to 68 min and 39 min (Bhabha) and >200 min and 18 min (beamstrahlung), at lowest and highest beam energy, respectively. It is

4.4. TOUSCHEK

Table 4.8: Touschek lifetime estimates from Mad-X for lowest and highest beam energies at FCC-ee, considering a single beam scenario with synchrotron radiation activated.

E_b [GeV]	τ [h]
45.6	81.48
182.5	11001.75

therefore unlikely that the beam lifetime at FCC-ee will be limited due to Touschek scattering.

4.5 Beamstrahlung

The last condition that is lifted is the absence of another beam. So far, this chapter introduced the effects of electromagnetic fields, external and internal scattering sources on the beam. Which lead subsequently to synchrotron radiation, scattering on Thermal Photons and residual gas atoms and the Touschek effect. If two beams are brought into collision, the field of one bunch will have an effect on the opposing bunch and the other way round, leading to **beamstrahlung** (BS).

General synchrotron radiation in an accelerator is a beam induced background. As such, it is always present with either one or both beams circulating. On the other hand, particles of one beam will be deflected by the electromagnetic field of the other beam during collisions. Deflected particles radiate photons [43]. The process is schematically visualized in Fig. 4.13.

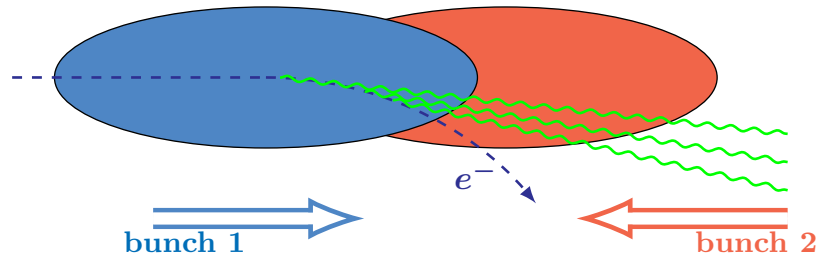


Figure 4.13: Phenomenological sketch of two bunches colliding head-on. Shown is the example trajectory of an electron that is deflected from the original path by the field of the opposing bunch. Synchrotron radiation is emitted due to this deflection.

For a given accelerator, the expected strength of beamstrahlung can be estimated according to [43] with the parameter Υ as defined in Eq. (4.75). In the context of this study, the beamstrahlung parameter, together with mean photon energy and number of photons/electron will be estimated for highest and lowest beam energies.

$$\Upsilon = \frac{2}{3} \frac{\epsilon_c}{E_b} = \frac{2}{3} \frac{\hbar\omega_c}{E_b} \quad (4.75)$$

Υ is a dimensionless and Lorentz invariant parameter, basically relating the critical photon energy ϵ_c with the initial beam energy E_b . Assuming Gaussian bunches, it can be averaged – Υ is not constant during collision.

$$\Upsilon_{av} \approx \frac{5}{6} \frac{Nr_e^2\gamma}{\alpha\sigma_z(\sigma_x + \sigma_y)} \quad (4.76)$$

Equation (4.76) shows that high intensity (number of particles per beam, N), high energy (γ) and a short bunch length (σ_z) can enhance beamstrahlung. Considering design parameters for FCC-ee, the beamstrahlung parameter estimates can be found in Tab. 4.9. These numbers show that the classical approximation holds, with $\Upsilon \ll 1$. The number of photons as well as the average photon energy can then

be derived using Eq. (4.77) and Eq. (4.78) – again assuming Gaussian beams [43].

$$n_\gamma \approx 2.59 \frac{\alpha^2 \sigma_z Y_{\text{av}}}{2\pi r_e \gamma} \quad (4.77)$$

$$\frac{\langle \hbar\omega \rangle}{E_b} \approx 0.462 Y_{\text{av}} \quad (4.78)$$

The average photon energy indicates that photons generated by this process can have fairly high energies. However, the radiation is usually emitted in narrow cones along the beam, therefore can be expected to leave the central interaction region without generating additional direct hits in close vicinity of the detector. Beamstrahlung should be considered during the design of the MDI – also with respect to the vacuum system. In order to account for possible issues in terms of power deposition, the effect of beamstrahlung will be further analyzed in Chapter 7.

Table 4.9: Quantities characterizing beamstrahlung at lowest and highest energy in FCC-ee.

E_b [GeV]	Υ [10^{-4}]	$\langle \epsilon \rangle$ [MeV]	n_γ/e^\pm
45.6 GeV	1.77	3.73	0.19
182.5 GeV	7.66	64.61	0.04

Another direct consequence of beamstrahlung is the energy loss of particles in the beam by radiating photons – as is the case with conventional synchrotron radiation. If this energy loss exceeds the momentum acceptance of a machine, particles will be lost from the beam and beamstrahlung can therefore limit the beam lifetime as well. It will further contribute to the beam tails and increases the energy spread in the beam. Additional effects of beamstrahlung are changes in bunch length and transverse emittance, which in turn influences the luminosity \mathcal{L} and its' measurement [44, 45].

Apart from radiation aspects, beamstrahlung can produce additional background in the detector, either via photon scattering or pair creation [23].

5 | The Simulation Tools

Simulations of particle backgrounds in the **MDI** are a complex process, based on different types of input. One program might be able to provide the machine lattice description and optical functions, but does not allow detailed tracking of particles in matter. On the other hand, a program describing the interactions of particles with matter (based on Monte-Carlo generators) needs to have an accurate geometry in order to deliver reliable predictions of possible backgrounds. Hence, it is required to interface different programs.

This chapter briefly introduces a flexible toolkit, **MDISim**, that combines several codes – each serving one particular purpose. **MDISim** is used for all simulations of the photon background in the framework of this thesis.

A strongly simplified example of a 10 m long dipole magnet which is bent to a full ring, referred to as **SingleBend** can be found in the appendix. Without real physical application, it serves purely for the purpose of illustrating the working principles of **MDISim**.

5.1 Basic Idea

MDISim – Machine-Detector-Interface Simulations – provides a flexible interface between different programs. Development of **MDISim** relies as much as possible on existing standard tools, extending or improving those wherever needed: **Mad-X**, **Root** and **Geant4**.

A typical work-flow diagram is depicted in Fig. 5.1, more details will be introduced below. Early applications of **MDISim** on synchrotron radiation have been reported in [46, 12] and [47] (for **FCC-hh**), while beam-gas backgrounds were estimated for **FCC-ee** using **MDISim** in [37] (also summarized in Chapter 4 of this thesis).

In order to simulate background processes in the interaction region of an accelerator, it is required to have a description of the machine lattice and magnetic fields, which guide a given particle beam through the elements. A second requirement, especially when employing a Monte-Carlo code such as **Geant4**, is specific information on the initial particle distribution and beam energy.

MDISim provides a geometry description of the accelerator lattice based on the **Mad-X TWISS** table in form of a **Geometry Description Markup Language (GDML)** model (additional information is available the appendix and in [48, 49]), generated using **Root**. It further reads the field information from the **Mad-X TWISS** tables. Geometry as well as field information are used as input in **Geant4**, where the magnetic fields are established individually in each magnet, depending on its type.

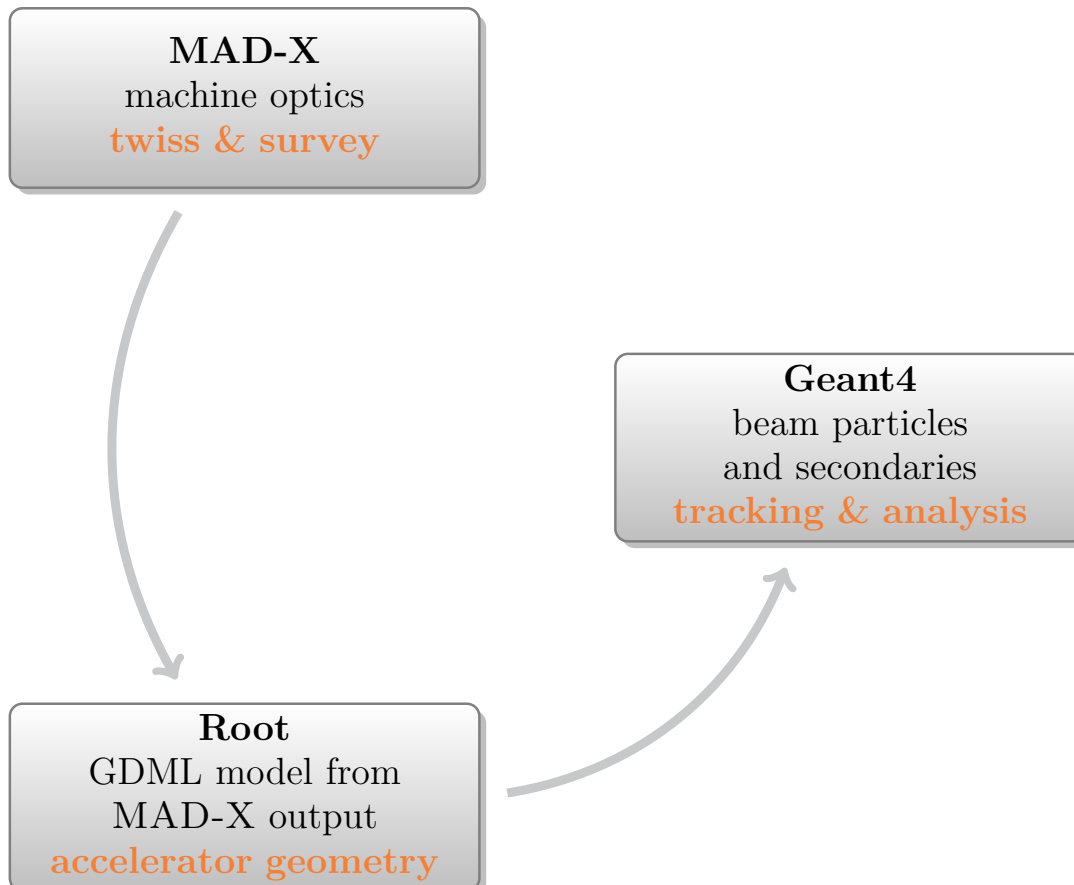


Figure 5.1: The three blocks that are combined with *MDISim* to study backgrounds in the *MDI*. All starts with the *TWISS* table from *Mad-X*, where machine lattice, optical functions and beam parameters are detailed. Geometry as *Geometry Description Markup Language (GDML)* file and field information are generated in a second step. Both are used in a third step, the detailed particle tracking in *Geant4*.

Mad-X further provides important input in terms of optical functions and beam parameters. With that information, the beam is generated at a starting position along the accelerator, which can be chosen by the user. An expanded description of this beam generator can be found in Section 7.2.

5.2 The Tools

Mad-X

The *Mad-X* *TWISS* table is used in *MDISim* for the lattice description (including the optical functions), and specifications of the magnetic fields. It further provides necessary information to generate a beam at a certain start position in *Geant4*. More information about *Mad-X* is available in the documentation [16].

Root

Root is a software framework widely used in high energy physics [50, 51].

Among its functionalities, it provides an interface to describe 3D geometries. This allows to generate whole detector models, such as *ATLAS* or *CMS* at *CERN*.

MDISim uses this feature to not only generate the required beam-pipe geometry, but also to establish a way of visualizing the track information from Geant4. Root can be used to show the accelerator geometry alongside with particle tracks and secondary particles such as synchrotron radiation photons (examples are displayed in Figs. A.2 and A.3).

Furthermore, Root can be used to do fundamental analysis on the data resulting from Monte-Carlo simulations with Geant4, in combination with its dedicated input-output tools. Data storage and access becomes very efficient using the C++ approach which is implemented in Root, as it is already used to store significant amounts of data [50]. This makes it a natural choice for data management with Geant4, since detailed particle tracking tends to produce a lot of information.

Geant4

Figure 5.1 depicts the last step in an ordinary simulation cycle with MDISim to be the detailed particle tracking in Geant4. The tracking capabilities of Geant4 are used in the context of this thesis for synchrotron radiation photons [52, 53].

With a worldwide collaboration between physicists and software engineers, it is open sourced and therefore allows for improvements and extensions – also from the user side. A given application can always be adjusted for the need of a certain simulation, making it the tool of choice for MDISim. Geant4 is available for free with exhaustive user guides and examples [52].

6 | SuperKEKB

At the **High Energy Research Facility (KEK)** in Tsukuba, Japan, the project SuperKEKB was initiated as a successor of the B-factory KEKB, in operation until 2009. SuperKEKB is an electron positron collider, supposed to upgrade the former KEKB factory with a 40 times higher luminosity to reach $\mathcal{L} = 8 \times 10^{35} \text{ cm}^{-2}\text{s}^{-1}$. Commissioning started in 2016 with Phase I and is currently ongoing. Physics requirements demand asymmetric beams, colliding a 4 GeV positron beam, the **Low Energy Ring (LER)** with a 7 GeV electron beam, also referred to as **High Energy Ring (HER)**.

In order to reach such high luminosities, a novel scheme was employed, called the *nano beam scheme*. It is based on small beams at the interaction point, invoking strong final focus magnets and a large crossing angle, among other features implemented in the lattice design [54].

These features make SuperKEKB interesting also for the **FCC-ee** design study. Novel techniques such as strong final focus magnets very close to the interaction point, partly covered by the detector solenoid and paired with a large crossing angle are characteristics which can be found in the **FCC-ee** design as well.

MDISim was developed mainly with a focus on simulating particle backgrounds in the **FCC-ee** interaction region, but not exclusively. It might be used for other machines as well. Hence, a comparison between simulation data from MDISim and actual data from a running machine could proof the performance of MDISim. In order to accurately model a complex interaction region, MDISim needs further development, especially considering a region where different magnetic fields are superimposed – as is the case at SuperKEKB.

This chapter introduces developments on MDISim which have been performed in the context of this study to arrive at a more realistic representation of the closed orbit of the **LER** at SuperKEKB.

6.1 Beam Parameters and General Layout

SuperKEKB is designed in a double ring layout, colliding both beams in a single interaction point where the Belle-II detector is located (Tsukuba straight section) – as depicted in Fig. 6.1.

In order to reach luminosities as high as $10^{35} \text{ cm}^{-2}\text{s}^{-1}$, the upgrade to SuperKEKB needs to introduce new concepts. Small beam sizes are supposed to be reached with an emittance as small as 3.2 nm and 4.6 nm in the horizontal and 8.64 pm and 12.9 pm in the vertical plane (values in these tuples correspond to **LER** and **HER**,

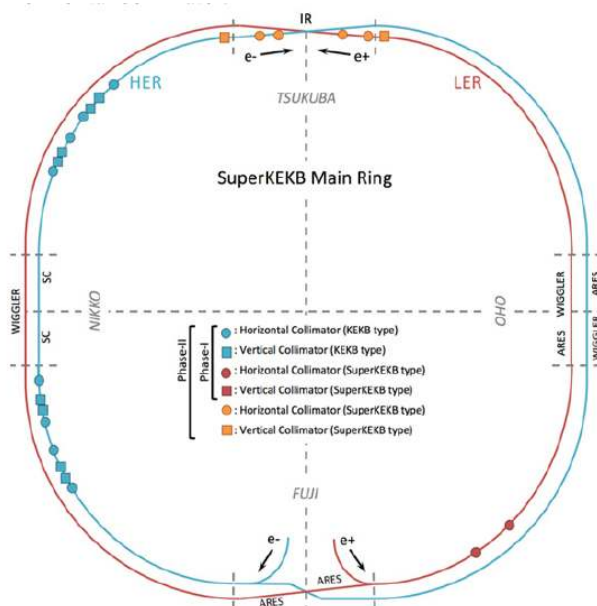


Figure 6.1: Layout of both SuperKEKB rings [55]. A low energy *positron beam* is brought into collision with a high energy *electron beam* at a single interaction point in the Belle II detector. The interaction region is located in the Tsukuba straight section. Injection is done in the Fuji section, while other straight sections host RF and wigglers (Nikko, Oho).

respectively). Strong final focus magnets provide focusing at the interaction point of $\beta_x^* = 32$ mm and 25 mm (LER, HER) and $\beta_y^* = 270$ μ m and 300 μ m (LER, HER).

Another important aspect to reach the luminosity goal is a large crossing angle $2\theta_x$ of 83 mrad. It allows to quickly separate the beams after collision and helps to reduce parasitic (unwanted) collisions. The crossing angle allows to reduce the vertical beam size via β_y^* , while not being limited by the bunch length to push the luminosity [56, 54].

The MDI layout of FCC-ee is strongly influenced by the large crossing angle.

As a third point, beam currents (I_b) need to be increased from those used at KEKB, to reach the high intensities required for the luminosity goal. For the electron beam (HER) the aim is to store 2.6 A, and 3.6 A for the positron ring (LER). A selection of design parameters is summarized in Tab. 6.1.

Significantly lower beam energies than at FCC-ee lead to less energy loss per turn (U_0) due to synchrotron radiation. Both beams lose no more than 2.43 MeV per turn. For the LER, the total radiated power amounts to 6.33 MW, while 6.32 MW can be expected in the HER.

Accordingly, critical energies (ϵ_c) are lower than what can be expected at FCC-ee. In the LER an average of 0.29 keV is estimated, while the HER will generate photons with average critical energies about 1.58 keV. These estimates assume a generic radius of $\rho \approx C_0/2\pi$.

However, synchrotron radiation must be studied carefully, given experiences from KEKB with damage in the detector due to synchrotron radiation – even at such relatively low energies.

Other background sources like Beam-Gas and Touschek scattering become important as well. The Beam-Gas background might be enhanced especially in newly installed sections of the beam pipe from out-gassing, resulting in an initially

Table 6.1: Selection of design parameters for SuperKEKB.

Parameter	Symbol	unit	LER	HER
Beam energy	E_b	GeV	4	7.007
Beam current	I_{beam}	A	3.6	2.6
number of bunches	k_{bun}		2500	2500
bunch current	I_{bunch}	A	0.00144	0.00104
circumference	C_0	m	3016.315	3016.315
particles/bunch	n_{part}	10^{10}	9.04	6.53
horizontal emittance	ϵ_x	nm	3.2	4.6
vertical emittance	ϵ_y	pm	8.64	12.9
emittance ratio	κ	%	0.27	0.28
horizontal beta at IP	β_x^*	mm	32	25.0
vertical beta at IP	β_y^*	mm	0.27	0.3
momentum compaction	α_p	10^{-5}	3.2	4.55
energy spread	σ_δ	10^{-4}	7.92	6.37
RF voltage	V_c	MV	9.4	15.0
bunch length	σ_z	mm	6	5.0
energy loss/turn	U_0	MeV	1.76	2.43

higher vacuum pressure [57].

6.2 The Interaction Region - Main Challenges

Optics design at SuperKEKB is not dominated by reducing potentially strong synchrotron radiation. But the interaction region layout still is rather complex due to other reasons, for example space constraints, given that the accelerator is installed in the former KEKB tunnel.

Figure 6.2 shows the optics ± 100 m around the interaction point ($S = 0$ m). While the optics in the FCC-ee interaction region are asymmetric to suppress the critical energy of synchrotron radiation photons generated upstream, the SuperKEKB design features symmetric optics.

Table 6.2 lists selected analytic estimates for the first 5 LER dipole magnets upstream and downstream of the interaction point. These values have been derived using the phase 2.1 lattice from 2018, applying equations introduced in Chapter 4 to characterize the dipole magnets. Critical energies do not exceed 2.5 keV, the last two upstream dipole magnets have critical energies of even less than 1 keV. Average photon energies do not reach 1 keV.

The central interaction region of SuperKEKB spans over ± 4 m and is shown in Fig. 6.3. Due to the energy asymmetry of the colliding beams and the corresponding Lorentz boost of the collisions, the interaction point is not located in the centre of the Belle II detector but at an offset.

The detector solenoid covers parts of the final focus quadrupoles, especially on the right side due to the given asymmetry of the interaction point. The final focus system is divided into several magnets, installed in two cryostats.

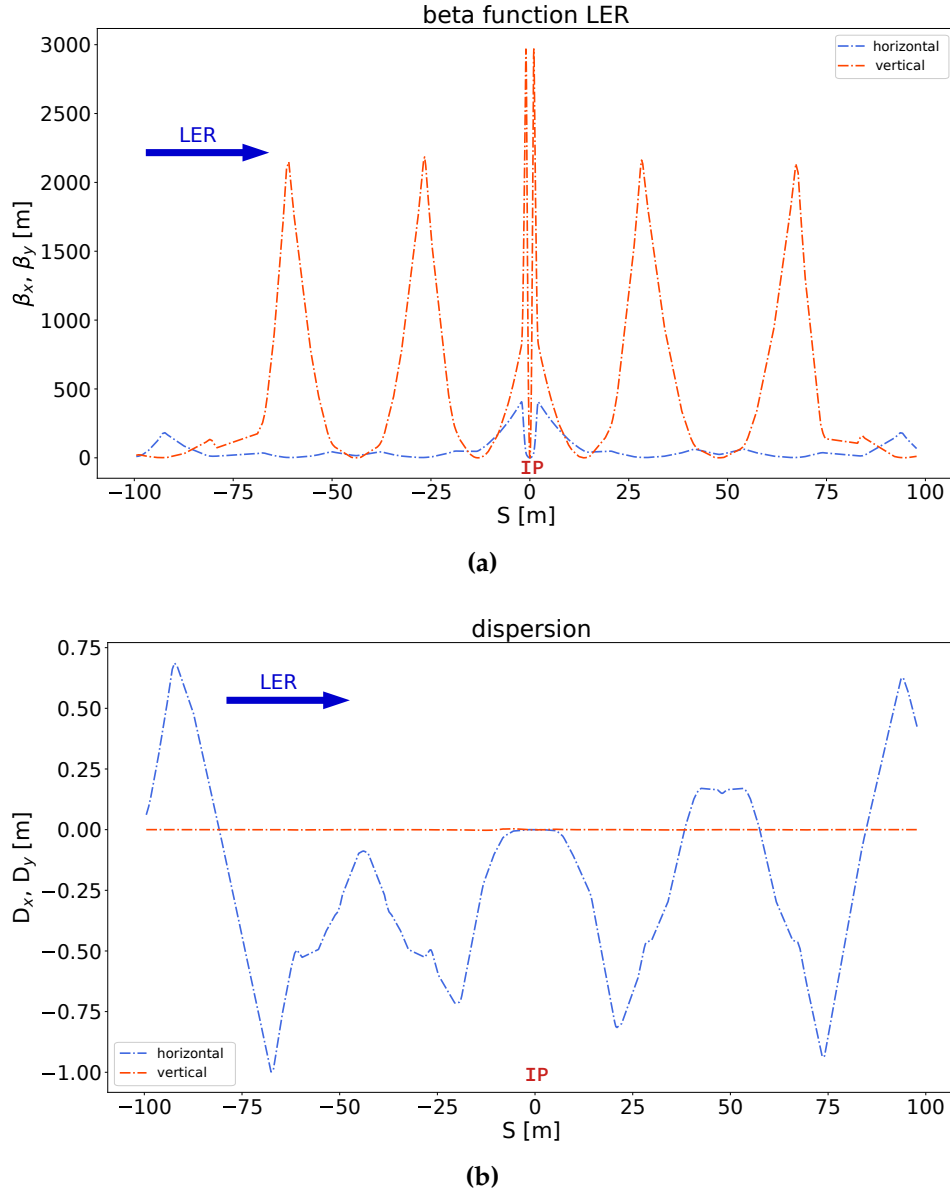


Figure 6.2: Optics in the interaction region of SuperKEKB. (a) shows the beta function reaching high values with strong focusing towards the **Interaction Point (IP)** ($S = 0$ m) and (b) the dispersion that is brought down to 0 at the interaction point. The optics are symmetric, contrary to FCC-ee where an asymmetric optics design was required to reduce the critical energy ϵ_c of incoming photons. These plots have been produced using SAD on the phase 2.1 lattice of the LER.

This complicated design of the **MDI**, with complex final-focus magnets, a strong detector solenoid of 1.5 T and the large crossing angle of 83 mrad also has significant effects on the closed orbit of the beam around the interaction point, which will be discussed below, among the most important aspects of the **MDI** design.

Table 6.2: Selection of parameters characterizing upstream (upper half) and downstream (lower half) dipole magnets close to the interaction point. These analytic estimates are for the LER with 4 GeV. Critical energies of upstream dipole magnets are reduced while approaching the interaction point. The last two upstream dipole magnets, BLCWRP.1 and BC1RP.1 are highlighted in turquoise.

NAME	S [m]	L [m]	ϵ_c [keV]	ρ [m]	B [T]	P_{SR} [kW]	$\langle\epsilon\rangle$ [keV]
BLY2RP.2	2988	4.16	2.08	68.4	0.195	11.5	0.639
BLC2RP.1	2996	4.16	2.1	67.7	0.197	11.8	0.645
BLC1RP.1	3008	2.235	1.77	80.4	-0.166	4.48	0.544
BLCWRP.1	3011	2.235	0.947	149.9	-0.089	1.29	0.292
BC1RP.1	3012	0.2811	0.182	781.9	-0.0171	0.00596	0.0559
BC1LP.1	4.313	0.2811	0.351	404.2	-0.033	0.0223	0.108
BLC1LP1.1	7.09	1.603	2.2	64.7	-0.206	4.97	0.676
BLC1LP2.1	9.771	2.235	0.616	230.4	-0.0579	0.546	0.19
BLC2LP.1	26.34	4.16	2.16	65.8	0.203	12.5	0.665
BLY2LP.1	34.02	4.16	2.18	65.1	0.205	12.7	0.671

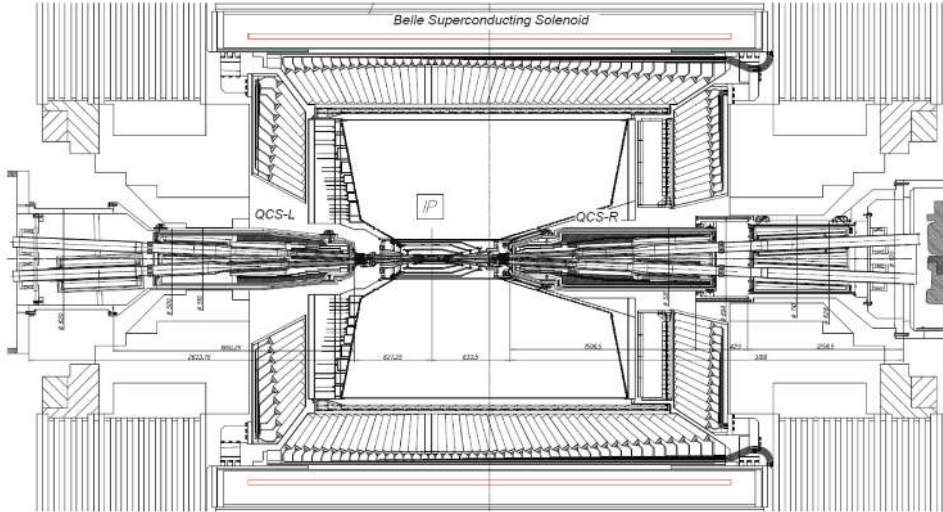


Figure 6.3: Technical drawing depicting a top view on the Belle II detector, showing the location of the interaction point and how the final focus cryostats (QCS-L/R) reach into the solenoid field [58]. The interaction point is located with an offset to the detector centre due to the asymmetric beams.

The Final Focus System

The final focus system at SuperKEKB consists of 5 superconducting and 3 normal conducting magnets. The superconducting final-focus magnets are assembled inside two cryostats (QCSL – left and QCSR – right) and reach gradients as high as 80 T/m. Such strengths are required to focus the beam down to μm horizontally and nm vertically.

Since the detector solenoid covers a significant part of the final-focus system, cancelling coils are used to shield the quadrupoles from the solenoid field, adding to the complexity of the MDI layout. Space constraints further complicate the design, as leakage fields of the magnet system of one beam would affect the other beam and vice versa. Iron blocks are supposed to minimize this leakage [58, 59]. QC1LP and QC1RP deliver the final focusing of the positron beam (LER) and are

located closest to the interaction point, with a distance of ± 0.93 m.

Beam Pipe apertures in the IR

While the beam is approaching the interaction point, it passes through consecutive aperture sections in the final focus magnets, each reduced in diameter until reaching the central chamber with a 10 mm diameter (from an initial 80 mm default diameter.).

Figure 6.4 shows a representation of the apertures through the LER final focus system ± 4 m around the interaction point. Different scales are applied on vertical and horizontal axis, respectively.

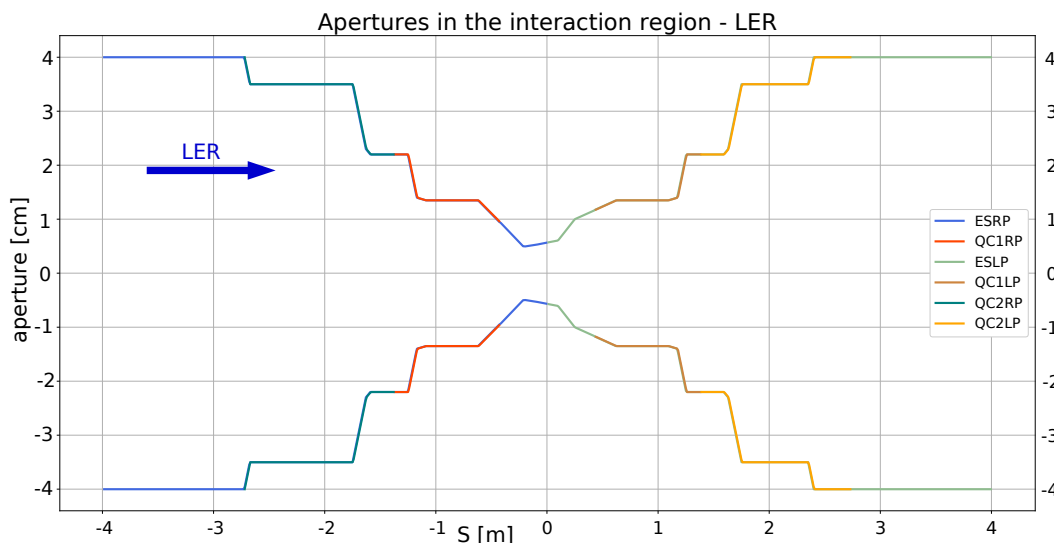


Figure 6.4: Dimensions of the beam pipe in the central interaction region. The interaction point is located at $S = 0$ m. Colors indicate different magnets – QC* represent final focus quadrupoles, ESL/RP denote the Belle II solenoid (where it is not superimposed with the final focus magnets).

Designing the vacuum system by subsequently reducing the beam pipe diameter towards the interaction point helps to collimate incoming synchrotron radiation and shield the central detector chamber. In case of SuperKEKB the central chamber is made from Beryllium, as planned for FCC-ee, with a cooling channel to mitigate heating due to synchrotron radiation and wall currents [58].

Care was taken in the lattice design to avoid radiation from the last upstream dipole magnets to directly hit the central chamber. The inner upstream beam-pipe additionally features a ridge (or sawtooth) structure to increase the photon diffusion and limit the amount of direct hits on the central Beryllium chamber [58].

To simulate the photon background in the SuperKEKB interaction region, a 3D model of the LER beam-pipe was generated with MDISim. The result is shown in Fig. 6.5 and represents the aperture restriction in the final-focus quadrupoles.

The Belle II Solenoid

The detector solenoid of Belle II covers an overall cylindrical volume of 3.4 m diameter and 4.4 m length [58] as depicted in Fig. 6.3. It generates a longitudinal field profile as shown in Fig. 6.6 and features a rather constant field of 1.5 T around

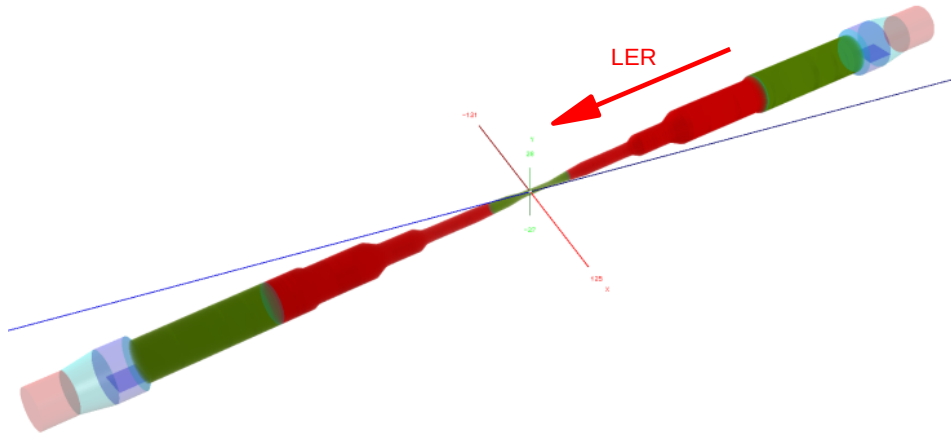


Figure 6.5: 3D model of the central interaction region geometry generated by MDISim in Root display. The LER beam is approaching from the top right corner and traverses the section with subsequently reduced aperture. This structure is supposed to limit the amount of synchrotron radiation that reaches the central detector chamber. Red elements represent the final focus elements, while parts covered purely by the solenoid are highlighted in green.

the interaction point. Measurable leakage can be observed in the QCS-R cryostat (location of the cryostats are indicated as grey areas in the same figure). Note, that the plot does not show the pure solenoid field but a combination, including the anti-solenoids on both sides, reaching almost -2.5 T to cancel the integral field $\int dsB_z$. Single field components are shown in Fig. 6.7 – results from an actual measurement [60].

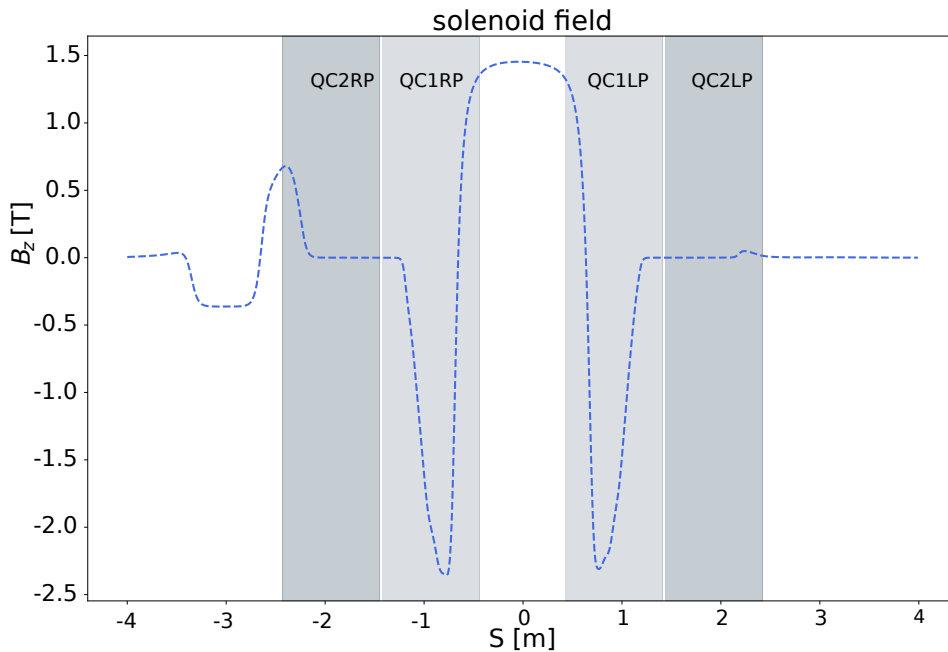


Figure 6.6: Representation of the solenoid field in the interaction region of SuperKEKB. The data is shown for the LER. Considerable leakage of the solenoid field is to be expected in the right final-focus cryostat QCR*. The interaction point is located in the centre at $S = 0$ m. Gray areas indicate the location of final focus cryostats.

As noted earlier, the field affects beam dynamics as it introduces additional X-Y coupling [56] but also influences the design orbit:

6.2. THE INTERACTION REGION - MAIN CHALLENGES

Since particles enter with a finite crossing angle of 83 mrad, fringe fields of the solenoid will additionally deflect the beam, depicted in Fig. 6.8. The resulting closed orbit around the interaction point is thus rather complex. This effect is even more relevant than for FCC-ee since the crossing angle at SuperKEKB is larger, with at the same time lower beam energies. Due to this deflection of the beam, synchrotron radiation will be emitted in the solenoid.

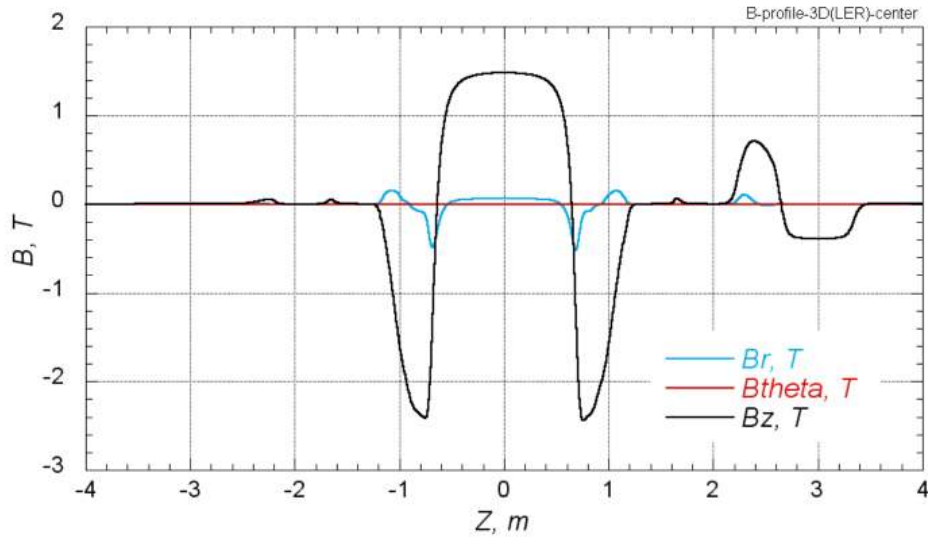


Figure 6.7: Single components of the solenoid field in the central interaction region from an actual measurement of the longitudinal, radial and azimuthal field components, done at KEK [60]. The blue line shows the fringe fields which add additional deflections to the beam orbit.

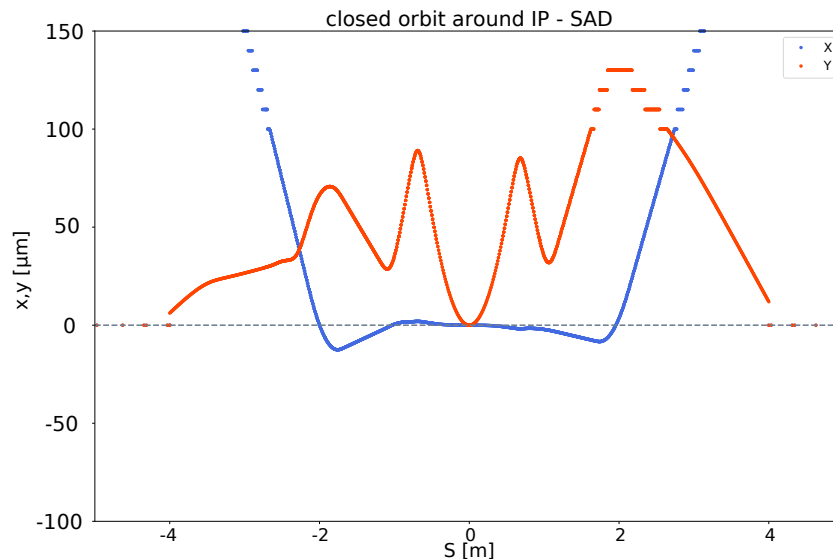


Figure 6.8: The closed orbit of the LER around the interaction point from a simulation in SAD. Especially in the vertical plane (y), the orbit is characterised by several wiggles.

In the context of this study, an estimation for critical energies of radiated photons is done. The particle enters the solenoid at an angle $\theta_x = 41.5$ mrad and is subject to a tilted field of 1.5 T. The field can be decomposed into two parts, the transverse

and longitudinal contribution B_{\perp} and B_{\parallel} :

$$\begin{aligned} B_{\perp} &= B_z \sin \theta_x = 0.0622 \text{ T} \\ B_{\parallel} &= B_z \cos \theta_x = 1.4987 \text{ T} \end{aligned}$$

Where the parallel component does not contribute to the deflection and subsequent synchrotron radiation.

A solenoid field in this configuration with a crossing angle will deflect the beam due to the component B_{\perp} . This deflection can be compared to the one happening in a dipole magnet – a similarity which allows to estimate the critical photon energy.

$$\epsilon_{c,\perp} = \frac{3}{2} \hbar c \gamma^3 K S_{\perp} \quad (6.1)$$

Where KS denotes the solenoid strength and was derived as in Eq. (6.2) (with the definition for the solenoid strength from Mad-X [16]).

$$KS_{\perp} = \frac{B_{\perp}}{B\rho} \quad (6.2)$$

At SuperKEKB, magnetic rigidity and Lorentz factor have the following values

$$\begin{aligned} B\rho_{\text{LER}} &\approx 13.34 \text{ Tm} \\ \gamma_{\text{LER}} &\approx 7.83 \times 10^3 \\ B\rho_{\text{HER}} &\approx 23.35 \text{ Tm} \\ \gamma_{\text{HER}} &\approx 1.37 \times 10^4 \end{aligned}$$

Such that the critical energy of photons generated in the solenoid amounts to

$$\epsilon_{c,\text{LER}} = 0.66 \text{ keV} \quad (6.3)$$

$$\epsilon_{c,\text{HER}} = 2.03 \text{ keV} \quad (6.4)$$

Considering the nominal critical energy for the **LER** of only 0.29 keV, the contribution from the solenoid generates radiation with roughly a factor of 2 higher critical energy. Following the same calculation, the critical energy for photons radiated by the **HER** in the solenoid amounts to ≈ 2 keV, about 1.3 times higher than the nominal critical energy.

As a short comparison of critical energies for photons generated in the detector solenoid at **FCC-ee**: At lowest beam energy (45.6 GeV) ϵ_c from the solenoid reaches 41.51 keV – about a factor 2 of the average critical energy of the entire machine. With 182.5 GeV beam energy, photons from the solenoid have critical energies of about 664.21 keV, which is roughly half of the average (1.25 MeV).

These estimates show that synchrotron radiation generated in the solenoid can reach fairly high critical energies and should not be neglected in a study of the photon background.

Tracking with MDISim

The last section of this chapter describes modifications in MDISim, done in the framework of this thesis, in order to better parametrize the magnetic fields in a

complicated interaction region such as at SuperKEKB.

Performing simulations with MDISim to estimate the photon background at SuperKEKB needs a careful modelling of the beam trajectory in the interaction region to arrive at realistic conclusions. Including the data from the SAD lattice, a simplified tracking in Geant4 was done in the context of this study, starting at the interaction point and traversing the positive side of the central interaction region.

Preparations & Considerations

To prepare MDISim for simulations which include complicated field arrangements, capabilities of the toolkit to process external data have been extended. External data in this case can be a field-map, describing the arrangement of magnetic fields. The example presented below considers the field configuration in the LER interaction region at SuperKEKB, taking into account the overlap of solenoid field components with the quadrupoles. This configuration was originally implemented in SAD (Strategic Accelerator Design [61]) using a fieldmap from actual measurements [60]. Relevant parameters have been extracted from the SAD lattice and processed for use with MDISim.

In the following subsection, the field representation in the SAD lattice will be explained.

The default tracking in MDISim – prior to any modifications of the program – resulted in a track as shown in Fig. 6.9. MDISim initially lacked the detailed field information, resulting in the straight track shown in that plot.

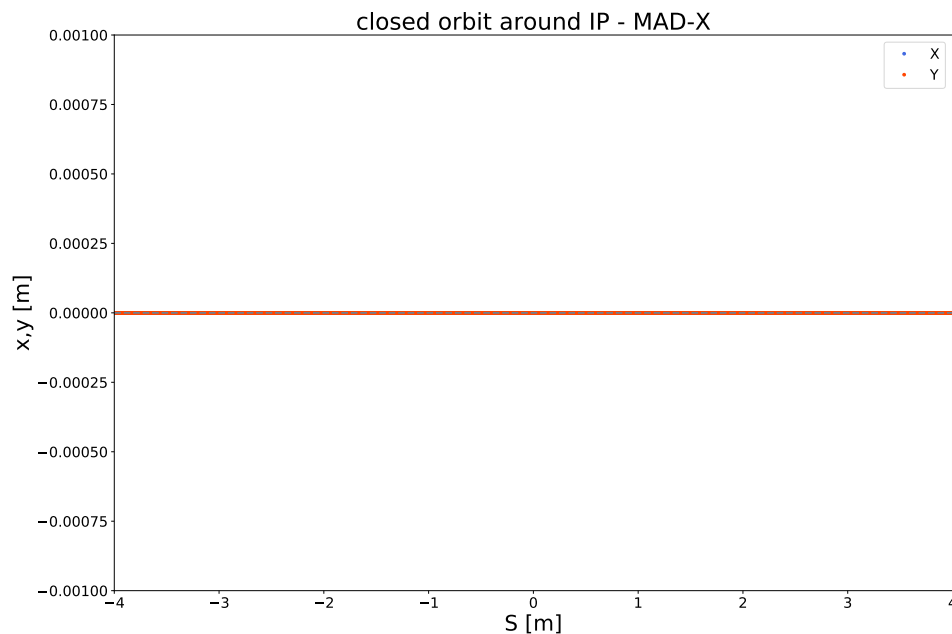


Figure 6.9: Initial closed orbit in Mad-X, which would then be subsequently processed with MDISim to simulate the photon backgrounds. It is not well reproduced – compare Fig. 6.8.

Representation in the SAD File

In the interaction region of SuperKEKB, several magnets are present. This results in an overlap of different fields, generating a complex superposition of the single

contributions. In general, the interaction region contains bending magnets (correctors), quadrupoles and the Belle II solenoid, basically spanning over the entire central interaction region ± 4 m in S.

This has to be reproduced in the theoretical model as accurate as possible. Hence, the SAD file uses a certain approach to represent these fields. In the following, the focus is on the LER (the procedure for the HER would be basically the same).

One important technique is the *slicing*, where magnets of length L are divided into N single blocks of length L/N. Solenoid as well as quadrupoles are sliced to model the overlap (Fig. 6.11).

The solenoid region is defined to span over ± 4 m around the interaction point, and allows only four element types to be inserted: DRIFT, BEND, QUAD and MULT. Main part for interaction region modeling will be:

- final focus magnets, QC1L/RP and QC2L/RP
- multipoles, ECSL/RP
- pure solenoid elements, ESL/RP

ESL/RP components – pure solenoid slices (solenoid without quadrupole overlap) – have a finite length of 1 cm and carry the longitudinal component of the detector field, which does not change with beam energy. That is applied for all pure solenoid regions which sandwich the final focus slices, as shown in Fig. 6.10. Field imperfections are represented by higher order terms in multipole slices of 0 length, ECSL/RP.

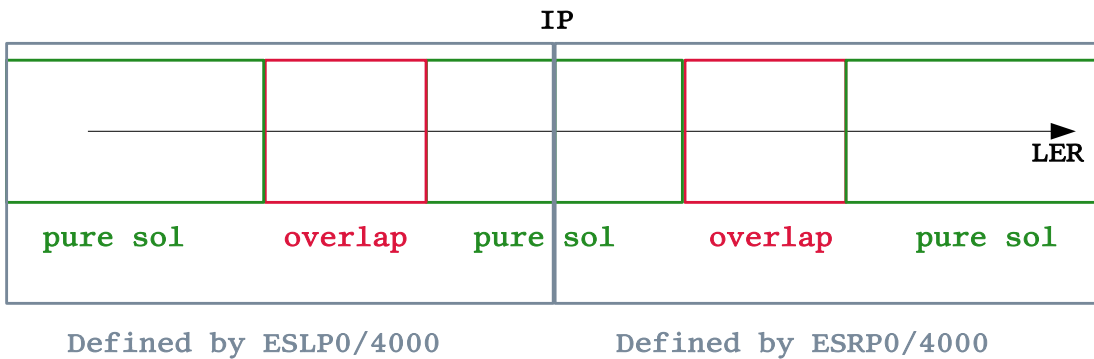


Figure 6.10: Conceptual sketch how magnetic fields in the interaction region are represented by different sections. Pure solenoids and overlap are defined within the overall solenoid region.

The overlap of detector field and final focus quads is the tricky part. It is represented as a unit of 0 length slices, always attached to a quadrupole, where only the quadrupole has a finite length $L \neq 0$ m.

ESLP460 . 1	SOLENOID
ECSLP461 . 1	MULTIPOLE
QC1LP465 . 1	QUADRUPOLE
ECSLP469 . 1	MULTIPOLE

Shown above is one example for such a unit within the overlap section. ESLP460 specifies B_z . ECSP461 and ECSP469 define all higher order terms of the solenoid and QC1LP465 represents the quadrupole. Such a unit is depicted in Fig. 6.11, where the space between single units is 0 in reality.

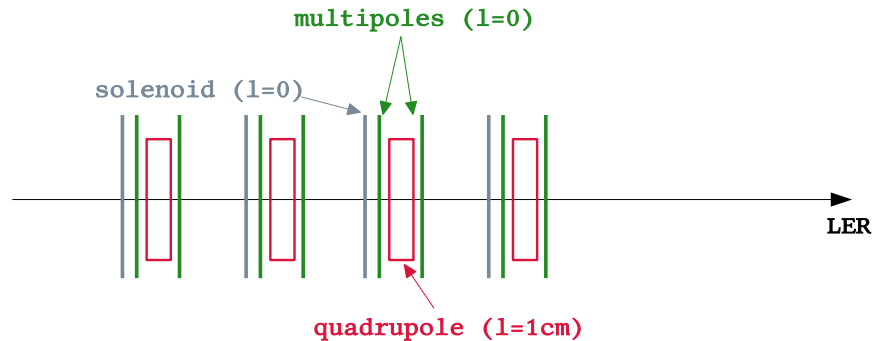


Figure 6.11: Example for the setup of single units in the *overlap* region. Each unit consists of solenoid, multipoles and quadrupole – represented as slices, where only the quadrupole slice has a finite length of $L \neq 0$. Multipoles carry field imperfections, while solenoid and quadrupole represent the main components.

Each multipole slice on both sides of a quadrupole represents the same multipole components. These components cannot be defined as attributes of the quad itself, since the quadrupole components can change, depending on the setting of the current optics: varying the current I_{quad} (due to optics tuning) would change the quadrupole component but not the solenoid components. Hence, both are separated.

Implementation in MDISim and Tracking

Field information provided with the SAD lattice – as described above – has been extracted and combined in an input file for MDISim. The magnetic fields are then established, based on the extracted components, inside corresponding volumes in Geant4. Figure 6.12 shows the tracking in Geant4, where the (LER) beam starts at the interaction point.

The result is comparable to the data shown in Fig. 6.7, except for a sign convention of B_z , which is internally adjusted to match the SAD closed orbit. Especially the fringe fields are now present (compare the blue curve in Fig. 6.12 with the light blue curve in Fig. 6.7).

Accordingly, field information in Geant4 was substantially improved, as demonstrated in Fig. 6.13. The closed orbit in the vertical plane (Fig. 6.13 (a)) is accurately modeled in the Geant4 tracking with MDISim, featuring the wiggles resulting from deflections due to fringe fields.

In the horizontal plane, slight deviations are still observable – the magnetic field information needs further checking to finally improve results in the horizontal plane as well (Fig. 6.13 (b)).

This progress is encouraging and proves that MDISim can successfully track particles even in a complex interaction region and handle the overlap of different magnetic fields. The vertical trajectory of the LER in SuperKEKB is very well

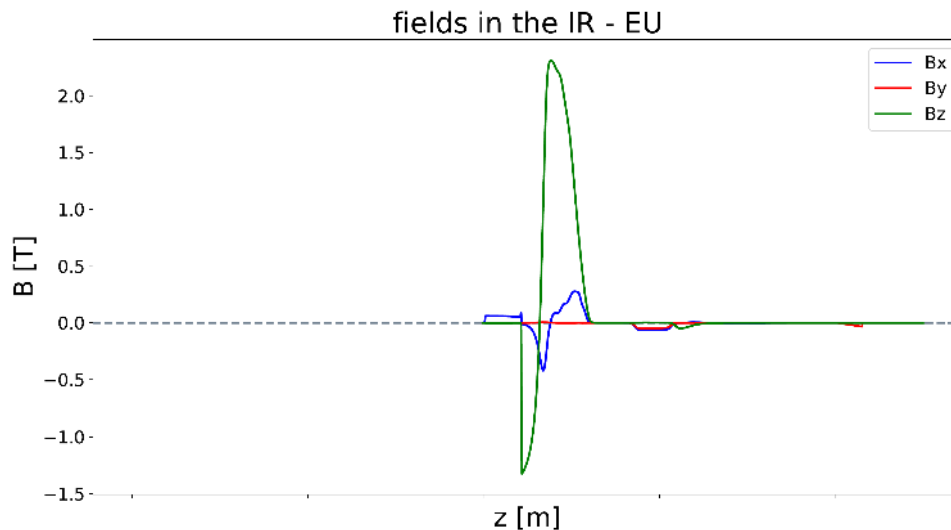


Figure 6.12: Magnetic fields as seen by a particle in Geant4 tracking with MDISim, starting from the interaction point ($z = 0$ m) and following the positive side of the central interaction region. Note, that the orientation of B_z (green) is reversed compared to Fig. 6.7 (black line) due to a sign convention in the field measurement.

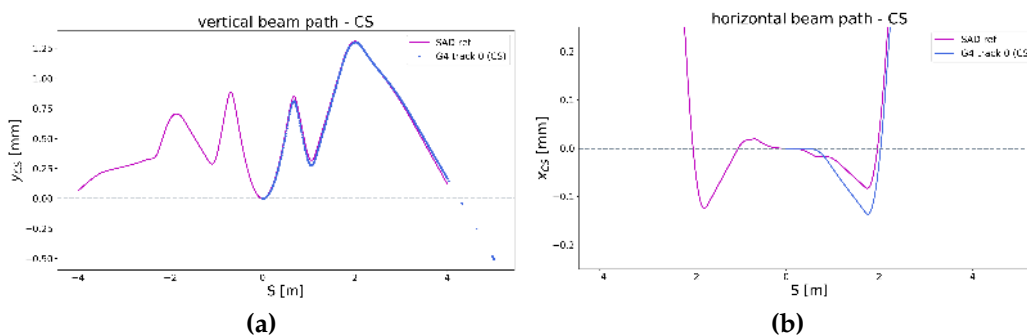


Figure 6.13: Results from tracking in Geant4. The design orbit in the vertical plane is well reproduced (a). In the horizontal plane, some deviation is still present (b), while the overall trend looks correct as well.

reproduced, while in the horizontal plane some offset is still observable, which is subject of future studies.

Next steps would be to track the beam through the entire interaction region and check if the design orbit is sufficiently reproduced.

After including the model for the central detector chamber, MDISim could be used for detailed simulations of the photon background at SuperKEKB with subsequent comparison of simulation data and actual measurements.

7 | Simulation Results

This chapter summarizes results from simulations of the photon background at FCC-ee.

The first part describes how the FCC-ee MDI is set up and which steps are required to arrive at a more detailed model, closer to the design than the baseline provided by MDISim.

Next follows a description of the beam-generator in the toolkit, that is extensively used to generate different particle distributions on which the beams in subsequent Monte-Carlo simulations are based.

A discussion of relevant upstream dipole magnets precedes a detailed characterization of the default expectable photon background at FCC-ee $t\bar{t}$. This part is very important as it provides the baseline background sample which is used to characterize the synchrotron radiation background in an ideal machine and will therefore be the reference.

With this basic characterization in place, the second part contains a detailed investigation of mitigation measures that are part of the interaction region layout as reported in the CDR [2].

Conditions in the central interaction region will need to be thoroughly examined in order to discover the extend of protection the synchrotron radiation masks can provide. Although this examination is based on the reference sample, changes of these conditions – for instance due to the presence of tails – will be discussed as well.

Those scenarios different from the default case are used in the last part of this chapter to evaluate collimation efficiency. Synchrotron radiation collimators are so far not included in the interaction region layout. The study presented here will propose an initial collimation setup which is based on conditions identified in the previous part. Using different scenarios, the efficiency of single collimators will be tested. Such a characterization can answer the question whether or not collimators can successfully add additional protection from the radiation background generated upstream.

7.1 The Geometry in MDISim

The most important design features characterizing the interaction region of FCC-ee have been introduced in Chapter 3. In the context of this thesis, MDISim has been modified to account for these details and establish a geometry which comes as close as possible to the design.

Automated Geometry Description – Single Beam Geometry

MDISim traverses the lattice description from Mad-X element by element and generates a geometry by setting up volumes based on type and aperture information of each element – final result is a model of the MDI.

Although MDISim is capable of generating both beam-pipe geometries of a double ring collider, simulations presented here are based on a single-beam geometry. Both beams circulate in separate beam-pipes and the background in common areas such as the central chamber can be – due to symmetry reasons – expected to simply double.

Such an approach reduces computational resources in running detailed Monte-Carlo simulations. The beam-pipe geometry of the positron beam is generated in a maximum extend of ± 800 m in z (Euclidean coordinates) around the interaction point – as shown in Fig. 7.1.

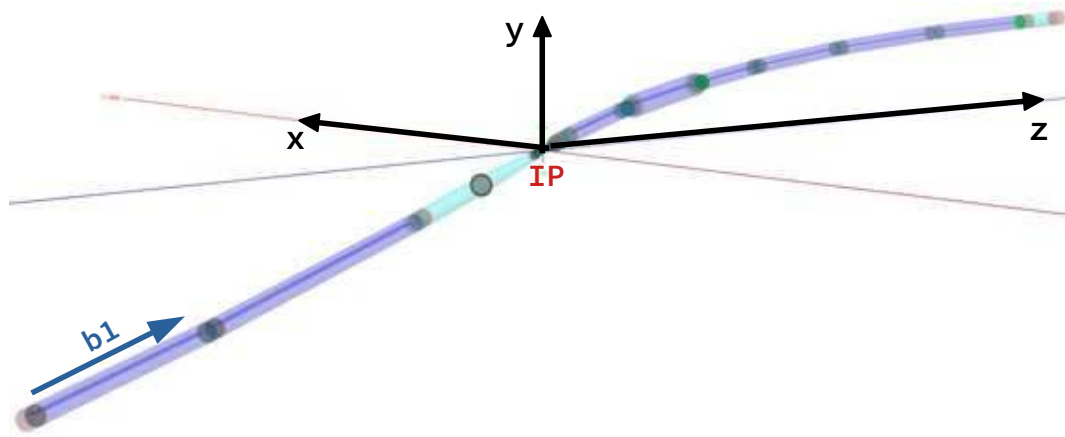


Figure 7.1: Automated 3D single beam geometry from MDISim, shown in Root display. The Euclidean reference coordinate system is indicated with black arrows. The starting point of the beam is located in the lower left corner, upstream of the Interaction Point (IP). The part downstream is shown in the upper right corner.

The start position of the beam is located in the lower left corner. The beam would propagate through the interaction point and continue in the downstream section, shown in the upper right corner.

Different colours indicate element types such as drift space (turquoise), dipole magnets (blue), quadrupoles (red) and sextupoles (green).

Figure 7.2 depicts the central interaction region (± 10 m around the interaction point). The image shows important details such as the final focus doublets (QC1L/R and QC2L/R) in red and the solenoid SOL2L/R in turquoise and yellow. Note the reduction in beam-pipe diameter around the interaction point. The Final Focus Quadrupoles (FFQ) are split in single elements as described in the CDR [2].

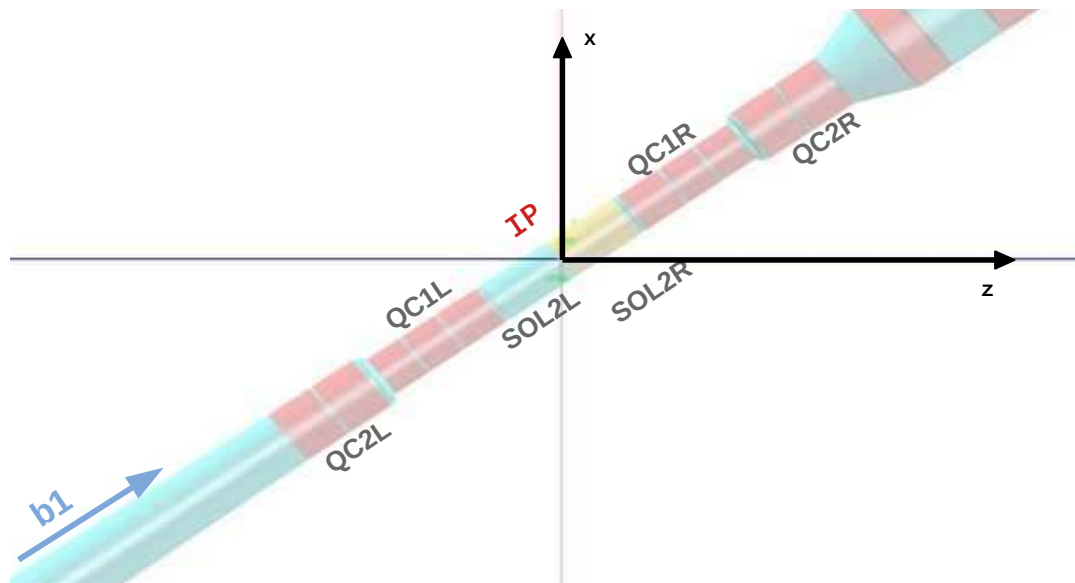


Figure 7.2: Close-up of the central interaction region of the automated 3D model from Fig. 7.1. Indicated are the final focus magnets and detector solenoid. This view also shows the aperture reduction from the default 70 mm upstream down to 30 mm at the **Interaction Point (IP)**.

Specific Details of the Geometry

The complexity of the interaction region design for FCC-ee contains details that can not be implemented based on an automatic sequence alone. These details rather need to be included manually in the model.

One such example is the central beam pipe chamber around the interaction point, other examples are movable collimators and fixed synchrotron radiation masks. All these features require modification of the geometry to be properly included in the MDI model that is then used for simulations of the photon background.

Central IP Chamber

In case of the FCC-ee MDI, Fig. 7.2 demonstrates how the automated single-beam geometry looks in the central interaction region. As shown earlier, the interaction point is located at the centre of a shared chamber, the *central detector chamber*. Figure 7.2, however, shows how the automated geometry neglects the central chamber which would be common to both beams.

Simulations based on this model would suffer in accuracy since the geometry is not well reproduced in this area – each beam would only see its own physical aperture.

The central chamber model is therefore integrated from external input for MDISim. A more detailed model has been developed by the Detector Group at CERN and is depicted in Fig. 7.3. It represents the current layout of the central beam-pipe within the detector, and covers the space between both front faces of the inner final focus magnets, QC1L and QC1R (yellow blocks in Fig. 3.9 of Section 3.2). The two separate beam-pipes are shown in red, the tungsten shielding in gray and the central beam-pipe chamber made out of Beryllium in light green. The image also features the disks of the luminosity calorimeter (LumiCal).

A geometry in Geant4 can be provided in form of different formats, for instance

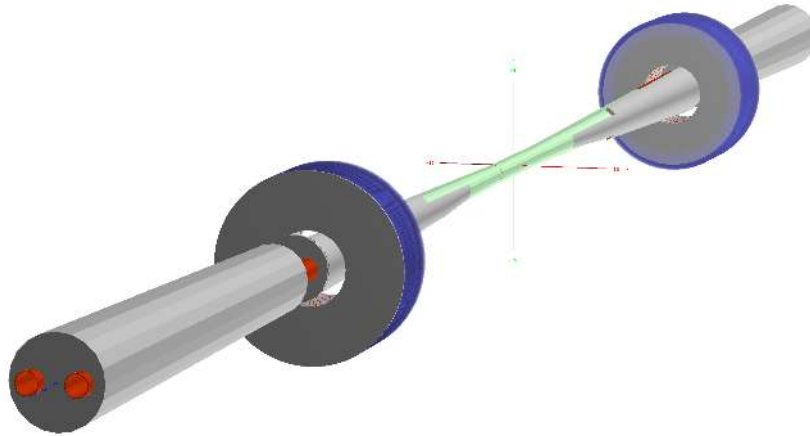


Figure 7.3: Model of the central chamber around the interaction point, presenting the external model by showing the beam pipes (red), tungsten shield (gray) and Beryllium chamber (green).

Geometry Description Markup Language (GDML) files [49]. Combining an automated geometry from MDISim with the central chamber model was done on the GDML level for the study presented here. One result is shown in Fig. 7.4.

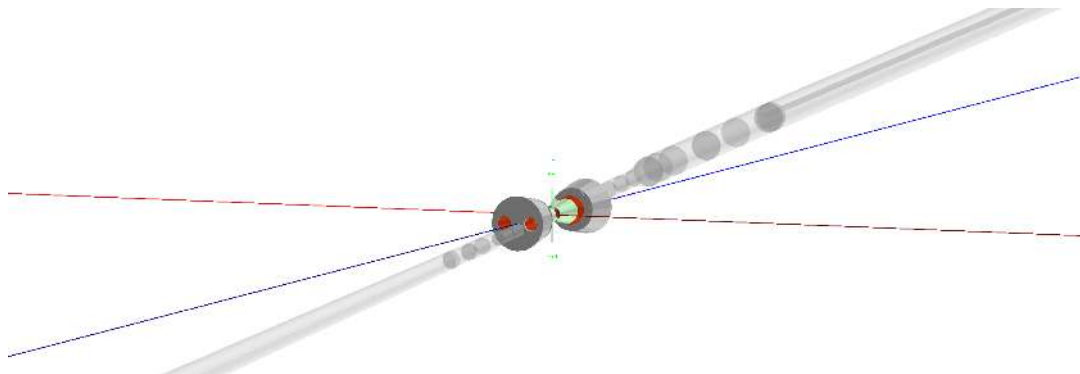


Figure 7.4: The central chamber model combined with an automated single-beam geometry from MDISim (transparent gray). Note that the LumiCal was excluded in this geometry and transverse dimensions have been scaled up to enhance visibility.

That picture presents – as an example – the central chamber model combined with the automated single-beam geometry (transparent gray). Note that the LumiCal was excluded and transverse dimensions have been scaled up to enhance visibility. This way allows to improve the single beam geometry to become significantly more accurate, while at the same time not relying on any other input format, which is convenient for the later use in Geant4. While combining those models, care must be taken to avoid any gaps or element overlaps between the single geometries.

Masks and Collimators

Masks. Synchrotron radiation masks are considered as one important aspect of the mitigation scheme. These absorbers – installed at a fixed location along the beam pipe – provide shielding of the central detector chamber around the interaction point. Forward and backward scattered photons shall be stopped by these masks.

The current 3D model is considering two such masks placed upstream of the interaction point, one between the final focus quadrupoles QC2L and QC1L, the other downstream of QC1L. Their longitudinal profile is shaped like a trapezoid, as demonstrated in Fig. 7.5. A 2 cm long tapering ensures smooth connection to the 2 cm long central absorber block, such that the whole mask is 6 cm long.

The reduction in beam pipe diameter is supposed to be 3 mm, from 15 mm to 12 mm in QC1L [2].

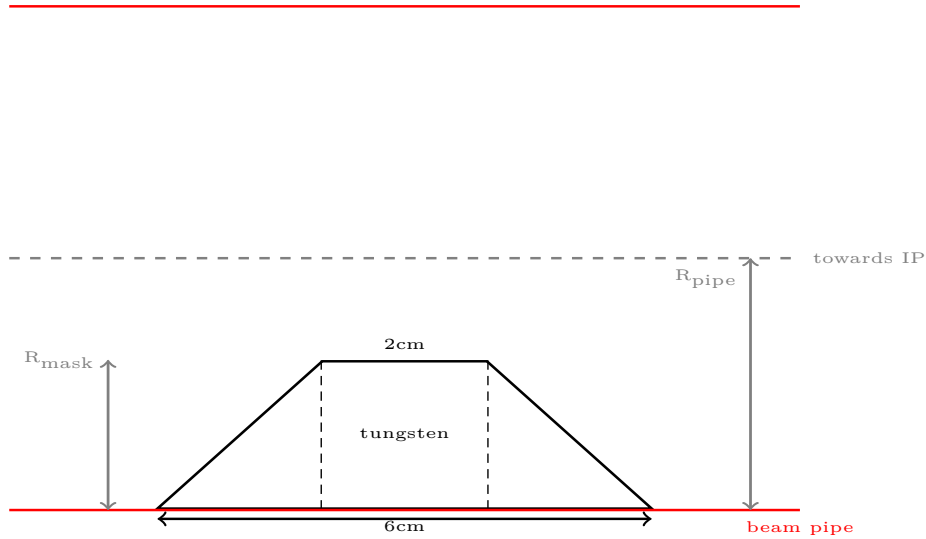


Figure 7.5: Longitudinal sketch of the mask geometry in the beam pipe. The absorber is supposed to reduce the beam-pipe radius by R_{mask} , thereby shadowing a certain section further downstream. Tapering towards the central absorber block ensures smooth connection and reduces the impact on impedance.

In order to represent these masks in MDISim, a certain drift space is divided into three sections by using markers which define the restricted aperture. The result is a central drift with smaller beam pipe diameter, connected to the outer elements with cones. Figure 7.6 (a) provides an application example of the geometry for a mask right after QC1. It creates a longitudinal profile exactly as the one foreseen in the design proposal. Following this approach, the mask will limit the aperture in the full azimuth, around the entire cross section, as indicated in Fig. 7.6 (b).

Collimators. Synchrotron radiation masks provide protection by a fixed restriction of the beam pipe diameter. Once installed, they do not allow any adjustment to changes in the background conditions. Steering errors or other changes in operation might lead to scenarios, where the synchrotron radiation background differs from the default/expected behaviour.

Collimators, on the other hand, increase flexibility in the mitigation scheme. These elements consist of movable jaws, in which absorber blocks are implemented such as shown in Fig. 7.7 – examples from LEP and SuperKEKB [62, 63].

These jaws can be steered to move closer to the beam or to open up, which allows adjustment with respect to tolerances in the beam orbit.

Figure 7.7 (b) shows an example of a horizontal collimator used in SuperKEKB. The beam pipe (shown in orange/red) is restricted by two movable jaws with

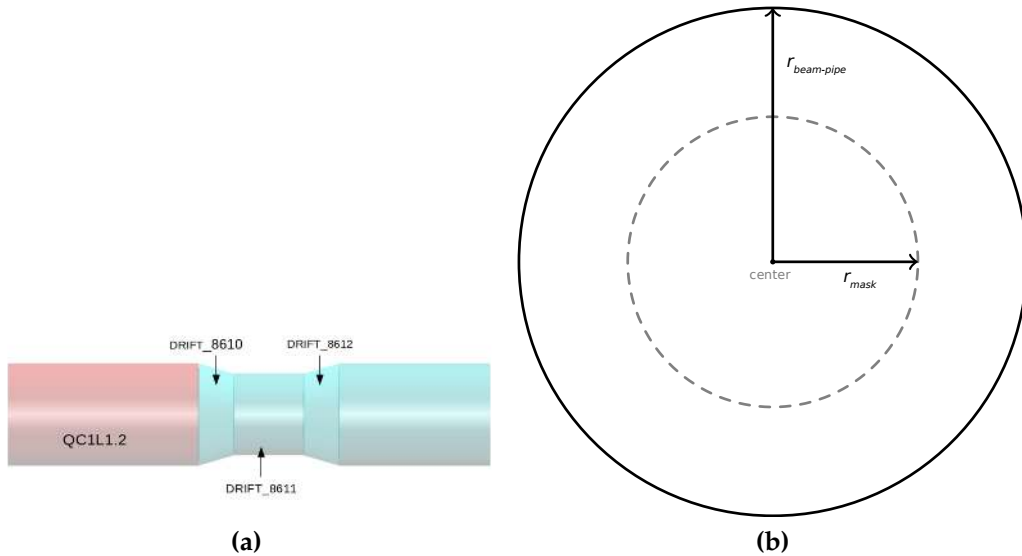


Figure 7.6: (a) 3D model in MDISim, showing how the synchrotron radiation masks are implemented. (b) sketch of the transverse cross section, showing how the mask would restrict the diameter in full azimuth.

small tungsten inlets in their tip. The jaws are water cooled, as indicated as small grey pipes running around the inside of each jaw.

Collimators are semi-automatically implemented in MDISim, using the same principle as for the masks: by dividing a drift space into three sections, an aperture restriction can be simulated. All collimators will have circular apertures. This simplification helps to generate a smooth geometry in the current version of MDISim, which can be used reliably in Geant4 tracking. Future developments can address these details and improve the accuracy of such a geometry.

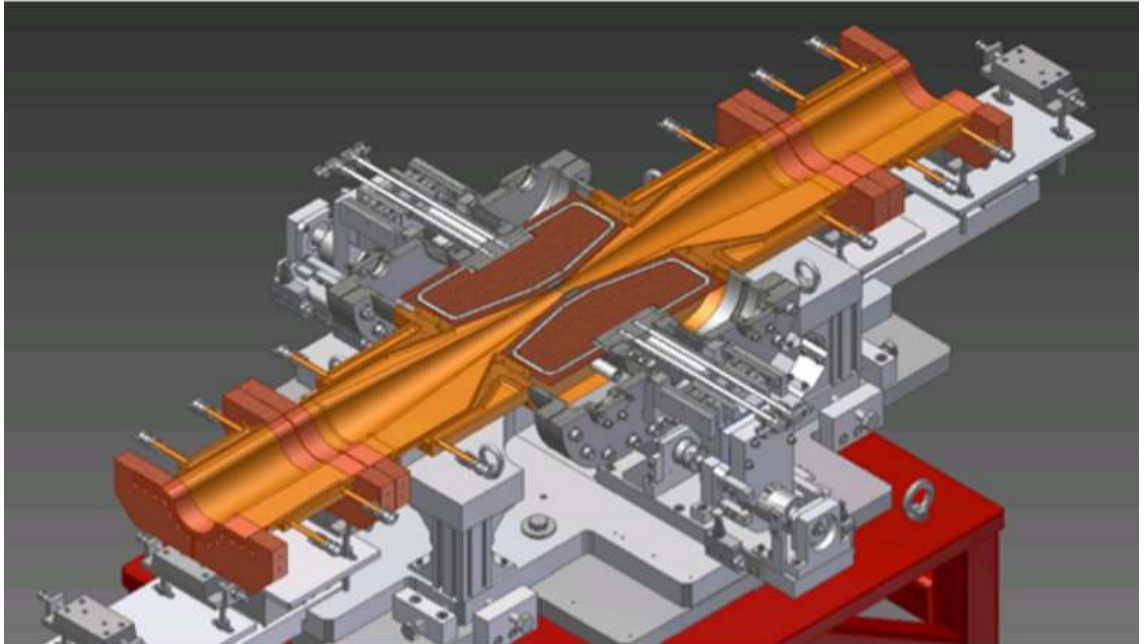
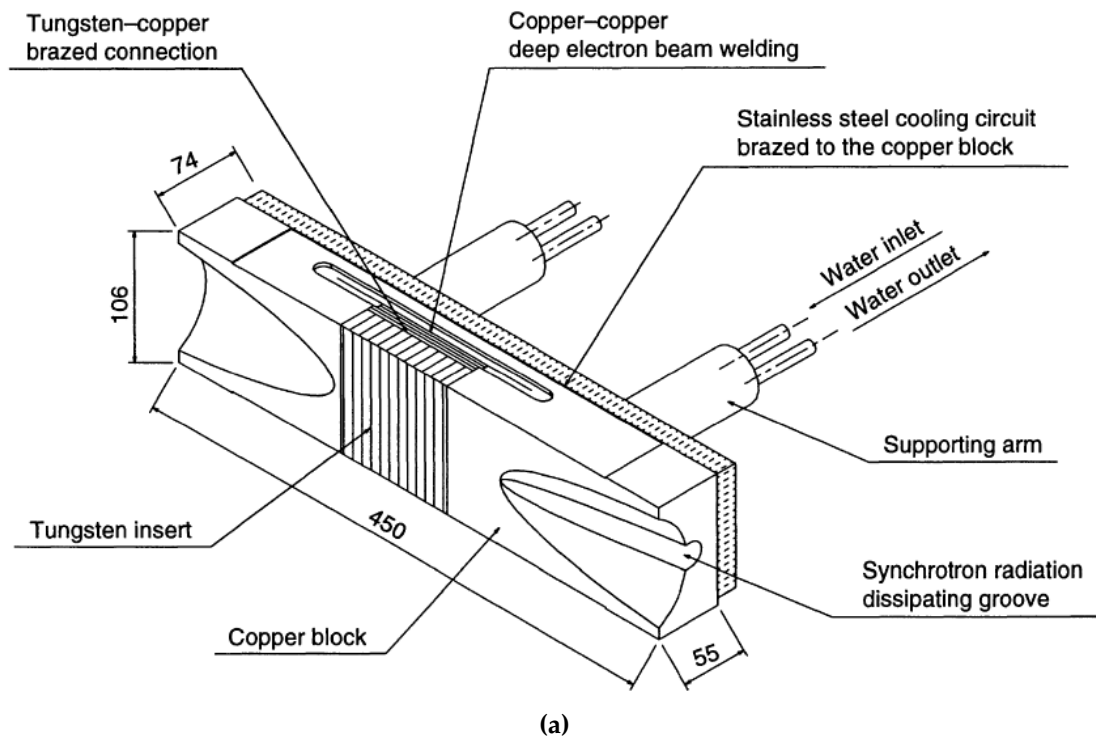
The approach is semi-automated because the diameter (representing the collimator closure) has to be modified manually for each run when collimator settings are changed. Figure 7.8 shows such a geometry in Root display. Note that the element in the center between two conical shaped elements can be specified to be made of a certain material. In the framework of this thesis, tungsten was used.

7.2 Beam Generator in MDISim

Generation of the beam-pipe geometry is one step towards a full simulation using MDISim. Another important step is to generate the beam, which will then be tracked through the geometry in Geant4. The beam consists of a certain number (N_{MC}) of primary particles – positrons for the simulations performed in the context of this study. N_{MC} can be considered as the bunch population in the Monte-Carlo simulation. Hence, in subsequent discussions, the term primaries refers to the primary particles of the beam.

MDISim allows several different configurations for initial particle distributions in a beam. Since these types are used in the simulation, principles will be briefly introduced, as well as the available options.

Per default, MDISim assumes a virtual point at which the particle distribution is



(b)

Figure 7.7: (a) collimator jaw used in *LEP3* [62]. In a basic copper jaw, an absorber block made from high-Z material is implemented (tungsten insert). (b) horizontal collimator type in *SuperKEKB* [63].

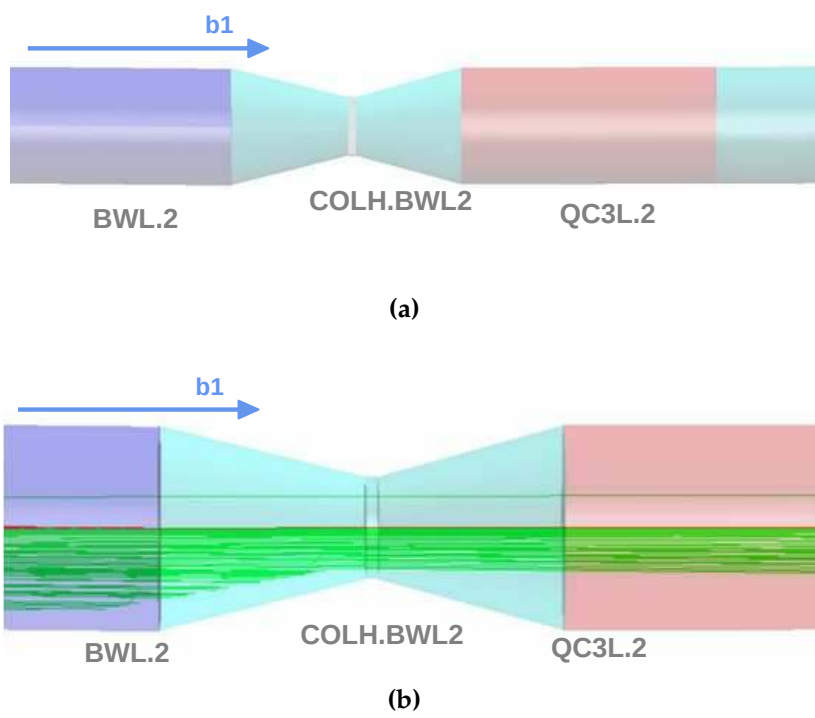


Figure 7.8: Top view on a small section of the beam pipe, right after the last upstream bend, BWL.2 (a) indicating the principle how a collimator is realized in MDISim. (b) same geometry with synchrotron radiation photons (green lines) to show how this element would block a certain amount of radiation.

generated, characterized by $\beta_{x,y} = 1$ m, $\alpha_{x,y} = 0$ and the absence of dispersion. As an example, to generate a Gaussian bunch in normalized coordinates, particles would be distributed according to Eq. (7.1) and (7.2).

$$x, x' \propto \exp \left[-\frac{(x - \mu)^2}{2\sigma_x^2} \right] \quad (7.1)$$

$$y, y' \propto \exp \left[-\frac{(y - \mu)^2}{2\sigma_y^2} \right] \quad (7.2)$$

These distributions are centered around $\mu = 0$ with a variance based on the beam size.

$$\sigma_{x,y} = \sqrt{\epsilon_{x,y} \beta_{x,y}} \quad (7.3)$$

In a next step, the distribution needs to be transformed to an actual point in the accelerator (Frenet-Serret or Courant Snyder coordinate system) with more complex Twiss parameters. An illustrative example would be a beam which is generated at the interaction point, but the actual start position for the simulation is 500 m upstream. Such a set-up requires to transfer the distribution to the start position, by applying a transformation matrix which represents all elements between the point where the beam is generated and the start position.

After this transformation, the distribution is transformed from normalized coordinates into the Courant-Snyder coordinate system which is achieved by applying

the inverse of the transformation matrix (2.14) in Chapter 2.

$$T^{-1} = \beta \begin{pmatrix} \frac{1}{\sqrt{\beta}} & 0 \\ -\frac{\alpha}{\sqrt{\beta}} & \sqrt{\beta} \end{pmatrix} \quad (7.4)$$

Where the Twiss parameters $\beta_{x,y}$ and $\alpha_{x,y}$ are both determined by the given lattice at the chosen start element and available in the Mad-X table. Mad-X can also provide (in particular using the TWISS command with RMATRIX option) the transformation to a general starting point at an element boundary, including non-zero dispersion.

Figure 7.9 shows a Gaussian distribution in normalized coordinates (a) and transformed to an actual start position (in this case the final focus magnet QC1L in FCC-ee) (b). Details on this transformation can be found in Chapter 2.

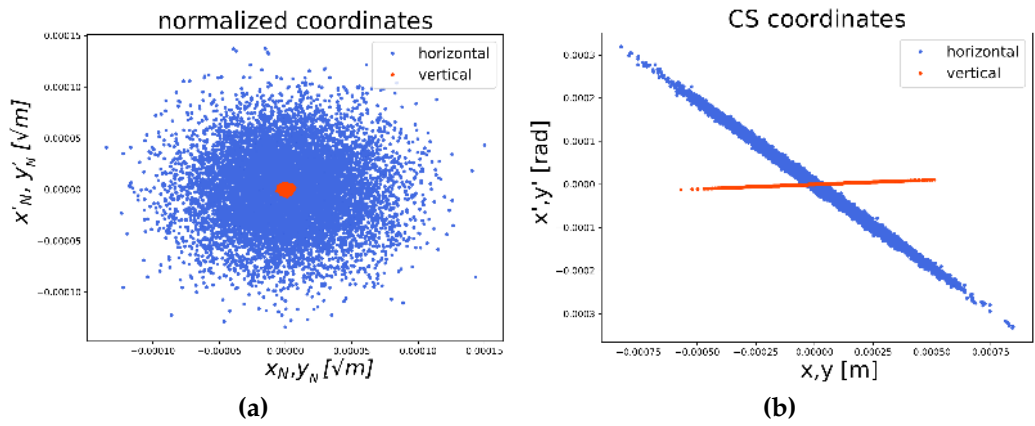


Figure 7.9: Particle distribution as generated at a virtual point (a) and transformed to the actual start position in the accelerator (b).

Once available in the accelerator coordinate system at the desired start element, a last step transforms the distribution to Euclidean space, such that it can be used in Geant4. Figure 7.10 demonstrates how a Gaussian example distribution would look like after that last step.

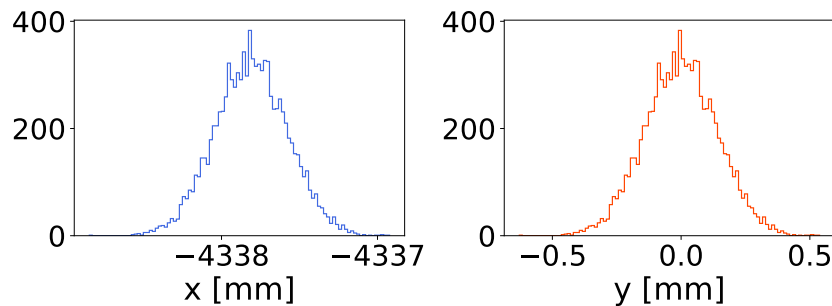


Figure 7.10: Gaussian distribution after the final transformation into Euclidean coordinates, ready to be used within Geant4. Note that the horizontal coordinate (left plot) is given relative to the magnet center (which is relative to the interaction point at $x,y,z = 0$), placed at a certain position $x \neq 0$ due to the crossing angle.

Available Beam Shapes

MDISim offers a choice of different initial particle distributions out of which the user can choose. Distribution types used in this thesis are:

- **Gaussian beam** – In most cases, simulations referring to default conditions will be based on an initial Gaussian distribution. It was introduced with this section (refer to Fig. 7.9 and 7.10).
- **Ring** – It will put all particles on a ring in phase space, at a certain amplitude specified by $N\sigma$, for example $20\sigma_x$ in the horizontal plane. Figure 7.11 illustrates the resulting distribution with a majority of particles at large amplitudes. This type is interesting to estimate influences of beam tails on the radiation backgrounds.

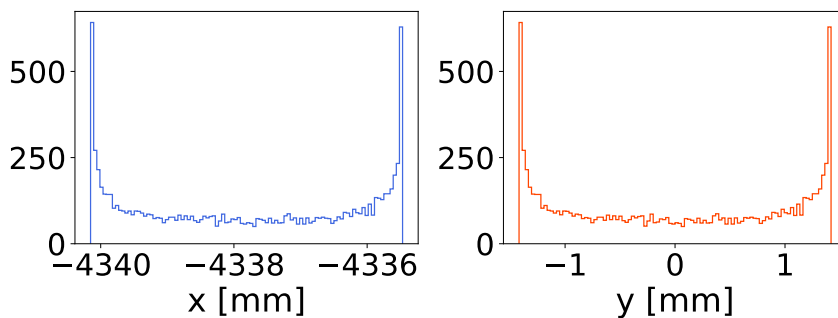


Figure 7.11: Example of the ring-type particle distribution transformed to Euclidean space. A majority of particles is located at large amplitudes.

Non-Gaussian Tails

In a real machine, tails of the beam will be populated by different mechanisms like Beam-Gas scattering or Beam-Beam interaction. Simulations, such as done for Beam-Beam effects, allow to estimate the non-Gaussian exponential tails of the beam in FCC-ee. Such a distribution is shown in Fig. 7.12 and was generated from corresponding data [64].

MDISim has been modified in the framework of this thesis in order to allow generating exponential tails. The distribution is realised using an exponential cut-off, generating tails out to a certain number of beam-sizes $N\sigma$. Figure 7.13 shows an example from MDISim in the horizontal plane with tails put to 5σ and 10σ to illustrate the concept. Note, that the bunch population N_{MC} has to be increased in order to sufficiently populate the tails.

7.3 Upstream Magnets

A significant amount of synchrotron radiation background is expected to come from upstream dipoles. The discussion of simulation results therefore starts with a characterization of these magnets.

Figure 7.14 shows all upstream bending magnets in the arc out to about 1.3 km in a 2D overview. A grey dashed line indicates the design orbit while grey solid lines represent the physical beam pipe. Those magnets are divided into three groups:

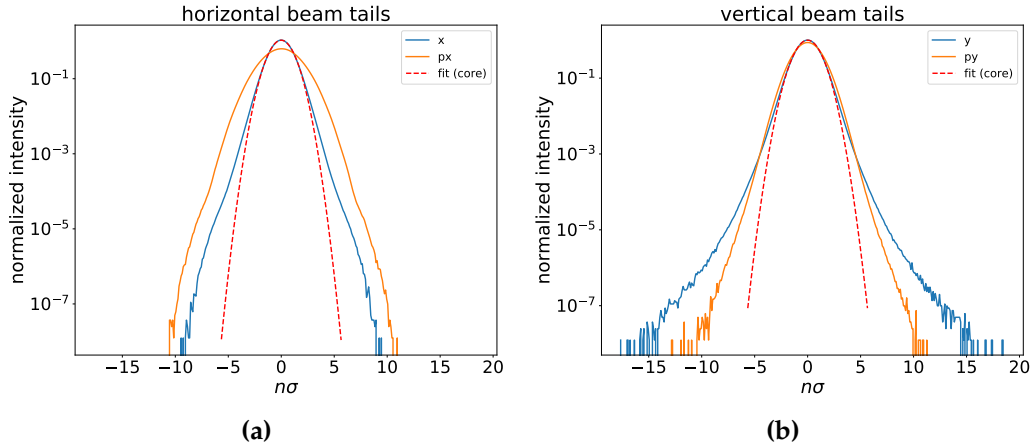


Figure 7.12: Data from Beam-Beam simulations to illustrate how exponential tails can look like. A fit for the pure Gaussian core is shown as red dashed line. The plot depicts horizontal x, x' (a) and vertical y, y' (b) coordinates.

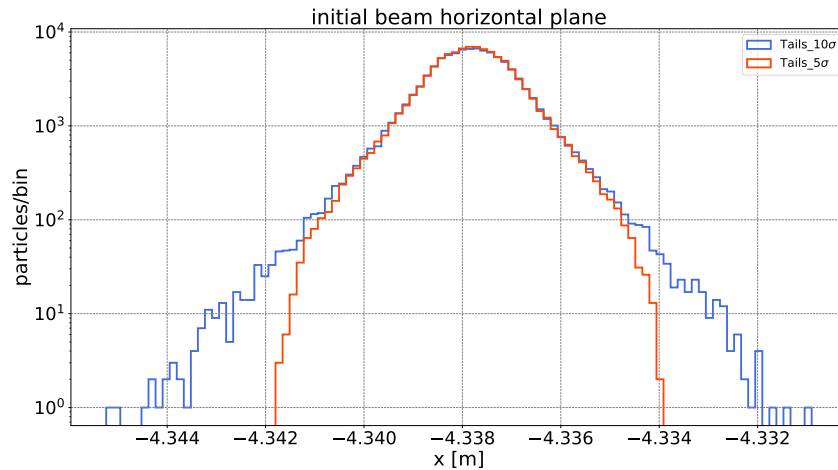


Figure 7.13: Demonstration of a beam having tails out to 5 σ and 10 σ , respectively.

- Elements located more than 800 m upstream are referred to as **Group 3**.
- A closer look on dipoles between 700 m to 0 m upstream is depicted in Fig. 7.15. Magnets BC5L2 to BC2L2 comprise **Group 2**.
- As required in the design guidelines, the last upstream bend (BWL . 2) ends a 100 m upstream of the interaction point. Another dipole (BC1L . 2) is located adjacent to BWL . 2 – both are considered as **Group 1**.

Dipoles of Group 3. This group of magnets is located in the outer arc, having a distance of around 1 km or more to the interaction point. At this point, radiation generated in these dipoles is not expected to directly travel towards the central interaction region. It would need multiple scattering to reach the straight section between 100 m to 0 m upstream of the detector, which is rather unlikely. Given the energy loss after several scattering events, a photon is more likely to be absorbed.

Dipoles of Group 2. These magnets are fairly far away from the interaction region with end positions between 500 m to 700 m. Photons generated in these

7.3. UPSTREAM MAGNETS

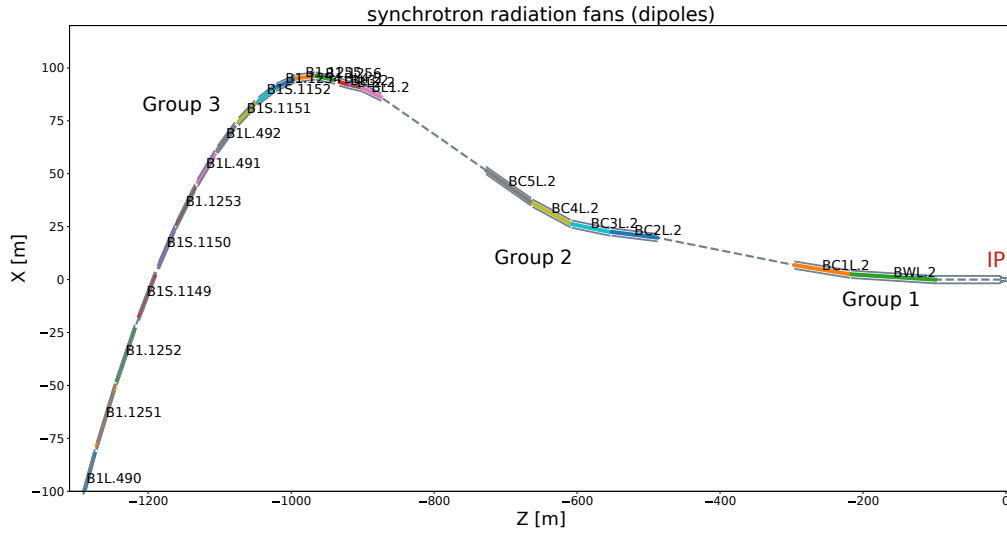


Figure 7.14: Overview showing a selection of dipole magnets in the arc upstream of the *Interaction Point (IP)* at $z = 0$ (Euclidean coordinates). The magnets can be divided in three separate groups, further described below. Note, that transverse dimensions are scaled by a factor of 50 to increase visibility.

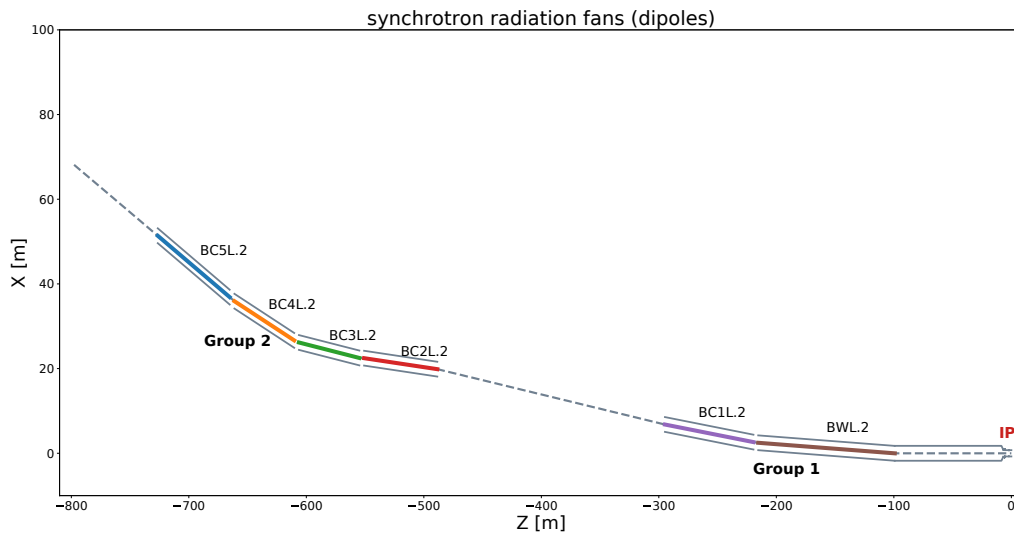


Figure 7.15: Close up on the last two magnet groups, which are more relevant for the interaction region. Group 2 includes dipole magnets about 500 m to 700 m upstream of the *Interaction Point (IP)*. Radiation from these magnets is not expected to reach the interaction region directly, without scattering or being reflected. Group 1 contains the last two upstream bending magnets.

dipoles are not expected to reach the interaction region directly. An additional section of around 200 m separates this group from Group 1. However, considering scattering processes and especially X-ray reflection, radiation generated in these dipoles might still propagate towards the interaction point indirectly. Characteristics for dipoles of this group are listed in Table 7.1. Given the high critical energies (ϵ_c) of these dipole magnets, they potentially generate radiation with considerable energy.

Dipoles of Group 1. With a distance of about 100 m to 220 m, the magnets BWL . 2 and BC1L . 2 are closest to the interaction point. A closeup of this group is shown in

7.3. UPSTREAM MAGNETS

Table 7.1: Selection of (energy dependent) parameters for the dipoles included in Group 2, assuming highest beam energy of 182.5 GeV. Those parameters have been motivated in Chapter 4. Note that L describes an integral length. n_γ represents the number of photons radiated *per single particle* (e^\pm), while n_{tot} denotes the total number of photons generated in a dipole – taking into account the whole bunch population.

	S [m]	L [m]	α [mrad]	ϵ_c [keV]	n_γ	P_{SR} [kW]	n_{tot} [10^{11}]	$\langle \epsilon \rangle$ [keV]
BC2L.2	550.8	62.23	-1.035	224	3.89	1.4	8.57	69.1
BC3L.2	606.3	51.36	2.2	578	8.28	7.64	18.2	178
BC4L.2	661.2	50.8	2.246	596	8.45	8.05	18.6	184
BC5L.2	726.4	61.17	-0.05405	11.9	0.203	0.00387	0.447	3.67

Fig. 7.16. Straight lines indicate the direction of synchrotron radiation emitted by these magnets. Table 7.2 details selected quantities. Both magnets emit photons with critical energies below 100 keV and meet the design constraint. BC1L.2 and BWL.2 will therefore emit radiation with less energy than the magnets in Group 2. Direct hits from BC1L.2 can also be considered as rather unlikely, but after scattering or reflection, photons from this magnet might easily reach the detector indirectly.

As for the last upstream dipole BWL.2, direct as well as indirect hits at the central beam pipe chamber can be expected. Part of the radiation is in good approximation parallel to the beam itself and will be difficult to stop by masks or collimators. Therefore, the last upstream bend is considered as most relevant for the MDI.

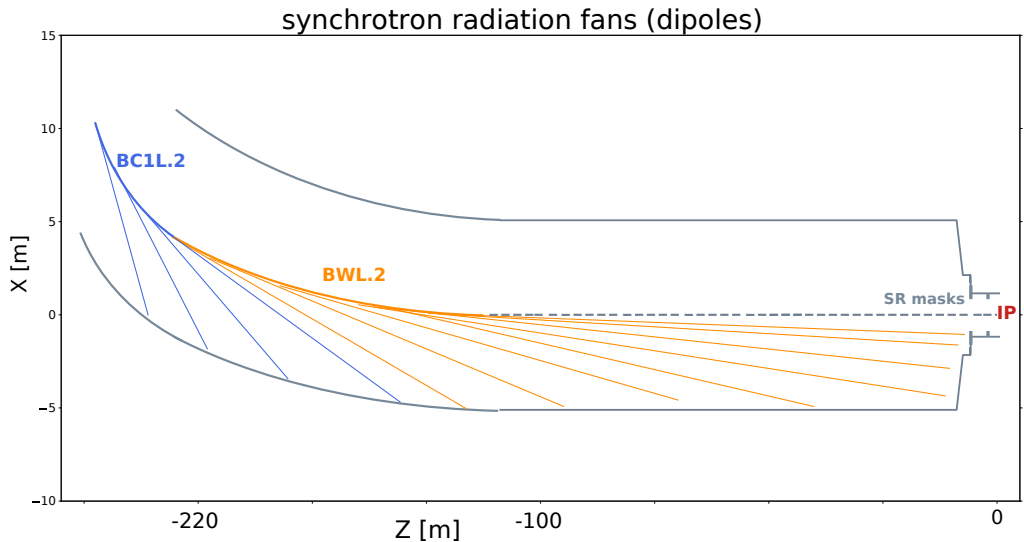


Figure 7.16: Schematic visualization of the last two upstream dipoles (Group 1). Straight solid lines indicate average trajectories of photons coming from the dipoles. Direct hits by photons generated in BC1L.2 can affect a section between 250 m and 120 m upstream, while photons emitted in BWL.2 would affect the whole upstream section from 100 m to 0 m. Note that part of the radiation from BWL.2 is in good approximation almost parallel to the beam. The synchrotron radiation masks are indicated close to the *Interaction Point (IP)*.

Table 7.2: Selection of (energy dependent) parameters for the dipoles included in Group 1, assuming highest beam energy of 182.5 GeV. Those parameters have been motivated in Chapter 4. Note that L represents an integral length. n_γ describes the number of photons radiated per single particle (e^\pm), while n_{tot} denotes the total number of photons generated in a dipole – taking into account the whole bunch population.

	S [m]	L [m]	α [mrad]	ϵ_c [keV]	n_γ	P_{SR} [kW]	n_{tot} [10^{11}]	$\langle \epsilon \rangle$ [keV]
BWL.2	215.4	116.2	0.8517	98.9	3.2	0.506	7.05	30.4
BC1L.2	294.8	75.29	0.4981	89.2	1.87	0.267	4.12	27.5

7.4 Statistics/Uncertainties

Before discussing the simulation results in detail, this section briefly addresses uncertainties which are involved in Monte-Carlo simulations for the photon background.

The results in the context of this thesis will be predominantly presented as histograms to visualize distributions such as

- hits on the beam-pipe wall (along z in Euclidean coordinates)
- photon energy (over a certain energy range)
- origin of synchrotron radiation photons (along z in Euclidean coordinates)

For this, the region of interest (either spatial or an energy range) will be divided in bins – a series of equidistant intervals – with a certain number of events falling into each single interval.

The number of bins (n_{bin}) has to be chosen carefully to avoid hiding any important features (n_{bin} too coarse) or adding too much noise (n_{bin} too high).

In this analysis, the number of bins n_{bin} has thus been chosen to be \sqrt{N} , where N represents the total number of entries given in a data set.

Each bin then has the statistical uncertainty of \sqrt{n} , with n entries per bin. An example is provided with Fig. 7.17. The value on the y-axis therefore is the count of photons per bunch which fall into a certain bin (photons/bin/bunch). The plot also features errorbars, representing the uncertainty according to \sqrt{n} . However, errorbars in histograms in subsequent sections are generally not shown to maintain comfortable visibility of the plots.

The simulation data is used to extract average values, for example mean energies of photons coming from a single magnet. Statistics determine the uncertainty on these values with a relative error $\sqrt{1/N}$, where N is the number of events on which a given average is based.

7.5 Default Conditions

The following section will establish baseline scenarios to characterize the expected photon background in the FCC-ee MDI.

These scenarios assume a machine with design parameters. Hence, they do not

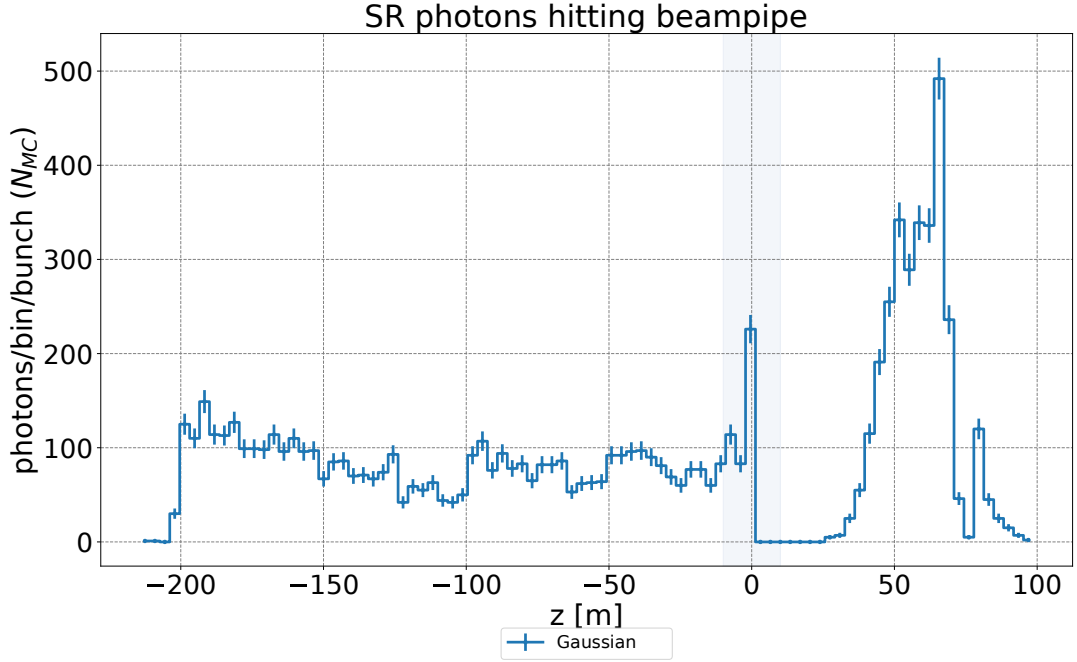


Figure 7.17: Example for errorbars in one of the typical histograms in the context of this study. Those uncertainties are based on \sqrt{n} , where n is the number of entries in one bin.

take into account any tolerances in the orbit, for example caused by magnet misalignments. The beam is therefore considered to not deviate from the design orbit C_0 .

A Gaussian distribution without strongly populated tails in both planes will serve as default case, which is used to look into certain characteristics of the synchrotron radiation. In order to estimate the effect of tails on the photon background, this analysis will use the ring-type distribution in MDISim to put the majority of particles in the bunch on large amplitudes. One sample contains horizontal tails and a vertical Gaussian distribution while a third sample features a Gaussian core in x and vertical tails.

These cases do not yet take into account X-ray reflection or scattering – the discussion rather focuses on photons of the *first generation*, which directly strike the vacuum chamber wall. First generation photons are those radiated directly from the beam particles.

Collimators are accordingly not yet added to the geometry, as these scenarios are purely meant to establish a default understanding. A bunch population of $N_{MC} = 10^4$ positrons has been chosen – as a good compromise between computing resources and statistics.

The beam starts 800 m upstream of the interaction point in order to initially include all dipole magnets of Group 2 and Group 1 in the sample.

Gaussian Beam

Figure 7.18 details the emission spectrum 800 m upstream ($z < 0$ m) and about 100 m downstream ($z > 0$ m) of the interaction point.

Referring to the classification of the upstream dipole magnets earlier in this analysis, it is possible to identify Group 2 and Group 1 in the plot. Between those two

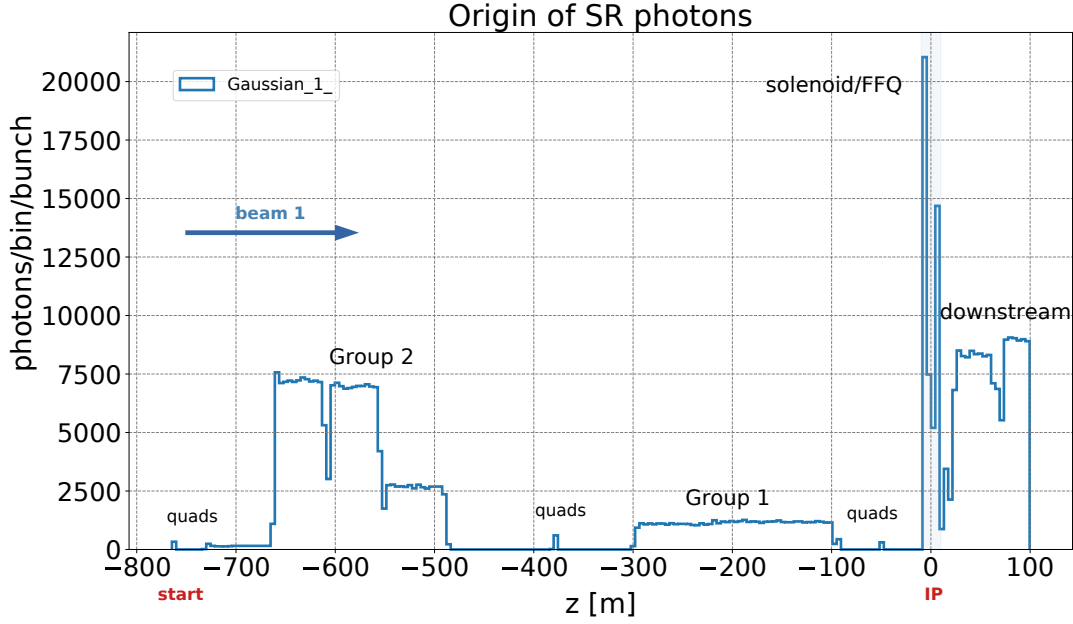


Figure 7.18: Photon emission spectrum along the beam trajectory. Two groups of upstream dipole magnets can clearly be identified, as well as the quadrupoles upstream. The final-focus doublet (FFQ) can be distinguished as well, very close to the **Interaction Point (IP)**.

groups, smaller contributions are visible – the quadrupole magnets. Even though bending magnets certainly generate most of the radiation background, focusing magnets will contribute to the radiation as well. Especially the final-focus quadrupoles in the small-beta insertion around the interaction point need more detailed inspection.

Figure 7.19 compares horizontal (a) and vertical (b) particle distributions in the bunch at different locations upstream of the interaction point.

Since not all particles pass exactly on axis (for instance 0 mm in the vertical plane), the quadrupoles have a non-zero contribution to the photon background, through mechanisms described earlier. Important quantities for three upstream quadrupoles are listed in Table 7.3, while radiation from final focus magnets is discussed in more detail below (Section 7.7).

Table 7.3: Analytic estimate of selected parameters for upstream quadrupoles. A positive normal quadrupole strength $K1L$ implies horizontal focussing ($K1$ as defined in [16] and $K1L$ as $K1$ times the quadrupole length). n_γ denotes the number of photons generated per single particle. k_0 is the inverse ‘equivalent bending radius’ (Section 4.1).

Magnet	S [m]	L [m]	K1L [m^{-2}]	k_0 [1/m]	ϵ_c [MeV]	n_γ	P_{SR} [kW]
QT1L.2	51.07	1	-0.005019	7.259e-05	0.979	0.2731	0.427
QC3L.2	96.21	3.5	0.01099	5.499e-05	0.742	0.724	0.858
QC4L.2	219.2	3.5	-0.01077	9.457e-06	0.127	0.1245	0.0254

These 1st generation photons in Fig. 7.18 will eventually strike the inner wall of the beam-pipe. Figure 7.20 depicts the distribution of those hits, excluding any secondary photons – for example from scattering.

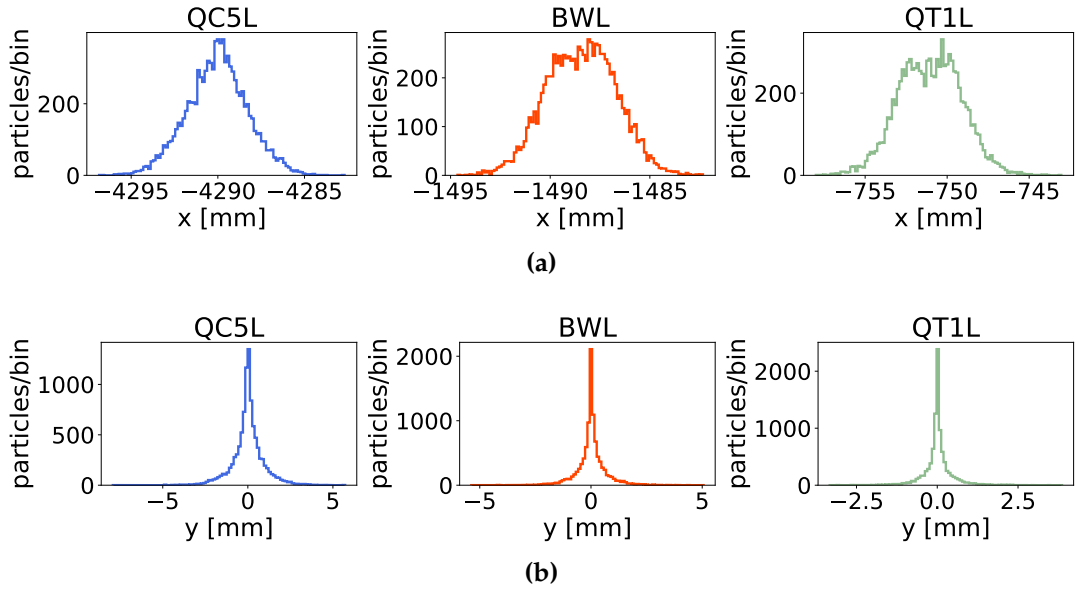


Figure 7.19: Horizontal (a) and vertical (b) particle distribution in the Gaussian bunch at the start element, *QC5L.2*, the last upstream bend, *BWL.2* and the last upstream quadrupole, *QT1L.2*. The beam-size is smaller in the vertical plane – according to an emittance ratio κ of almost 0.2%. Note again, in the horizontal scale of the upper row, the magnet center is offset from 0 due to the crossing angle at *FCC-ee*.

The distribution of the entire upstream part features a characteristic saw-tooth-like pattern, caused by the curvature in the dipole magnets. For shorter dipole magnets with a rather small bending radius (e.g. for *BC4L.2* and *BC3L.2*) the hits are more concentrated as compared to longer bending magnets with larger radius.

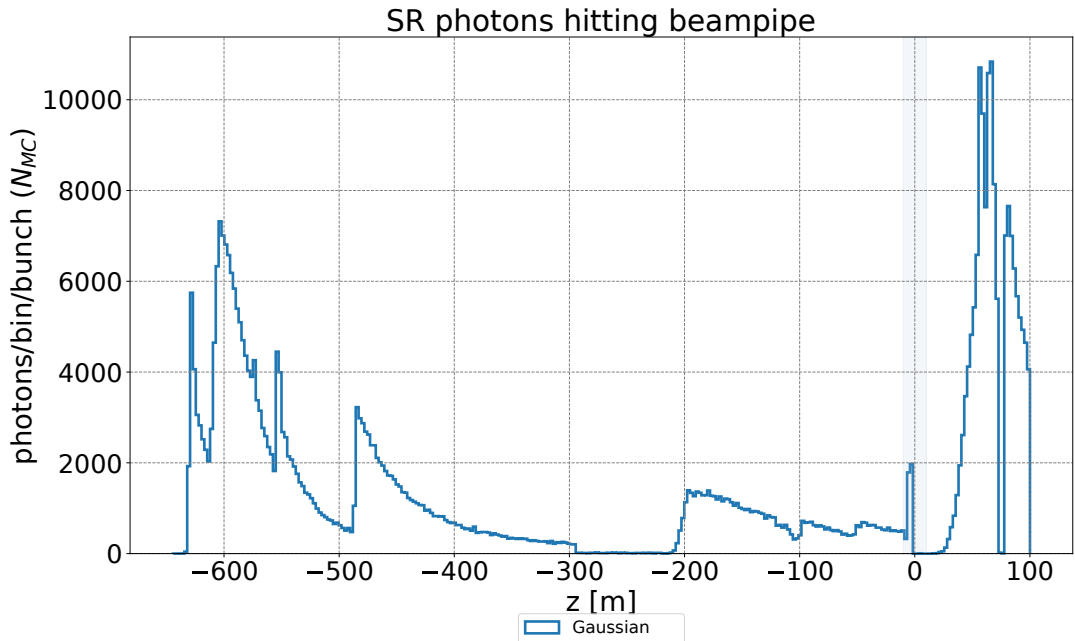


Figure 7.20: Distribution of hits on the beam-pipe wall. A characteristic saw-tooth shaped pattern can be observed upstream of the *Interaction Point (IP)*, related to the curvature in the dipole magnets.

Downstream of the interaction point, within in a section of 50 m to 100 m an

accumulation of hits is registered, caused by photons coming from upstream dipoles, quadrupoles, the final focus doublet and the detector solenoid. The discussion will focus on these later.

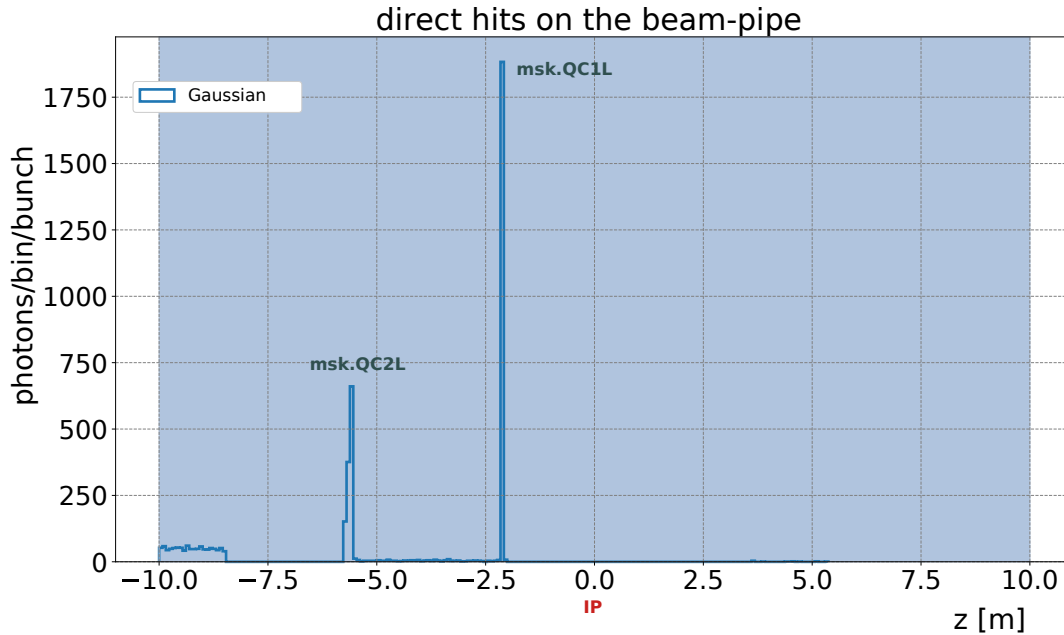


Figure 7.21: Enhanced view of the central interaction region in ± 10 m around the **Interaction Point (IP)**. The two upstream synchrotron radiation masks are clearly visible, as many hits are concentrated on those absorbers. The detector region ℓ^* remains, however, free of direct hits from 1st generation photons.

One aspect of the **MDI** design is to ensure that conditions for the experiments are as clean as possible. Since that means to minimize the background around the interaction point, it is also important to stop as many photons as possible upstream of the detector.

The simulation presented here shows that – assuming rather ideal conditions with a Gaussian bunch on axis – the detector area (defined by $\ell^* \pm 2.2$ m around the interaction point) remains free of direct hits. Fig. 7.21 presents an enhanced view of the central interaction region, ± 10 m in z on both sides of the interaction point. The synchrotron radiation masks upstream of the interaction point provide shielding for the detector area. A significant amount of direct hits is concentrated on those absorbers. However, this discussion does not yet account for photons scattered forward or backward from surrounding elements.

A short analysis of photon energies will wrap up the discussion of the default scenario, before investigating the energy of photons striking the vacuum chamber wall in different sections of the interaction region.

The general distribution is shown in Fig. 7.22, highlighting the fact that the radiation can exhibit fairly high energies between 10 MeV to 30 MeV. The dashed red line represents 100 keV photon energy, which was defined as a global design constraint based on **LEP** experience.

As has been laid out in Section 3.2, photons having energies in the several ten MeV range are difficult to stop. Hence, a careful characterization of the synchrotron radiation is required to answer two questions:

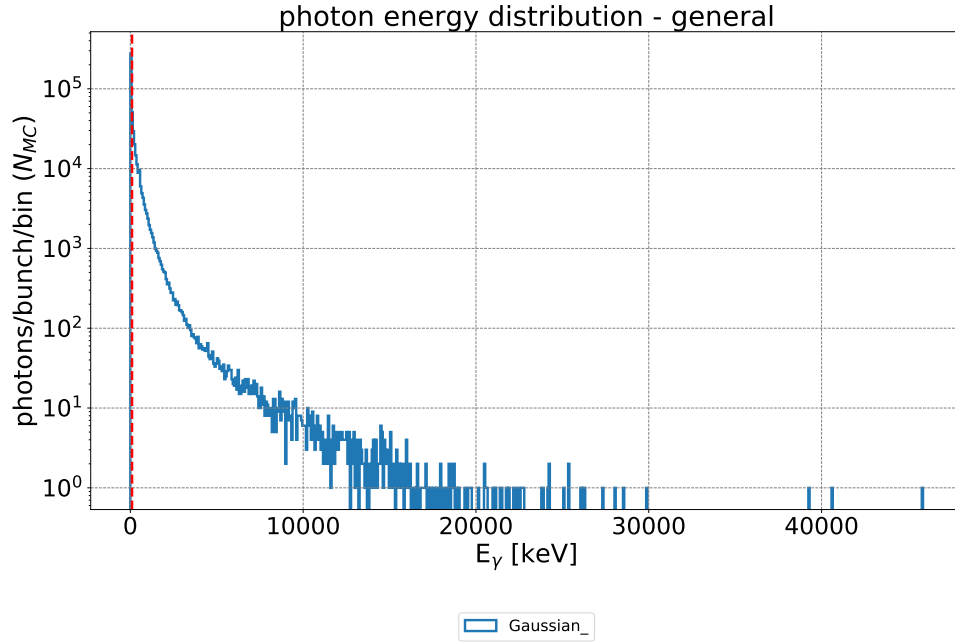


Figure 7.22: Total energy of the synchrotron radiation emitted in the sample. The vertical red dashed line highlights a 100 keV photon energy. The so called high-energy tail of this distribution easily reaches out to 10 MeV, few events even to 20 MeV.

- were are those photons created?
- which areas of the MDI are affected?

The simulation performed in the context of this thesis can already at this stage show some trends to preliminary answer these questions.

Figure 7.23 breaks down the energy spectrum of Fig. 7.22 into two classes, corresponding to the fundamental types of a linear lattice: dipole (BEND) and quadrupole (QUAD) magnets. It allows to understand the high energy contribution, which is clearly generated in the quadrupoles with higher mean energy $\langle \epsilon \rangle$. For the bends, the simulation data shows an average $\langle \epsilon \rangle$ of (167.04 ± 0.26) keV, while quadrupoles emit photons with on average (603.78 ± 2.32) keV.

As to where these photons go, MDISim has been modified in the framework of this study to include information of the element from which a photon originates. Figure 7.24 demonstrates this feature by showing where the photons from all quadrupoles strike the vacuum chamber wall. This feature will be extensively discussed in the following parts of this analysis.

The data shows how the radiation from quadrupoles affects mainly the downstream section between 20 m to 150 m. A small concentration of hits can be observed in a region 200 m to 100 m upstream as well. However, this contribution is located at least 100 m upstream of the detector and much smaller compared to what strikes the downstream section.

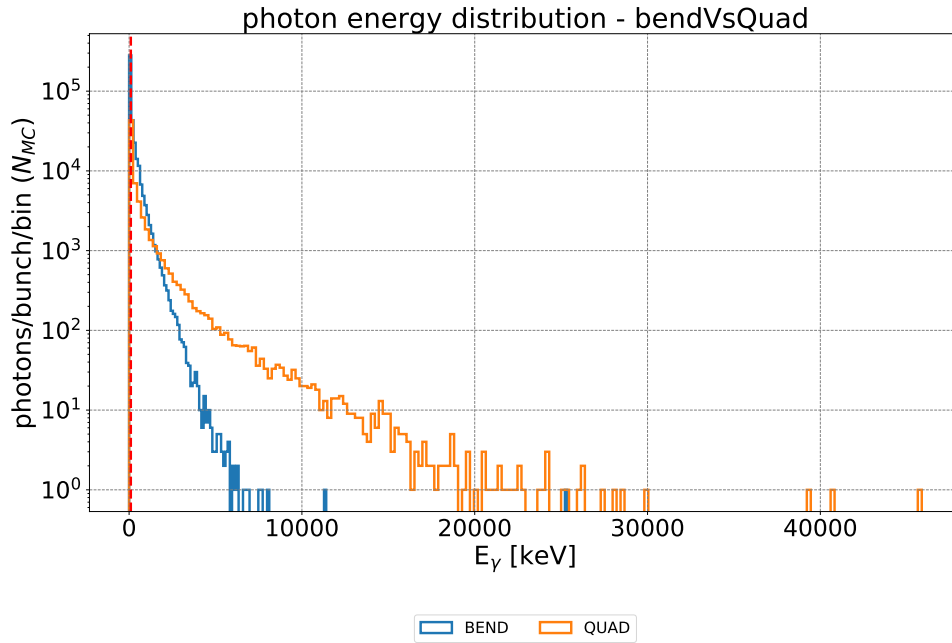


Figure 7.23: Energy spectra of *dipole* (blue) and *quadrupole* (orange) magnets from a Gaussian beam, including all magnets of Group 1 and Group 2, starting 800 m upstream. A red dashed line represents 100 keV photon energy. The plot indicates that high energy photons are mainly coming from the quadrupole magnets.

Direct Hits – Photon Energy

Before leaving the default scenario, a preliminary discussion of the photon energy in different sections of the FCC-ee interaction region shall be provided. Special focus here is on the energy of a photon at the moment of impact on the vacuum chamber wall.

That step is important since it enhances the understanding of which energy regimes become relevant for the central interaction region, especially the detector region. Such a study can help as important input for the design of the vacuum system, but also to understand photon interactions with the beam-pipe material (more of this below, see Section 7.8).

Considering the FCC-ee design, it is reasonable to split the interaction region into three parts:

- First an upstream part after the last dipole magnet BWL.2, within 100 m to 10 m upstream – referred to as *straight section*.
- Second, an area stretching ± 10 m around the interaction point – referred to as *central interaction region*. Within the central interaction region, the region defined by ℓ^* (± 2.2 m around the interaction point) is especially interesting as the detector will be located there (compare introductory description in Section 3.2).
- Third, the downstream part 10 m to 100 m from the interaction point – referred to as *downstream section*. Note, that radiation emitted here will generally leave the interaction region without striking the central chamber wall, except for events that might backscatter from downstream elements.

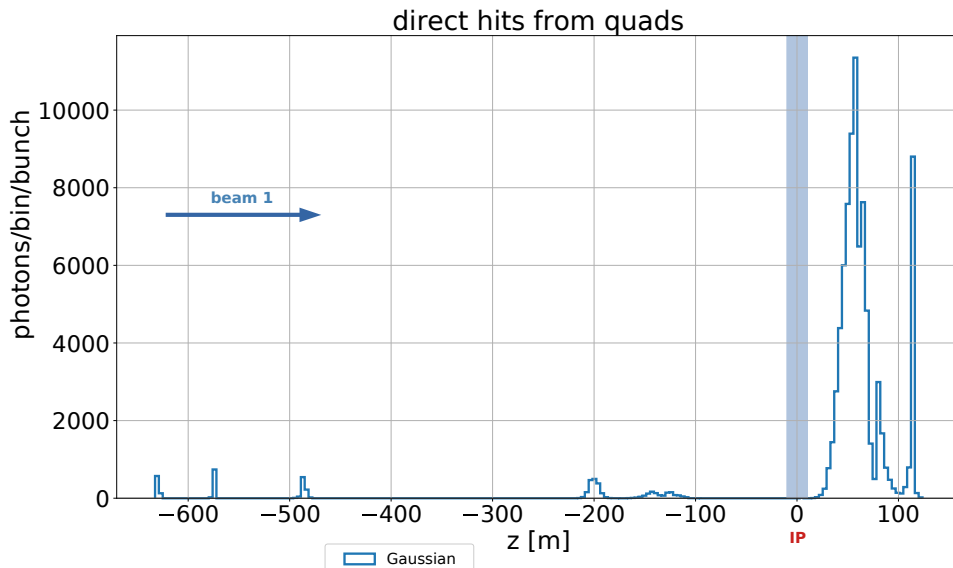


Figure 7.24: Distribution of 1st generation photons – exclusively from quadrupole magnets – striking the vacuum chamber wall in the FCC-ee interaction region. Most of these photons strike the downstream section between 20 m and 150 m.

Straight section. Figure 7.25 displays the energy distribution in the upstream part. The data allows to conclude that energies of photons striking the vacuum chamber wall in this region appear low compared to the general energy distribution in Fig. 7.22.

The plot shows that a significant amount of photons is stopped in the material – discernible from a characteristic spike at the lower end of the distribution, close to 0 keV. Excluding those events, the mean photon energy is around (122.97 ± 2.69) keV – still fairly high, considering the design energy limit of 100 keV.

Central IR. The energies of photons striking the beam-pipe within the central interaction region are presented in Fig. 7.26. The distribution appears to be rather similar to Fig. 7.25. The energy – with a mean of (127.34 ± 5.38) keV – is identified to be no lower than in the upstream part. Note a slightly higher relative uncertainty due to a smaller amount of entries.

As stated earlier, design principles for the FCC-ee MDI include to lower the critical energy ϵ_c of photons originating in upstream bending magnets. The constraint for these *weak bends* was set to 100 keV. The two plots of Fig. 7.25 and 7.26 allow to conclude that the principle is working, at least for the given scenario presented here: Energies of photons which strike the central interaction region do not reach out to several MeV.

Downstream section. The energy spectrum of photons striking the downstream section (Fig. 7.27) reveals a completely different shape than the former two. The distribution extends into high energies and shows a majority of entries between 100 keV to 2500 keV with a mean $\langle \epsilon \rangle$ of (424.70 ± 1.57) keV. This can be considered as direct result of contributions by focusing magnets around the interaction point and the detector solenoid. Additional high energy

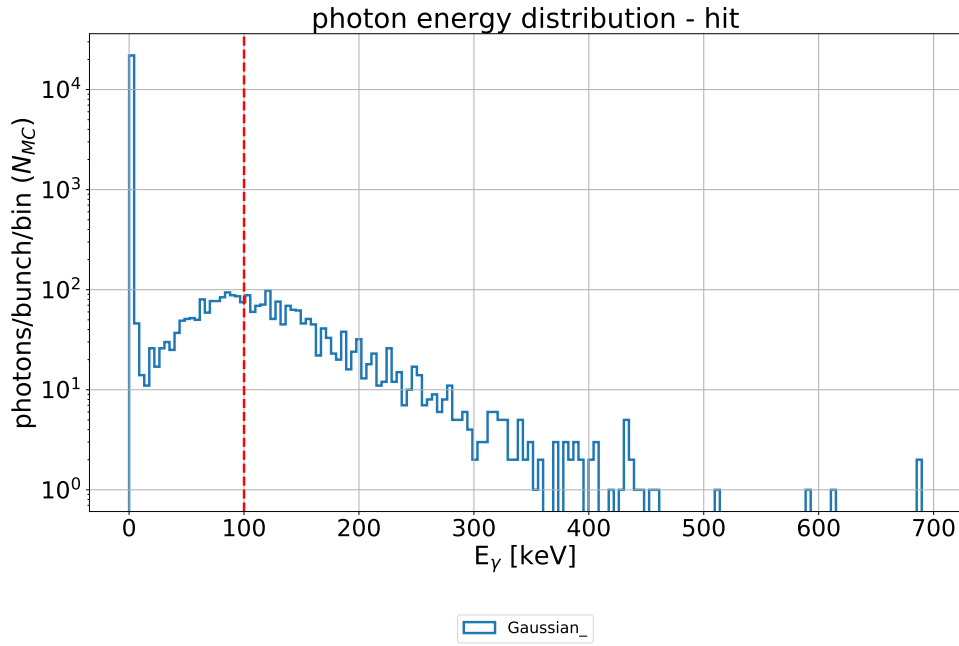


Figure 7.25: Distribution of energies for photons striking the vacuum chamber wall in the straight section (100 m to 10 m upstream of the interaction point). The vertical red dashed line highlights a 100 keV photon energy.

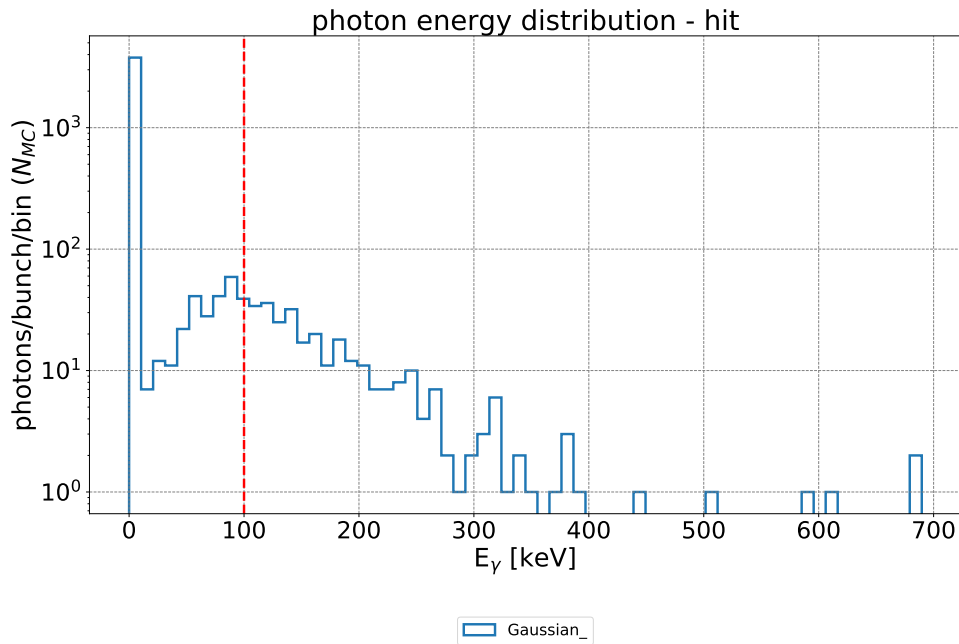


Figure 7.26: Energy of photons striking the beam-pipe wall within ± 10 m around the interaction point. The distribution is comparable to Fig. 7.25 but shows fewer entries. Less events reach this section of the interaction region. The vertical red dashed line highlights a 100 keV photon energy.

photons are emitted from downstream bending magnets. Those magnets have smaller bending radii and therefore higher critical energies than the last upstream dipole magnets. ϵ_c of those downstream dipoles reaches more than 100 keV and can even extend to MeV – details are summarized in Table 7.4.

With this default scenario in place, the simulation performed can be used to arrive at some important preliminary conclusions:

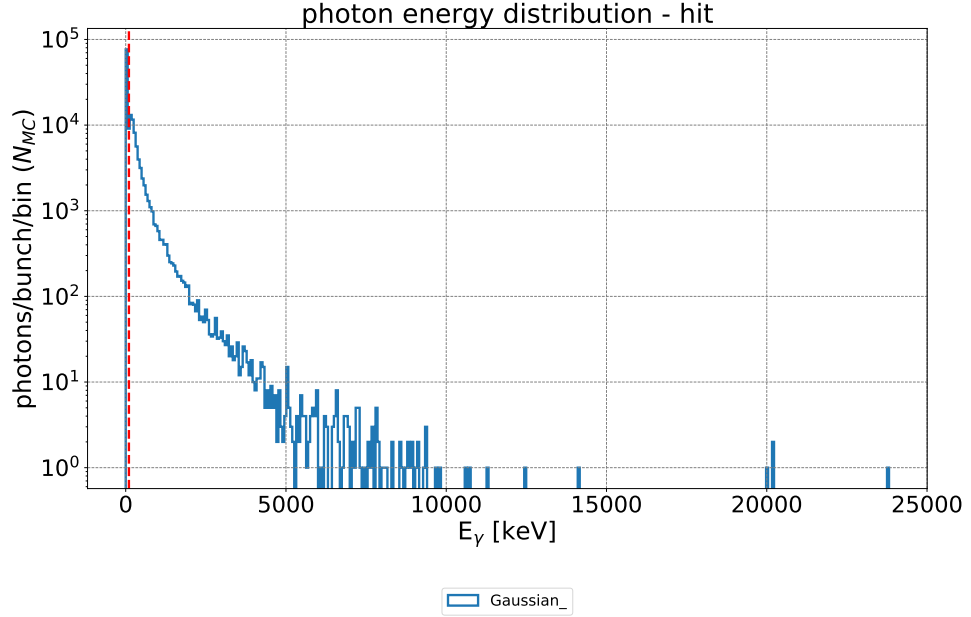


Figure 7.27: Energy of photons striking the beam-pipe wall downstream of the interaction point. The vertical red dashed line highlights a 100 keV photon energy.

Table 7.4: Analytic estimate of (energy dependent) parameters for the first five downstream bends at FCC-ee $t\bar{t}$ with 182.5 GeV beam energy. Those parameters have been motivated in Chapter 4. Note that L describes an integral length. n_γ denotes the number of photons radiated per single particle, while n_{tot} extrapolates that out to the entire bunch population.

	S [m]	L [m]	α [mrad]	ϵ_c [keV]	n_γ	P_{SR} [kW]	n_{tot} [10^{11}]	$\langle \epsilon \rangle$ [keV]
BC1.1	63.68	40.61	2.08	691	7.83	8.64	17.2	213
BC2.1	68.55	0.7729	-0.08218	1430	0.309	0.708	0.68	441
BC3.1	114.6	41.93	2.308	742	8.68	10.3	19.1	229
BC4.1	150.5	31.18	0.7774	336	2.92	1.57	6.43	104
BC5.1	195.6	41.08	2.96	972	11.1	17.3	24.5	299

- The characterization allows to show where photons are generated upstream and which sections of the interaction region are affected by direct hits of 1st generation photons.
- The detector chamber ($z \pm 2$ m around the interaction point) remains free of hits, due to basic protection provided by the synchrotron radiation masks.
- Contributions of single types of magnets can be identified and show which energy regimes are relevant. This allows to relate the high energy photons to quadrupole magnets, most of which affect only the downstream section of the MDI.
- Photons affecting the straight section or the central interaction region are of considerably lower energy than in the downstream section. This observation supports the design principle of using *weak bends* upstream of the interaction point.

The remaining part of this section will establish two additional scenarios, which

consider a very strong population of tails. Different mechanisms such as scattering (within the same bunch or for example on Thermal Photons) or interactions with the other beam during collisions lead to beam tails – as has been measured at LEP [36].

While horizontal tails result directly from scattering, vertical tails can be generated by mechanisms such as coupling or residual dispersion. These are introduced by skew magnets or detector solenoids, thereby redistributing horizontal emittance in the vertical transverse plane.

In practical terms, this means a certain fraction of the bunch population is located at higher sigma than the core. Accordingly, the following scenarios can be used to enhance the understanding of trends – how does the radiation background evolve with tails? On the other hand, those cases allow an investigation of the effect that collimators have at different locations.

Horizontal Tails

Tail scans at LEP showed that horizontal tails on average barely exceed an amplitude of $15 \sigma_x$ [36].

In the context of this thesis, it is important to understand the trends. For this purpose, a strong population of large horizontal amplitudes out to $15 \sigma_x$ is assumed. The ring-type particle distribution in MDISim is used to generate the beam, while the bunch population of $N_{MC} = 10^4$ remains unchanged and no orbit tolerances are assumed.

Such an extreme scenario allows insight into the changes of the photon background when tails are populated, while at the same time keeping computational resources on a reasonable level.

Figure 7.28 shows the transverse particle distribution in three different elements upstream of the interaction point. The distribution features the ring horizontally but a Gaussian core in the vertical plane.

Only the most important changes wrt. to the default scenario are shortly pointed out. The tail scenarios are rather introduced in order to have them available for specific comparisons in the further course of this analysis.

Figure 7.29 (a) provides a comparison of the distribution of direct hits by photons on the beam-pipe wall. While the saw-tooth shaped pattern upstream does not change much, a significantly higher amount of direct hits is observable around the interaction point and especially over the downstream section.

An interesting comparison in this context is to look at hits purely caused by the quadrupole magnets in Fig. 7.29 (b) and (c). More photons strike the vacuum chamber wall in a section between 200 m and 0 m upstream. Particularly around the interaction point, horizontal tails cause a measurable amount of direct hits. Radiation from two upstream quadrupoles, QC3L.2 and QT1L.2, now reaches the central interaction region and the synchrotron radiation masks as shown in Fig. 7.29 (c).

Another point can be found while comparing the energy distributions of the two samples – default and horizontal tails as depicted in Fig. 7.30. With strong horizontal tails, the radiation from quadrupoles reaches the MeV range with (1808.88 ± 3.63) keV – an increase by roughly a factor 3. Radiation from the dipoles

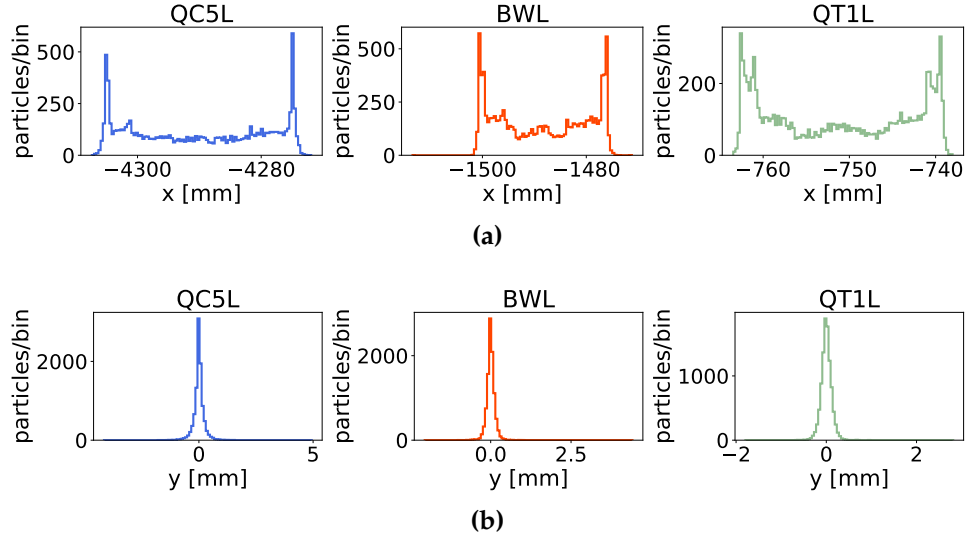


Figure 7.28: Transverse particle distributions in three upstream elements. Particles are concentrated at large amplitudes in the horizontal plane. The vertical plane exhibits a Gaussian core.

differs by only 11 % between both cases and remains on average below 200 keV. The difference in the dipole magnets can be explained by changes in the bending radius to which the photon energy is sensitive, according to Eq. (4.20) in Section 4.1, that expresses the dependence on the inverse radius. For particles at large amplitudes, this radius is either smaller or larger than for particles in the average Gaussian bunch since the distance to the reference axis changes more significantly.

Vertical Tails

A third scenario assuming vertical tails is now introduced, where the ring-type particle distribution is used with maximum amplitudes around $50 \sigma_y$ and a Gaussian core in the horizontal, as shown in Fig. 7.31. Assuming that about 75 % of horizontal tails at $10 \sigma_x$ (75 % from 6.68 mm at BWL.2 corresponds to 5.01 mm) are shifted (for example through coupling) into the vertical plane, this would correspond to roughly $50 \sigma_y$ (with a vertical beam size at BWL.2 of $\sigma_y = 104.06 \mu\text{m}$). This allows to investigate the influence of strong vertical tails on the synchrotron radiation background and to find differences with the previous scenarios. The particle distributions at the start element (QC5L.2) and two other upstream magnets are shown in Fig. 7.31 (a) and (b).

Since the general distribution of hits, as shown in Fig. 7.20 and 7.29 (a) does not show significant differences, the attention is immediately drawn to the quadrupoles. Figure 7.32 (a) shows the distribution of hits from photons generated in upstream quadrupoles. As before, the downstream section sees much more photons directly striking the vacuum chamber wall, than compared to the default case. Interesting in this context is the observation that even more direct strikes are registered close around the interaction point.

In Fig. 7.32 (b), a close-up of the central interaction region highlights strong concentrations of photons affecting the inner synchrotron radiation mask and also areas within ℓ^* . The outer mask is not as strongly hit by photons as the inner

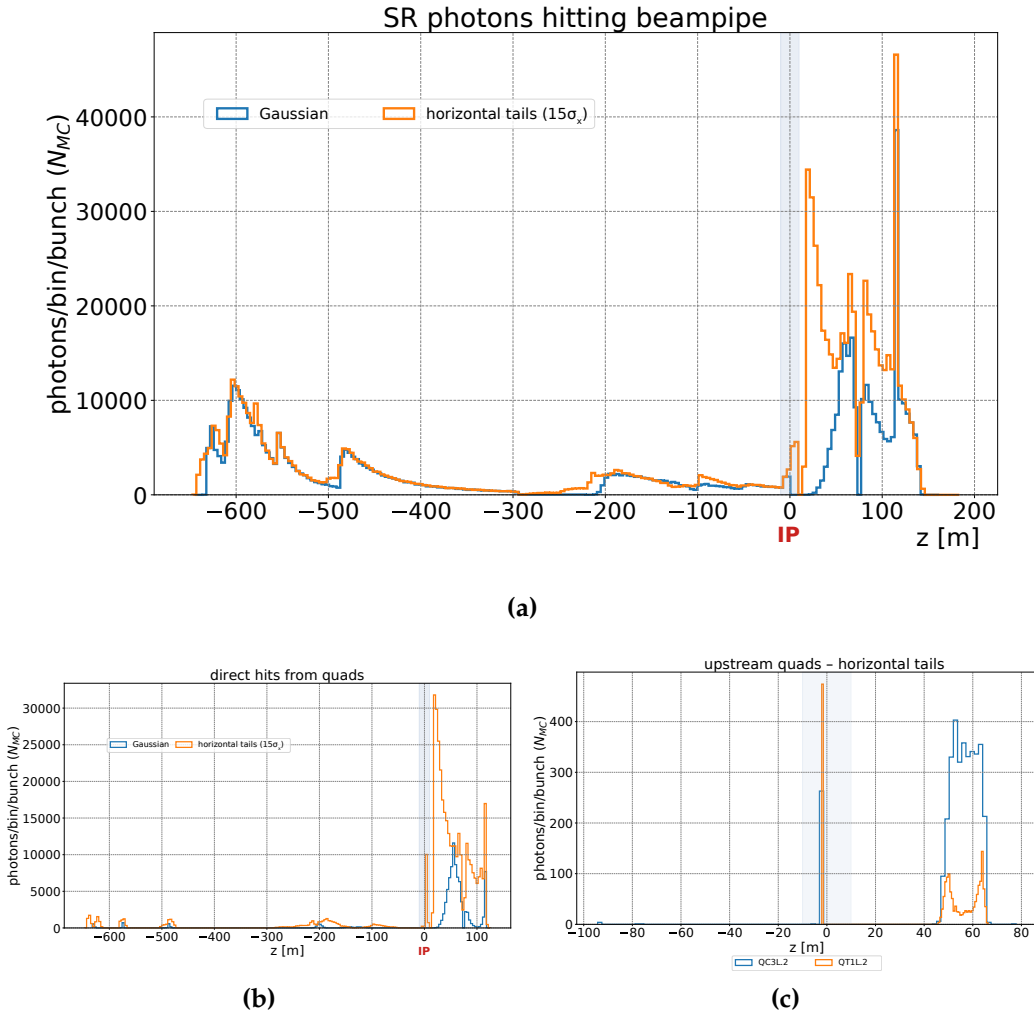


Figure 7.29: Comparison of the distribution of direct hits for default (blue) and the tail sample (orange). (a) entire interaction region. Especially around the **Interaction Point (IP)** and in the downstream section, significant increases of the amount of direct hits are observable. (b) direct hits only from quads, confirming the observation. (c) hits from upstream quadrupoles QC3L.2 and QT1L.2.

mask.

7.6 Interaction with the Beam-pipe Material

The previous section introduced a default scenario with a Gaussian bunch. Therein, a distribution of locations where photons directly strike the inner beam-pipe wall was presented. The description also included energy distributions of these photons.

Before looking further into the photon background in the interaction region, this section briefly describes interaction processes after synchrotron radiation photons strike the vacuum chamber wall. Are most of them directly absorbed or rather reflected – an interesting question for the background protection scheme.

To answer this question, the straight section upstream of the interaction point is investigated first, before addressing the downstream section. The following discussion is based on the default scenario, considering a Gaussian bunch on axis

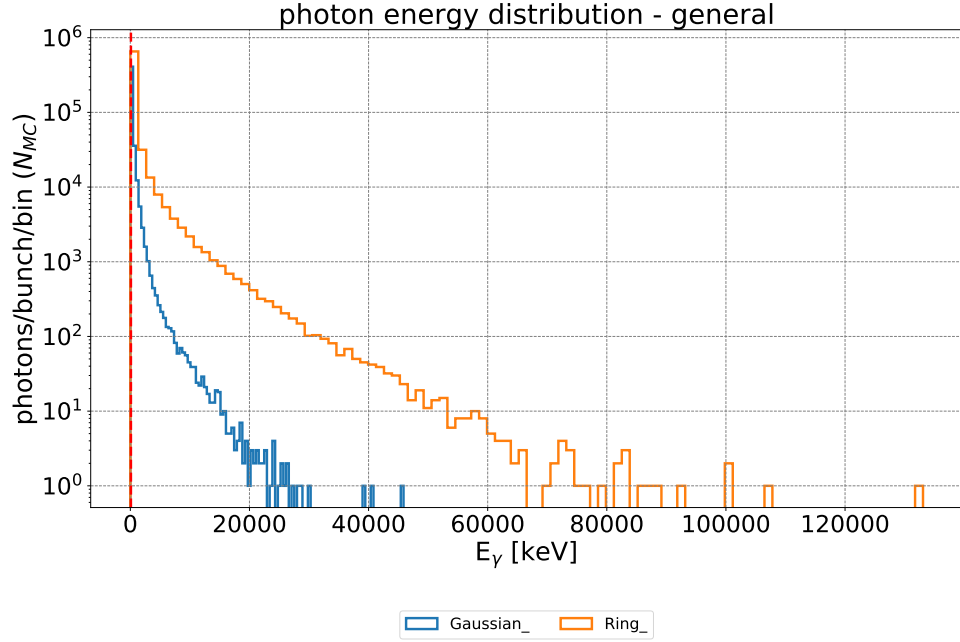


Figure 7.30: Energy distribution of the emitted synchrotron radiation photons. *Gaussian sample* (blue) and *horizontal tails* (orange). Once horizontal tails are considered, a much stronger high energy section of the distribution is observable. Where highest photon energies reached out to 10 MeV in the default case, they can now easily exceed 20 MeV.

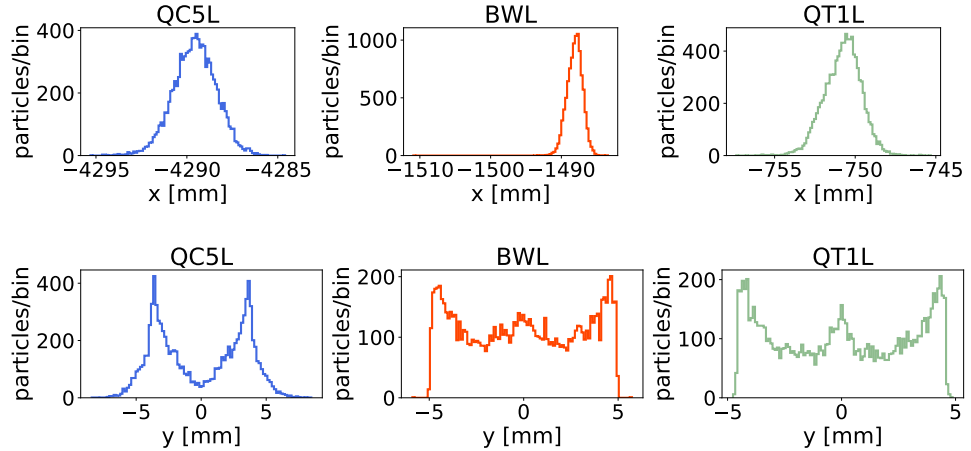


Figure 7.31: Transverse particle distributions for vertical tails in three upstream elements. Particles are concentrated at large amplitudes in the vertical plane, while the horizontal plane features a Gaussian core.

with a population of $N_{MC} = 10^4$ positrons.

Figure 7.33 depicts the distribution of interactions which produce secondary electrons when photons interact with the beam-pipe material. Note, that the simulations presented here assume the beam-pipe of FCC-ee to be made out of copper [2].

The photoelectric effect is dominant all the way upstream of the interaction point. By absorbing a photon, an electron is released from the material. Since the photon is absorbed in the process, it is favorable in terms of photon mitigation as the photon does not scatter off the beam-pipe wall.

7.6. INTERACTION WITH THE BEAM-PIPE MATERIAL

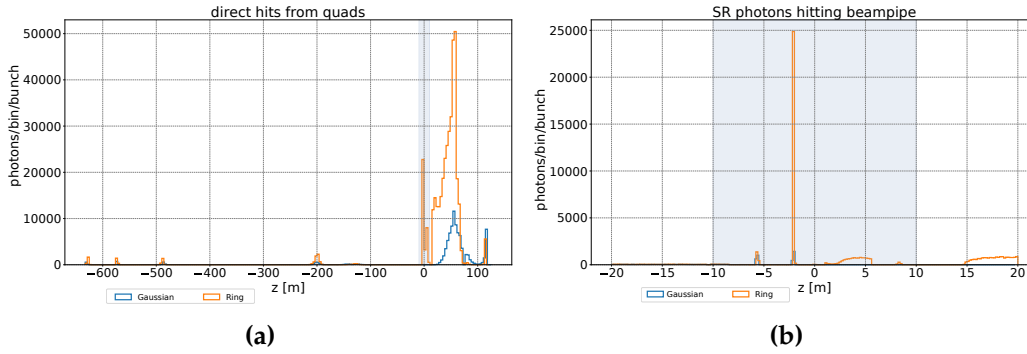


Figure 7.32: Comparison of the distribution of direct hits for default (blue) and the vertical tail sample (orange). Around the interaction point and in the downstream section, vertical tails lead to a significant increase of direct hits, especially at the inner mask.

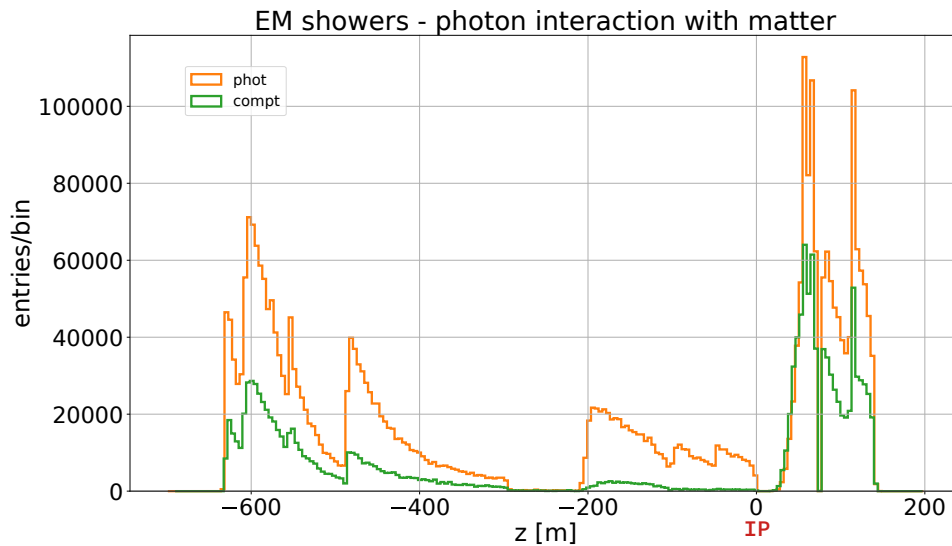


Figure 7.33: Photon interactions with the beam-pipe material. The plot shows a distribution of effects which take place up- and downstream of the **Interaction Point (IP)**. The Photoelectric effect is dominant upstream, while the number of Compton scattered events significantly increases downstream of the interaction point.

Compton scattering, on the other hand does not absorb the photon directly. It rather scatters with electrons of the material and might escape again – depending on the energy. The data shows, however, that Compton scattered events are not as numerous upstream as they are downstream of the interaction point. Compton scattering occurs even less particularly in the straight section between 100 m upstream and the interaction point – a close-up is shown in Fig. 7.34 (a) together with the energy profile of events in that region in (b).

Especially the low-energy range is dominated by the photoelectric effect instead of Compton scattering. For the straight section, Compton-scattered events peak at energies above 100 keV but below 200 keV. An interesting feature of Fig. 7.34 (b) is the K-shell at nearly 10 keV for the photoelectric effect in copper.

Downstream of the interaction point, the number of Compton scattered events – relative to the photoelectric effect – increases drastically, as depicted in Fig. 7.35 (a). The observation can be related to higher photon energies in this area, generated

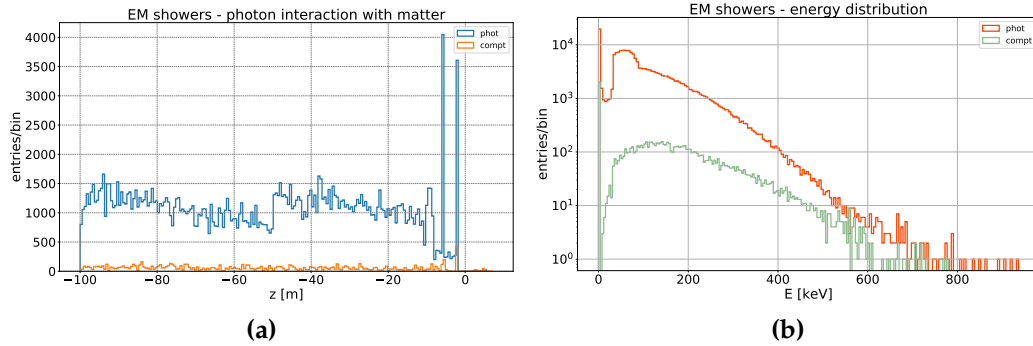


Figure 7.34: (a) photon interactions with the beam-pipe material upstream in the straight section. (b) energy distribution for interactions in the straight section (z between -100 m to 10 m). The Photoelectric effect clearly dominates this entire energy regime.

in final focus quadrupoles and the detector solenoid around the interaction point. Another contribution comes from rather strong downstream dipole magnets. Energy distributions for the downstream section of the MDI are shown in Fig. 7.35 (b). Due to the higher photon energies involved, Compton scattering dominates the spectrum, reaching even 6 MeV to 8 MeV.

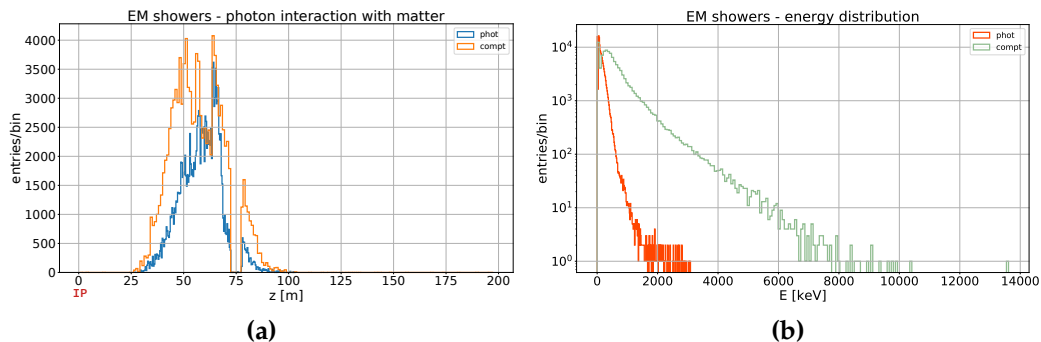


Figure 7.35: Photon interaction with the beam-pipe material downstream of the *Interaction Point* (IP) (a). Energy distribution of the interaction processes (b). Compton scattering is much more relevant and includes significantly higher photon energies than upstream.

A closer look on those events which lead to scattering of photons – Compton and Rayleigh scattering – is interesting. Figure 7.36 displays how often a photon scatters before being either absorbed or before they scatter through the beam-pipe wall.

Most photons clearly scatter only once. For Compton scattering, however, a certain fraction that scatters a second time is found, while only very few scatter a third time.

Rayleigh scattered photons rarely scatter twice.

By selecting only events where photons are scattered off the beam-pipe wall, it is possible to identify serious scattering sources upstream of the interaction point. Figure 7.37 (a) depicts the location of events where photons are scattered off the vacuum chamber wall. As mentioned in the context of Fig. 7.36, two processes in this sample cause photons to scatter: the Compton effect and Rayleigh scattering. The amount of scattered events drastically increases only downstream of the

7.6. INTERACTION WITH THE BEAM-PIPE MATERIAL

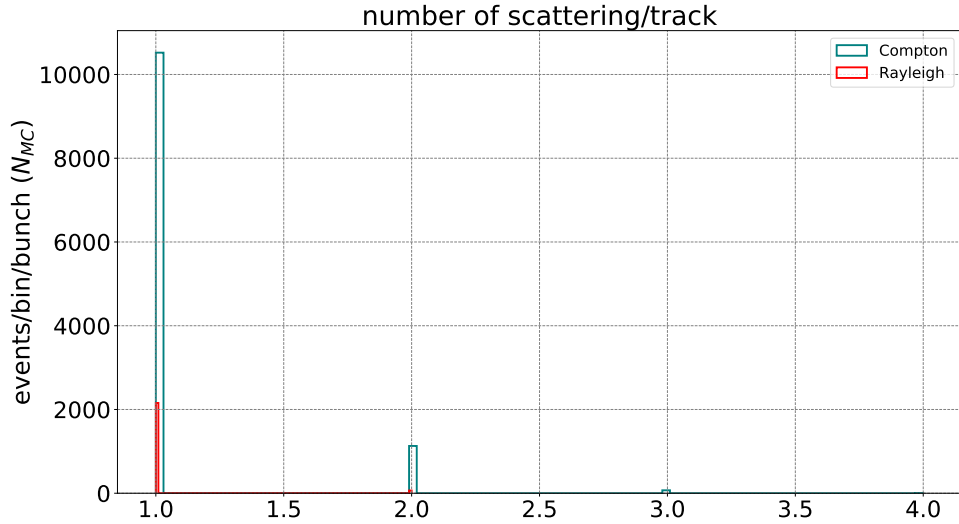


Figure 7.36: Most photons are only once Compton scattered before absorption or exiting the beam-pipe. Some do scatter two or three times. Rayleigh scattered photons rarely scatter a second time.

interaction point, while the rate is moderate upstream, in accordance with the observations at the beginning of this section.

A total of 516286 ± 719 synchrotron radiation photons was generated in the sample, out of which 95262 ± 309 events do scatter, a fraction close to 18.5%. From those events, 86189 ± 294 are subject to Compton-scattering, while 9073 ± 95 are Rayleigh-scattered.

An enhanced view of the straight section between 100 m upstream and 10 m downstream is displayed in Fig. 7.37 (b), showing that a significant amount of events is concentrated on the masks.

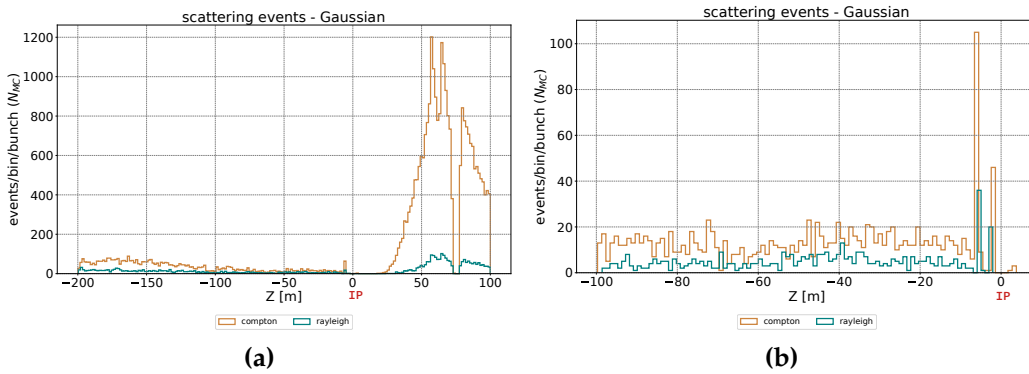


Figure 7.37: Selection of scattered events over the entire region (a) and the straight section (b). A drastic increase of the amount of scattered events is only observable downstream of the **Interaction Point (IP)** while it is moderate upstream. The close up in (b) shows scattered events in the straight section upstream of the interaction point, some of which will be concentrated on the masks.

Energy distributions of scattered events in those regions are provided in Fig. 7.38 (a) and (b). The simulation shows a mean energy of Compton-scattered photons of about (319.32 ± 1.09) keV and those due to Rayleigh scattering approximately (143.12 ± 1.50) keV. Figure 7.38 (b) depicts how the energies of scattered events within the straight section (from 100 m upstream to the interaction point) are dis-

tributed.

In that region, Rayleigh scattered events have an average of (76.02 ± 3.43) keV and Compton scattered photons (127.45 ± 3.52) keV. These mean energies are significantly lower than their average based on the entire data set, which is beneficial for the background mitigation in the MDI. The averages are summarized in Table 7.5.

Table 7.5: Average energies of scattered photons based on the entire data set (Overall) and a selection between 100 m upstream and 10 m downstream (interaction region).

	Overall	IR
Compton	(319.32 ± 1.09) keV	(127.45 ± 3.52) keV
Rayleigh	(143.12 ± 1.50) keV	(76.02 ± 3.43) keV

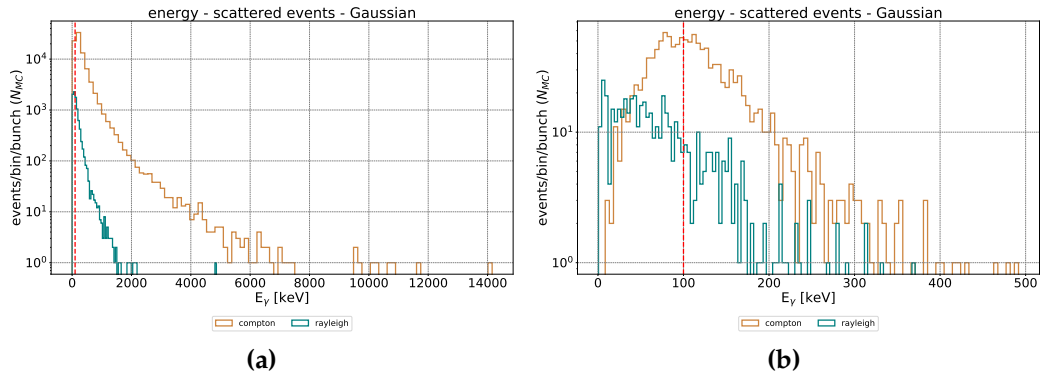


Figure 7.38: Energy distributions of scattered photons. (a) the distribution based on the entire data-set shows that Rayleigh scattered photons have less energy than those after Compton-scattering. (b) energy distribution of events only between 100 m upstream and 10 m downstream. A red dashed vertical line represents 100 keV photon energy.

An increased amount of scattered events is registered on the synchrotron radiation masks in the central interaction region, as depicted in Fig. 7.37 (b). Those will be discussed thoroughly below (Section 7.8).

7.7 Radiation from Special Magnets

The previous section was concerned with general features of the synchrotron radiation background in the FCC-ee MDI. The data showed already that certain types of magnets contribute in different ways. A feature which became clearer after comparing the default scenario with samples that consider a high population of the beam tails.

This part highlights the contribution of selected types of magnets. Due to their location or the critical energies of emitted photons, magnets such as the detector solenoid or the final focus quadrupoles shall be investigated carefully to identify their contribution to the photon background in the MDI, considering especially the region close around the detector.

Radiation from Final-Focus Magnets

Among the quadrupole magnets of the lattice, final focus magnets can be considered as a special case:

- they are located very close to the detector and the interaction point, with an ℓ^* of only ± 2.2 m
- they are significantly stronger than the other upstream quadrupoles (a comparison is provided by Tables 7.3 and 7.6).
Critical energies (ϵ_c) of the final focus quadrupoles can reach tens of MeV, much higher than for quadrupole or dipole magnets farther upstream

Table 7.6: Parameters characterizing upstream final focus quadrupoles QC2L and QC1L. A positive normal quadrupole component K1 means horizontal focusing. n_γ is the number of photons radiated per single beam particle.

Magnet	S [m]	K1L [m^{-2}]	k_0 [1/m]	ϵ_c [keV]	n_γ	P_{SR} [kW]
QC1L1.1	3.4	-0.1963	3.244e-05	437.4	0.1464	0.102
QC1L2.1	4.48	-0.164	4.391e-05	592.1	0.1652	0.156
QC1L3.1	5.56	-0.1638	6.052e-05	816.1	0.2277	0.297
QC2L1.1	7.11	0.1294	5.524e-05	744.8	0.2597	0.309
QC2L2.1	8.44	0.16	7.423e-05	1001	0.349	0.558

Figure 7.39 presents the energy distribution of the upstream final-focus doublet. (a) shows energies from the Gaussian sample. (b) and (c) depict the spectrum for the other two scenarios, considering horizontal and vertical tails, respectively.

In general, the radiation is quite strong, easily reaching photon energies between 2.5 MeV and 5 MeV in case of the default sample.

An interesting feature is observable in Fig. 7.39 (b) and (c), since – depending on either horizontal or vertical tails – the outer (QC2L) or inner quadrupole (QC1L) dominate the energy spectrum. Mean energies for all scenarios are summarized in Table 7.7 – note that these numbers are given in keV.

Table 7.7: Average energies of photons generated in the upstream final focus doublet in keV. The table lists data for the default sample, together with horizontal and vertical tails, showing that the energy almost always reaches the MeV range once tails are present.

	default	horizontal tails	vertical tails
QC2L2	1053.80 \pm 11.82	3068.92 \pm 18.07	1584.37 \pm 12.77
QC2L1	782.66 \pm 9.83	2087.41 \pm 14.38	1626.04 \pm 13.53
QC1L3	899.67 \pm 11.25	2249.63 \pm 16.53	3513.30 \pm 22.35
QC1L2	843.77 \pm 12.04	1531.51 \pm 13.68	3597.22 \pm 22.33
QC1L1	608.82 \pm 9.12	966.17 \pm 9.74	3030.11 \pm 18.40

Mean energies based on the default scenario in Table 7.7 are in the same range as the analytic estimates presented in Table 7.6. Deviations can be explained by the fact that the analytic estimate does not take into account a distribution of particles at random distance from the axis – as is the case with the Monte-Carlo simulations.

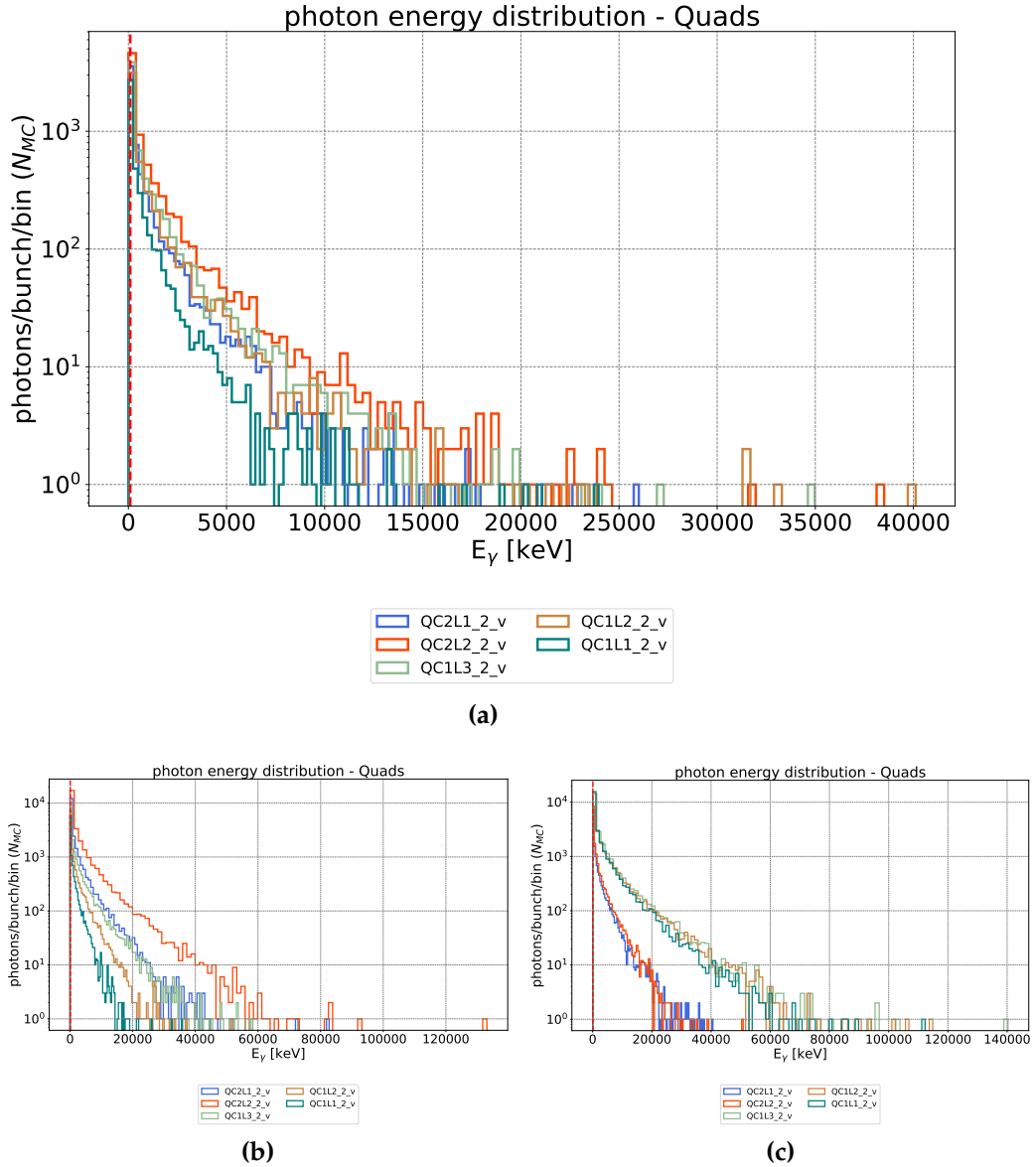


Figure 7.39: Energy spectrum of the two upstream final focus quadrupoles. (a) default scenario, (b) horizontal and (c) vertical tails. While in the first case, all quadrupoles exhibit comparable energies, with horizontal tails the outer quadrupole (QC2L) and with vertical tails the inner quadrupole (QC1L) becomes dominant.

With energies of several MeV, it is important to know where these photons go. Figure 7.40 shows that – based on the default scenario – the radiation coming from the final focus quadrupoles leaves the interaction region and strikes the beam-pipe wall some 20 m to 100 m downstream of the interaction point.

So far, no evidence can be found that this radiation would cause direct hits within ℓ^* – given the default scenario with a Gaussian beam on axis, without explicit tails.

If tails are considered, as shown in Fig. 7.41 (a) and (b), the situation changes noticeably. The distribution of direct hits is shifted much closer towards the central interaction region.

As a bottom-line – with tails, radiation from final focus quadrupoles does not only assume higher energies, it also tends to strike the vacuum chamber wall

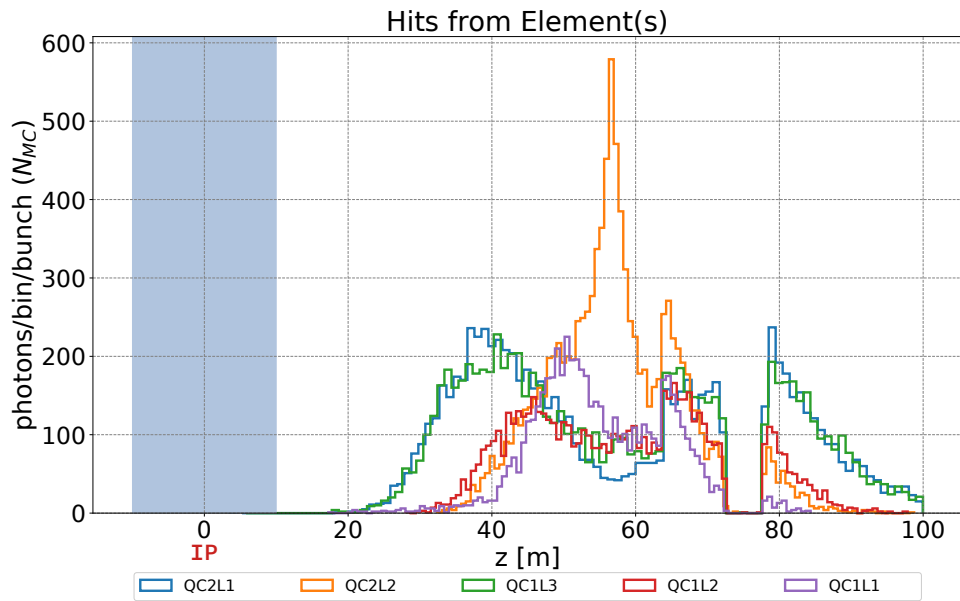


Figure 7.40: Distribution of hits by photons generated in the upstream final focus doublet. A downstream section between 20 m to 100 m is affected, confirming that the central interaction region ($z \pm 10$ m, highlighted in blue) is not subject to direct hits.

significantly closer to the detector area. For strong vertical tails, hits are even registered within ℓ^* , as detailed in Fig. 7.41 (c).

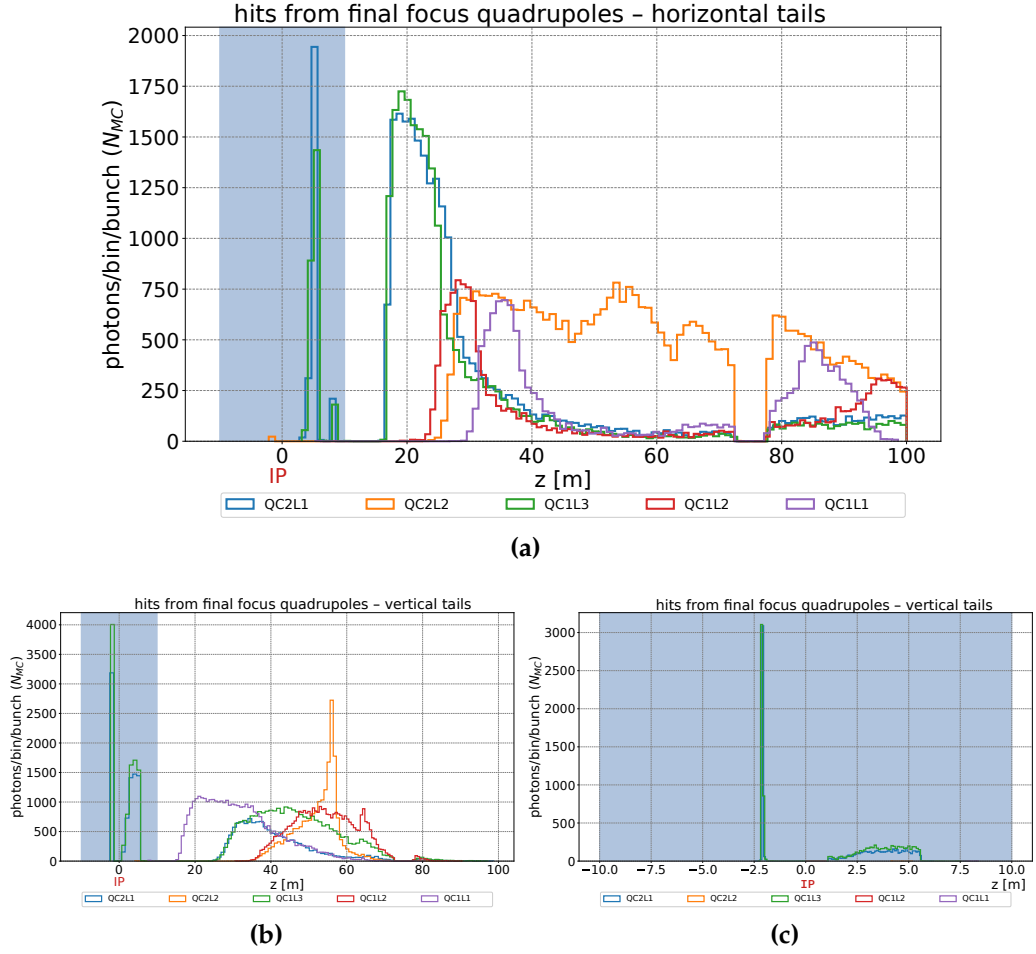


Figure 7.41: Distribution of hits by photons generated in the upstream final focus doublet for samples exhibiting tails. (a) horizontal and (b) vertical tails cause the distribution to shift closer to the central interaction region. (c) details the situation in the central interaction region, showing a significant amount of hits on the inner mask.

Radiation by the Detector Solenoid

The detector solenoid and related effects in terms of synchrotron radiation has been introduced in the context of SuperKEKB. An analytic estimate of the critical photon energy will be done, which can be cross-checked with the simulation data.

Considering the crossing angle at FCC-ee, the beam enters the solenoid at an angle $\theta_x = 15$ mrad and is subject to a tilted solenoid field, which will deflect the beam. That deflection leads to the emission of synchrotron radiation.

By estimating a deflection angle of the beam, critical energies of radiated photons can be derived. Decomposing the field into two parts, the transverse and longitudinal contribution, gives effective fields B_{\perp} and B_{\parallel} :

$$B_{\perp} = B_z \sin \theta_x = 0.029 \text{ T}$$

$$B_{\parallel} = B_z \cos \theta_x = 1.99 \text{ T}$$

The expected deflection of the beam is caused by B_{\perp} and can be compared to the deflection in a dipole magnet. Which allows to estimate the critical photon energy, according to Eq. (7.5).

$$\epsilon_{c,SOL} = \frac{3}{2} \hbar c \gamma^3 K S_{\perp} \approx 641 \text{ keV} \quad (7.5)$$

Where KS denotes the solenoid strength, following definition for the solenoid strength in Mad-X [16]. With the highest beam energy of 182.5 GeV at FCC-ee ($t\bar{t}$), Lorentz factor γ and beam rigidity have the following values

$$B \approx 609 \text{ Tm}$$

$$\gamma \approx 3.57 \times 10^5$$

A critical energy of about 641 keV is a factor of six higher than the upper limit for the *weak bends* upstream.

Fig. 7.42 compares photon energies from the solenoid with the bend radiation upstream of the interaction point. It shows that radiation from the detector solenoid is much harder than the radiation from dipole magnets of Group 1. A mean energy of photons originating from the solenoid of

$$\langle \epsilon \rangle = (206.56 \pm 2.41) \text{ keV} \quad (7.6)$$

can be found, which is about 1/3 of the estimated critical energy and therefore in accordance with Eq. (4.18) of Section 4.1.

For comparison: mean photon energies of the *weak bends* BC1L.2 and BWL.2 are around 30 keV. However, photons from the solenoid are not generally significantly more energetic than radiation from other dipole magnets – as evident when considering dipoles in Group 2 and comparing Fig. 7.42 (a) with (c).

Since two other scenarios are established, which consider a strong population of either horizontal or vertical tails, cross-checking the energy distributions of these with the baseline scenario in Fig. 7.42 (a) is possible.

Figure 7.43 therefore compares the situations of **default sample (blue)** with **horizontal (green)** and **vertical tails (orange)**, respectively.

Considering horizontal tails, the simulation gives an average photon energy of $(208.17 \pm 2.40) \text{ keV}$ – the same as from the default sample, within the uncertainty. As for the case with vertical tails, the mean photon energy is slightly higher, assuming $(274.99 \pm 2.94) \text{ keV}$.

Photons generated in final focus quads actually leave the central interaction region without causing direct hits in the vicinity of the detector, as was shown above. The situation only changes once strong tails are present.

Since the energy contribution of the solenoid is not negligible, it will be as well determined whether or not photons from it directly strike the vacuum chamber wall in close vicinity of the detector.

Figure 7.44 (a) depicts the distribution of spatial momentum with which photons emerge from the solenoid. It shows a longitudinal momentum p_z of approximately 1 for the majority of photons, while the transverse momenta (p_x, p_y) are found to be close to 0. Thus, the radiation can be considered as strongly forward collimated, an observation confirmed by the default data set shown in blue Fig. 7.44 (b). Direct hits on the inner beam pipe wall caused by photons generated in the solenoid are distributed on a narrow region of 50 m to 60 m downstream of the interaction point. Therefore much more narrow than the radiation from final focus quadrupoles, which was distributed in 20 m to 100 m downstream (compare Fig. 7.40).

Considering horizontal tails, as shown in green in the same plot, the distribution broadens out but the general observation does not differ. Only with vertical tails,

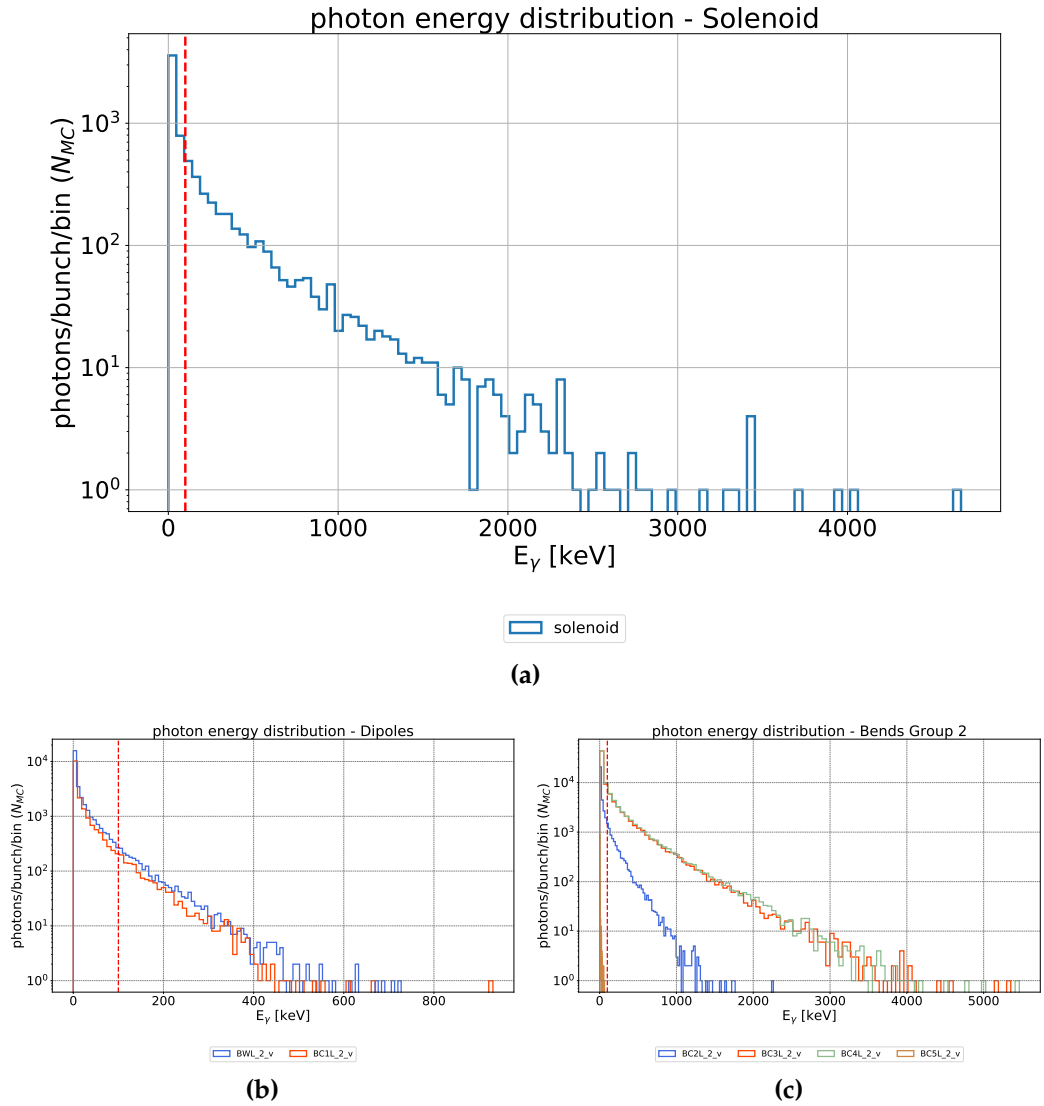


Figure 7.42: Comparing the photon energies of the solenoid (a) with the upstream bends of Group 1 (b) and Group 2 (c). The solenoid generates radiation with higher energies than the weak bends (Group 1) but not higher in energy than stronger bends upstream (Group 2).

the distribution (in orange) noticeably shifts towards the interaction point, causing direct hits within the central interaction region.

One detail needs special consideration. The simulation shows that radiation from the final focus quadrupoles as well as from the detector solenoid hits the beam-pipe wall in the same section between 20 m and 100 m downstream of the central interaction region. Hence, this part of the vacuum chamber can be considered as a region of accumulated heating by the power input through photons with considerable energies. The final-focus magnets alone radiate – assuming ideal conditions – about 3.85 kW in total, according to Table 7.6. Even if only part of this radiation reaches this area, still kW of radiation power per bunch are deposited.

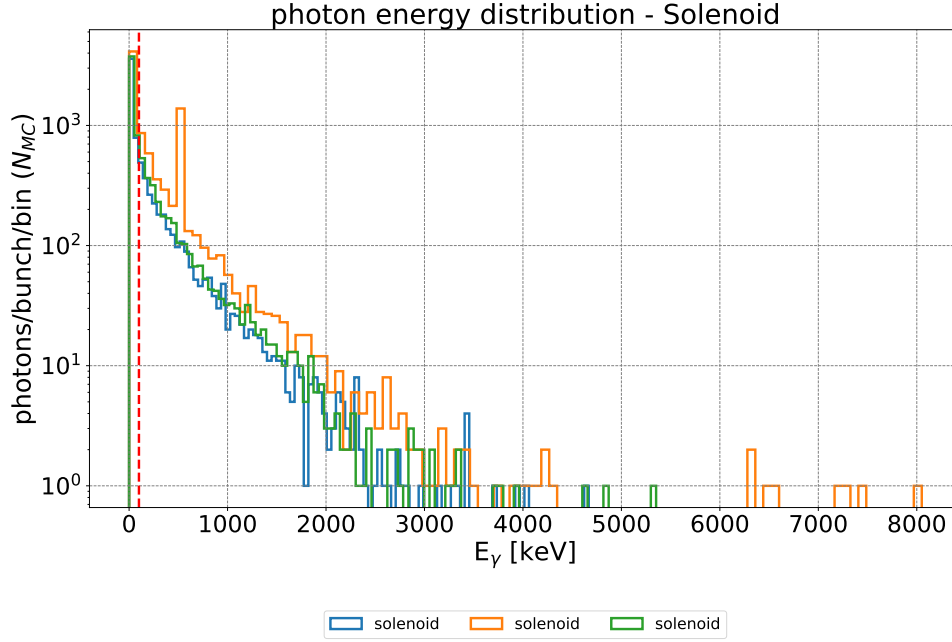


Figure 7.43: Direct comparison of the energy distribution concerning synchrotron radiation from the solenoid between default (blue), horizontal (green) and vertical tails (orange). The distributions do not differ significantly.

Beamstrahlung

Due to the deflection of particles in one bunch by the strong field of the other bunch during collision, additional radiation is generated more or less directly at the interaction point. In the framework of this thesis, MDISim is used to study the synchrotron radiation background, focusing on a single beam. In the current configuration, MDISim does not allow to estimate beamstrahlung, which is why the following estimates are based on Guinea-Pig [65] instead.

Guinea-Pig can provide detailed data on the beamstrahlung photons (individual energies and momenta), as well as their average energy $\langle \epsilon \rangle$ and the number of photons n_γ radiated per macroparticle. From the averages per beam, the total radiated power P_{SR} can be estimated with Eq. (7.7).

$$P_{SR,BS} = E_{\gamma,tot} \frac{e}{\tau_{BSP}} \quad (7.7)$$

Where the overall energy of beamstrahlung is calculated according to Eq. (7.8).

$$E_{\gamma,tot} = \frac{n_\gamma}{n_{MP}} N_p \langle \epsilon \rangle \quad (7.8)$$

Note that n_{MP} represents the number of macro particles used in Guinea-Pig, while N_p is the bunch population. τ_{BSP} is the bunch spacing with 3396 ns at FCC-ee $t\bar{t}$ [2].

Table 7.8 summarizes the mean photon energies $\langle \epsilon \rangle$ and radiated power, estimated for lowest and highest beam energy in FCC-ee. Note that the radiated power P_{SR} is given per beam and interaction point, during one bunch crossing.

The radiation can be considered as strongly forward collimated, by looking at the angles of transverse momenta in Fig. 7.45, which also features Gaussian fits on the

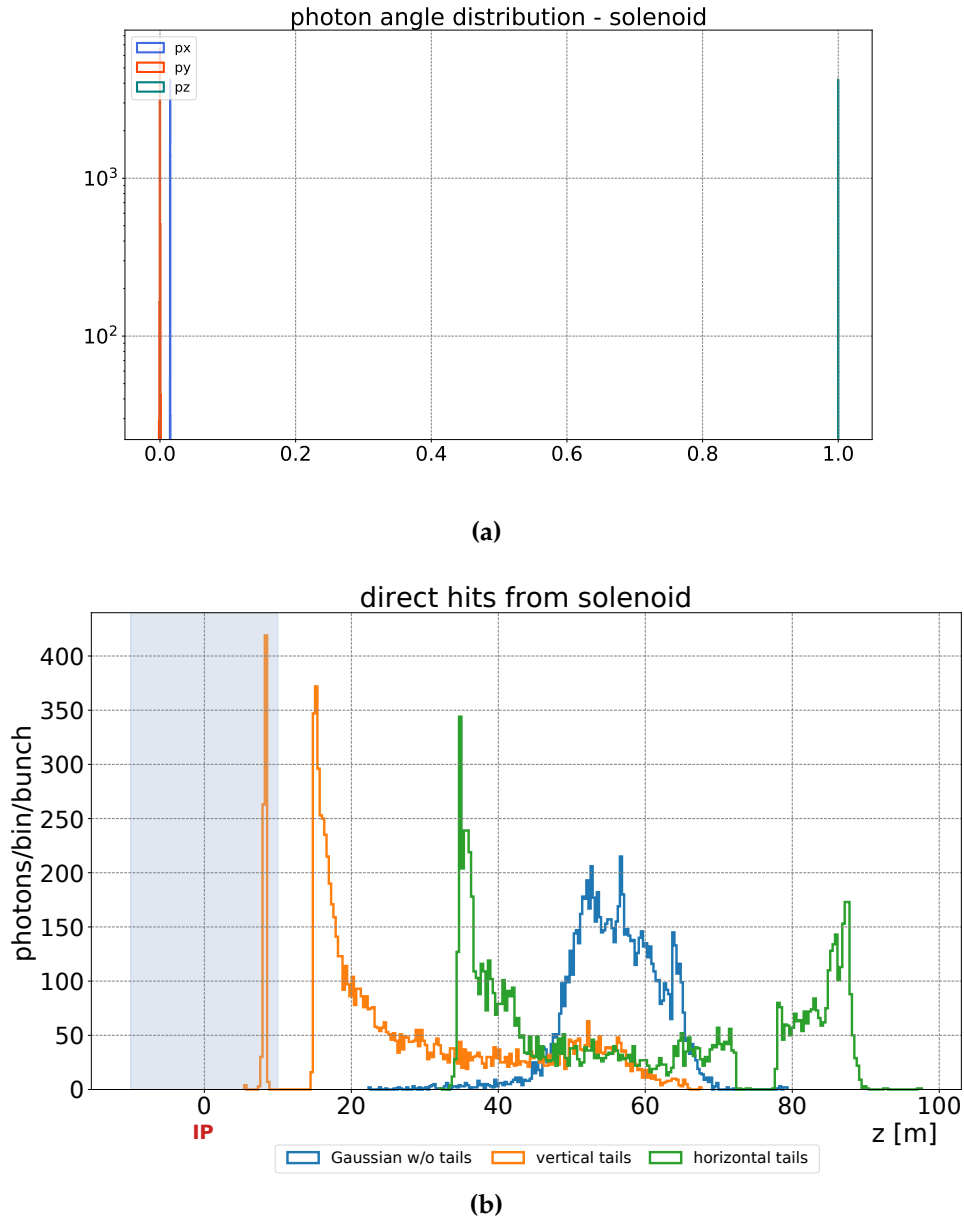


Figure 7.44: Radiation from the detector solenoid. (a) distribution of angles with which photons emerge from the detector solenoid. As transverse momenta (p_x , p_y) are centered around 0 and the longitudinal momentum p_z around 1, radiation from the solenoid can be considered as strongly focused in forward direction. (b) distribution of direct hits on the beam-pipe wall by photons from the solenoid. The plot shows the default together with a scenario where the beam exhibits tails. While the default affects a narrow region between 50 m to 60 m, the case with tails results in a broader distribution. The central interaction region is highlighted in blue ($z \pm 10$ m).

Table 7.8: Beamstrahlung parameters at lowest and highest energy in FCC-ee, derived with Guinea-Pig. Note that the radiated power is given per beam and interaction point during one bunch crossing.

E_b [GeV]	$\langle \epsilon \rangle$ [MeV]	P_{SR} [kW]
45.6 GeV	2.09	405.23
182.5 GeV	69.75	185.94

data. In the horizontal plane, an average angle of about $11 \mu\text{rad}$ is found, while the spread in the vertical plane is even smaller with about $1 \mu\text{rad}$.

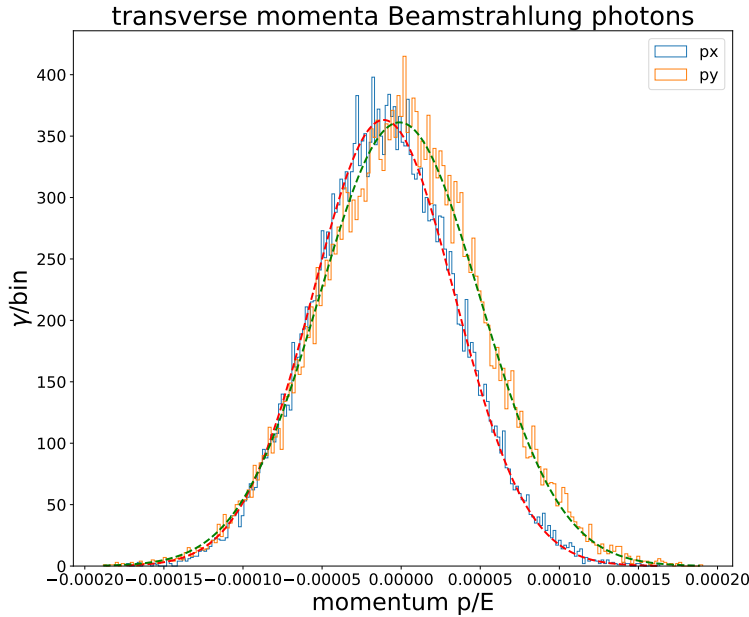


Figure 7.45: Distribution of angles with which beamstrahlung photons emerge in both transverse planes, x and y . Gaussian fits to derive mean angles are shown as dashed lines.

Yet again, almost 200 kW of radiation power might reach the downstream section of the beam-pipe for FCC-ee $t\bar{t}$, where already radiation from the final focus quadrupoles and the detector solenoid will strike the beam pipe wall.

7.8 Fixed Mitigation Measures for Synchrotron Radiation

The introductory scenario featured a Gaussian bunch on axis to establish a baseline characterization of the photon background.

In this section, fixed mitigation measures will be introduced. *Fixed mitigation measures* refers to details of the design which can not be changed, such as:

- *weak bends* and asymmetric interaction region design
- synchrotron radiation masks upstream of the interaction point.

Simulations with MDISim will be used to estimate the effect of these measures and to assess the degree of protection they can provide, based on the default scenario.

Geometry Characteristics

First measure to protect the interaction region from synchrotron radiation is to reduce the energy and amount of photons reaching the central interaction region. In case of FCC-ee this is achieved by an asymmetric layout of the optics design.

The bending radius of the last upstream dipoles is increased to reduce critical energies (ϵ_c) as well as the number of photons emitted per electron (or positron) (n_γ).

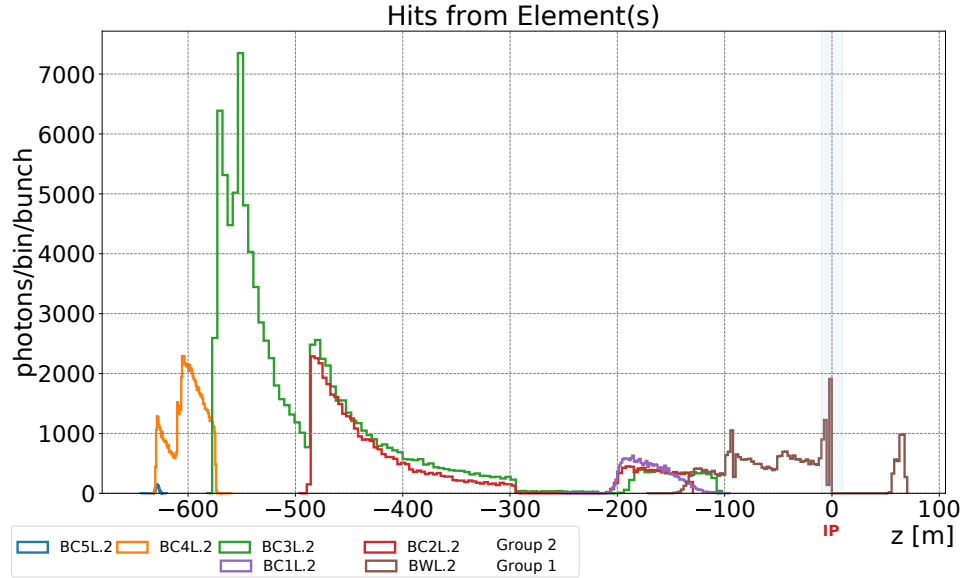


Figure 7.46: Distribution of hits on the beam-pipe wall, caused by photons from the second and first group of magnets. Shown is the entire section from 800 m upstream towards 100 m downstream. The plot shows that radiation from Group 2 does not reach the straight section (100 m upstream to Interaction Point (IP)). Only photons from the last upstream dipole magnet directly reach the central interaction region.

This chapter started with a classification of the upstream dipole magnets in Section 7.3. Basic geometric estimates allowed to conclude that only synchrotron radiation from the last two upstream dipoles (Group 1) may reach the close vicinity of the detector directly.

Figure 7.46 shows again the distributions of direct hits on the beam-pipe wall but this time, hits are related to elements from which photons actually originate.

Direct hits by photons from dipole magnets in Group 2 (with much harder radiation than those of Group 1) affect only a section of the interaction region between 650 m to 120 m upstream of the detector. No photons from this group can reach the central interaction region (± 10 m in z) directly.

Out of Group 1, BC1L.2 contributes in the section between 200 m and 100 m upstream, but especially the dominant role of BWL.2 becomes clear. An enhancement of this detail is provided in Fig. 7.47. The plot shows the contribution of direct hits from BWL.2, along the whole straight section and especially in the central interaction region. Considering direct hits of 1st generation photons, BWL.2 is the only magnet which affects the central interaction region and therefore possibly the detector area.

A close-up of the central region, as depicted in Fig. 7.48 confirms this observation. It allows to observe that, while the whole upstream region of the beam-pipe is exposed to radiation, the area ℓ^* of ± 2.2 m around the interaction point at $z = 0$ m stays free of direct hits.

Two characteristic peaks upstream of the interaction point indicate the location of the fixed synchrotron radiation masks, which will be the focus of the next subsection. The simulations show that the synchrotron radiation masks provide

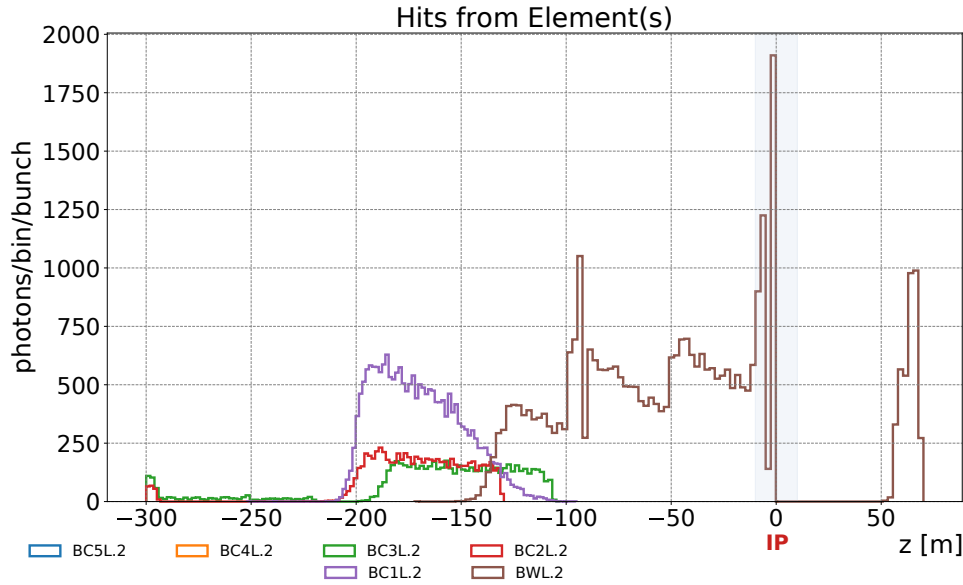


Figure 7.47: Distribution of direct hits by photons coming from upstream magnets. Shown is the region 300 m upstream of the **Interaction Point (IP)** ($z = 0$ m) towards 60 m downstream. The last upstream bend, **BWL.2** is the only magnet which affects the straight section between 100 m to 0 m upstream of the interaction point with direct hits.

substantial shielding of the detector area – at least considering data from the default scenario.

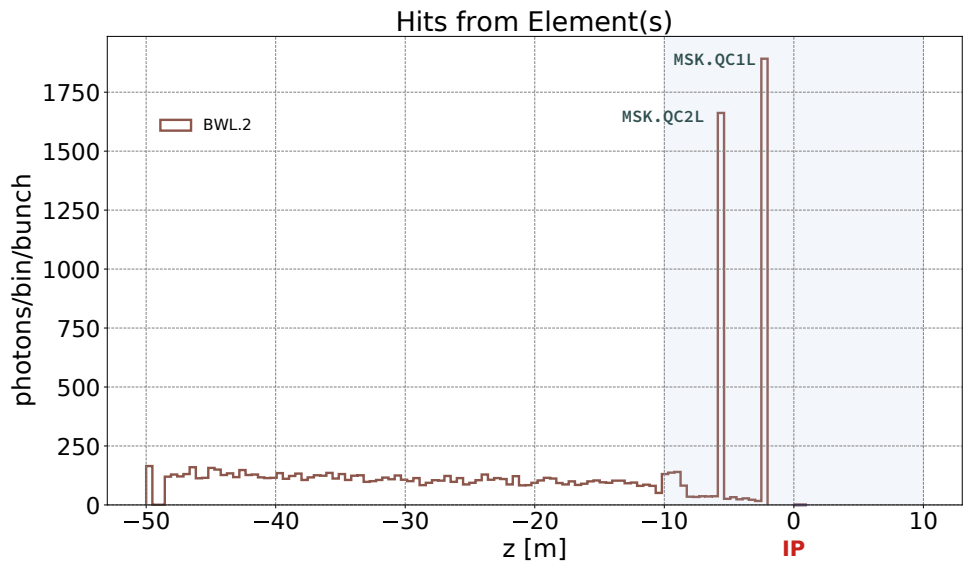


Figure 7.48: Hits on the beam-pipe in the interaction region within ± 50 m. Only **BWL.2** contributes with direct hits in this area. Note, how the innermost distance between last magnet and **Interaction Point (IP)** (ℓ^* , $z \pm 2.2$ m) remains free of hits, while a significant amount of photons strikes both synchrotron radiation masks (**MSK.QC2L** and **MSK.QC1L**).

Upstream Beam-pipe Shape

Figure 7.49 depicts a top view on the upstream beam-pipe geometry, showing that the last beam-pipe section between QT1L and QC2L assumes a conical shape.

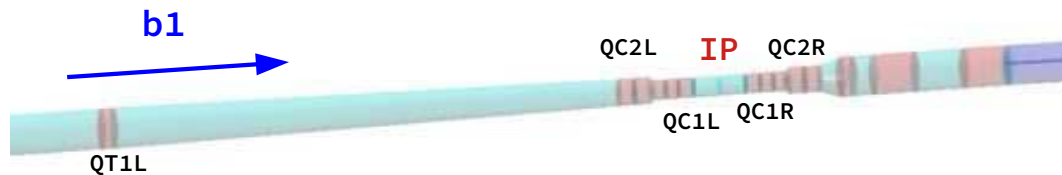


Figure 7.49: The upstream beam-pipe geometry from the last upstream quadrupole QT1L.2 down through the central interaction region to the first downstream bending magnet. It shows the last upstream beam-pipe section with a conical shape, ending right at the entrance of QC2L. Note that this feature was kept in the updated geometry shown in Fig. 7.4.

Initially, the geometry did not include this feature. However, it is possible to show that this design can help to reduce the amount of photons even reaching the central interaction region (± 10 m in z), by gently reducing the beam-pipe diameter.

The effect is demonstrated in Fig. 7.50 which visualizes data from an earlier **Monte-Carlo** sample with a bunch population of $N_{MC} = 10^3$.

The plot in (a) shows how a certain fraction of photons – otherwise striking the inner beam-pipe wall rather close to the interaction point – is redistributed over a section within 50 m upstream.

Figure 7.50 (b) depicts the situation within the central interaction region (± 10 m around the interaction point). Without the beam-pipe tapering, a significant amount of direct hits between 10 m to 8 m upstream would be registered (represented by the **blue histogram**).

Masks

The current design of the **MDI** in **FCC-ee** foresees synchrotron radiation masks at certain locations (refer to Section 7.1).

The geometry in the presented simulations with MDISim includes two masks installed:

- right downstream of QC1L, 2.1 m away from the interaction point – MSK.QC1L
- between QC1L and QC2L at 5.6 m upstream of the interaction point – MSK.QC2L

The effect of these masks on the general background will now be investigated, before addressing aspects such as energy deposit and scattering of photons off the masks. The characterization can help to decide in which cases collimation further upstream becomes relevant in order to relax the conditions at the masks.

Direct Hits on the Masks

Figure 7.51 shows two interesting details in the central interaction region. **Blue** depicts the case without and **orange** the case with masks.

The outer mask coincides with an aperture restriction right at the exit of QC2L, which is why the peaks in both samples appear at the same location around 5.6 m upstream.

A second detail can be found by looking in the region ± 2.5 m around the interaction point. Without a mask, photons can be registered to directly strike the central

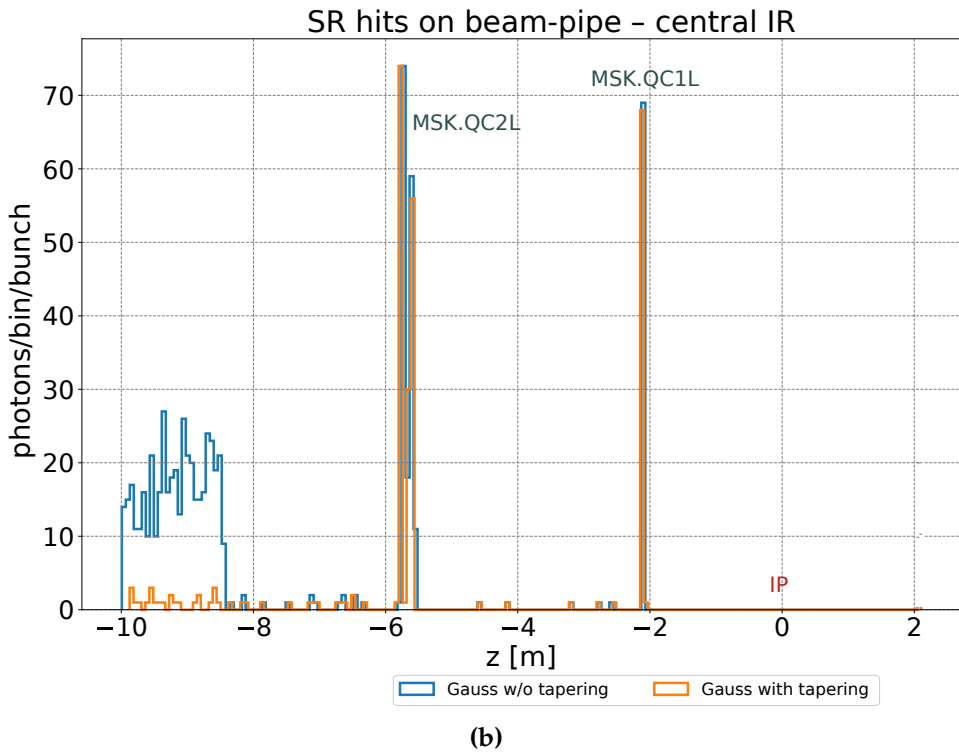
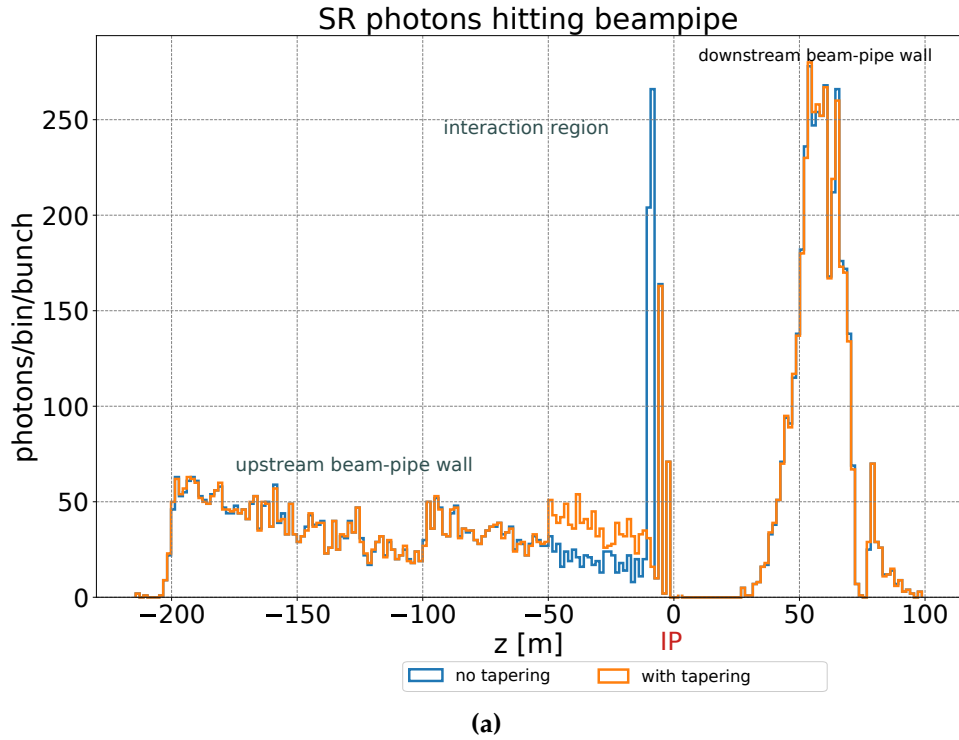


Figure 7.50: Distribution of hits on the beam-pipe wall for two scenarios *with* (orange) and *without* (blue) tapering of the upstream beam-pipe. (a) shows the distribution in the entire region covered by the simulation, while (b) presents a close-up of the central interaction region. Part of the direct hits on the beam-pipe very close to the detector are redistributed further upstream in case of a tapered beam-pipe. This shows that the tapering blocks a certain fraction of photons which would otherwise strike the beam-pipe rather close to the *Interaction Point* (IP).

chamber. The inner mask MSK.QC1L improves that by shielding that region (within ℓ^*).

The outer mask MSK.QC2L can absorb part of the synchrotron radiation which would otherwise directly strike the beam-pipe wall at the aperture limitation between QC2L and QC1L. So much for the longitudinal distribution of hits within the central interaction region.

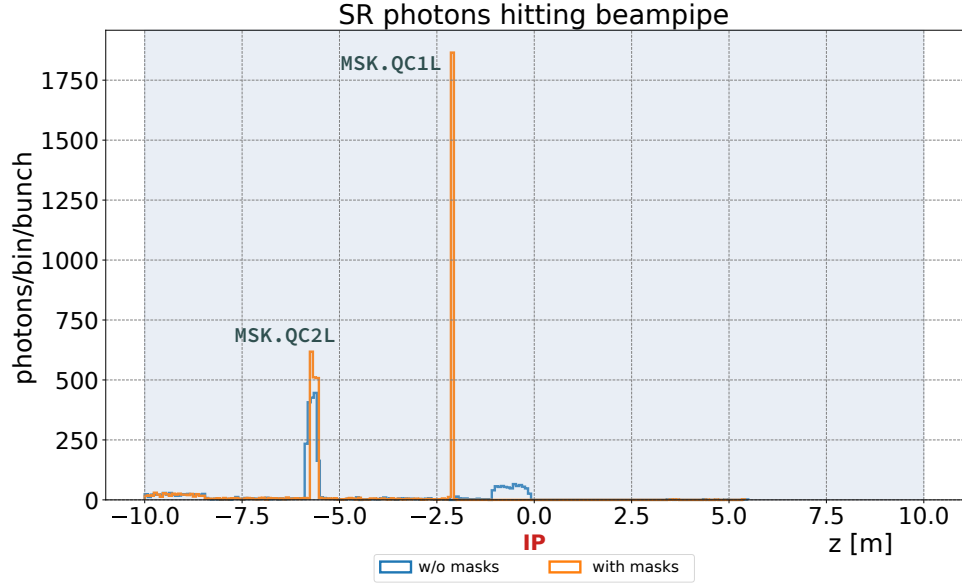


Figure 7.51: Distribution of hits on the beam-pipe wall in the central interaction region. The plot shows two datasets in overlay: plain photon background without masks (blue). Photon background with masks inserted (orange). Synchrotron radiation masks can effectively reduce the amount of hits within ℓ^* .

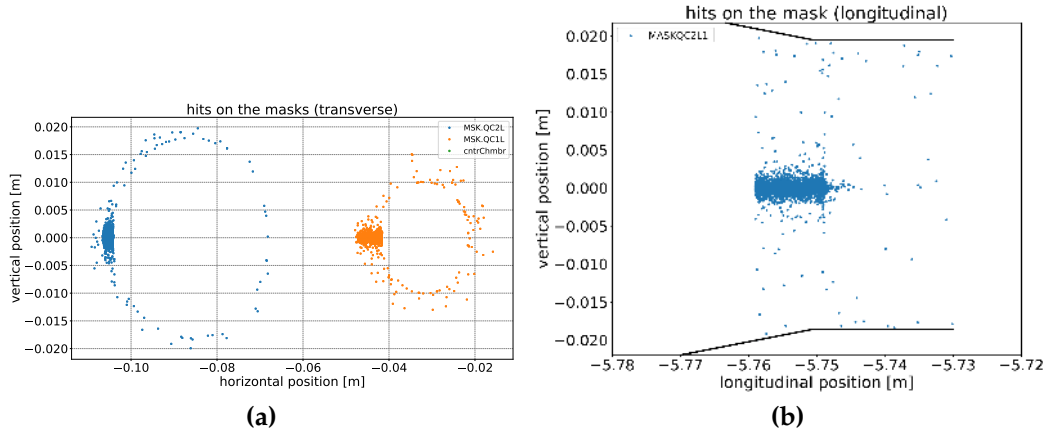


Figure 7.52: Transverse distribution of hits on the masks in (a), considering the default scenario. Note that MSK.QC2L has a larger beam-pipe radius than the inner mask. Most hits are located around the horizontal plane (compare density of hits around vertical 0). (b) longitudinal distribution of hits on MSK.QC2L with the physical aperture indicated by black solid lines.

The simulation also provides information about the transverse distribution of hits, as demonstrated in Fig. 7.52 (a). Most photons hit the mask in a limited horizontal area, according to the density of points in the plot. Together with the plot in Fig. 7.52 (b), the data confirms that the synchrotron radiation is emitted mostly in the horizontal plane.

Figure 7.52 (b) visualizes the vertical position of hits on MSK.QC2L along z and

also shows the reduction in aperture – indicated by black solid lines. Hits are concentrated horizontally on the front face of the mask, where a sloped section ensures smooth connection to the default beam-pipe diameter.

In order to expand the characterization and find changes with respect to the default case, the two tail scenarios are used. The influence of tails on the protection scheme must be examined.

Figure 7.53 compares how the situation with masks from Fig. 7.51 changes, once significant tails are present.

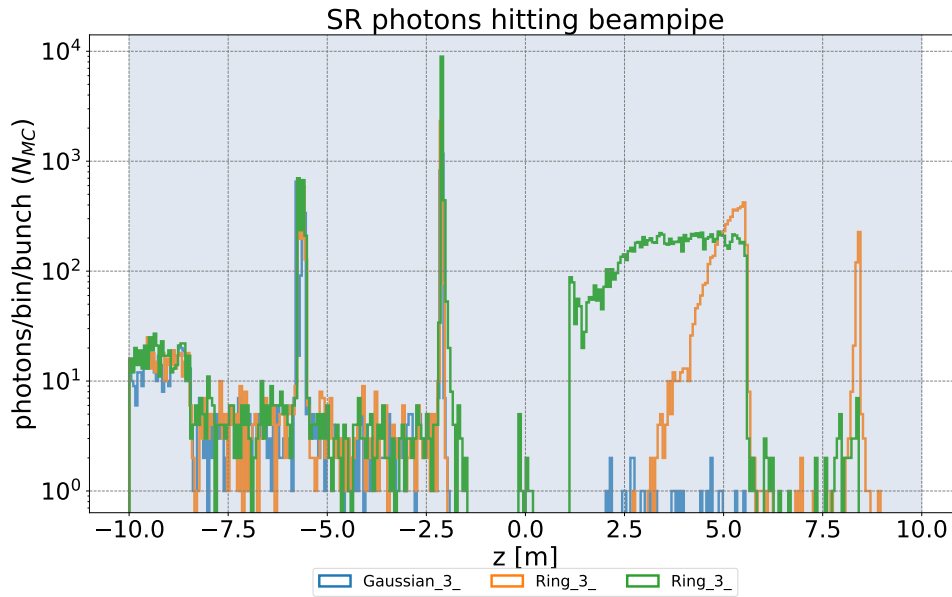


Figure 7.53: Distribution of direct hits in the central interaction region, comparing *default scenario* (blue) with *horizontal* (orange) and *vertical* (green) tails. Despite the spikes on the masks, the data shows a significant accumulation of hits downstream, moving closer to the interaction point at $z = 0$ m. Note the semi-logarithmic scale to enhance details.

The whole section between 0 m and 10 m downstream of the interaction point basically remains free of hits in the default scenario. Considering tails, the simulation shows a clearly increasing amount of photons striking this area, now also affecting the region within ℓ^* .

The number of hits on the inner mask MSK.QC1L is rapidly enhanced with strong vertical tails. Figure 7.54 depicts that detail in the transverse plane.

MSK.QC1L is affected in the entire azimuth, not only horizontally anymore.

With the tails, photons striking the central chamber are registered as well, despite the shielding by masks – as shown by the green dots in the same plot.

The data from the performed simulations shows strong hints that the masking becomes less efficient once a beam with significant tails passes the interaction region.

While the masks in that case may still protect the detector from photons originating in upstream dipole magnets, they can not shield it from photons generated in the final-focus magnets. Moreover, photons from the quadrupoles QC3L.2 and QT1L.2, located about 90 m and 50 m upstream, reach the masks once horizontal tails are considered (refer to Fig. 7.29 of Section 7.5).

These observations support the concept of using collimators further upstream to

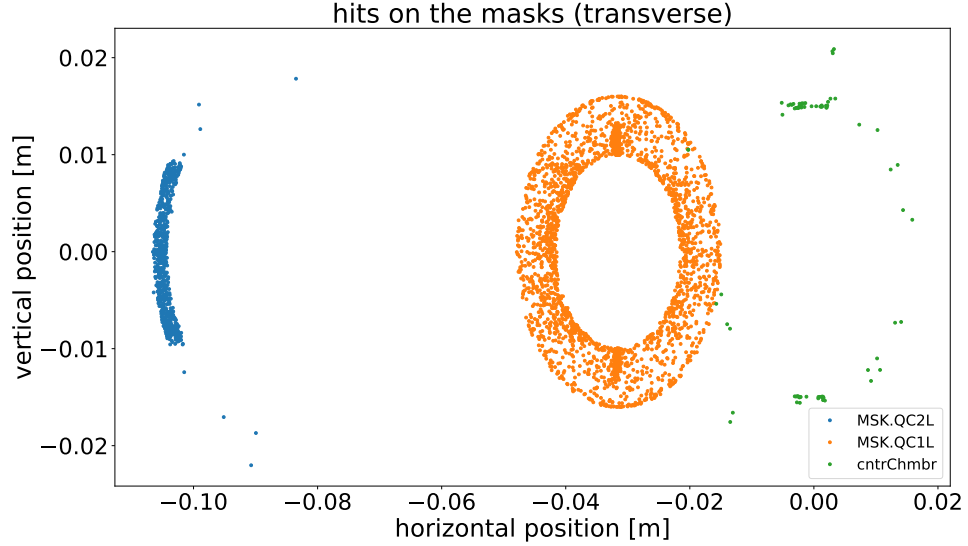


Figure 7.54: Direct hits on the synchrotron radiation masks in a scenario considering significant vertical tails. The amount of photons striking MSK.QC1L is much higher in this case, affecting the mask in the entire azimuth. Photons directly striking the central chamber are registered as well – which was not observed in the default case.

generally relax the conditions within the central interaction region.

In a next step, the energy profile of synchrotron radiation photons striking the masks will be studied, before determining which fraction scatters through the mask.

Energy Deposit & Scattering

Photons striking the masks reveal an energy profile similar to Fig. 7.25 or 7.26 of Section 7.5 – a distribution based on the default case is shown in Fig. 7.55 (a). Most of the photons will lose all energy when being absorbed, leaving a remaining fraction with energies between 100 keV to 200 keV.

With horizontal tails, the energy at MSK.QC1L is significantly higher than for the default case, as shown in Fig. 7.55 (b).

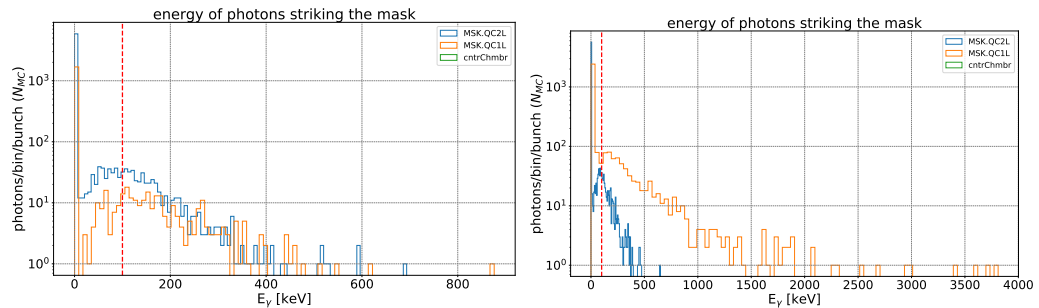


Figure 7.55: Energy distribution of photons striking the masks. (a) default case considering a Gaussian bunch. A majority of events is located in the low energy region between 0 keV to 10 keV. The remaining part is distributed between energies of 100 keV to 200 keV. (b) considering horizontal tails, the energy of photons striking MSK.QC1L is much higher than in the default case.

A detailed Monte-Carlo simulation, as done in the context of this study, would have to consume considerable resources to simulate the full bunch population.

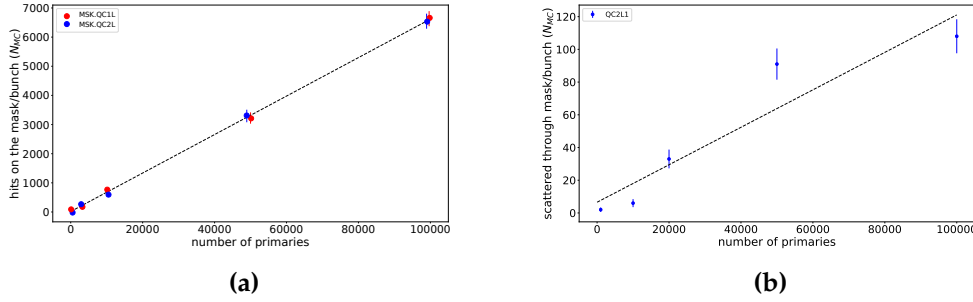


Figure 7.56: Number of hits on the masks as function of the bunch population in the *Monte-Carlo* simulation, N_{MC} . A linear extrapolation is possible.

A linear extrapolation of the number of photons in the following for a full bunch population is using a factor N_p/N_{MC} . N_p is the bunch population of 2.3×10^{11} particles at FCC-ee $t\bar{t}$ and N_{MC} the number of particles in the bunch used for the Monte-Carlo simulation that has been slightly increased to 10^5 . A plot showing the number of hits on the mask as function of N_{MC} is depicted in Fig. 7.56. At both masks, this trend is linear – as expected.

Without synchrotron radiation masks, the simulation predicts a rate of about 1.28×10^{10} photons/bunch (assuming an uncertainty of \sqrt{N}) striking the central chamber with an average energy of (121.30 ± 0.75) keV. This is based on the default scenario with a Gaussian bunch. With the masks inserted, the rate drops to 0. Table 7.9 summarizes the prediction of photon rates at the masks, together with the fraction that would scatter through and the respective mean energies $\langle \epsilon \rangle$. The upper part refers to the default case, the central part to horizontal and the lower part to vertical tails.

Table 7.9: Estimations for photon rates at the masks and fraction of events that scatter through. The numbers are given for one bunch crossing (BX). Upper part: default scenario, central part: horizontal tails and lower part: vertical tails. The uncertainty of the number of photons/bunch is assumed to be \sqrt{N} and not shown in the table. A relatively high uncertainty on the mean energy of scattered photons is caused by low statistics.

Mask	total/BX [10^{10}]	$\langle \epsilon \rangle$ [keV]	scat./BX [10^8]	fraction [%]	$\langle \epsilon \rangle$ [keV]
MSK.QC2L	1.54	15.77 ± 0.19	3.45	2.4	119.94 ± 11.54
MSK.QC1L	0.42	26.44 ± 0.59	1.15	2.7	126.04 ± 12.22
MSK.QC2L	1.49	15.56 ± 0.19	3.22	2.2	121.5 ± 116.9
MSK.QC1L	0.98	103.07 ± 1.81	2.99	3.1	365.11 ± 35.13
MSK.QC2L	1.49	17.75 ± 0.22	4.11	2.8	115.34 ± 11.10
MSK.QC1L	0.81	182.85 ± 1.21			

Events which scatter through the masks reveal fairly high mean energies of more than 100 keV. The average photon energy at the inner mask is higher when tails are considered, which also applies to the amount of scattered photons. An energy profile of events for the default scenario is presented in Fig. 7.58. The fraction of events which scatter through the mask is not far from 2.5 %, which is in accordance with earlier simulations [66].

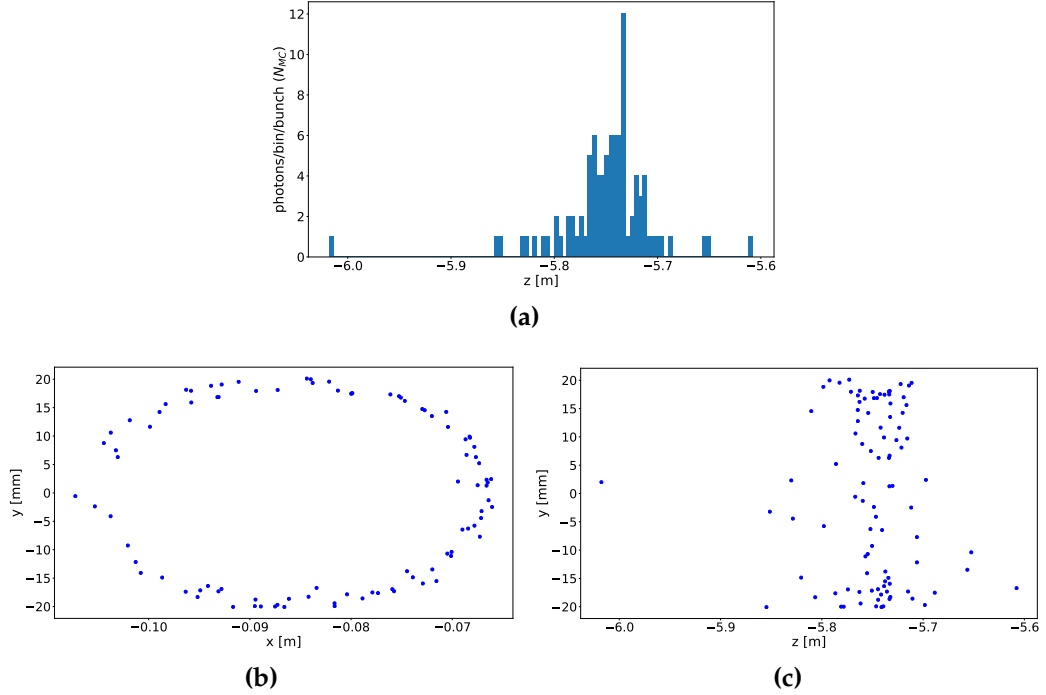


Figure 7.57: Spatial details about photon scattering off the outer mask, MSK.QC2L. (a) longitudinal distribution of position where scattered photons strike the beam-pipe wall again. (b) and (c) transverse and longitudinal plots of these locations. Scattered photons mostly stay in close vicinity of the mask.

Figure 7.57 (a) displays where the photons hit the beam-pipe wall after scattering off the mask MSK.QC2L. The data is taken from the horizontal tails sample and considers only events which scatter back into the beam-pipe.

Figure 7.57 (b) and (c) help to understand that these photons scatter mostly from one point on the mask to another. It is not possible to observe massive scattering in either forward or backward direction, to locations upstream or downstream of MSK.QC2L. However, the sample lacks statistics – simulations with a higher bunch population (N_{MC}) could allow a stronger statement on the amount of forward and backward scattering.

In order to estimate an average of the synchrotron radiation power which would arrive at the masks, Eq. (7.9) will be used, with a bunch spacing τ_{BSP} of 3396 ns at FCC-ee $t\bar{t}$.

$$\langle P_{msk} \rangle = \langle \epsilon \rangle \frac{N_p}{N_{MC}} \frac{e}{\tau_{BSP}} \quad (7.9)$$

The result of this estimate is summarized in Table 7.10. Again, the upper part considers the default case, the middle part horizontal and the lower part vertical tails.

While the estimated synchrotron radiation power arriving at the outer mask remains almost constant, it increases by a factor 7 at the inner mask with horizontal tails. This change can be related to the much higher mean photon energy $\langle \epsilon \rangle$ at MSK.QC1L. An even higher increase of almost a factor 12 is observed with vertical tails.

About 10 W/mm can usually be handled by a copper surface, with special types

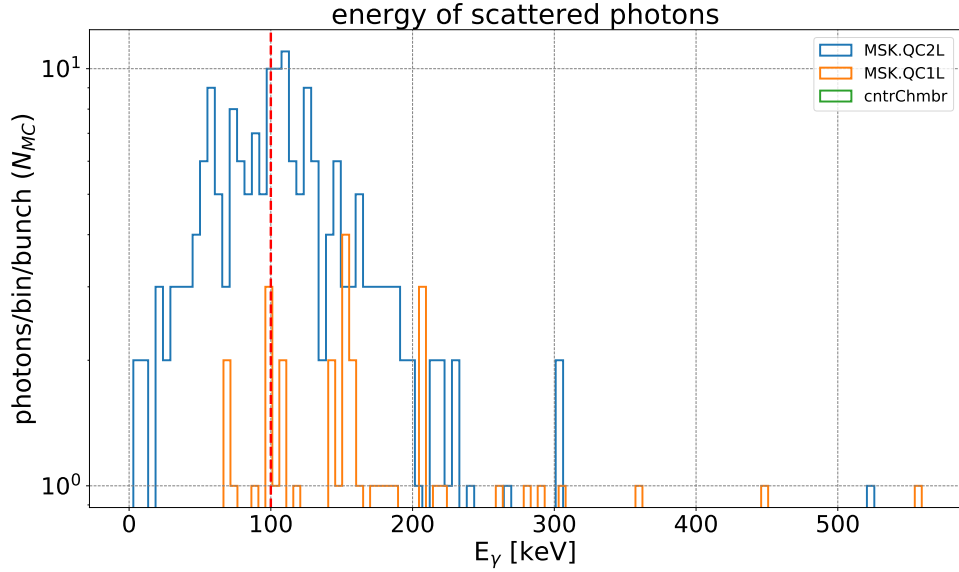


Figure 7.58: Energy distribution of photons scattering through the masks. No hits on the central chamber are registered in this sample. The distribution has a mean around 123 keV. A red dashed line indicates 100 keV photon energy.

Table 7.10: Estimation of the synchrotron radiation power per bunch, arriving at the masks.

Scenario	Mask	$\langle \epsilon \rangle$ [keV]	P_{SR} [W]
default	MSK.QC2L	15.77 ± 0.19	11.42 ± 0.28
	MSK.QC1L	26.44 ± 0.59	5.67 ± 0.26
horizontal tails	MSK.QC2L	15.56 ± 0.19	10.89 ± 0.27
	MSK.QC1L	103.07 ± 1.81	65.49 ± 2.21
vertical tails	MSK.QC2L	15.86 ± 0.22	11.86 ± 0.29
	MSK.QC1L	182.85 ± 1.21	65.49 ± 2.67

of copper even up to 20 W/mm [67]. Which means that the results summarized in Table 7.10 at MSK.QC2L seem to be generally in a manageable range – based on the default scenario. If tails are considered, the power input can increase to much higher values, as indicated by the estimates at MSK.QC1L.

Intermediate Conclusion – Central IR Protection

Simulations in the context of this study showed that fixed synchrotron radiation masks can provide substantial shielding of the detector area. However, the extent of that protection is very sensitive to the initial conditions of the beam. Experience at LEP showed that background conditions in the MDI depend strongly on those conditions.

The simulations presented here primarily serve to understand the trends – how does the background evolve, once the beam is off axis, does exhibit tails, etc.?

It was shown that with a Gaussian bunch on axis, no photons are registered to strike the central chamber. The energy profile of photons impacting on the masks is similar to those in the upstream section and the rate of photons scattering through the masks is with 2.5 % comparable to earlier simulations, therefore not

considered to be an issue for the detector. Hence, with the ideal scenario, the masking seems efficient enough in a first approximation.

However, if strong tails are considered, the masking quickly appears less efficient. Evidence was found, that the energy profile as well as the scattering rate change in a scenario with many particles at large amplitudes. This observation applies especially to the inner mask, which is located at a distance of only 2.1 m from the interaction point.

Assuming masks from special copper material, they could handle power inputs on the order 10 W/mm to 20 W/mm. Simulations in the context of this study indicate that the synchrotron radiation power can easily exceed this limit with tails present.

These scenarios do not even consider X-ray reflection. With this effect, protection by the masks can quickly become more and more insufficient, as the masks can not be moved closer to the beam to enhance the shadowing downstream. Studies at LEP proofed how useful an extended collimation system has been in reducing the backgrounds [68]. Collimators at about 200 m and 120 m (so called *far-out collimators*) have been used to mitigate effects of X-ray reflections and bend radiation from far upstream in the arc.

In the last part of this analysis, collimators will therefore be added to the MDI geometry. Based on the three (by now well known) scenarios, the influence of single collimators on the background conditions will be studied.

7.9 Mitigation Through Collimators

Collimators consist of one or two movable absorber blocks, called jaws – the principle geometry has been depicted earlier in Section 7.1. Unlike the synchrotron radiation masks, collimators offer more flexibility, as the jaws allow to move the absorber either closer to the beam or further away. Collimators can be used in different scenarios, such as reducing beam-halo or mitigating synchrotron radiation.

It is important to find suitable settings for these collimators, preferably at positions where the beam tends to be small. As a consequence, the collimator jaw could then move closer to the beam core. An illustration is provided in Fig. 7.59 – the closer a jaw can move to the core (the smaller $N\sigma$), the more synchrotron radiation photons will be stopped, as the jaw reaches further into the synchrotron radiation bulk. This results in an enhancement of the shadowed region downstream and a reduction in the photon rate.

But at the same time the jaws should not be positioned too close to the beam. At FCC-ee, depending on the location and the beam profile (core and presence of halo), $N\sigma$ can range on average between 5σ and 20σ , while dynamic aperture requirements demand to stay off distances of $15\sigma_x$ and less ($60\sigma_y$ in the vertical plane).

Once the jaw cuts into the halo or the beam core itself, particles of the beam will strike the absorber material. Since the beams at FCC-ee have high energies, a considerable amount of interaction products can be expected. In such a case, collimators will only add to the background instead of minimizing it. Direct

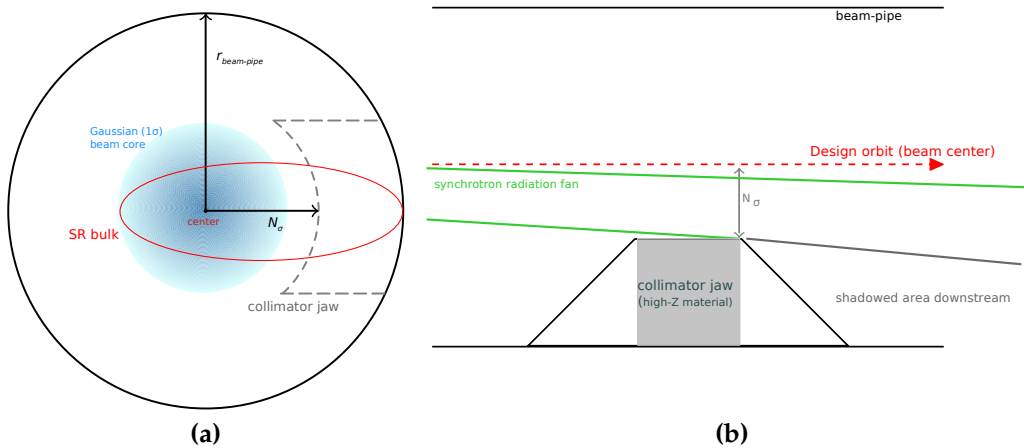


Figure 7.59: (a) transverse sketch of settings for one collimator jaw. Shown is the 1σ beam core and the distance between core and jaw expressed in $N\sigma$. The physical aperture is indicated by the outer black circle. The red ellipse represents the synchrotron radiation bulk, emitted by particles in the beam. (b) longitudinal sketch of a collimator jaw which intercepts a certain fraction of the synchrotron radiation fan. Depending on the distance $N\sigma$, the shadowed area downstream becomes either longer or shorter.

damage of the collimator by the beam is also possible, while additionally this would lead to particle loss, lifetime reduction or impedance enhancement. Another point to consider is the longitudinal distance between collimators and central interaction region. This distance should be as long as possible to keep scattered photons and possibly produced interaction products far away from the experimental region (the detector).

In this final section of the presented analysis, a discussion of possible locations for collimators upstream of the central FCC-ee interaction region will be done. After integrating the collimators into the geometry, the three scenarios which have been discussed earlier (default, aka Gaussian bunch, horizontal and vertical tails) are used to study the effect of those collimators.

Discussion of Locations and Settings

The current MDI design of FCC-ee has adopted a few principles which have been introduced or learned during LEP operation. To define an initial proposal for a collimation scheme at FCC-ee, a short overview of the LEP interaction region layout – as displayed in Fig. 7.60 is given.

Horizontal collimators at LEP have been installed far out, already at more than 200 m upstream, to intercept the full bend radiation from the very arc. The term *full bend radiation* refers to the critical energy ϵ_c of arc dipole magnets of on average 724 keV (at 105 GeV beam energy), higher than those of the last upstream dipole magnets having only 10 % of the arc dipole strength (*weak bend radiation*) [9].

Another horizontal collimator at about 120 m upstream protects the interaction region from weak bend radiation, generated in the last bending magnets.

Other horizontal and also vertical collimators are installed closer to the interaction point, for example near collimators at ± 15 m around the central detector chamber [69].

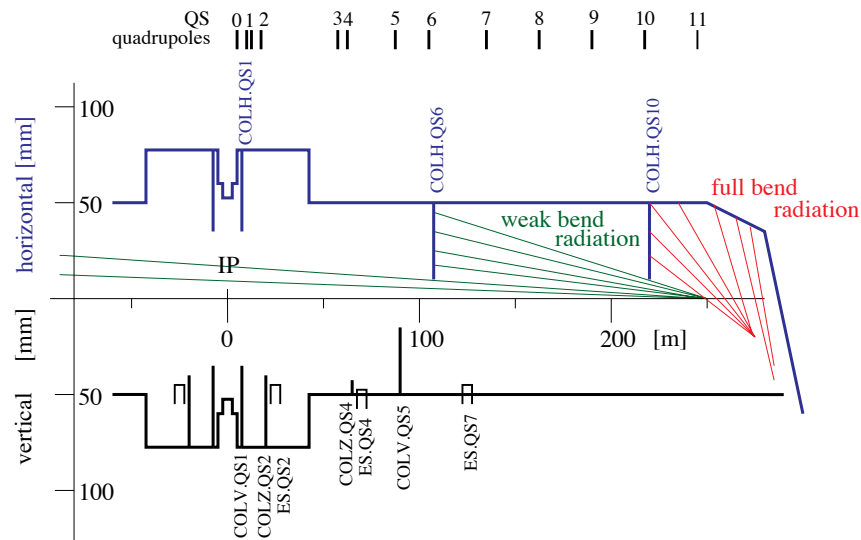


Figure 7.60: Example sketch of the *LEP* interaction region, showing how radiation is intercepted by horizontal and vertical collimators [9]. The plot schematically shows the straight section on one side of the *Interaction Point (IP)* and indicates the physical apertures in horizontal and vertical plane in mm. It also indicates two types of radiation: full bend radiation from the arc dipoles and weak bend radiation from the last upstream dipoles with reduced strength (10 % of the arc dipoles). As can be seen, horizontal collimators far out at 120 m and more than 200 m are used to intercept the majority of horizontal radiation fans. Especially the full bend radiation is intercepted more than 200 m upstream.

While studying the *FCC-ee MDI*, three different groups of upstream bending magnets have been introduced in Section 7.5. Their impact in terms of synchrotron radiation on the central interaction region was discussed therein.

Based on the initial scenario, Group 1 was found to be most relevant, especially the last upstream bend, *BWL . 2*. Both magnets of this group are depicted in Fig. 7.61 and Fig. 7.62, indicating their radiation fans. Adopting the terminology from Fig. 7.60, synchrotron radiation from these two dipole magnets – *BC1L . 2* and *BWL . 2* – could be referred to as *weak bend radiation*.

The second to last dipole, *BC1L . 2*, generates a radiation fan which directly affects only a section between 250 m to 120 m upstream, which can be confirmed by data from simulation samples, as shown in Section 7.5. Note again, that this does not yet take into account the possibility of X-Ray reflection. Considering that effect, photons from this magnet indeed may reach the interaction region after a single reflection on the beam-pipe wall, as indicated by dashed-dotted lines in Fig. 7.61. Installing collimators downstream of *BC1L . 2* would, however, be difficult due to limited space in this area. Referring to the default scenario, collimators as far as 200 m upstream might not be required as direct radiation from *BC1L . 2* does not reach the central interaction region.

Figure 7.62 shows how photons from *BWL . 2* would reach the central interaction region directly. The discussion of the default scenario (refer to Section 7.5) showed that *BWL . 2* is – to first order – the most relevant dipole, considering ideal conditions: it affects the entire straight section upstream of the interaction point and the central interaction region.

Collimators in the straight section, downstream of *BWL . 2*, can be expected to prove useful in mitigating radiation far upstream, before reaching the central interaction

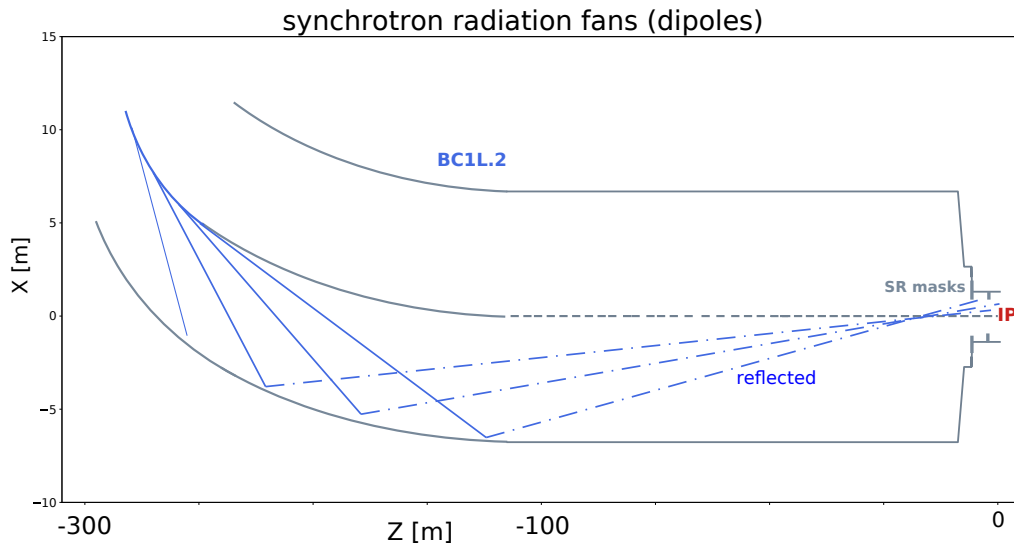


Figure 7.61: Radiation fans generated by the second to last upstream bend, BC1L.2. As indicated with straight blue lines, radiation from this dipole affects mainly an upstream section between 250 m to 120 m. An observation also confirmed during the earlier discussion of the initial scenarios. The dashed-dotted lines indicate possible X-ray reflected photons, which can reach the central interaction region after single reflection off the beam-pipe wall.

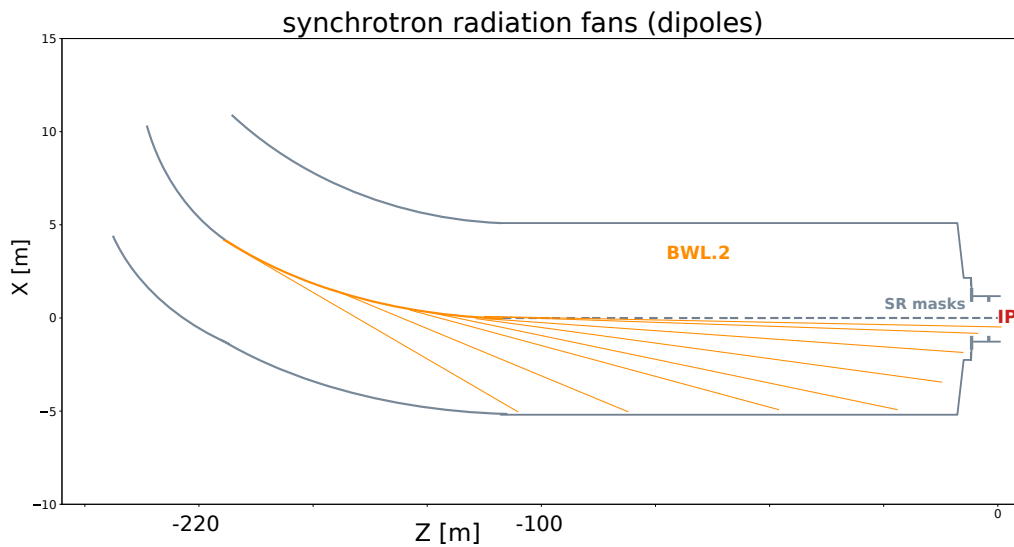


Figure 7.62: Radiation fans from the last upstream dipole, BWL.2 indicated with straight lines. Photons from this magnet are very likely to reach the Interaction Point (IP) directly and affect the entire straight section from 100 m to 0 m upstream.

region.

Furthermore, the section downstream of BWL.2 provides sufficient space, being free of other magnets with the exception of two quadrupoles, QC3L.2 around 93 m and QT1L.2 at 50 m. Collimators could therefore be inserted within these 100 m at different locations.

Figure 7.63 shows a proposal how this space could be used by three horizontal collimators to intercept most of the radiation further upstream, thereby relaxing the conditions in the central interaction region. To further assess possible collimator locations, beam sizes upstream of the interaction point will be reviewed.

The horizontal beam size can be calculated by taking into account amplitude

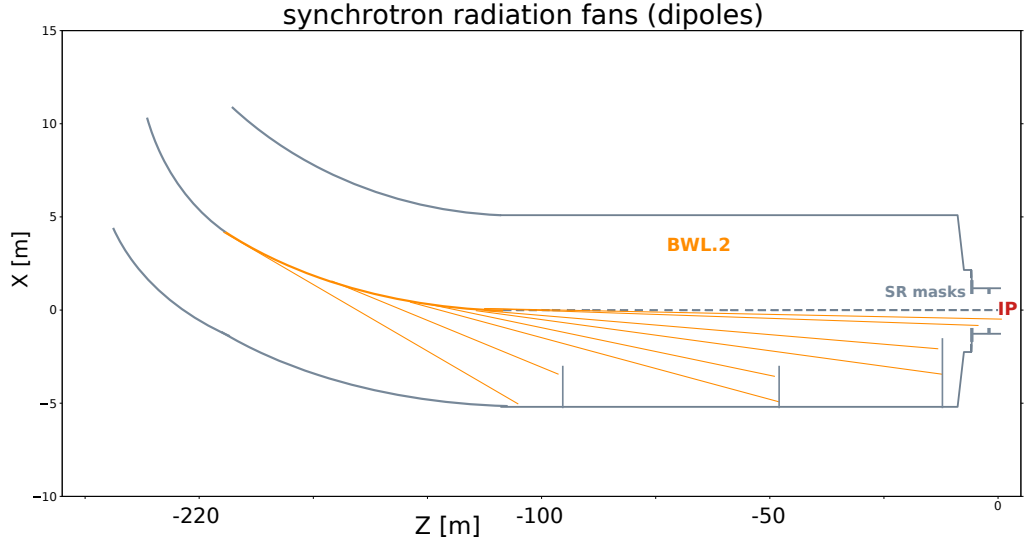


Figure 7.63: A possible scenario of having three horizontal collimators intercepting the radiation fans coming from the last upstream bend. As an initial proposal, collimators are inserted around 90 m, 50 m and 10 m upstream. Shown are only the jaws on the outward side (towards negative x) since this is the most affected region.

function $\beta(s)$, nominal emittance ϵ_{nom} , dispersion D and momentum spread σ_δ as in Eq. (7.10) [36]. Note, that the beam amplitude as well as dispersion are functions of the actual particle position s .

$$\sigma_x = \sqrt{\beta_x(s)\epsilon_{x,\text{nom}} + (D_x(s)\delta_p)^2} \quad (7.10)$$

For the vertical plane, it is sufficient to assume (to first order) that the dispersion is negligible, such that Eq. (7.10) reduces to Eq. (7.11).

$$\sigma_y = \sqrt{\beta_y(s)\epsilon_{y,\text{nom}}} \quad (7.11)$$

Figure 7.64 shows the horizontal beam size within the last 100 m upstream, as well as the location of the three collimators and the two upstream synchrotron radiation masks.

The light green curve represents 1σ envelope, while brown dashed and blue dotted lines show $10\sigma_x$ and $20\sigma_x$ envelopes.

It is not possible to register significant changes in the beam size while it propagates through the straight section downstream of BWL.2 – Table 7.11 gives a quantitative overview. The data shows hints that the horizontal beam size tends to decrease between QT1L.2 and PQC2LE.2.

All three collimators in the 3D model will feature a circular aperture in order to facilitate the geometry integrity in the GDML. With flat beams, as expected at FCC-ee $t\bar{t}$, a circular aperture should be a sufficiently accurate assumption for a conceptual study – the majority of synchrotron radiation photons is emitted in a horizontal bulk as depicted in Fig. 7.59. The analysis at the masks (compare Fig. 7.52 of Section 7.8) confirms this assumption.

Dynamic Aperture Requirement

To fully understand which range of settings is available, the dynamic aperture requirements need to be taken into account. At FCC-ee, *top-up injection* is foreseen

7.9. MITIGATION THROUGH COLLIMATORS

Table 7.11: Possible collimator positions upstream of the interaction point. Names refer to elements after which a collimator is supposed to be installed. Different estimates indicate how close collimator jaws can be set to the beam. Red colored entries represent settings which affect the dynamic aperture.

Name	β_x [m]	σ_x [μm]	$10\sigma_x$ [mm]	$15\sigma_x$ [mm]	$20\sigma_x$ [mm]
BWL.2	333.36	697.66	6.98	10.46	13.95
QC3L.2	303.68	665.87	6.66	9.99	13.32
QT1L.2	329.07	693.14	6.93	10.40	13.86
PQC2LE.2	237.60	588.99	5.89	8.83	11.78

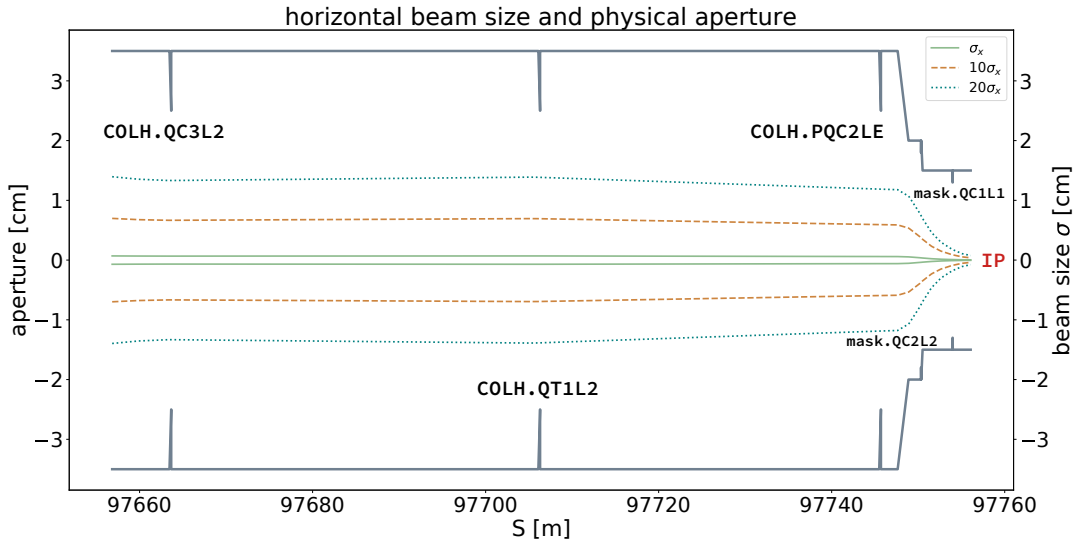


Figure 7.64: Top view on the beam pipe (solid grey line) for the last 100 m upstream, with a generic radius of 35 mm until the aperture limits towards the **Interaction Point (IP)** (right end of the plot). The horizontal beam size is shown with a 1σ envelope, together with the $10\sigma_x$ (brown dashed) and $20\sigma_x$ (blue dotted) envelopes. Vertical solid lines indicate possible collimator jaws. The horizontal beam envelope is not subject to significant changes over the last 100 m, apart from the final focusing when it approaches the interaction point. However, it tends to decrease downstream of QT1L.2.

which – together with sufficient energy acceptance – requires a minimum dynamic aperture. Dynamic aperture studies have been done at each of the energy settings to determine minimum required aperture and are presented elsewhere [2, 19]. The result for FCC-ee $t\bar{t}$ is shown in Fig. 7.65. With a colour scale the plot visualizes how many turns a particle survives as function of horizontal and vertical position. White corresponds to 45 or more turns, while dark blue means that a particle is lost after a maximum of 5 turns.

Collimators should not cut in the dynamic aperture, which limits the closure to $\geq 15\sigma_x$ in the horizontal and $\geq 60\sigma_y$ in the vertical plane, according to the plot in Fig. 7.65. A few settings are collected in Table 7.11 – those of which too small highlighted in red.

Assuming a circular aperture, the restriction in the vertical plane is less stringent: $60\sigma_y$ correspond to 6.40 mm at QC3L.2 and 5.24 mm at PQC2LE.2 – close to the $10\sigma_x$ envelope and therefore already below the dynamic aperture requirement. Therefore the limitation is mainly in the horizontal plane.

In summary, the following simulations will consider a circular collimator aperture,

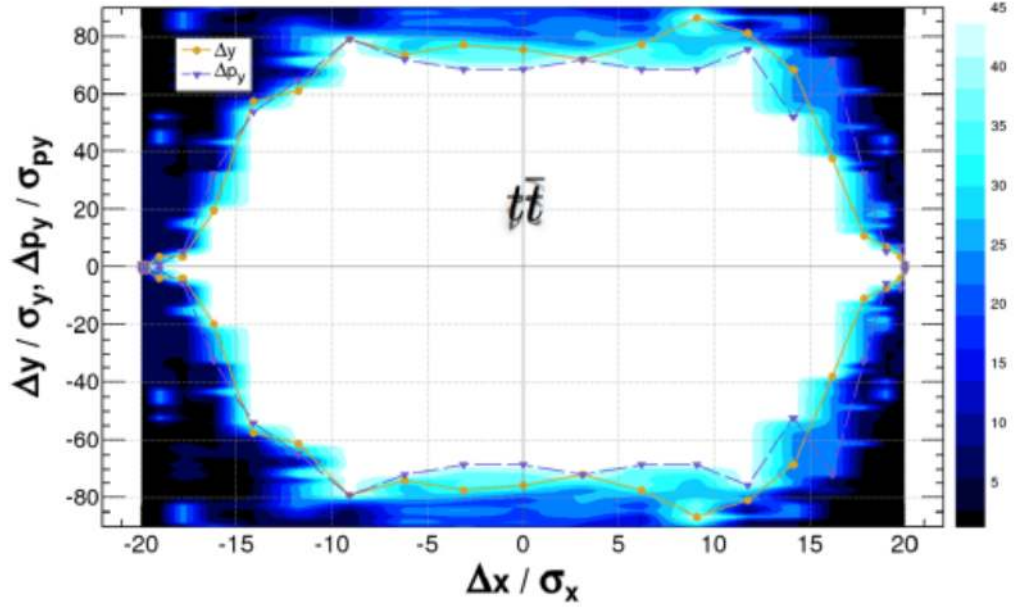


Figure 7.65: Resulting dynamic aperture for the highest beam energy at FCC-ee ($t\bar{t}$). The number of turns a particle survives, depending on its horizontal and vertical position, is represented by the colour scale. White corresponds to 45 turns or more and dark blue to 5 turns or less. The plot indicates a horizontal aperture requirement for top-up injection of $15\sigma_x$ and $60\sigma_y$ in the vertical plane [2].

starting with an opening of more than $20\sigma_x$. The opening will be subsequently reduced to study the effect on the photon rate at certain locations – as explained in more detail below.

Changes in the Geometry

In the context of the following simulations, three initial collimators are considered as baseline setup: COLH.QC3L2, COLH.QT1L2 and COLH.PQC2LE. All three elements have been introduced as new default in the geometry, depicted in Fig. 7.66.

The nomenclature represents the collimator type – in this case horizontal (COLH), and the element located next to the collimator, for example QC3L.2. These collimators can be completely opened, using an aperture of 35 mm for COLH.QC3L2 and COLH.QT1L, while the maximum opening for COLH.PQC2LE corresponds to the slightly reduced aperture of about 21.13 mm, due to the beam-pipe tapering introduced in Section 7.8. Once completely opened, the resulting photon background shows no difference compared to the initial scenarios, as in a real machine where collimators can be completely opened.



Figure 7.66: Top view on the updated geometry in Root display over the last 100 m upstream. Three collimators inserted after QC3L.2, QT1L and right at the entrance to the interaction region. The tapered beam-pipe downstream of QT1L is visible as well, indicating that COLH.PQC2LE needs a smaller aperture when completely opened than the other two collimators, which defaults to 35 mm.

The following simulations will test the effects of single collimators on the photon backgrounds, while the other two collimators are left fully open. These studies do not yet consider a combination of several collimators.

Background Rates and Collimation Efficiency Plots

The previous subsection introduced three possible collimator locations and discussed briefly the available settings in terms of jaw position. Further, restrictions through dynamic aperture requirements were mentioned. In order to prepare the collimation study, a brief introduction to the concept of *collimation efficiency* is given. This efficiency will be used afterwards to evaluate the performance of a collimator. A typical *collimation efficiency plot* is depicted in Fig. 7.67.

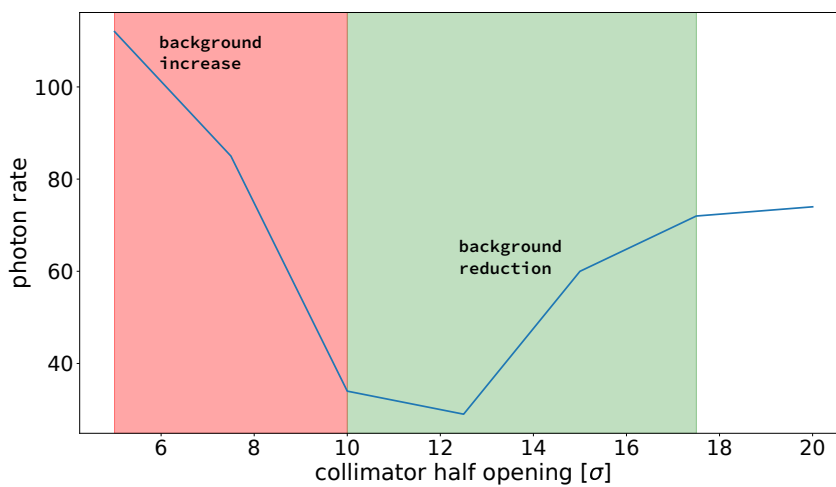


Figure 7.67: Typical shape of a collimation efficiency plot, highlighting in green where the collimator settings lead to a reduction in backgrounds. The red area shows a steep increase in background once the collimator jaw moves too close to the beam. In that case, high energetic particles from the beam start to directly interact with the absorber, which causes a shower of additional particles.

The photon rate at a certain position is monitored as function of collimator *half opening*, which is expressed in terms of $N\sigma$ relative to the center of the vacuum chamber – as demonstrated in Fig. 7.59 (a).

Once the jaw moves towards the beam, more and more photons will be blocked, corresponding to a range of settings where the background is reduced – shown as green area in Fig. 7.67. Within some margin, the background rate remains in a rather constant minimum, before steeply increasing again (represented as red area in the plot). Such an enhancement of backgrounds is observable once the collimator jaw moves too close to the beam, cutting into the halo or even the core of the beam itself.

Particles in the beam thus directly interact with the absorber material, thereby generating more and more secondaries – which eventually results in an increase of backgrounds. This range of settings must therefore be avoided, as it turns a collimator itself into a significant source of background instead of leading to a reduction.

The following discusses collimation efficiency plots based on the Monte Carlo data from MDISim. As regions of interest where chosen:

- the outer upstream synchrotron radiation mask, MSK.QC2L
- the inner upstream synchrotron radiation mask, MSK.QC1L
- the central detector chamber ± 1 m around the interaction point – shown as green area in Fig. 7.68

While discussing the effect of synchrotron radiation masks, it was already pointed out that adding protection further upstream can help to relax the conditions within the central interaction region. Which is why the masks have been chosen as points for measuring the collimation efficiency. The central detector chamber is added for obvious reasons as it is the most sensitive location.

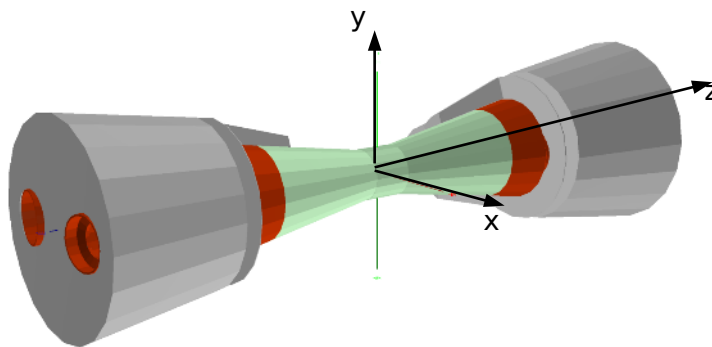


Figure 7.68: The central chamber is shown in green, stretching about ± 1 m around the interaction point. It is used as additional reference to register background rates by synchrotron radiation photons. Note that transverse dimensions of the model have been scaled by a factor of 10, solely to improve visibility. The luminosity counter (LumiCal) is not shown in this picture. Black arrows indicate the Euclidean reference system in Geant4.

Collimation Efficiency – Gaussian Bunch

The first case to be studied is based on the Gaussian bunch with $N_{MC} = 10^4$ primaries in the beam (default scenario). Starting with the collimator farthest from the interaction point, the discussion will cover them subsequently in the following paragraphs.

Before discussing efficiency plots for each collimator, the effect of collimators on the distribution of hits on the beam-pipe wall is briefly highlighted as an introductory example of the effect.

Figure 7.69 compares the generic distribution of direct hits on the beam-pipe wall within 300 m upstream and 100 m downstream without (a) and with the far-out collimator COLH.QC3L2 inserted (b). The plot in (b) demonstrates how the shadowed region downstream of the collimator extends when the collimator aperture (opening) is reduced.

A second set of plots in Fig. 7.70 demonstrates the effect of the near collimator COLH.PQC2LE. The distribution of hits is shown within -20 m to 10 m around the interaction point for three different closures. **20 mm half opening** shows basically

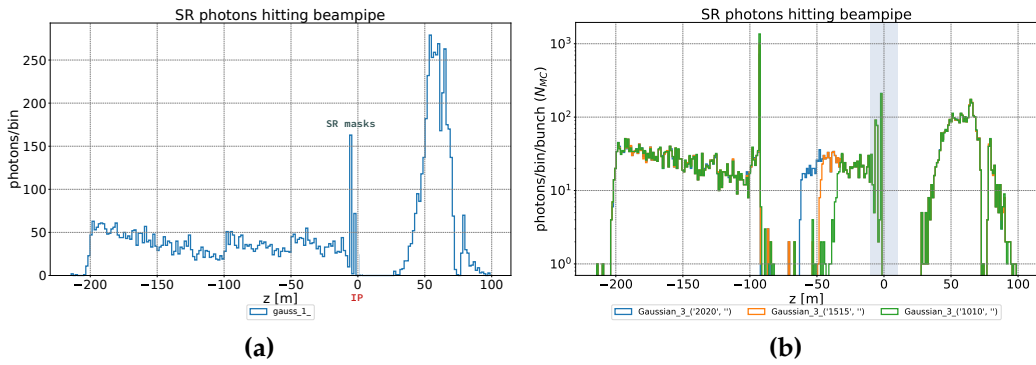


Figure 7.69: Distribution of hits on the inner beam-pipe wall from a Gaussian bunch of 10^4 primaries. (a) baseline scenario with all collimators completely open. (b) Example of different collimator settings of COLH.QC3L2 at 90 m upstream. Shown are half openings of 20 mm, 15 mm and 10 mm, as indicated in the legend. Note a semi-logarithmic scale in (b) to enhance the details.

no reduction, while **10 mm half opening** reduces the amount of photons noticeably at both masks.

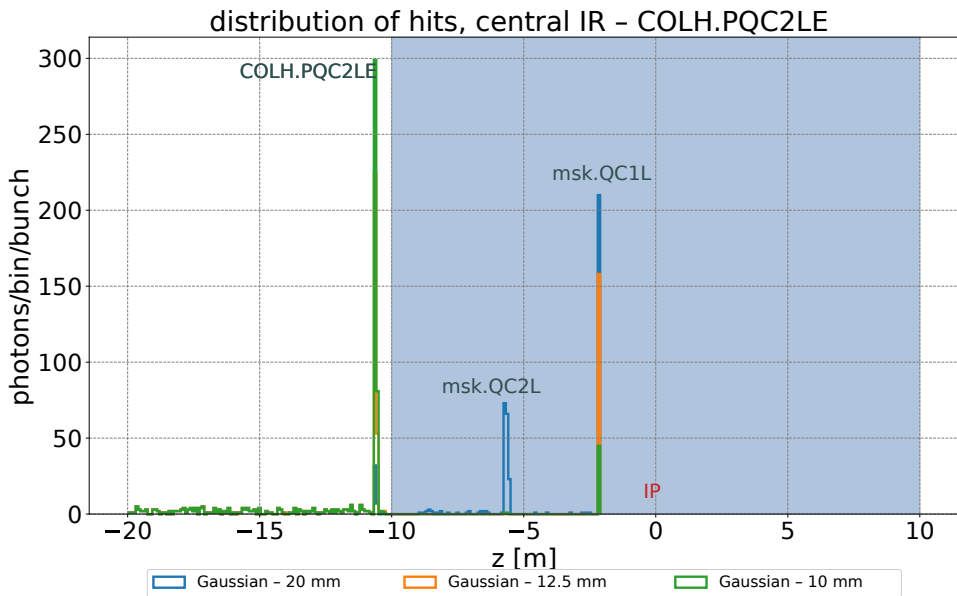


Figure 7.70: Comparing different closures of the close collimator, COLH.PQC2LE with settings between 15 mm to 10 mm. The plot proves, how a **12.5 mm half opening** already provides effective shielding of the interaction region, while with **10 mm half opening**, hits are further reduced.

This short set of examples is concluded with a demonstration of background enhancement in Fig. 7.71. The plot presents data with the intermediate collimator, COLH.QT1L2: using a half opening of 1 mm (cutting well into the $3\sigma_x$ beam core), the background in the central interaction region is clearly enhanced. The arrival time of photons changes accordingly, which is shown in Fig. 7.71 (b) and (c): while the arrival time is well above 150 ns with a half opening of 17.5 mm, it reduces to below 50 ns with a smaller aperture of only 7.5 mm – photons originate from locations much closer to the interaction point. This can be considered as a strong hint for additional interactions resulting from distortions of the beam by the collimator jaw. This means that the collimator setting reached the red area of

Fig. 7.67.

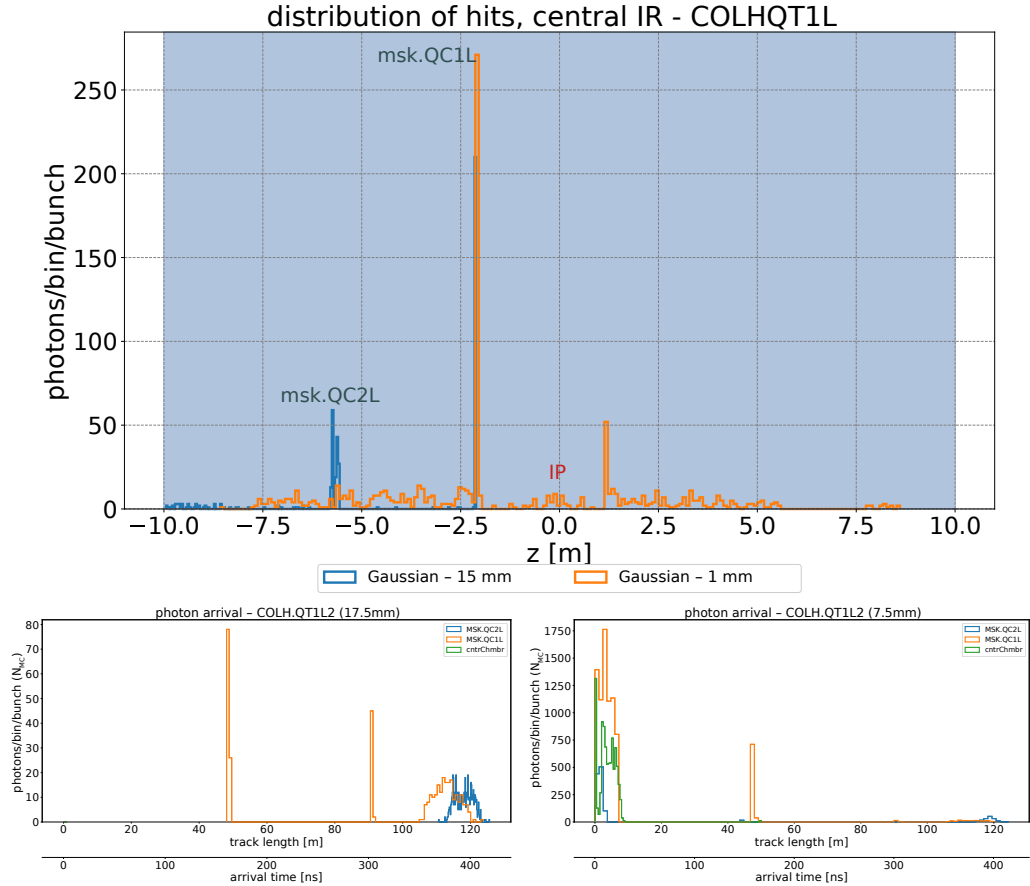


Figure 7.71: The interaction region in case of two half openings of COLH. QT1L2. While the 15 mm setting does not show an increase in the background, the 1 mm setting significantly enhances the photon rate at the central chamber ($z \pm 1$ m around the **Interaction Point (IP)**). (b) and (c) show the photon arrival times for hits at the synchrotron radiation masks and the central chamber. From an initial ≥ 150 ns with 17.5 mm opening, photons with much less arrival time (≤ 50 ns) reach the locations for a sample with tighter settings of only ≤ 7.5 mm.

Far-out Collimator – QC3L.2. The set of collimation efficiency plots starts with the collimator farthest away from the interaction region, right at the exit of QC3L. 2 (see Fig. 7.64) – around 90 m upstream of the interaction point.

The data in Fig. 7.72 shows that this collimator needs to be closed down to apertures below 5 mm in order to significantly reduce the photon rate at MSK.QC2L. A setting which would correspond to $7.5 \sigma_x$.

It is not possible to register any suppression of the rate at the inner mask MSK.QC1L, only an increase in the photon rate for a closure below $5 \sigma_x$. For this scenario, no direct hits in the central chamber are registered.

As shown by the vertical blue line in Fig. 7.72, COLH.QC3L2 would have to clearly cut far into the dynamic aperture before showing an effect in this scenario.

Intermediate Collimator – QT1L.2. A second possible collimator location is right at the exit of the quadrupole QT1L. 2, about 50 m upstream of the interaction point. Figure 7.73 depicts the corresponding efficiency plot.

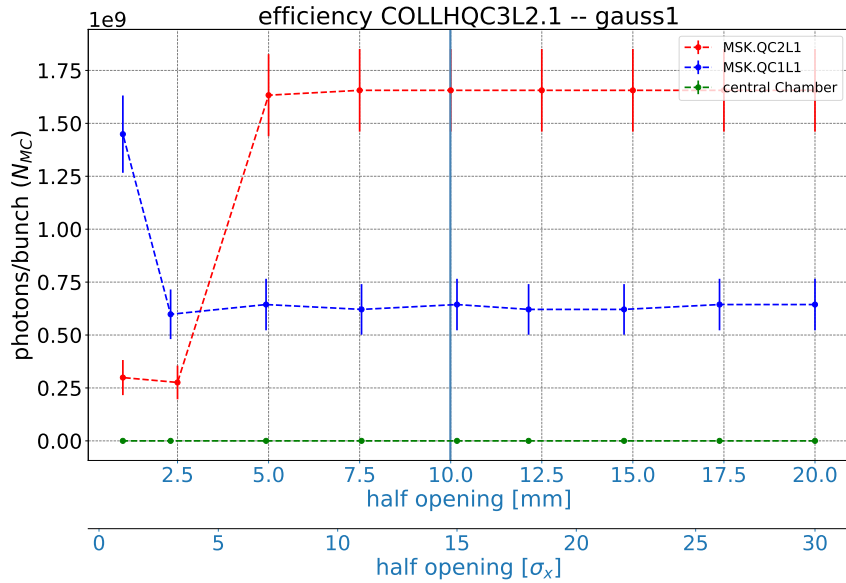


Figure 7.72: Predicted photon rate at both synchrotron masks. A collimator around 100 m upstream can reduce the photon rate at MSK.QC2L with a half opening of less than 5 mm. No reduction in background is observed at the inner mask MSK.QC1L. No direct hits in the central chamber are registered. A half opening of 35 mm would correspond to a fully opened collimator. The vertical line denotes $15 \sigma_x$ (dynamic aperture requirement).

Half openings of less than 12.5 mm reduce the photon rate at the outer mask significantly. With an aperture of below 10 mm, the rate at the inner mask is reduced as well. These settings correspond to $18 \sigma_x$ and $14 \sigma_x$, respectively. For the outer mask, COLH.QT1L2 offers a larger range of settings: the minimum is more pronounced than for the inner mask. An increase of direct hits at the central chamber is observed only with half openings of less than $5 \sigma_x$, correlated with rising backgrounds at the inner mask.

With this collimator, it is possible to reduce the photon rate at the outer mask while staying out of the dynamic aperture. However, the minimum at the outer mask is only reached with closures below $15 \sigma_x$. The same applies for a reduction of the photon rate at the inner mask – observable only well below the dynamic aperture range.

Near Collimator – PQC2LE. The last collimator for this first scenario is located about 10 m upstream of the interaction point. Figure 7.74 presents the efficiency of this collimator, showing how the expected photon rate drops already from 20 mm (outer mask) and from about 15 mm (inner mask). These settings correspond to $34 \sigma_x$ and $25 \sigma_x$, offering a large range of possible settings for this collimator. The rate of direct hits in the central chamber increases if the collimator is closed down to less than $10 \sigma_x$ and below, simultaneously with an increase at the inner mask.

The data allows to conclude that – given a Gaussian beam on axis without tails – the near collimator COLH.PQC2LE is most effective in reducing the photon rate at the synchrotron radiation masks.

While staying outside the dynamic aperture range of $15 \sigma_x$, it can reduce the rate at the outer mask to 0, even offering some margin by keeping the photon rate at a minimum, still above $15 \sigma_x$. The photon rate at the inner mask is reduced with

7.9. MITIGATION THROUGH COLLIMATORS

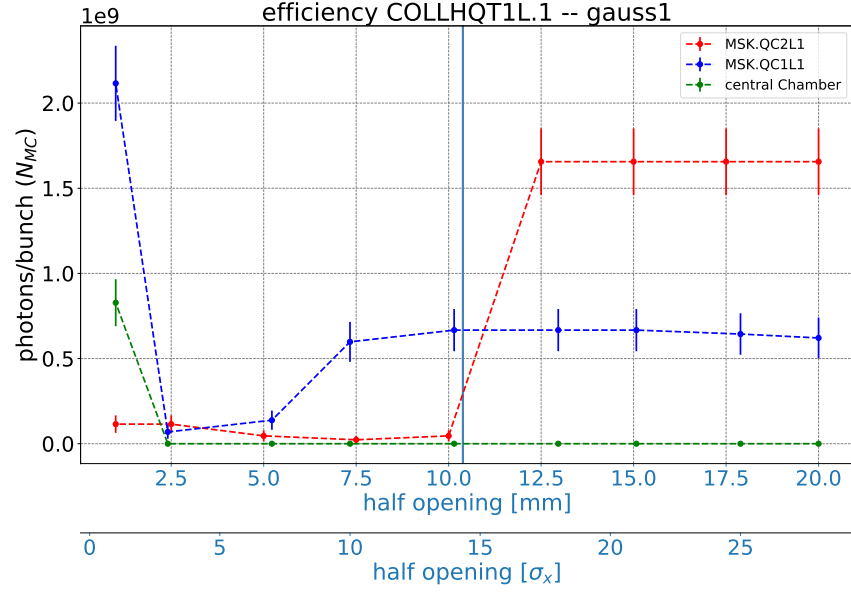


Figure 7.73: A collimator right at the exit of QT1L.2, about 50 m upstream, shows effects with half openings of less than 12.5 mm at the outer mask. The inner mask benefits from a reduction of direct hits if the collimator is closed to 7.5 mm and less. The rate of direct hits in the central chamber is enhanced with openings of less than 2.5 mm. A half opening of 35 mm would correspond to a fully opened collimator. The vertical line denotes $15 \sigma_x$ (dynamic aperture requirement).

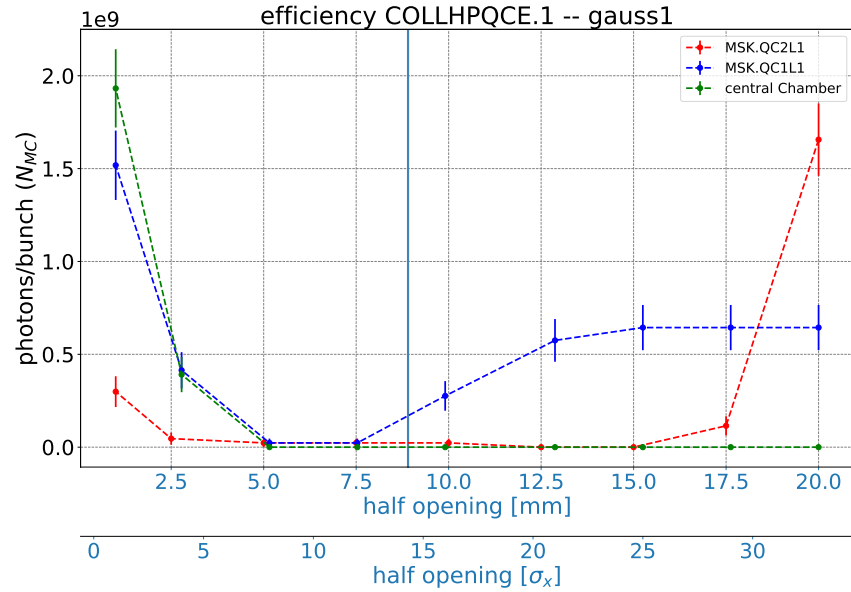


Figure 7.74: Efficiency of the near collimator COLH.PQC2LE, located about 10 m upstream of the interaction point. A reduction of the photon rate at the outer mask is achieved with half openings starting above $30 \sigma_x$. The photon rate at the inner mask decreases with closures of less than $25 \sigma_x$. Note that an increase of direct hits at the central chamber correlates with an increase at the inner mask. A half opening of 35 mm would correspond to a fully opened collimator. A vertical line denotes the $15 \sigma_x$ dynamic aperture requirement.

settings above $15 \sigma_x$ but the minimum for this location is only achieved by cutting into the dynamic aperture.

Collimation Efficiency – Horizontal Tails

The next set of collimation efficiency plots will be discussed for horizontal tails. Given the collimation efficiency in the previous scenario, the study now focuses on the impact of tails on the efficiencies in order to characterize their role in the background mitigation.

As before, the discussion does address all three collimators, one after the other.

Far-out Collimator – COLH.QC3L2. Contrary to the initial example (shown in Fig. 7.72), with horizontal tails, the collimator COLH.QC3L2 (at about 100 m distance from the interaction point) reduces the photon rates with closures well above the dynamic aperture requirement. The amount of direct hits on the outer mask MSK.QC2L is reduced with settings between $22.5 \sigma_x$ to $15 \sigma_x$, as depicted in Fig. 7.75.

The inner mask MSK.QC1L can benefit from a reduction of direct hits, if the collimator jaw is moved to positions between $18 \sigma_x$ to $15 \sigma_x$.

An increase of photon rates at both locations with closures less than $15 \sigma_x$ is in accordance with the fact that most particles are located at $15 \sigma_x$. Hence, the collimator jaw starts to cut into the tail.

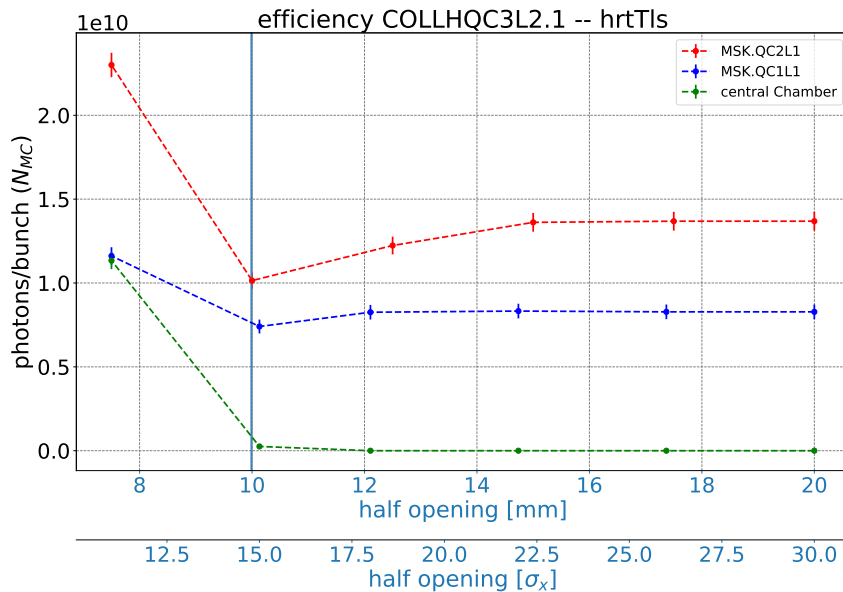


Figure 7.75: The photon rate on upstream synchrotron radiation masks as function of the jaw position of COLH.QC3L2, considering horizontal tails. The collimator is more efficient on the outer mask MSK.QC2L, reducing the rate from half openings of $22.5 \sigma_x$ to $15 \sigma_x$. A reduction of the photon rate at the inner mask is observable with closures between $18 \sigma_x$ to $15 \sigma_x$. Both locations show a steep rise in the photon rate with closures less than $15 \sigma_x$ as the jaw starts to cut into the halo. A vertical blue line denotes $15 \sigma_x$ – the dynamic aperture requirement.

Intermediate Collimator – COLH.QT1L2. The next collimator is located right at the exit of quadrupole QT1L.2, about 50 m upstream. The data samples show improved efficiency as well in Fig. 7.76. With closures between $25 \sigma_x$ to $15 \sigma_x$, the outer mask benefits from a reduction of the photon rate. Even the inner mask MSK.QC1L now sees a reduction of direct hits, in a narrow margin of settings ranging from $18 \sigma_x$ to $15 \sigma_x$. Both ranges are above the dynamic aperture requirement.

Settings below $15 \sigma_x$ lead to an enhancement of the background – which is related to interactions of the beam with the collimator jaw that starts to cut into the tail.

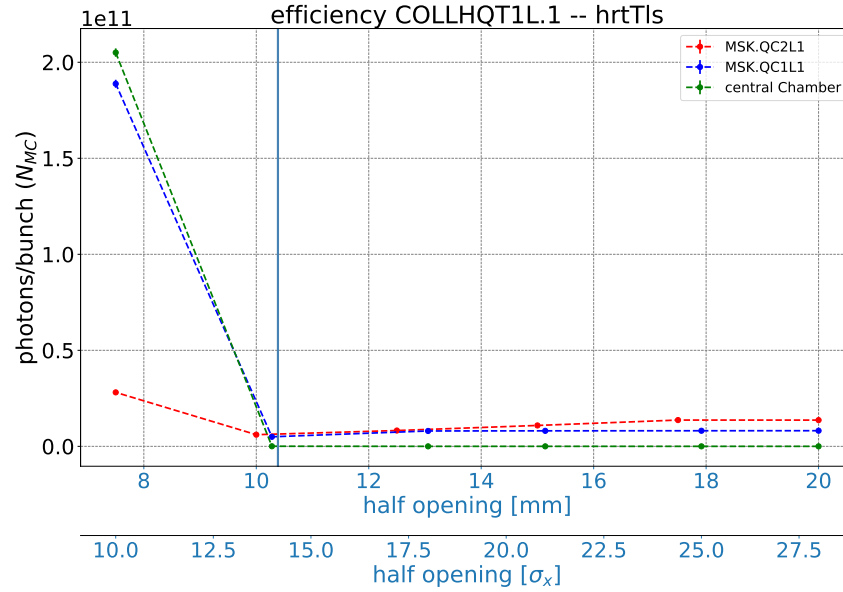


Figure 7.76: The photon rate on upstream synchrotron radiation masks as function of the jaw position of COLH.QT1L2, considering horizontal tails. The rate at the inner mask is now reduced as well by this collimator. At the outer mask, MSK.QC2L, a reduction in the amount of photons between $25 \sigma_x$ to $15 \sigma_x$ is observable. Jaw positions of less than $15 \sigma_x$ lead to significant increase in the photon rate at both locations and the central chamber – again caused by the jaw cutting into the tail. A vertical blue line denotes the $15 \sigma_x$ dynamic aperture requirement.

Near Collimator – COLH.PQC2LE. The third collimator is located 10 m upstream of the interaction point. Considering the inner mask, MSK.QC1L, it does reduce the photon rate with closures between $20 \sigma_x$ and $16 \sigma_x$, as shown in Fig. 7.77. The outer mask MSK.QC2L shows a reduction in the photon rate with jaw positions of about $34 \sigma_x$ and below, developing a broad minimum between $25 \sigma_x$ and $16 \sigma_x$. An increase of the photon rate is observed at both locations and the central chamber simultaneously with jaw positions of less than $15 \sigma_x$ – in accordance with the observations for the previous two collimators.

If horizontal tails start to dominate the radiation background, the far-out collimators COLH.QC3L2 and COLH.QT1L2 become much more relevant compared to a Gaussian bunch on axis without tails.

The far collimators can help to reduce an increased amount of photons coming from the upstream bends and quadrupoles.

Still, the importance of the near collimator, COLH.PQC2LE proves to be unchanged when horizontal tails are present. It offers a broad margin of settings, leading to a reduction of the photon rate. COLH.PQC2LE shows the highest efficiency of all three collimators – based on the data that was analysed so far.

In the framework of this study, a scenario based entirely on vertical tails is included. A discussion of collimation efficiency in that case will follow in the next subsection.

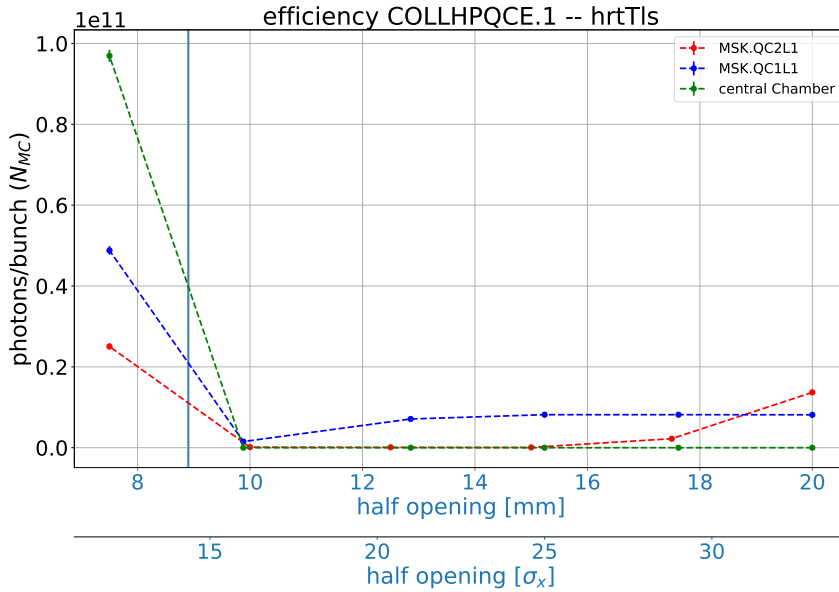


Figure 7.77: Effect of the near collimator, COLH.PQC2LE, about 10 m upstream of the interaction point, considering horizontal tails. Assuming a pure halo case with all beam particles on a ring at $15 \sigma_x$, this collimator reduces the photon rate at the outer mask from apertures of less than $34 \sigma_x$. The inner mask benefits from a reduction in rate between $25 \sigma_x$ and $21 \sigma_x$. At both locations and the central chamber, an increase of photons with half openings below $21 \sigma_x$ is observable. A vertical blue line denotes the $15 \sigma_x$ dynamic aperture requirement.

Collimation Efficiency – Vertical Tails

With horizontal tails, evidence could be found that far-out collimators become more relevant in mitigating the direct photon background (considering no scattering or X-ray reflection) than compared to the default scenario with a pure Gaussian bunch on axis.

In order to study the effect with pure vertical tails, the following discussion addresses the last set of collimation efficiency plots – based on data from the corresponding scenario with vertical tails out to $50 \sigma_y$ of Section 7.5.

Far-out collimator – COLH.QC3L2. The collimator around 90 m upstream falls basically back to the performance observed in the initial case (compare Fig. 7.78 and 7.72).

From slightly above $10 \sigma_x$, a reduction in the photon rate at the outer mask is visible, a setting well below the dynamic aperture requirement of $15 \sigma_x$. No reduction at the inner mask MSK.QC1L1 is observable, like in the initial case of Fig. 7.72.

Since this scenario considers a Gaussian core in the horizontal and vertical tails at $50 \sigma_y$, the collimator jaw does not cut in the beam core or the halo with closures above 4 mm. Therefore, the plot does not show an increase in the photon rate as observed before.

Significant horizontal tails might be effectively mitigated by this collimator, based on the data shown in Fig. 7.75. For vertical tails, however, the efficiency does not differ from the initial scenario.

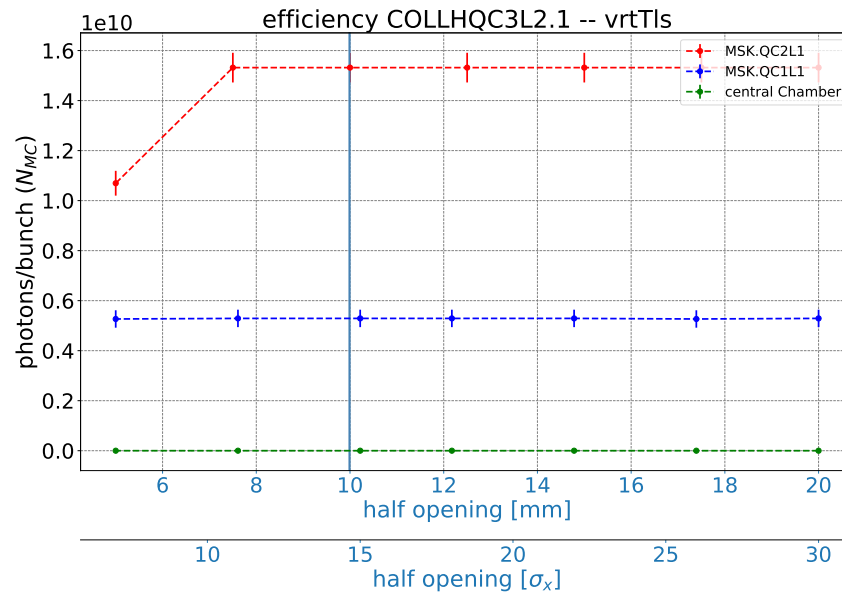


Figure 7.78: Photon rate at the upstream synchrotron radiation masks as function of the closure of the far-out collimator COLH.QC3L2, considering vertical tails. No effect at none of the masks is observed for half openings above $15\sigma_x$. A blue vertical line denotes the $15\sigma_x$ dynamic aperture requirement.

Intermediate collimator – COLH.QT1L2. What was observed with the far-out collimator, COLH.QC3L2, applies as well to the intermediate collimator, COLH.QT1L2: the performance is comparable to the initial scenario – compare plots 7.79 and 7.73.

Outside of the horizontal dynamic aperture of $15\sigma_x$, the photon rate is reduced only at the outer mask MSK.QC2L1. The collimator offers a certain range of settings where the rate remains in a minimum but then the jaw would cut into the dynamic aperture.

No reduction at the inner mask MSK.QC1L1 with jaw positions above $15\sigma_x$ is observable.

Near collimator – COLH.PQC2LE. Between closures of $35\sigma_x$ to $8\sigma_x$, COLH.PQC2LE leads to a reduction in the rate at MSK.QC2L1. The photon rate is kept at a minimum with settings of $25\sigma_x$ to $10\sigma_x$. Therefore, even when staying outside of the dynamic aperture, the photon rate can be significantly minimized.

The inner mask benefits from a decrease in the photon rate from settings below $25\sigma_x$. The minimum is only achieved below $15\sigma_x$, therefore the jaw would cut in the dynamic aperture. Still, the photon rate can be reduced at the inner mask as well while staying outside of the dynamic aperture.

Analysing the scenario with purely vertical tails shows that the collimation efficiency is basically comparable to the observation in the default scenario with a purely Gaussian bunch on axis.

It appears that the radiation background upstream of the central interaction region does not differ much, which is why the collimators do not have a significantly different influence on the photon rate at the synchrotron radiation masks.

The simulations of the vertical tails scenario showed a significant contribution of hits on the mask to originate from the upstream final focus magnets, as detailed

7.9. MITIGATION THROUGH COLLIMATORS

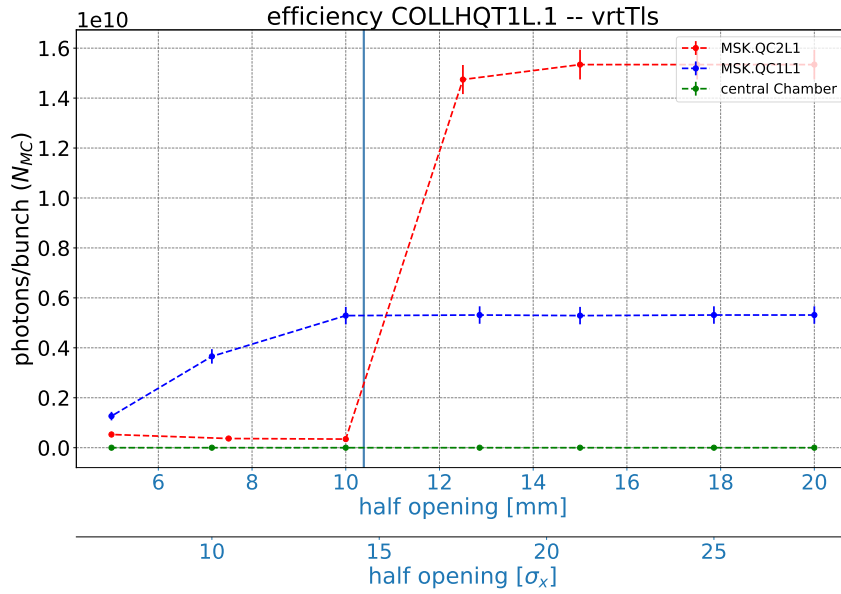


Figure 7.79: Collimation efficiency of the intermediate collimator QT1L.2, about 50 m upstream. The scenario considers purely vertical tails at $50 \sigma_y$ while having a Gaussian core in the horizontal plane. The photon rate at the outer mask can be reduced with openings of $17.5 \sigma_x$ and below, for the inner mask only settings of $10 \sigma_x$ and below lead to a reduction – well below the dynamic aperture requirement (indicated by the blue vertical line).

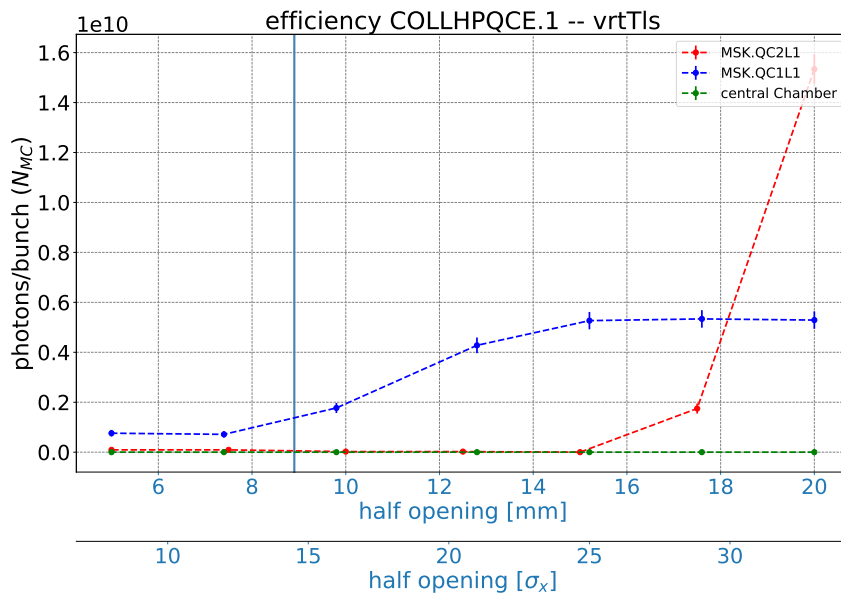


Figure 7.80: Collimation efficiency of the near collimator COLH.PQC2LE, in a scenario considering only vertical tails. Shown is the rate of expectable photons as function of the collimator half opening. The rate at the outer mask is reduced starting from about $35 \sigma_x$ half opening. With closures of less than $25 \sigma_x$, the inner mask benefits from a reduction as well. A blue vertical line denotes the $15 \sigma_x$ dynamic aperture requirement.

in Fig. 7.41 of Section 7.7. Those magnets are located very close to the interaction point and upstream collimators can not be expected to reduce this part of the radiation background – which is in accordance with the observations described in this subsection.

Summary on Collimation

Three scenarios were introduced, which allowed to study the evolution of the synchrotron radiation background in the FCC-ee interaction region from default (ideal) conditions to cases with strong tails. The simulations performed in the context of this study established a baseline to assess efficiencies of different collimators at changing positions upstream to mitigate the synchrotron radiation background.

An evaluation of the efficiency of a given collimator was done by using the photon rate at both synchrotron radiation masks and the central detector chamber – the goal was to minimize this rate or even bring it down to 0.

This subsection will finally wrap up the study of an initial collimation proposal by quickly summarizing the most important points learned from the study above.

- **Default conditions.** The collimation study started with a scenario based on a Gaussian bunch on axis. This beam did not exhibit a strong population of tails (particles at higher amplitude) and can therefore be considered as the *ideal case*. The far-out collimator (about 90 m upstream) could not reduce the photon rate at the masks while staying outside of the $15\sigma_x$ dynamic aperture.

The intermediate (about 50 m upstream) collimator could at least reduce the rate at the outer synchrotron radiation mask, with jaw positions above $15\sigma_x$. The inner mask would only benefit with settings significantly below the dynamic aperture requirement.

A collimator about 10 m upstream proved to be most useful in this scenario. With jaw positions well outside the dynamic aperture, the collimator could reduce the photon rate at the outer mask, even reaching a stable minimum for a range of settings. The inner mask benefits from a reduction of the rate – however, the minimum for this mask is reached only with jaw positions of less than $15\sigma_x$.

- **Horizontal tails.** The second scenario assumed a beam still on axis, but with a majority of particles at $15\sigma_x$ in the horizontal plane. A Gaussian core was kept in the vertical plane, to decouple the effects of horizontal and vertical tails.

It was possible to observe an increased efficiency of the far-out and intermediate collimator. Both could lead to a reduction of the photon rate at the synchrotron radiation masks while staying above the dynamic aperture requirement. However, in both cases a steep increase of the photon rate can be observed with jaw positions of less than $15\sigma_x$. The reason is simply that the jaw starts to cut in the tail of the beam.

Same applies to the near collimator, about 10 m upstream. Still, this collimator is most effective in this scenario, as it reduces the rate at the outer mask and reaches a minimum with jaw positions well outside of the dynamic aperture. The rate at the inner mask is also reduced, only not as efficiently as at the outer mask.

- **Vertical tails.** The third scenario reversed the settings: while keeping a Gaussian core in the horizontal, most particles in the vertical were placed at $50\sigma_y$ to represent strong vertical tails. Both of the collimators further upstream (about 50 m and 90 m, respectively)

fell back to the performance in the initial case. Only the near collimator about 10 m upstream from the interaction point could reach a significant reduction of the photon rates at both masks while keeping the jaw outside of the dynamic aperture.

From this initial study of a possible collimation scheme, a few points can be learned already.

Assuming an ideal case (Gaussian bunch perfectly following the design orbit, no tails), the synchrotron radiation masks appear sufficient to protect the central detector chamber. The simulations performed in the context of this study showed that the photon background – considering only 1st generation photons and direct hits – can be mitigated by these fixed absorbers.

However, experience from other machines, such as **LEP** or SuperKEKB showed, that background in the **MDI** is always a complicated, ever evolving subject that needs careful consideration – ideal conditions are rarely found in reality.

As soon as significant tails have been considered in the simulation, evidence could thus be found that fixed masks are struck by an increasing amount of photons, which tend to exceed the energy limitation of 100 keV. Hence, the power arriving at those masks can quickly overcome what is usually considered to be manageable. Especially at the inner mask, the fraction of photons scattering through the absorber increases in this case.

Without even considering X-ray reflection and multiple scattering, the scenarios investigated in the previous sections illustrate that a sophisticated collimation scheme upstream can help to mitigate the photon background and relax conditions in the central interaction region. Every photon which does not even reach the masks is one problem less for the detector.

Far-out and intermediate collimators can noticeably reduce enhanced synchrotron radiation at both masks, coming from horizontal tails. In that case, the upstream quadrupoles contribute to the background in the central interaction region. While the collimator jaws could stay out of the dynamic aperture – with positions between $25 \sigma_x$ to $15 \sigma_x$ – the photon rate was still reduced.

With vertical tails (actually the same observation as in the default case), far-out and intermediate collimators can not effectively reduce the photon rate, which – in this case – is caused by the final focus magnets and therefore too close to the detector.

Finally, it should be emphasized that the close collimator, about 10 m upstream, is **in every scenario** very effective in reducing the photon rate at the fixed masks. This collimator can mitigate the synchrotron radiation with jaw positions well above the dynamic aperture, even offering a margin of settings without cutting into the $15 \sigma_x$ requirement.

Final remark. The synchrotron radiation background depends on many external parameters – the particle distribution, if the beam is off- or on-axis, if there are strong tails or not – to name just a few. For that reason, backgrounds in the **MDI** of an accelerator should be rather considered as a dynamic and ever evolving subject, which changes over the course of operation.

8 | Conclusion

The **Future Circular Collider** study to investigate possibilities of circular colliders for future high-energy physics has taken the next step with publications of the **CDR** in 2019 and the update of the European Strategy for Particle Physics in June 2020 [2, 4].

This thesis gives an overview over the most important background processes and presents a first study of a possible collimation scheme to reduce the photon backgrounds in the interaction region.

Extensive Monte-Carlo simulations have been performed and benchmarked with SuperKEKB using MDISim.

To characterize the current state (based on the **CDR**), the **FCC-ee MDI** geometry model was refined to more closely match the foreseen layout, therefore including the central detector chamber model as well as upstream synchrotron radiation masks.

Benchmarking the simulation tools with the SuperKEKB interaction region in the context of this study shows that MDISim is able to reproduce the rather complicated closed orbit of the positron beam at SuperKEKB.

Background considerations have been taken into account in the basic **FCC-ee** layout and interaction region design. The last bending magnets, as seen from the experiments, have limited strength and are kept far from the detector.

This design is reviewed and studied here with emphasis on the synchrotron radiation background. The most important findings are that the synchrotron radiation background depends significantly on initial conditions of the beam. The **MDI** layout as foreseen in the **CDR** works well assuming ideal conditions.

Energies of photons reaching the interaction region and central chamber were found to be of sufficiently low energy, as demonstrated by a detailed study of the photon energy and interactions with the beam-pipe material. Hard radiation (high energy photons) from dipoles further upstream is kept at least 120 m away from the detector or is generated some tens of m or further downstream of the interaction point.

However, the study also showed that radiation from special magnets can generate photons of considerably higher energy than those from upstream dipole magnets. Especially with the presence of beam-tails, the scenario changes and additional collimation further upstream becomes favorable.

Synchrotron radiation masks improve the shielding of the central chamber. However, the analysis in this thesis showed that those masks are subject to a strong photon flux. Such a photon flux will lead to heating in the material and secondaries from scattering – conditions due to both effects can be relaxed by the use

of upstream synchrotron radiation collimators.

The discussion of an initial collimation proposal therefore concludes the presented study. Between the last upstream bend and the interaction point, taking into account the evolution of the beam size in this area, three positions have been identified which are suitable to host synchrotron radiation collimators.

This analysis allowed to conclude that synchrotron radiation collimators can help to significantly reduce the amount of photons reaching the central interaction region. Those collimators could be put at locations upstream, keeping sufficient distance from the detector.

As a comprised overview on expectable background effects in the FCC-ee MDI, the analysis presented in this thesis can complement the current conceptual design. More importantly, a detailed study of the synchrotron radiation, for the first time using a Monte-Carlo approach on the FCC-ee MDI, is an important continuation of early steps directed in this field [46, 14].

A second, extended five year study has just been launched and will address more technical details including magnet and vacuum chamber prototypes.

The conceptual studies with the algorithms and codes used and developed here have been chosen to be easily extendable, with in particular the possibility to 'plug in' detailed mechanical designs based on standard data and exchange formats.

In continuation of the work presented in this thesis, the integration of a more realistic vacuum chamber model is certainly on top of the list. A second point are X-ray reflections, which should be estimated since this effect can potentially change the conditions of the photon background. Orbit deviations, for instance caused by magnet misalignments should be included as well.

Simulating the synchrotron radiation in the SuperKEKB MDI and comparing with actual data could further proof the performance of MDISim – now that the basic suitability has been proven.

Future background studies should as well cover injection induced backgrounds. This would require to connect the simulation of the FCC-ee injector chain and main ring complex. Injected beams can be expected to generate spikes in background rates due to non-Gaussian beams. Those could be studied in the main ring using the techniques developed and described in the context of this thesis.

A | Geometry Transformations within MDISim

A.1 General Considerations

Mad-X provides the accelerator description in Frenet-Serret Coordinate System (or Courant-Snyder, CS) as illustrated in Fig. 2.2. Contrary to that, Root and Geant4 are based on Euclidean Coordinates (EU). Such a fundamental difference in reference coordinates requires MDISim to provide an inherent coordinate transformation formalism to translate between both systems, according to (A.1). This translation is an important tool for the presented study.

$$v_{\text{CS}} = \begin{pmatrix} x \\ y \\ s \end{pmatrix} \Leftrightarrow v_{\text{EU}} = \begin{pmatrix} x \\ y \\ z \end{pmatrix}$$

The Frenet-Serret system describes particle motion in an orthogonal coordinate system moving along the *design orbit*, as introduced in section 2.1 with Fig. 2.2.

Fundamental blocks of building an orbit in Mad-X are **bending magnets** and **straight elements**.

The reference orbit is defined entirely through dipole magnets, specifying an angle α , the length L and therefore a radius of curvature ρ . All other elements (quadrupoles, kickers, sextupoles, drifts, etc.) are treated as straight and therefore provide only their length L in terms of the design orbit [16].

The variables L and α are used for the transformation from the Courant-Snyder to Euclidean coordinate systems, in a combination of translation and rotation.

$$\mathbf{V}_i = W_{i-1} \mathbf{R}_i + \mathbf{V}_{i-1}, \quad (\text{A.1})$$

Where \mathbf{R}_i denotes the translation and W_i the rotation (or orientation). An index i refers to the current element, with the previous element indicated by $(i-1)$. As noted earlier, two cases are distinguished :

1. **Straight elements.** Bending angle α is zero, applies to all elements, except bends. The resulting coordinate transformation is a shift by element length L . The vector \mathbf{R} simplifies to

$$\mathbf{R}_i = \begin{pmatrix} 0 \\ 0 \\ L \end{pmatrix} \quad (\text{A.2})$$

The rotation matrix W is then simply the identity and for each step the same:
 $W_i = W_{i-1} = I$.

2. **Bending magnet.** Arc segments are characterized by a bending angle α and radius :

$$= L/\alpha \quad (\text{A.3})$$

With L being the arc length. This can be expressed as translation vector (A.4).

$$R_i = \begin{pmatrix} (\cos \alpha - 1) \\ 0 \\ \sin \alpha \end{pmatrix} \quad (\text{A.4})$$

The orientation W_i is a combination of three matrices for rotations about the axes x, y and s , respectively:

- x-axis: $W_\phi = \begin{pmatrix} 1 & 0 & 0 \\ 0 & \cos \phi & \sin \phi \\ 0 & -\sin \phi & \cos \phi \end{pmatrix}$
- y-axis: $W_\theta = \begin{pmatrix} \cos \theta & 0 & \sin \theta \\ 0 & 1 & 0 \\ -\sin \theta & 0 & \cos \theta \end{pmatrix}$
- s-axis: $W_\psi = \begin{pmatrix} \cos \psi & -\sin \psi & 0 \\ \sin \psi & \cos \psi & 0 \\ 0 & 0 & 1 \end{pmatrix}$

A general rotation in 3D space, defined by angles θ, ϕ and ψ , would be represented in the combination

$$W_i = W_\theta W_\phi W_\psi \quad (\text{A.5})$$

If any of these angles is 0, the corresponding matrix simplifies to the identity matrix. For a **flat machine**, $\phi = \psi = 0$ and $W_\phi = W_\psi = I$. In which case the only rotation would be done about the y -axis and expressed by W_θ .

Note, that the Mad-X coordinate system is always orientated clockwise, as **beam1** is oriented clockwise in the **LHC** convention, see Fig. A.1. Effects of a second beam, having the same charge as beam 1 would thus have to be reversed [16].

A.2 SingleBend – An Example

For a better understanding of the steps which usually conclude a full simulation in MDISim, an illustration is done using the SingleBend example.

A 10 m long dipole magnet is bent to a full ring of 2π and sliced into 10 pieces. The geometry is flat, which means that ϕ and ψ are both 0. Further, the ring is not rotated about the y -axis, $\theta = 0$. In total, the orientation W_i thus equals the identity I .

First thing to do is to run Mad-X on the example, specifying a positron beam with energy $E_b = 10$ GeV. Table A.1 presents a selection of parameters from the resulting TWISS table.

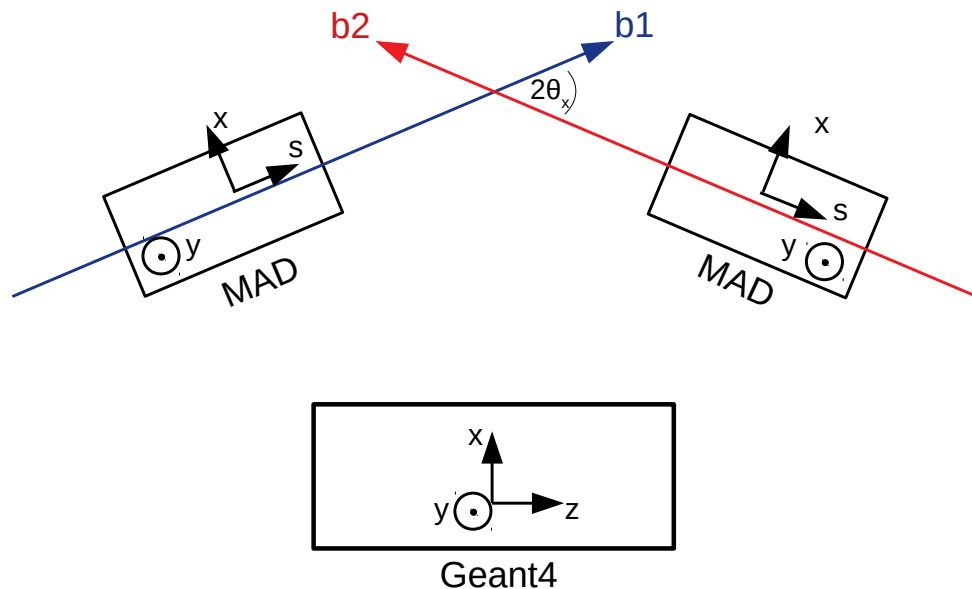


Figure A.1: Local coordinate system that is used by Mad-X with Geant4 system for reference. The sketch shows the LHC convention with beam1 moving clockwise. $2\theta_x$ denotes a possible horizontal crossing angle between both beams. If beam2 has the same charge, effects of magnetic elements need to be reversed.

After a completed Mad-X run, the information stored in the TWISS is used to generate a geometry. Parameters such as APERTYPE and APER define which element will be generated. In this example, each element has a circular aperture of 10 cm radius, which would default to a tube or a torus, based on the ANGLE parameter.

Since the SingleBend is divided in 10 pieces, each slice will be a torus-segment, where the curvature of that segment is defined by length L and ANGLE. Together, these elements complete the ring, as depicted in Fig. A.2 in Root display. This geometry is provided as GDML input to Geant4 for the particle tracking.

The last step is completed by tracking in Geant4. Figure A.3 (a) shows the primary particle track as red trajectory within the beam pipe. Note, that the particle loses energy due to synchrotron radiation and therefore slightly spirals inwards. Tracks of synchrotron radiation photons are shown in Fig. A.3 (b) as green straight lines. Note, that only part of the tracks are displayed in order to enhance visibility.

Even though a real accelerator lattice can be expected as much more complex, the steps shown here would be the same to perform a simulation of the photon background.

A.2. SINGLEBEND – AN EXAMPLE

Table A.1: A selection of parameters stored in the TWISS table after a successful Mad-X run. Parameters such as S , L , $ANGLE$, $APERTYPE$ and $APER$ are used to generate a 3D geometry as input for Geant4. But the table also features optical functions, for example the oscillation amplitudes β_x and β_y . Note that the attribute $APERTYPE$ is always $CIRCLE$ and therefore not explicitly shown.

NAME	KEYWORD	S	BETX	BETY	L	ANGLE	APER_1
START	MARKER	0	5	2	0	0	0
STRTM	MARKER	0	5	2	0	0	0
MBDEN	DIPEDGE	0	5	2	0	0	0
BND1	SBEND	0.5	4.57	2.13	0.5	0.314	0.1
BND2	SBEND	1.63	1.73	3.32	1.125	0.71	0.1
BND3	SBEND	2.75	0.62	5.78	1.125	0.71	0.1
BND4	SBEND	3.88	3.10	9.50	1.125	0.71	0.1
BND5	SBEND	5	4.99	14.5	1.125	0.71	0.1
BND6	SBEND	6.13	3.10	20.76	1.125	0.71	0.1
BND7	SBEND	7.25	0.62	28.28	1.125	0.71	0.1
BND8	SBEND	8.38	1.73	37.07	1.125	0.71	0.1
BND9	SBEND	9.5	4.57	47.13	1.125	0.71	0.1
BND10	SBEND	10	4.99	52	0.5	0.314	0.1
MBDEX	DIPEDGE	10	4.99	52	0	0	0
ENDM	MARKER	10	4.99	52	0	0	0
END	MARKER	10	4.99	52	0	0	0

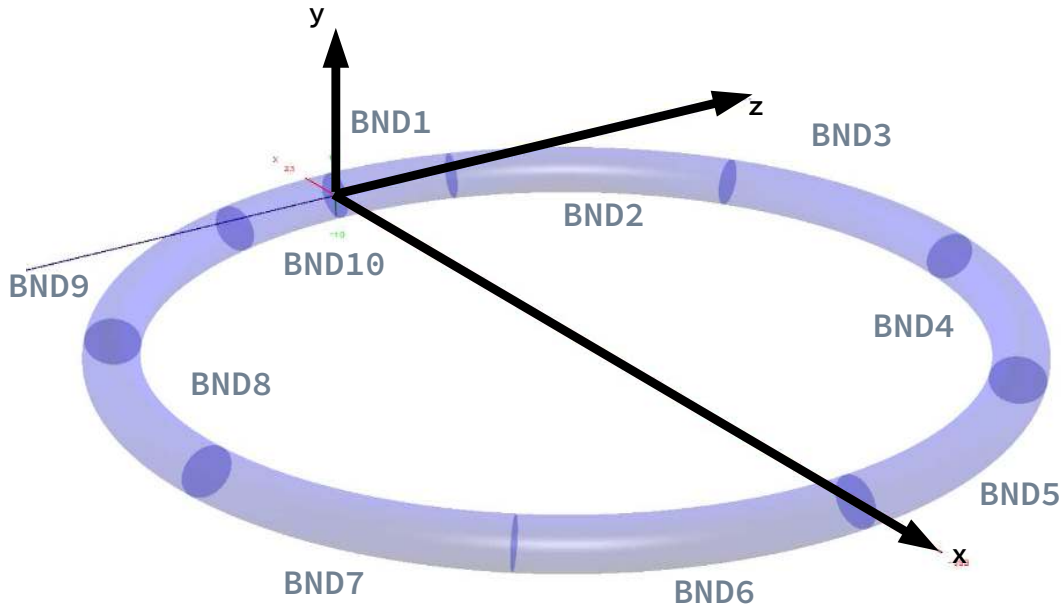


Figure A.2: Display of the generated 3D geometry for the SingleBend example in Root display. The ring is sliced into 10 parts, each part a torus-segment as denoted in the figure, as well as the axes of the Euclidean reference system.

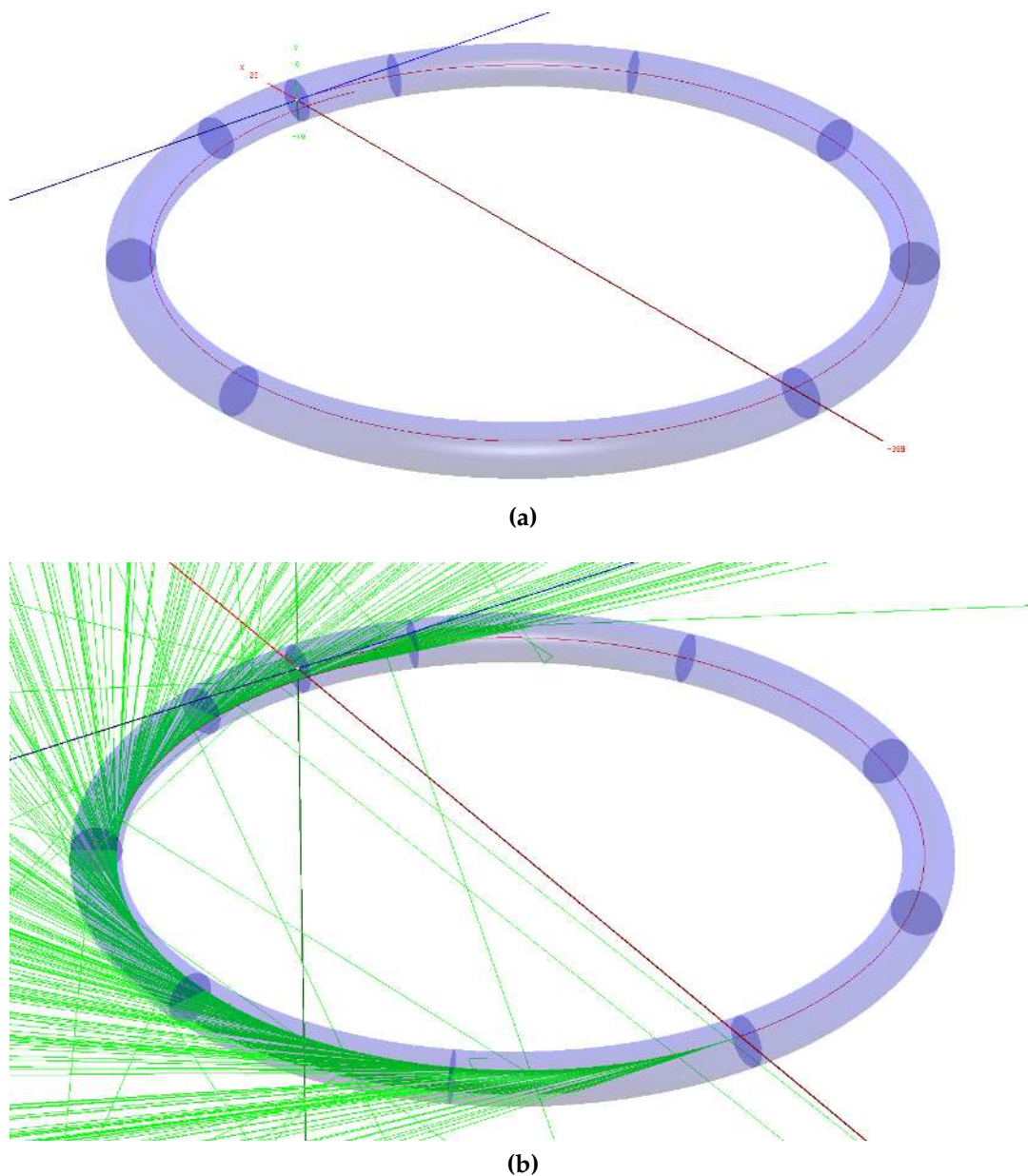


Figure A.3: Display of tracking results from Geant4 in Root display. (a) the trajectory of the primary beam in red. Note that it slightly spirals inwards as the particle loses energy from emitting synchrotron radiation. (b) selection of photon tracks along the beam trajectory as green straight lines. Note, that all other interaction processes had been switched off to purely display synchrotron radiation photons.

Bibliography

- [1] T. Nakada, "The European Strategy for Particle Physics: Update 2013," Tech. Rep. CERN-ESU-003, CERN, Geneva, 2013. Online available at: <https://cds.cern.ch/record/2690131>.
- [2] M. Benedikt, A. Blondel, O. Brunner, M. Capeans Garrido, F. Cerutti, J. Gutleber, P. Janot, J. M. Jimenez, *et al.*, "Future Circular Collider," Tech. Rep. CERN-ACC-2018-0057, CERN, Geneva, December 2018. Submitted for publication to Eur. Phys. J. ST.
- [3] A. Abada, M. Abbrescia, S. S. AbdusSalam, I. Abdyukhanov, J. Abelleira Fernandez, A. Abramov, M. Aburaia, A. O. Acar, P. R. Adzic, *et al.*, "FCC-hh: The Hadron Collider," *The European Physical Journal Special Topics*, vol. 228, pp. 755–1107, July 2019.
- [4] The European Strategy Group, "2020 Update of the European Strategy for Particle Physics," Tech. Rep. CERN-ESU-013, CERN, Geneva, 2020. Online available at: <https://cds.cern.ch/record/2720129>.
- [5] C. Adolphsen, "The International Linear Collider Technical Design Report - Volume 3.I: Accelerator R&D in the Technical Design Phase," Tech. Rep. arXiv:1306.6353, Argonne National Lab. (ANL), June 2013.
- [6] A. Robson, P. Burrows, N. Catalan Lasheras, L. Linssen, M. Petric, D. Schulte, E. Sicking, S. Stapnes, and W. Wuensch, "The Compact Linear e^+e^- Collider (CLIC): Accelerator and Detector," Tech. Rep. arXiv:1812.07987, CERN, December 2018.
- [7] The CEPC Study Group, "CEPC Conceptual Design Report: Volume 1 - Accelerator," Tech. Rep. arXiv:1809.00285, CEPC Study Group Collaboration, September 2018.
- [8] A. Blondel, P. Janot, N. Alipour Tehrani, P. Azzi, P. Azzurri, N. Bacchetta, M. Benedikt, F. Blekman, M. Boscolo, *et al.*, "FCC-ee: Your Questions Answered," Tech. Rep. arXiv:1906.02693, European Particle Physics Strategy Update 2018-2020, June 2019. Contribution to the European Particle Physics Strategy Update 2018-2020, available online <https://cds.cern.ch/record/2679488>.
- [9] G. von Holtey *et al.*, "Study of Beam Induced Particle Backgrounds at the LEP Detectors," *Nucl. Instrum. Meth.*, vol. A403, pp. 205–246, 1998.

- [10] R. Bailey, B. Balhan, C. Bovet, B. Goddard, N. Hilleret, J. M. Jimenez, R. Jung, M. Placidi, M. Tavlet, and G. von Holtey, "Synchrotron Radiation Effects at LEP," in *6th European Particle Accelerator Conference (EPAC 98)*, June 1998.
- [11] B. J. Holzer, "HERA: Lessons Learned from the HERA Upgrade," in *Final CARE-HHH Workshop on Scenarios for the LHC Upgrade and FAIR*, p. 5, November 2009.
- [12] M. Boscolo, O. Blanco-Garcia, N. Bacchetta, E. Belli, M. Benedikt, H. Burkhardt, M. Gil Costa, K. Elsener, E. Leogrande, *et al.*, "Machine Detector Interface for the e^+e^- Future Circular Collider," in *62th ICFA ABDW on High Luminosity Circular e^+e^- Colliders, eeFACT2018*, no. arXiv:1905.03528, p. 6, May 2019.
- [13] M. Boscolo, H. Burkhardt, and M. Sullivan, "MDI Studies: Layout and Synchrotron Radiation Estimate in the FCC Interaction Region," *Physical Review Accelerators and Beams*, vol. 20, Jan. 2017.
- [14] H. Burkhardt and M. Boscolo, "Tools for Flexible Optimisation of IR Designs with Application to FCC," in *6th International Particle Accelerator Conference*, p. TUPTY031. 3, 2015.
- [15] K. Wille, *Physik der Teilchenbeschleuniger und Synchrotronstrahlungsquellen. Eine Einfuehrung*. Teubner, 1992.
- [16] H. Grote, F. Schmidt, L. Deniau, G. Roy, and I. Tecker, *The MAD-X Program User's Reference Manual*. CERN, 5.02.12 ed., 2016.
- [17] S. Peggs and T. Satogata, *Introduction to Accelerator Dynamics*. Cambridge University Press, 2017.
- [18] W. Herr and T. Pieloni, "Beam-Beam Effects," in *CAS - CERN Accelerator School: Advanced Accelerator Physics*, no. arXiv:1601.05235. arXiv:1601.05235, pp. 431–459. 29 p, January 2016. 29 pages, contribution to the CAS - CERN Accelerator School: Advanced Accelerator Physics Course, Trondheim, Norway, 18-29 Aug 2013.
- [19] K. Oide *et al.*, "Design of beam optics for the future circular collider," *Phys. Rev. Accel. Beams*, vol. 19, p. 111005, November 2016.
- [20] C. Cook, B. Goddard, P. Lebrun, J. Osborne, Y. Robert, C. Sturzaker, M. Sykes, Y. Loo, J. Brasser, and R. Trunk, "FCC Civil Engineering – Tunnel Optimisation." Talk at the FCC Week 2016, <https://indico.cern.ch/event/438866/book-of-abstracts.pdf>, April 2016.
- [21] A. Wolski, "Low-Emittance Storage Rings," pp. 245–294. 50 p, July 2015. Presented at the CERN Accelerator School CAS 2013: Advanced Accelerator Physics Course, Trondheim, Norway, 18-29 August 2013.
- [22] B. Holzer, "Lattice Design in High-energy Particle Accelerators," no. arXiv:1601.04913, pp. 61–100. 40 p, 2014. 40 pages, contribution to the CAS - CERN Accelerator School: Advanced Accelerator Physics Course, Trondheim, Norway, 18-29 August 2013.
- [23] G. Voutsinas, N. Bacchetta, M. Boscolo, P. Janot, A. Kolano, E. Perez, M. Sullivan, and N. Tehrani, "Luminosity- and Beam- Induced Backgrounds for the

- FCC-ee Interaction Region Design,” no. CERN-ACC-2017-160, p. WEPIK004. 4 p, 2017.
- [24] M. Sullivan, “IR Layout with SR Masks and Shielding,” January 2018. Talk on the FCC-ee MDI Workshop, available online: https://indico.cern.ch/event/694811/contributions/2863801/attachments/1592752/2521296/sullivan_IR_issues.pdf.
- [25] A. M. Kolano, “Mitigation of Synchrotron Radiation from IR.” Talk at the FCC Week 2018, available online: https://indico.cern.ch/event/656491/contributions/2939123/attachments/1629676/2597213/SR_backgrounds_FCCweek_18_.pdf, April 2018.
- [26] J. D. Jackson, *Classical Electrodynamics*. Wiley, 1998.
- [27] M. Sands, “The Physics of Electron Storage Rings: An Introduction,” in *International School of Physics, Enrico Fermi, Course XLVI: Physics with Intersecting Storage Rings Varenna, Italy, June 16-26, 1969*, vol. C6906161, pp. 257–411, 1969.
- [28] R. P. Walker, “Synchrotron radiation,” in *CAS - CERN Accelerator School : 5th General Accelerator Physics Course*, pp. 437–459, 1994.
- [29] H. Burkhardt, “Radiation Generated at the IP.” Talk in the 105th FCC-ee Optics Design Meeting, available online: https://indico.cern.ch/event/854159/contributions/3592124/attachments/1924594/3185040/RadFromIP_2019_10.pdf, October 2019.
- [30] A. Hofmann, “Characteristics of Synchrotron Radiation,” in *CAS - CERN Accelerator School : Synchrotron Radiation and Free Electron Lasers*, pp. 1–44, 1998.
- [31] M. Brugger, H. Burkhardt, B. Goddard, F. Cerutti, and R. G. Alia, *Interactions of Beams with Surroundings*, pp. 183–203. Springer International Publishing, 2020.
- [32] A. Wolski, *Beam Dynamics in High Energy Particle Accelerators*. World Scientific, 2014.
- [33] V. I. Telnov, “Scattering of Electrons on Thermal Radiation Photons in Electron-Positron Storage Rings,” *Nuclear Instruments and Methods in Physics Research Section A: Accelerators, Spectrometers, Detectors and Associated Equipment*, vol. 260, no. 2-3, pp. 304–308, 1987.
- [34] B. Dehning, A. Melissinos, F. Perrone, C. Rizzo, and G. Von Holtey, “Scattering of High Energy Electrons off Thermal Photons,” *Physics Letters B*, vol. 249, no. 1, pp. 145–148, 1990.
- [35] H. Burkhardt, “Monte Carlo Simulation of Scattering of Beam Particles and Thermal Photons,” Tech. Rep. SL-Note-93-73-OP, CERN, Geneva, Jul 1993.
- [36] I. Reichel, *Study of the Transverse Beam Tails at LEP*. PhD thesis, Rheinisch-Westfälische Technische Hochschule Aachen, 1998. Presented on 3 July 1998.
- [37] M. Boscolo, O. Blanco-García, H. Burkhardt, F. Collamati, R. Kersevan, and M. Lueckhof, “Beam-gas Background Characterization in the FCC-ee IR,” in *Journal of Physics: Conference Series*, vol. 1067, p. 022012, IOP Publishing, 2018.

- [38] Y.-S. Tsai, "Pair Production and Bremsstrahlung of Charged Leptons," *Reviews of Modern Physics*, vol. 46, no. 4, p. 815, 1974.
- [39] R. Kersevan and J.-L. Pons, "Introduction to MOLFLOW+: New Graphical Processing Unit-Based Monte Carlo Code for Simulating Molecular Flows and for Calculating Angular Coefficients in the Compute Unified Device Architecture Environment," *Journal of Vacuum Science & Technology A: Vacuum, Surfaces, and Films*, vol. 27, pp. 1017–1023, August 2009.
- [40] J. Le Duff, "Single and Multiple Touschek Effects," in *CAS - CERN Accelerator School : 5th Advanced Accelerator Physics Course*, no. LAL-RT-88-08, p. 17, June 1988.
- [41] A. Piwinski, "The Touschek Effect in Strong Focusing Storage Rings," Tech. Rep. DESY-98-179, DESY, November 1998.
- [42] Website of the MAD project, "MAD - Methodical Accelerator Design." Online: <http://mad.web.cern.ch/mad/>.
- [43] K. Yokoya and P. Chen, "Beam-Beam Phenomena in Linear Colliders," *Lect. Notes Phys.*, vol. 400, pp. 415–445. 38 p, April 1991.
- [44] K. Ohmi and F. Zimmermann, "FCC-ee/CepC Beam-Beam Simulations with Beamstrahlung," in *5th International Particle Accelerator Conference*, no. CERN-ACC-2014-0172, p. 4, July 2014.
- [45] G. Voutsinas, E. Perez, M. Dam, and P. Janot, "Beam-beam Effects on the Luminosity Measurement at FCC-ee," *JHEP*, vol. 1910, pp. 225–248, August 2019. Version 3: Now published in JHEP.
- [46] M. Boscolo, H. Burkhardt, and M. Sullivan, "Machine Detector Interface Studies: Layout and Synchrotron Radiation Estimate in the Future Circular Collider Interaction Region," *Phys. Rev. Accel. Beams*, vol. 20, pp. 011008–1–011008–7, January 2017.
- [47] F. Collamati, M. Boscolo, H. Burkhardt, and R. Kersevan, "Synchrotron Radiation Backgrounds for the FCC-hh Experiments," in *Journal of Physics: Conference Series*, vol. 874, p. 012004, IOP Publishing, 2017.
- [48] R. Chytracsek, J. McCormick, W. Pokorski, and G. Santin, "Geometry Description Markup Language for Physics Simulation and Analysis Applications," *IEEE Trans. Nucl. Sci.*, vol. 53, p. 2892, October 2006.
- [49] CERN, *GDML User's Guide*, 2.8 ed., 2020.
- [50] I. Antcheva, M. Ballintijn, B. Bellenot, M. Biskup, R. Brun, N. Buncic, P. Canal, D. Casadei, O. Couet, V. Fine, *et al.*, "ROOT—A C++ Framework for Petabyte Data Storage, Statistical Analysis and Visualization," *Computer Physics Communications*, vol. 180, no. 12, pp. 2499–2512, 2009.
- [51] The website of the ROOT project, "ROOT - Data Analysis Framework." Online: <https://root.cern.ch/>.
- [52] The website of the GEANT4 project, "Geant4 - A Simulation Toolkit." Online: <http://geant4.web.cern.ch/>.

- [53] S. Agostinelli, J. Allison, K. Amako, J. Apostolakis, H. M. Araújo, P. Arce, M. Asai, D. A. Axen, S. Banerjee, *et al.*, “GEANT4 – A Simulation Toolkikt. GEANT4.,” *Nucl. Instrum. Methods Phys. Res., A*, vol. 506, pp. 250–303. 54 p, July 2002.
- [54] P. Raimondi, D. N. Shatilov, and M. Zobov, “Beam-Beam Issues for Colliding Schemes with Large Piwinski Angle and Crabbed Waist,” *arXiv e-prints*, p. 12 p, February 2007.
- [55] T. Ishibashi, Y. Suetsugu, and S. Terui, “Collimators for SuperKEKB Main Ring,” in *Proc. of International Particle Accelerator Conference (IPAC’17), Copenhagen, Denmark, 19 May, 2017*, no. 8 in International Particle Accelerator Conference, (Geneva, Switzerland), pp. 2929–2932, JACoW, May 2017. Online: <https://doi.org/10.18429/JACoW-IPAC2017-WEPIK009>.
- [56] Y. Ohnishi, T. Abe, T. Adachi, K. Akai, Y. Arimoto, K. Ebihara, K. Egawa, J. Flanagan, H. Fukuma, Y. Funakoshi, *et al.*, “Accelerator Design at SuperKEKB,” *Progress of Theoretical and Experimental Physics*, vol. 2013, no. 3, 2013.
- [57] S. Vahsen, P. Lewis, I. Jaegle, H. Nakayama, A. Aloisio, F. Ameli, M. Barrett, A. Beaulieu, *et al.*, “First Measurements of Beam Backgrounds at SuperKEKB,” *Nucl. Instrum. Methods Phys. Res., Sect. A*, February 2018.
- [58] T. Abe, I. Adachi, K. Adamczyk, S. Ahn, H. Aihara, K. Akai, M. Aloi, L. Andricek, K. Aoki, *et al.*, “Belle II Technical Design Report,” Tech. Rep. arXiv:1011.0352. KEK REPORT 2010-1, KEK, November 2010.
- [59] N. Ohuchi, B. Parker, M. Tartaglia, T.-H. Kim, K. Aoki, Y. Ohnishi, Y. Arimoto, M. Kawai, H. Sugimoto, G. Velev, *et al.*, “Final-Focus Superconducting Magnets for SuperKEKB,” in *The 9th International Particle Accelerator Conference (IPAC’18)*, April 2018.
- [60] Y. Arimoto *et al.*, “Solenoid Field Calculation of the SuperKEKB Interaction Region,” *Conf. Proc.*, vol. C1205201, pp. 3548–3550, 2012.
- [61] The website of the SAD project, “SAD - Strategic Accelerator Design.” Online: <http://acc-physics.kek.jp/SAD/>.
- [62] C. Wyss, *LEP design report, v.3: LEP2*. Geneva: CERN, 1996. Vol. 1-2 publ. in 1983-84.
- [63] T. Ishibashi, S. Terui, and Y. Suetsugu, “Low Impedance Movable Collimators for SuperKEKB,” *Proceedings of the IPAC ’17*, vol. 17, pp. 14–19, 2017.
- [64] D. Shatilov. private communication.
- [65] D. Schulte, “Beam-beam simulations with GUINEA-PIG,” in *5th International Computational Accelerator Physics Conference*, pp. 127–131, September 1998.
- [66] M. Sullivan, “Preliminary Look at the FCC-ee IR Layout,” April 2016. Talk at the FCC-ee MDI Meeting #2, available online: https://indico.cern.ch/event/505685/contributions/2016962/attachments/1251831/1846172/FCC_IR_Layout_04Apr16_meeting_sullivan.pdf.
- [67] M. Sullivan. private communication.

BIBLIOGRAPHY

- [68] H. Burkhardt. private communication.
- [69] G. Von Holtey, "LEP Main Ring Collimators," Tech. Rep. CERN-LEP-BI-87-03, CERN, Geneva, February 1987.

Acknowledgement

May people guided me on the path to bring this thesis to a successful end. I would like to express deepest gratitude to all of them. Special thanks go out to:

Dr. Helmut Burkhardt, who agreed not only to supervise the topic of background process in the FCC-ee MDI but also accepted me as a Doctoral Student. We had countless fruitful discussions, covering a wide range of background processes, particle physics and coding. He advised me on how to get started with MDISim and continued to share his expertise. He also gave many comments which lead to improvement of the presented thesis.

Prof. Wolfgang Hillert accepted me as a PhD student and agreed to be my university supervisor. He provided support in all formal questions and allowed me to present my work in seminars at DESY.

Dr. Frank Zimmermann for helping me with his contacts in the field and opening up the way to KEK. He enabled me to join the SuperKEKB commissioning and established contacts with the responsible people at KEK.

Last but not least he put a lot of effort in helping me to stay at CERN as COAS in times of the crisis around COVID-19.

Prof. Katsunobu Oide, for his patience in many discussions we had about SAD and the translation to Mad-X. He also helped me with questions about FCC-ee and SuperKEKB optics.

Dr. Hiroyuki Nakayama agreed to be my supervisor at KEK and was always available to answer questions and helping me to understand the SuperKEKB interaction region design. He further allowed me to stay at the control room during background studies to gain direct impressions on accelerator operation.

Dr. Demin Zhou took some of his precious time to explain me the complicated interaction region modelling of SuperKEKB in SAD. Without the insight provided by him, achievements with MDISim on SuperKEKB wouldn't have been possible.

Dr. Yoshihiro Funakoshi and Prof. Makoto Tobiyama for allowing me to visit KEK two times, in 2018 and 2019 and supporting my stay.

Mrs. Sachiko Arimoto for her selfless commitment to facilitate my visit at KEK and taking care of many arrangements and preparations.

Dr. Tokio Kenneth Ohsaka, who took his part in shaping my stay in Japan into a pleasant experience and helped to overcome all struggles and problems that are inevitably encountered while visiting a foreign country for the first time. He

never failed to remind me how important the successful completion of the thesis would be whenever I struggled to keep focus.

Mr. Mike Sullivan, who was always willing to share his expertise on the MDI design and committed a great deal of time for discussions with me while we both stayed at KEK.

Mrs. Manuela Boscolo who coordinates the FCC-ee MDI design efforts at CERN. She introduced me to the design team and allowed many possibilities for presentations and discussions and suggested me to provide input for the FCC conferences in 2018 and 2019.

Dr. Michael Benedikt and Dr. Frank Zimmermann as project leaders of the FCC-ee, for giving opportunities to present my work at conferences.

Dr. Rüdiger Schmidt, who kindly agreed to read my thesis and provided detailed feedback which could only improve the final result.

Dr. Bernhard Holzer not only gave me chances to present my work during several occasions, he was always happy to discuss aspects of accelerator physics over a coffee and read and commented this thesis extensively.

I would also like to thank Dr. Ralph Aßmann at DESY for suggesting this topic as a PhD thesis and supporting me in my intention to become a PhD student at CERN.

Dr. Massimo Giovannozzi as leader of the HSS section in the BE-ABP group at CERN for being always available to answer questions and support me with formal issues and enabled the participation in training courses.

Emmanuel Perez for sharing his insight in Beamstrahlung and GuineaPig. He was available for many discussions and never hesitated to help me. He also provided the 3D model of the central chamber and gave support while I integrated it in our model.

Kyrre Ness Sjobaek and Veronica B. Olsen for sharing their expertise in coding with me. Countless discussions with them helped me out of the many pitfalls along the way of introduction to C++, UNIX, Git, python and others.

Michael Hauschild for accepting me as a student in the Wolfgang Gentner program at CERN. He also allowed me to present my work during the semi-annual meetings at CERN.

To my family and friends who helped me to find new motivation whenever it was needed. Especially Ricco, who facilitated long hours of writing with his feathery presence.

Above all, thanks go out to my parents. Their support seemed to have known no limits and carried me all the way towards a successful completion of this thesis. Without them, I wouldn't have been able to spend several years at CERN to focus entirely on the PhD research.